THE DEVELOPMENT AND UTILIZATION OF INELASTIC ELECTRON TUNNELING SPECTROSCOPY AS A SURFACE VIBRATIONAL PROBE WITH AN EMPHASIS ON THE STUDY OF CHEMISORPTION AND HETEROGENEOUS CATALYSIS

Thesis by

William Matthew Bowser

In Partial Fulfillment of the Requirements
for the Degree of

Doctor of Philosophy

California Institute of Technology
Pasadena, California

1980

(Submitted February 11, 1980)

Acknowledgments

I would like to express my appreciation to my research advisor, W. Henry Weinberg, for his assistance and support through the course of this research. I would also like to thank Blair F. Lewis for his generous help, especially in the early stages of this work.

I appreciate also the assistance and friendship of the other members of our research group in particular, as well as the other students I have come to know here. I would like to extend special thanks to Howard E. Evans for his considerable contribution to my stay here.

There are many other people to whom I would like to express my appreciation, especially, Kathy Lewis, George Griffith, Chic Nakawatase, Ray Reed, Henry Smith and John Yehle.

The National Science Foundation, The American Vacuum Society, the Department of Health, Education and Welfare as well as Caltech have all contributed to my financial support during the course of this work.

Abstract

Inelastic electron tunneling spectroscopy (IETS) has been used to investigate the vibrational structure of molecular species bound to, or contained in, the insulating layer of Al-insulator-Pb tunnel junctions. The insulating layer, prepared by the exposure of the Al electrode to an oxygen plasma discharge, was studied via IETS and was found to be an oxide rather than a hydroxide. An oxide with appreciable hydroxide content could be prepared under certain conditions. An X-ray photoelectron spectroscopic (XPS) study of this oxide layer was also carried out to further facilitate comparison to commercial aluminas. IETS was used to investigate the chemisorption on this oxide of phenol and three derivatives of phenol: catechol, resorcinol and hydroquinone. Phenol adsorbs as a phenoxide ion, catechol and resorcinol lose both of their acidic protons upon chemisorption, whereas hydroquinone only loses one proton, bonding as a mono-ion. This study demonstrated the high sensitivity and resolution of IETS. IETS was also used in the study of supported metal catalysts. The adsorption of ethanol on silver particles supported on alumina was studied, extending the use of IETS in supported metal catalysis. An important area of current research is concerned with the fixing of metal cluster compounds on substrates to form catalysts. IETS was used to study the interaction of $[RhCl(CO)_2]_2$ on alumina, the first reported study of a metal carbonyl complex via IETS. This complex decomposes upon chemisorption, leaving, predominantly, isolated $Rh(CO)_2$ species on the surface. In contrast, $Ru_3(CO)_{12}$ is seen, via IETS, to retain its molecular structure upon adsorption on alumina. A method for heating the IETS sample easily and quickly is also presented.

TABLE OF CONTENTS

Chapter I

Introduction

There is no question as to the technological importance of surface science, not only in the part it plays in any given field, but also in the number of areas where surface and interfacial phenomena take a significant role. In addition to chemisorption and heterogeneous catalysis, which have obviously close ties to surface science, areas such as materials and microelectronics have also an interest in what occurs at the surface. Materials research must consider such phenomena as corrosion, adhesion, lubrication and friction and wear. The microelectronic industry must understand epitaxial growth mechanisms, Schottky barrier formation and the interfacial physics occurring in metal-oxide-semiconductor (MOS) structures.

Adsorption and heterogeneous catalysis is one important field where surface science is making a significant contribution to the understanding of the physics and chemistry involved. This area is also one in which the knowledge gained through basic and applied research has the potential of yielding significant economic as well as technological returns in the future. Consider that catalysis contributes, at some point, in the production of more than 20% of all commercial goods (1) and, more specifically, contributes to the production of over 90% of all chemical products (1). Thus, even slight gains in the efficiency of catalysts can have a significant economic effect. Catalysts contribute also to the environmental quality by reducing pollution as, for example, in the use of automotive exhaust catalytic converters. More efficient catalysts also reduce industrial waste by-products by more complete utilization of the raw materials. This also contributes to the conservation of our natural resources.

The efficiency of a catalyst is determined by several of its properties. First is selectivity: for a given set of reactants, what proportion of the product distribution is the desired material? Second is the yield: how completely are the reactants used with the catalyst present? Third is the turnover number: how often does each exposed catalytic center take part in a molecular reaction? Fourth: how much energy must be put into the system for the desired chemical reactions to take place? Thus, the most efficient catalyst would be one that would, for a given set of reactants, produce the largest percentage of the desired product while most completely and rapidly using the reactants with the least amount of energy input.

Most commercial catalysts in use today were developed, essentially, by a method of trial-and-error. That is, an experimental catalyst was made up following a certain recipe which was developed empirically, and its macroscopic properties (e.g., selectivity, yield, turnover number) were studied to determine its efficiency in a given reaction. Significant improvements in catalysts have been achieved over the years by following this routine, and further refinements will probably continue to be made in this manner. However, the ultimate goal in heterogeneous catalysis is to be able to design a specific catalyst to most efficiently enhance a given reaction. In order to make progress toward this goal, a firm understanding of how catalysts function on a molecular level is imperative.

Research in the area of fundamental catalysis is presently flourishing due, in large part, to the discovery and development of several surface analytical tools which yield much information about the processes occurring at a surface on an atomic scale. The atomic constituents present in the

surface region may be determined, often quantitatively, with the use of Auger spectroscopy (2) and X-ray photoelectron spectroscopy (3). The electronic state of the surface may be probed using ultraviolet (4) and X-ray photoelectron spectroscopies. Adsorption and desorption mechanisms may be studied by means of thermal desorption mass spectrometry (5) and work function measurements (6). The geometry of single crystal surfaces and the structure and long range order of adsorbates on single crystal surfaces may be studied using low-energy electron diffraction (7) (LEED). More recently, surface extended X-ray absorption fine structure spectroscopy (SEXAFS) has begun to yield information on the short range order of adsorbate-adsorbent systems (8). Vibrational information on surface-adsorbate systems may be obtained from infrared (IR) spectroscopy (9), surface laser Raman spectroscopy (10), high resolution electron energy loss spectroscopy (EELS) (11) and inelastic electron tunneling spectroscopy (IETS) (12 - 15). All of these techniques complement each other, and, when used in conjunction, a great deal may be learned about the surface and its interaction with adsorbates.

Vibrational spectroscopies are especially useful in their ability to yield much information on several types of surface phenomena, such as surface bonding, surface concentrations, adsorption kinetics, adsorbate orientation, adsorbate-adsorbate interactions and surface reactions. Often vibrational spectra may be used as a "fingerprint" technique in determining exactly what species are present.

The three most versatile vibrational probes used in surface research are IR spectroscopy, EELS and IETS. Each method has its own advantages and disadvantages, as shown in Table I. They should be considered as

complementary techniques rather than any one being the perfect probe.

The work presented in this thesis deals with one of these techniques: inelastic electron tunneling spectroscopy. The proposed goal of this work was twofold: (1) To contribute to the development of IETS into a useful and versatile surface vibrational probe, and (2) To demonstrate its usefulness to the field of chemisorption and heterogeneous catalysis through the investigation of several adsorption systems.

Inelastic electron tunneling spectroscopy (IETS) is a relatively recent technique, first discovered and successfully interpreted by Jaklevic and Lambe (16) in 1966. IETS makes use of a planar, thin film metal-insulator-metal tunnel junction. By applying a potential across this junction and analyzing the resulting current vs. voltage properties, vibrational information about molecular species in the insulator region may be obtained, as described below. Thus, by adsorbing a molecular species of interest on the surface of the insulating layer before the second metal electrode is deposited, vibrational information on this adsorbate may be found. Since its discovery, a number of papers have been published dealing not only with chemisorption and catalysis but with such diverse fields as adhesion (17), radiation damage (18), detection of trace substances (19), and molecular biology (20).

In all the work presented in this thesis an aluminum-aluminum oxide-adsorbate-lead junction composition was used. Aluminum was selected for the first metal electrode, primarily, for two reasons. First, aluminum is a convenient metal to work with. High quality thin films of Al are easily evaporated in vacuum. Also, aluminum may be oxidized in an oxygen plasma, forming a dense, continuous oxide layer 15 to 30 Å thick with very good

insulating properties. These are important characteristics for the insulating barrier of the tunnel junction. The second reason for choosing Al is that the resulting oxide, upon which the adsorption studies are carried out, may be used as a model for commercial aluminas which are important not only as supports for high surface area dispersed metal catalysts but also for the catalytic properties of the alumina itself.

There were also two reasons for choosing lead as the second metal electrode material. First, lead atoms are chemically inert and have a large ionic radius. Thus, when the Pb is deposited, it is unlikely that the Pb will interact chemically with the adsorbate-adsorbent system under study. Also, since the atoms are large, diffusion of the Pb past the adsorbate molecules into the oxide is minimized, which is important in maximizing the intensity of the adsorbate IET spectrum. The second reason for choosing Pb is that it has a rather high superconducting transition temperature so the lead is a superconductor at the temperature at which the IET spectra are measured (4.2 K). This increases the resolution of the technique (21).

The experimental procedure followed in the preparation of IETS tunnel junctions is quite straightforward. As mentioned above, these junctions are thin film devices and are completely fabricated at the time of the experiment. The steps followed in the preparation are illustrated in Fig. 1. Since these devices involve the evaporation of metals and require a clean, contaminant free environment, the entire junction fabrication process is carried out in a high vacuum system. The substrates used for the tunneling samples are glass microscope slides (25x11x1 mm), carefully cleaned and blown dry with high purity nitrogen gas. Electrical

contact pads of In solder are attached as shown in Fig. 1(a). The substrate is mounted in the vacuum system and the chamber is evacuated. Next, an Al strip of approximate dimensions 2 mm wide by 20 mm long by 800 Å thickness is evaporated (Fig. 1(b)). The thin leads extending from the side of the main Al strip are used in the resistive heating of the sample, as described in Chapter 2 of this thesis. This fresh Al film is then oxidized in a plasma discharge initiated in 0.12 to 0.16 torr of high purity oxygen gas. The oxygen pressure is adjusted to stabilize the discharge at 20 mA. The oxidation time is selected, essentially, by trial-and-error so that the resistance of the completed junction for a given adsorbate exposure lies in the range 20 to 200 ohms. A similar plasma discharge in water vapor and deuterium oxide vapor has been successfully used, as described in Chapter 3. Other methods of oxidation have been employed, such as thermal oxidation in air (22) or dipping in liquid water (23). This group, however, favors the plasma oxidation in oxygen in that this method produces an oxide of low hydroxide content (important in modeling commercial aluminas), and also with this method the junction need not be exposed to the atmosphere and possible air borne contaminants. This oxide layer must be uniform and pin hole free so that the primary current which may flow through it will be by electron tunneling.

It is on the surface of this aluminum oxide layer that the experiments of interest are carried out. This may involve the investigation of the oxide itself (Chapter 3), adosrption of organic acids (Chapters 4 and 5) on the oxide surface, the deposition of small amounts of a metal and subsequent exposure to an adsorbate (Appendix E) or the reaction of metallic compounds, such as transition metal carbonyls, with the aluminum oxide

(Chapters 6 and 7).

The final step in the junction preparation is the evaporation of the lead cross strips, illustrated in Fig. 1(c), completing the Al-Al oxide-adsorbate-Pb geometry. The crossed strip geometry of the sample allows for a four-point probe investigation of the junction current-voltage characteristics.

The phenomenology of the IETS process which occurs in these junctions may be understood from elementary quantum mechanics and conservation of energy. We can view the metal-insulator-metal junction from a distance-energy point of view, as illustrated in Fig. 2, where the horizontal axis represents position along a line perpendicular to the junction plane, and the vertical axis represents increasing electron energy. In the low temperature limit, the electrons in the two metals completely fill the states available to them up to the Fermi level, E_F. The states above E_F remain empty, and the transition from filled to empty states is quite sharp. When no potential drop exists across the barrier, the Fermi levels in the two metals are aligned. As a potential, eV, is applied across the junction, the Fermi levels of the metals shift with respect to each other. Classically, no current would flow at this point, since no electrons would have sufficient energy to pass over the barrier. Quantum mechanically, however, there is a finite probability that electrons incident on the barrier in the filled states below the Fermi level of the left-hand metal may tunnel through the barrier into previously empty states above the Fermi level in the right-hand metal. These tunneling electrons result in an appreciable current flow for thin barriers (on the order of 20 Å). A vast majority of these electrons tunnel elastically, that is, without

losing any energy as they traverse the insulating layer. This process is represented by the horizontal dashed line in Fig. 2. If a vibrator, such as an adsorbed molecule, is present in the barrier region, then, as the applied potential exceeds the energy required to excite a vibration ($eV > \hbar\omega$), electrons as they tunnel through the barrier may couple to this vibrator and excite it. The electron then loses $\hbar\omega$ of its energy but may still find an empty state above E_F in which to enter the right-hand metal. The coupling between the electron and the vibrator (molecule) may result from the electron's charge interacting with either the molecule's permanent dipole, or the charge may polarize the molecule and interact with the resulting induced dipole. Thus, both IR and Raman active vibrations may be excited. These inelastically tunneling electrons augment the current already flowing through the elastic channel. This manifests itself as a very small, sharp change in slope in the current vs. voltage curve of the junction or as a small step increase in the junction conductance, as illustrated in Fig. 3. This effect is very small, representing a change in conductance on the order of one percent, and so would be very difficult to detect from a current/voltage (I-V), or a conductance vs. voltage (σ-V) curve. To enhance the visibility of this feature, one further derivative is taken. When the second derivative of the current with respect to voltage $\left(\frac{d^2I}{dV^2} = \frac{d\sigma}{dV}\right)$ is plotted against applied potential, this inelastic feature appears as a sharp peak located at $eV = \hbar\omega$ (Fig. 3(c)). In reality, the adsorbed molecules contribute many features representing the normal modes of vibration. The oxide itself, as well as the metal electrodes, also contribute structure. Thus, the IET spectrum looks very much like an infrared absorption spectrum or a Raman frequency shift

spectrum.

As illustrated in Fig. 2, the right-hand metal electrode is represented as being a superconductor, which, in practice, is the case. In IETS, the width of the inelastic feature depends on the sharpness of the Fermi levels in the two metals. Thus, the actual measurements are carried out with the samples held at 4.2 K, immersed in liquid helium, to reduce the thermal smearing of the Fermi levels to an acceptable level. At this temperature the Pb is, in fact, a superconductor. The presence of a superconductor as one of the electrodes has the effect of shifting the position of the inelastic peak by a small amount and slightly perturbing the shape of the feature. These effects may be explained by considering the properties of a superconductor. When a metal becomes a superconductor, a narrow electron energy gap (of width 2Δ) forms at the Fermi level. Also, the electron density of states is perturbed near E_F, resulting in a sharp, unusually large density of electron states just above and just below the gap. Since E_F lies at the center of this gap, inelastic tunneling cannot occur until the applied potential exceeds $\hbar\omega + \Delta$. This shifts the apparent energy of the feature up by Δ. Experimentally, this shift is seen to be slightly less than Δ (24), resulting in a shift of 1.01 meV for Pb at 4.2 K. The redistribution of electron states has the effect of slightly sharpening the inelastic peak and producing a slight undershoot on the high energy edge of the feature (21). This actually increases the resolution as compared to a normal metal at the same temperature and, thus, may be considered an advantage. The undershoot, however, must be taken into account when finding accurate integrated peak intensities (25). The superconducting state may be quenched by the application of a magnetic field.

Experimentally, the IET spectrum is measured electronically using an AC modulation and harmonic detection technique. A slowly varying DC potential is applied across the barrier and provides the spectral energy scale. This potential is generally ramped from 30 to 500 meV. Below 30 meV, the phonon contribution from the superconducting lead overwhelms any vibrational structure which may be present. On the high energy end, 500 meV lies above the highest vibrational feature present (the surface hydroxyl stretching mode at 450 meV). On top of this DC ramp potential is superimposed a small (2 meV rms or less) AC modulation potential. The desired second derivative is then found by measuring the voltage occurring across the junction at the second harmonic of the modulation frequency.

In practice, the ramp modulation supply sources are seen by the junction as constant current sources. Constant current sources are used because of their relative simplicity and stability (26). Constant voltage IETS supplies have been devised (27) but are not in general use. Since a constant current source is used, the measured second harmonic voltage is actually proportional to $\frac{d^2V}{dI^2}$ rather than $\frac{d^2I}{dV^2}$. This can be seen by representing the time dependent voltage drop across the junction as $V(I_o + \delta I \cos\omega t)$, where I_o is the DC current applied and δI is the amplitude of the modulation applied at frequency ω. Expanding this voltage in a Taylor series, we arrive at

$$V(I_o + \delta I \cos\omega t) = V(I_o) + \delta I\left(\frac{dV}{dI}\right)_{I_o} \cos\omega t + \frac{(\delta I)^2}{2}\left(\frac{d^2V}{dI^2}\right)_{I_o} \cos^2\omega t + \ldots \quad .$$

Noting that $\cos^2\omega t = \frac{1}{2}(1 + \cos 2\omega t)$, we see that

$$V_{2\omega} = \frac{(\delta I)^2}{4}\left(\frac{d^2V}{dI^2}\right)_{I_o} \quad .$$

This derivative is related to the desired function, $\frac{d^2I}{dV^2}$, by the simple relation

$$\left|\frac{d^2I}{dV^2}\right| = \sigma^3\left|\frac{d^2V}{dI^2}\right|$$

where σ is the dynamic conductance, $\frac{dI}{dV}$. Since σ is a slowly varying function over the voltage range of interest, the two derivatives are very nearly proportional to each other. Thus, in most cases, the desired information may be obtained from the measured spectrum. A method to convert to d^2I/dV^2 is described in Appendix B, and is useful when calibrated absolute intensities are desired.

A schematic for the electronics used in an analog IETS detection system is shown in Fig. 4. A computer controlled digital data acquisition system is presently in use in this laboratory and is described in detail in Appendix A.

As noted above, the resulting IET spectrum is analogous to an IR or Raman spectrum. IETS, however, has several advantages over IR and Raman for molecules adsorbed on aluminum oxide. As mentioned above, IETS is sensitive to both IR and Raman active modes and, in fact, it has been predicted (28) that IETS should reveal modes forbidden to both infrared and Raman (this, however, has not been demonstrated experimentally).

A second significant advantage of IETS is its sensitivity. It has been demonstrated with benzoic acid (29) that as little as one-thirtieth of a monolayer may be detected with IETS. Since the junctions used in this study were only 200 microns square, this represents a total of approximately 10^{10} molecules. A second study has detected the effect of the minor constituent in a 1%/99% isotopic mixture adsorbed on alumina through

IETS (30).

Due to this extremely high sensitivity, very low surface area samples may be used. Thus, uniformity over the entire surface of the sample is quite probable. The same cannot be claimed for the very high surface area alumina powders which must be used with IR spectroscopy.

Another advantage over infrared spectroscopy is the availability of the spectral range between 30 and 125 meV (240 to 1000 cm^{-1}) which is usually unavailable to IR due to the strong absorption by the alumina itself.

Finally, since the sample is prepared at the time of the experiment inside a high vacuum chamber, the entire history of the sample may be controlled.

There are, however, disadvantages to IETS as well. IETS must be considered a "snapshot" type of picture. The surface composition, generally, is frozen in when the Pb overlayer is deposited. Also, the measurements are made after the junction is completed, i.e., after all the reactions have taken place. Thus, one cannot follow the course of a reaction in real time as may be done with IR spectroscopy.

Also, the presence of the top Pb electrode perturbs the IET spectrum (31) and in some cases may even take part in the surface reaction, as described in Chapter 6.

One major weakness of IETS is the lack of a usable, well defined theory. From an experimentalist's point of view, the theory should be at such a stage of development that one could routinely be able to work backward and determine the orientation of the molecule from the observed spectrum. Progress is being made in this direction, but the analyses

still require much numerical computation even for simple molecules (32), and the results are not totally accurate.

The first theory of IETS was developed by Scalapino and Marcus (33) soon after the discovery of this effect. This theory uses Bardeen's transfer Hamiltonian formalism and a WKB approximation for the electron wavefunctions within the barrier region. The oxide is treated as a rectangular barrier, and the molecular vibration is approximated by an oscillating dipole within the barrier. The interaction potential between the electron charge and this dipole is treated as a time dependent perturbation on the static barrier potential. The Golden rule is used to determine both the elastic and inelastic transition (tunneling) probabilities and thus the relative contributions of the elastic and inelastic current. They determine also a form for $\frac{d^2I}{dV^2}$. As mentioned above, this theory treated dipolar (that is, IR active) excitations. Soon thereafter, Jaklevic and Lambe (34) extended this theory to include induced dipolar (Raman active) excitations. This simple theory accounted for the appearance and order of magnitude intensities seen in IET spectra and also confirmed that both infrared and Raman active vibrations should be observed with approximately equal intensity. This theory showed also an orientation effect, predicting that those modes with a dipole moment perpendicular to the oxide surface should be significantly more intense than those vibrations which occur parallel to the surface. Quantitative comparison between experiment and theory, however, did not prove profitable.

Later, Kirtley, Scalapino and Hansma (28) improved on this theory removing some of the obvious shortcomings. Partial charges were introduced, i.e., assigning each atom in a molecule a partial charge, and allowing the

atoms within the molecule to undergo normal mode vibrations. Multiple images due to the presence of the parallel metal electrodes were also included as well as the dielectric constant of the oxide. Also, nonconservation of momentum parallel to the interface plane was allowed. These improvements resulted in a significantly more realistic, but also more complex, theory. Work using this theory to analyze the orientation of the $CH_3SO_3^-$ ion on aluminum oxide (32) proved very encouraging; however, the analysis required a significant amount of numerical calculation.

Several other theories have been formulated to circumvent the Bardeen transfer Hamiltonian and WKB approximations (35 - 37). However, only the theory by Kirtley et al. has been shown to be at all useful in the analysis of real IET spectra.

One shortcoming of most theories is the prediction that IETS intensities should scale as the number of vibrators present, n. Experimental study using radioactively labeled benzoic acid (29), however, shows an intensity that scales as $n^{1.4}$ for submonolayer coverages. Two proposals have been advanced to explain this effect. Cunningham, Weinberg and Hardy (38) propose that cooperative motion in the adsorbate layer could explain this non-linear dependence. A second possible explanation (29) is simply that the effective barrier through an adsorbed molecule is thicker than the barrier in areas where no adsorbate is present. Thus, more current flows in regions where no adsorbate is present decreasing the relative number of electrons which interact with the adsorbate.

In order to make use of the theory when it becomes generally usable, the IETS data must be in a form amenable to analysis by the theory. Since all theoretical calculations are carried out for the quantity d^2I/dV^2,

that is the most logical form that the experimental spectra should take. Appendix B describes a procedure to convert the second derivative data measured in this lab into d^2I/dV^2 as a function of eV in absolute units of $(ohms\text{-}meV)^{-1}$.

Thus, we see that IETS is a useful technique for the investigation of adsorbates bound to an aluminum oxide surface. With the further development of the theory IETS will, no doubt, prove to be even more useful.

The proposed goal of the research presented in this thesis was two-fold. The first goal was to contribute to the development of the relatively new tool, IETS, both through the design of versatile experimental apparatus as well as through the development of new experimental techniques to take advantage of the potential of IETS as a surface vibrational probe. The second goal was to demonstrate the usefulness of IETS to the study of the important field of chemisorption and heterogeneous catalysis through the investigation of several adsorbate systems of interest to the field. The attainment of these objectives, we believe, was realized through the following achievements and studies. Several contributions were made toward the development of IETS as an experimental tool:

(i) A method was developed to resistively heat and simultaneously measure the temperature of the thin Al film used as the first metal electrode (described in Chapter 2). This technique allows for rapid heating of the tunneling sample, and in particular the aluminum oxide film. Since only the region in the immediate vicinity of the sample is heated, desorption of possible contaminants from other regions of the preparation apparatus is minimized. Also, cooling of the sample is rapid, again, since only a limited region was heated. The ability to

heat the sample is very important when investigating such phenomena as temperature dependent reactions and activated adsorption. This technique has proven itself useful in the IETS studies of the oxide barrier region (Chapter 3), the temperature dependent adsorption of ethanol (39), acetaldehyde and acetic acid (40) on aluminum oxide, the temperature dependent adsorption of $Zr(BH_4)_4$ on alumina and its subsequent interaction with H_2O, D_2O and D_2 (41), and the thermal oxidation of $Ru_3(CO)_{12}$ adsorbed on alumina (Chapter 7).

(ii) Apparatus was designed to allow for the cooling of the IETS samples to temperatures below 170 K. Sample cooling is important in studying species which interact only weakly with aluminum oxide. This provision proved useful in the study of the adsorption and interaction of $[RhCl(CO_2)]_2$ (Chapter 6) and $Ru_3(CO)_{12}$ (Chapter 7) on Al_2O_3.

(iii) A technique was devised for forming a heavily hydroxylated aluminum oxide barrier by means of a plasma discharge initiated in water vapor. This technique was useful in elucidating the composition of the barrier region (Chapter 3).

(iv) A convenient means of introducing and subliming low vapor pressure solid adsorbates during sample preparation was devised and proved very useful in the studies of $[RhCl(CO)_2]_2$ and $Ru_3(CO)_{12}$.

Since the insulating layer of the IETS junction is to be used to model the surface of aluminum oxide catalysts, an understanding of the compositional and chemical nature of this insulating layer is imperative. Two studies reported in this thesis contributed significantly toward this understanding.

(v) An IETS study of clean junctions (junctions with no intentional

adsorbate present) in which the insulator was formed by oxidizing the Al film in various atmospheres as a function of temperature showed that the insulators formed in an oxygen plasma discharge are indeed aluminum oxides, not hydroxides. The hydroxyl modes seen represent surface hydroxyl groups. Oxides containing bulk hydroxide may be formed also, by using H_2O as the oxidizing gas at room temperature. This study is presented in Chapter 3.

(vi) An accurate means of investigating the chemical environment of the atomic constituents of a sample is X-ray photoelectron spectroscopy (XPS). Appendix D presents the results of an XPS investigation of the insulators formed on freshly evaporated thin Al films when exposed to various atmospheres. This work was done in conjunction with Howard E. Evans. This study showed that XPS is capable of distinguishing between the oxides formed in different manners. The results were presented in several different ways. When XPS results for commercial aluminas become available, a direct comparison between IETS oxides and the commercial aluminas may be made.

Several studies were carried out also to demonstrate the usefulness of IETS to the field of chemisorption and hetergeneous catalysis.

(vii) The first series of studies, presented in Chapters 4 and 5, involved the room temperature adsorption of phenol and the phenol derivatives, catechol, resorcinol and hydroquinone, on aluminum oxide as studied with IETS. These studies demonstrated the utility of IETS in determining surface bonding information concerning complex organic molecules. These studies demonstrated also the resolution and sensitivity available routinely in adsorption studies as well as

illustrating the ability to distinguish between similar chemical species bound to alumina. The ability of IETS to detect inter-adsorbate interactions was demonstrated also.

An area of great importance to heterogenous catalysis is that involved with the investigation of small metal clusters bound to an oxide support and the molecular species which interact with these supported metal systems. The applicability of IETS to the investigation of metals supported on aluminum oxide is demonstrated in the following three studies.

(viii) Appendix E presents an investigation, carried out with Howard E. Evans, on the room temperature adsorption of ethanol on alumina supported silver particles. This study demonstrated the ability of IETS to gain information on the interaction of organic molecules with metals. The ability of IETS to distinguish between identical adsorbate species, differing only in binding site, was demonstrated also.

(ix) A technique that is currently of great interest is the fixing of organometallic and metal cluster compounds on oxide supports as a means of producing supported metal catalysts with unique catalytic properties. The following two studies demonstrate the feasibility of using IETS in the investigation of such systems. The first, reported in Chapter 6, involves the investigation of the adsorption and subsequent decomposition of $[RhCl(CO)_2]_2$ on a hydroxylated alumina surface. IETS proved useful in identifying the surface species present.

(x) The final work, discussed in Chapter 7, represents a preliminary investigation of the adsorption of $Ru_3(CO)_{12}$ on a hydroxylated

aluminum oxide surface. This study showed that a transition metal carbonyl may be adsorbed on alumina in molecular form and subsequently oxidized. This results in a fully oxidized Ru surface constituent.

With the contributions listed above, we believe that the stated goals have been met.

Each of the following six chapters as well as Appendices D and E is a self-contained presentation of the IETS studies mentioned above. Chapter 2 describes the scheme developed for resistively heating and simultaneously measuring the temperature of the Al film of the IETS junction. The third chapter presents an IETS study of the composition of the insulating layer formed during junction fabrication. Chapters 4 and 5 present the IETS investigation of phenol, catechol, resorcinol and hydroquinone adsorbed on alumina. The adsorption and decomposition of $[RhCl(CO)_2]_2$ is discussed in Chapter 6. Chapter 7 presents the study of the adsorption and oxidation of $Ru_3(CO)_{12}$ on aluminum oxide. Appendices D and E represent studies carried out jointly with Howard E. Evans. An XPS investigation of the thin oxide films which have been used as tunneling barriers is presented in Appendix D. Appendix E describes an IETS study of ethanol adsorption on silver particles supported on the alumina surface.

Chapter 8 presents a summary of the work presented in this thesis.

Appendix A describes in detail the electronics used in the measurement of IET spectra as well as instructions for the use of these electronics.

Appendix B describes what is involved in the calibration of first and second derivative tunneling spectra and presents a computer program to carry out this calibration.

Appendix C discusses the considerations which need to be taken into account when designing an IETS junction fabrication system and describes three such systems.

References

1. Class notes, CHE 162, Caltech, W. H. Weinberg, Prof., 1975.
2. L. E. Davis, N. C. MacDonald, P. W. Palmberg, G. E. Riach and R. E. Weber, Handbook of Auger Electron Spectroscopy, Physical Electronics Div. Perkins-Elmer Corp. Eden Prairie, MN., 1976.
3. E.g., M. Cardona and L. Ley, Topics in Applied Phys. 26, (1978).
4. D. E. Eastman and M. I. Nathan, Physics Today, April (1975) p. 44.
5. P. A. Redhead, Vacuum 12, 203 (1962).
6. E.g., J. R. MacDonald and C. A. Barlow, Jr., J. Chem. Phys. 39, 412 (1963).
7. M. A. Van Hove and S. Y. Tong, Surface Crystallography by LEED: Theory, Computation and Structural Results, Springer-Verlag, New York, 1979.
8. E.g., L. I. Johansson and J. Stöhr, Phys. Rev. Letters 43, 1882 (1979). J. Stöhr, L. I. Johansson, I. Lindau and P. Pianetta, Phys. Rev. B 20, 664 (1979).
9. L. H. Little, Infrared Spectra of Adsorbed Species, Academic Press, New York, 1966.
10. R. P. Cooney, G. Curthoys and N. T. Tam, Advan. Catal. 24, 293 (1975).
11. H. Froitzheim, in Electron Spectroscopy for Surface Analysis, H. Ibach, ed., Springer-Verlag, New York, 1977, Chapter 6.
12. P. K. Hansma, Phys. Letters C 30, 145 (1977).
13. W. H. Weinberg, Ann. Rev. Phys. Chem. 29, 115 (1978).
14. T. Wolfram, Ed., Inelastic Electron Tunneling Spectroscopy, Springer-Verlag, Berlin (1978).

15. P. K. Hansma and J. Kirtley, Acc. Chem. Res. 11, 440 (1968).

16. R. C. Jaklevic and J. Lambe, Phys. Rev. Letters 17, 1139 (1966).

17. H. W. White, L. M. Godwin and T. Wolfram, J. Adhesion 9, 237 (1978).

18. P. K. Hansma and M. Parikh, Science 188, 1304 (1975).

19. Y. Skarlatos, R. C. Baker, G. L. Haller and A. Yellon, Surface Sci. 43, 353 (1974).

20. E.g., P. K. Hansma and R. V. Coleman, Science 184, 1369 (1974). M. G. Simonson, R. V. Coleman and P. K. Hansma, J. Chem. Phys. 61, 3789 (1974).

21. J. Klein, A. Léger, M. Belin and D. D´efourneau, Phys, Rev. B 7, 2336 (1973).

22. E.g., R. V. Coleman, R. C. Morris and J. E. Christopher, Methods of Experimental Physics VII, Solid State Physics, ed., R. V. Coleman, Academic Press, 1974, section 1.5.1.2.

23. J. Klein and A. Léger, Phys. Letters 30A, 96 (1969).

24. J. Kirtley and P. K. Hansma, Phys. Rev. B 13, 2910 (1976).

25. R. Magno and J. G. Adler, J. Appl. Phys. 49, 5571 (1978).

26. R. G. Keil, K. P. Roenker and T. P. Graham, Appl. Spect. 30, 1 (1976).

27. M. V. Moody, J. L. Paterson and R. L. Ciali, Rev. Sci. Instrum. 50, 903 (1979).

28. J. Kirtley, D. J. Scalapino and P. K. Hansma, Phys. Rev. B 14, 3177 (1976).

29. J. D. Langan and P. K. Hansma, Surface Sci. 52, 211 (1975).

30. M. Kroeker and P. K. Hansma, Surface Sci. 67, 362 (1977).

31. J. R. Kirtley and P. K. Hansma, Phys. Rev. B 12, 531 (1975).

32. J. Kirtley and J. T. Hall, Phys. Rev. B, submitted.

33. D. J. Scalapino and S. M. Marcus, Phys. Rev. Letters 18, 459 (1967).

34. J. Lambe and R. C. Jaklevic, Phys. Rev. 165, 821 (1968).

35. Eg., T. E. Feuchtwang, Phys. Rev. B 10, 4121 (1974); T. E. Feuchtwang, Phys. Rev. B 10, 4135 (1974); W. C. Leipold and T. E. Feuchtwang, Surface Sci. 50, 1 (1975).

36. A. D. Brailsford and L. C. Davis, Phys. Rev. B 2, 1708 (1970); L. C. Davis, Phys. Rev. B 2, 1714 (1970).

37. G. K. Birkner and W. Schattke, Z. Physik 256, 185 (1972).

38. S. L. Cunningham, W. H. Weinberg and J. R. Hardy, Appl. Surface Sci. 2, 640 (1979).

39. H. E. Evans and W. H. Weinberg, J. Chem. Phys. 71, 1537 (1979).

40. H. E. Evans and W. H. Weinberg, J. Chem. Phys. 71, 4789 (1979).

41 H. E. Evans and W. H. Weinberg, J. Am. Chem. Soc.,in press.

Table I

Advantages and Disadvantages of EELS, IRAS and IETS

Spectroscopy	Advantages	Disadvantages
EELS	High sensitivity: The detection limit is ~0.1% of a monolayer and the sampling area is ~1 mm^2. Wide spectral range: Features are observable from ~240 cm^{-1} upward.	Low resolution: The FWHM of the elastically reflected beam is typically 80 cm^{-1}. Relative difficulty of construction. Limited to use in low-pressure systems ($\lesssim 10^{-6}$ torr).
IRAS	High resolution: The typical resolution is ~3 cm^{-1}. Relative ease of construction. Can be used at high ambient pressures to simulate conditions of real catalysts.	Rather low sensitivity: The ratio of the scattering cross sections for EELS and IRAS has been estimated to be ~200:1 (38), although detection of 0.1% of a monolayer of CO can be achieved (Section III.B). Narrow spectral range: Observable features are typically limited to the region above 1500 cm^{-1} by solid-state IR detector technology and sensitivity, noise and interference.
IETS	High sensitivity: The detection limit is ~0.1% of a monolayer, and the sampling area is ~1 mm^2. Wide spectral range: Features are observable from ~240 cm^{-1} to above 8000 cm^{-1}. High resolution: The typical resolution is ~3 cm^{-1}. Relative ease of construction. Ability to simulate and study real catalytic systems: In its utility for examining adsorption on reduced supported metallic clusters and supported homogeneous cluster catalysts, this technique is complementary to IRAS.	Sample limitations: This probe cannot be applied to adsorbates on bulk metallic substrates. It is limited to examination of amorphous oxide surfaces, or metallic particles or inorganic cluster compounds supported on the oxide. Sample preparation technique: This may be thought of as a matrix isolation technique in which dynamic surface phenomena cannot be monitored in real time.

Figure Captions

Fig. 1: Representation of IET sample preparation procedure showing (a) clean glass substrate with attached electrical leads, (b) evaporation of aluminum strip, followed by oxidation, exposure to reactants, and (c) deposition of top metal electrodes. Electrical connections are not shown in part (c) for sake of clarity.

Fig. 2: Schematic energy diagram for both elastic (horizontal dashed line) and inelastic (oblique dashed line) electron tunneling through a barrier of width ℓ. E_1 is the initial energy and E_2 the final energy, separated by $\hbar\omega_o$ (a vibrational excitation energy). E_{F1} and E_{F2} are the respective Fermi levels in the two metals, $2\Delta_2$ represents the superconducting gap in metal 2, and eV is the bias voltage.

Fig. 3: Schematic representation showing the effect of a vibrational excitation at energy eV_o on the tunneling current and its first (dI/dV) and second (d^2I/dV^2) derivatives as a function of voltage (V).

Fig. 4: Schematic of IETS analog measurement electronics.

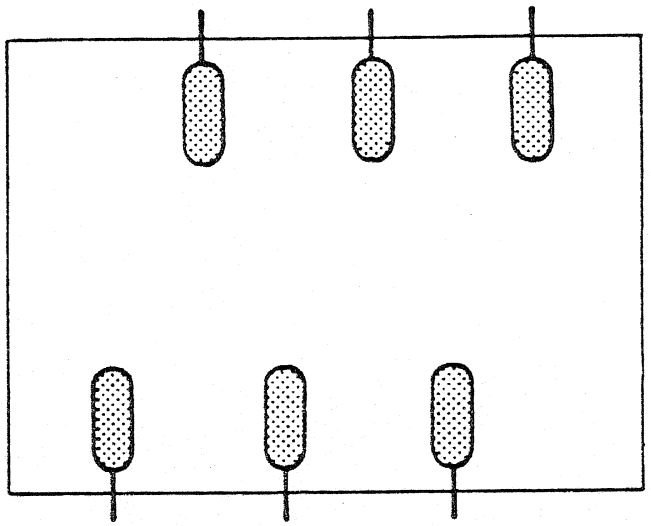

a.

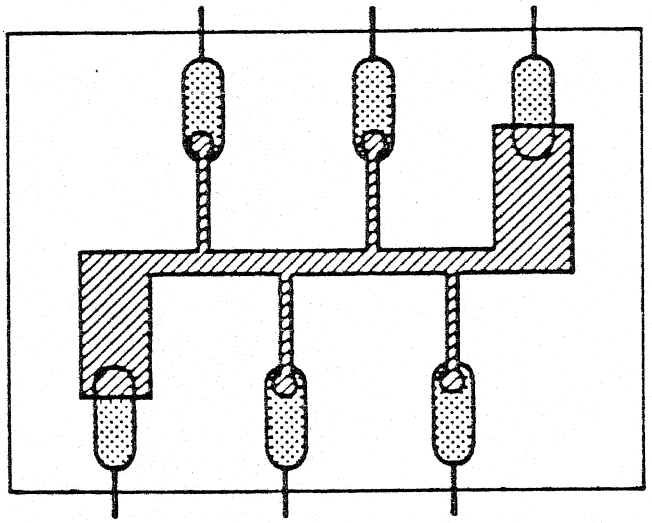

b.

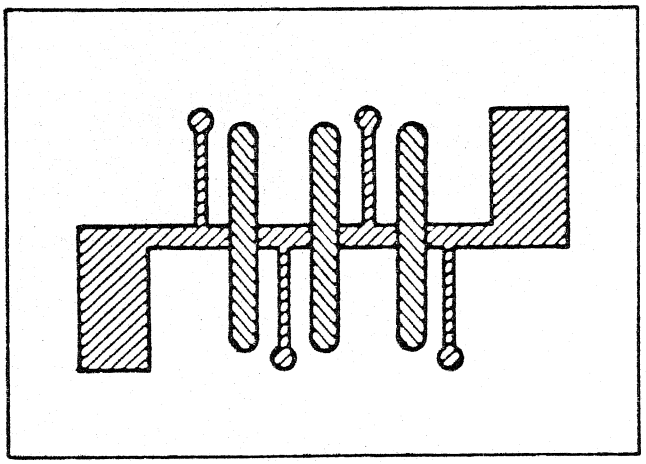

c.

In Al Pb

Fig. 1

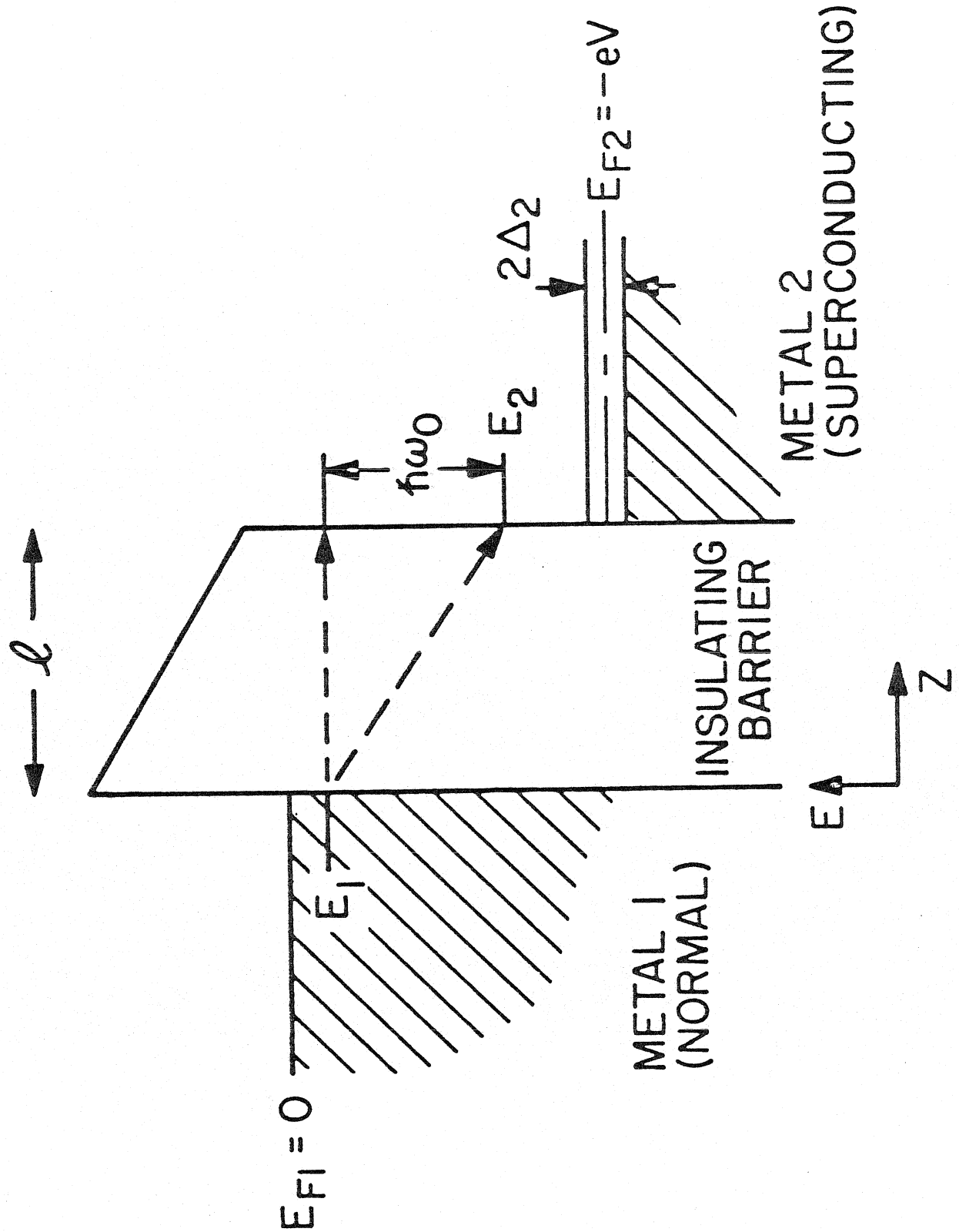
$E_{F1} = 0$
E_1
METAL 1
(NORMAL)
INSULATING
BARRIER
METAL 2
(SUPERCONDUCTING)
E_2
$\hbar\omega_0$
$2\Delta_2$
$E_{F2} = -eV$
ℓ
E
Z

Fig. 2

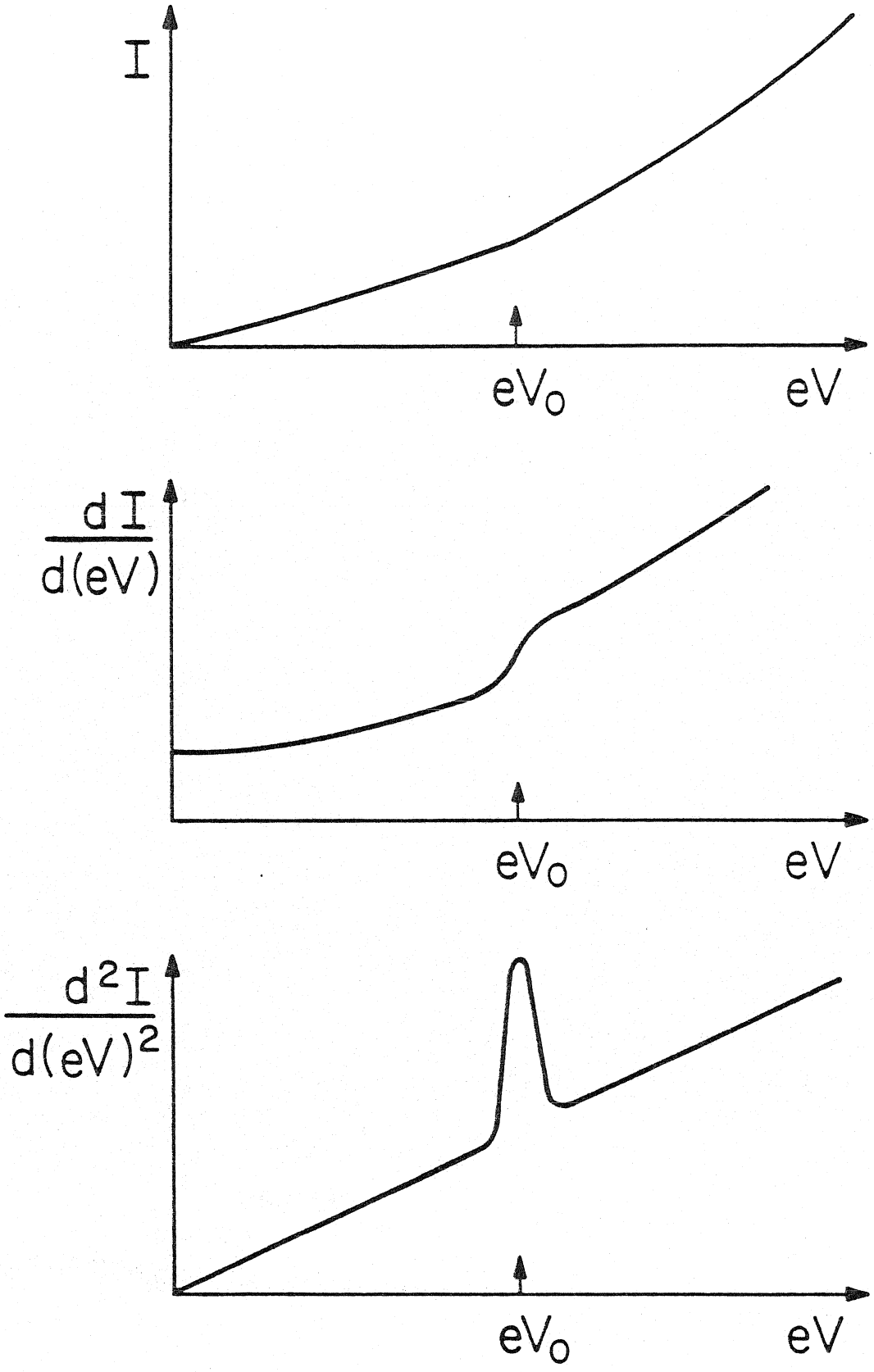

Fig. 3

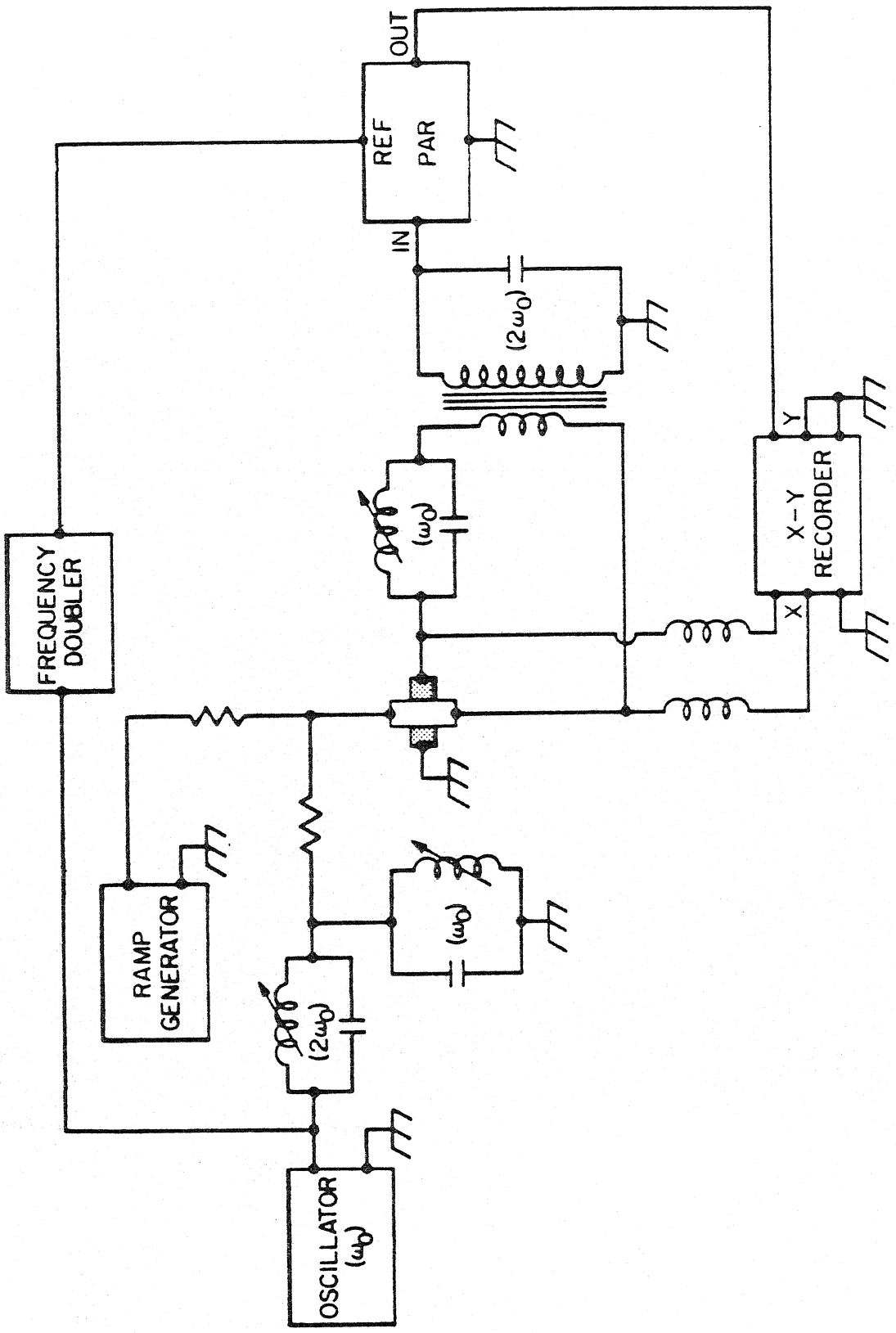
OUT
REF
PAR
IN
$(2\omega_0)$
(ω_0)
Y
X-Y
RECORDER
X
FREQUENCY
DOUBLER
RAMP
GENERATOR
(ω_0)
$(2\omega_0)$
OSCILLATOR
(ω_0)

Fig. 4

Chapter II

Sample Heating and Simultaneous Temperature Measurement in Inelastic Electron Tunneling Spectroscopy

Abstract

A method is described whereby the oxide surface in Inelastic Electron Tunneling Spectroscopy (IETS) experiments may be heated resistively with its temperature simultaneously measured via a four-point probe scheme. The utility of the method insofar as surface chemistry experimentation is concerned is demonstrated by following the dehydroxylation of the Al_2O_3 barrier in an Al-Al_2O_3-Pb tunnel junction as the preparation temperature is increased from 20 to 250°C.

Inelastic Electron Tunneling Spectroscopy (IETS) is a powerful experimental technique for studying the vibrational structure of species adsorbed on solid surfaces (1 - 4). In IETS, the second derivative of the electron tunneling current with respect to applied bias voltage (d^2I/dV^2) is measured as a function of bias voltage as electrons tunnel inelastically through a thin oxide barrier in a metal-oxide-metal junction configuration. This second derivative representation of the experimental data is proportional to the oscillator strengths of the vibrational modes of the molecular species present on the oxide surface, and thus IETS provides molecular structural information of species adsorbed on the oxide surfaces. However, if the kinetics of surface chemical reactions are to be measured using IETS, it is necessary to be able to vary and simultaneously to measure the temperature of the oxide substrate during the course of the reaction. We report herein a simple scheme whereby this may be accomplished, and as an example of the utility of our method, we present the observed dependence of the extent of hydroxylation of the insulator upon the temperature at which the oxidation (in H_2O vapor) is carried out.

Although the sample heating and temperature measurement method we propose is of general applicability, we shall discuss the special case of Al-Al_2O_3-Pb tunnel junctions due to our interest in the surface chemistry of Al_2O_3 (4). In our IETS experimental methodology, an Al film 1.3 mm x 20 mm x 1000 Å is evaporated onto a glass support, and the Al is then oxidized in a plasma discharge of either O_2 or H_2O in order to form an insulating Al_2O_3 barrier which is approximately 25 - 30 Å in thickness. It is at this stage in the junction preparation that we would like to be able to vary the temperature of the Al_2O_3 as we carry out chemisorption and

catalytic reaction studies on the oxide surface (prior to the evaporation of the top Pb film which isolates the adsorbates present on the oxide in an inert matrix).

Since the Al film has a resistance on the order of 10 Ω, the strip may be easily heated resistively. We found that in all cases less than 400 mA were needed to heat the Al film to well over 100°C. This procedure selectively heats the Al film and its oxide surface (which, collectively, we will refer to as the sample), without excessively heating large areas within the vacuum chamber and thus desorbing possible contaminants. With this heating method, the most convenient way to measure the temperature of the sample is to determine the change in resistance of the Al film. The temperature may then be calculated using the temperature coefficient of resistance.

For a metal, the temperature dependence of the resistance is given by the relation $R = R_o(1 + \alpha T)$ where R_o is the resistance at 0°C, and α is the temperature coefficient of resistance (5). In the case of an initial temperature T_i other than 0°C, we have

$$R = R_i[1 + b(T - T_i)] \equiv R_i(1 + b\Delta T) \qquad (1)$$

where R_i is the resistance at $T = T_i$ and b is the modified temperature coefficient of resistance, i.e., $b = \frac{\alpha}{1 + \alpha T_i}$. By rearranging terms in Eq. (1), we find

$$T = T_i + \frac{1}{b}\frac{(R - R_i)}{R_i} = T_i + \frac{1}{b}\frac{\Delta R}{R_i} \qquad (2)$$

which allows us to determine the temperature if T_i, R_i and b are known and if R is measured. Since we heat resistively the Al film, the optimum way to determine its resistance is to monitor the heating current (I) and

measure the voltage drop (V_s) along the film. In practice, I is found by measuring the voltage drop produced (by I) across a 10.14 Ω reference resistor, and the measurement of V_s is made using a four-point probe (to eliminate effects due to contacts to the film) (6). Adopting this point of view, Eq. (2) may be written as

$$T = T_i + \left(\frac{V_s}{I} - R_i \right) \frac{1}{R_i b} \tag{3}$$

The mask used for the Al evaporation was specifically designed to facilitate these four-point measurements. Four thin strips 0.4 mm in width were added to the more standard junction geometry (see Refs. 1 and 4) leading away from the sample (see Fig. 1b). These strips were made thin to minimize heat conduction from the sample during heating while providing the electrical contacts necessary for the voltage measurements. Electrical connections were made through wire leads attached, before the Al evaporation, to the glass support with either indium solder or silver paint (see Fig. 1a and 1b). With this configuration, the heating current was supplied through leads A and B (referring to Fig. 1b), while the voltage (and thus resistance) was measured between leads 1 and 2, 2 and 3, or 3 and 4. Each of the three sections of the Al film defined by these leads includes the area to be covered by a single Pb cross strip as shown in Fig. 1c.

Thus, if the temperature coefficient of resistance of the Al film were known, Eq. (3) could be used to determine the temperature. However, in many cases it has been observed that the physical properties of thin metal films differ from the properties of the same bulk materials (7). Thus, we may not assume that the temperature coefficient of resistance of

our thin Al films has the bulk Al value. This implies the coefficient must be determined experimentally. Rearranging terms in Eq. (1), we find $\frac{\Delta R}{R_i} = b\Delta T$, i.e., by plotting $\Delta R/R_i$ as a function of ΔT we should obtain a line the slope of which is b, and the intercept of which is at the origin.

This calibration was carried out by heating the glass support (and thus the Al film) at a uniform rate while monitoring its temperature with a thermocouple. Thus, we know the temperature of the sample when each resistance measurement is made, and $\Delta R/R_i$ as a function of ΔT may be found. For these calibration runs, the glass support was clamped to a copper block which was heated from outside the vacuum system with a Variac-controlled cartridge heater (Hot Watt Superwatt 3/8" x 1-1/2", 100 W, 115 V). A good thermal contact between the support and the copper block was assured by using a low vapor pressure, high temperature vacuum grease (Dow Corning 11 compound). An iron-constantan thermocouple was attached to the glass support near where the Al strip was evaporated allowing the temperature to be monitored directly.

We found that upon initial heating, the Al films showed annealing effects. The plot of $\Delta R/R_i$ as a function of ΔT showed nonlinear behavior, especially in the temperature range between 50 and 150°C where the curve showed first a decrease and then an increase in slope, finally becoming linear above 150°C. Also, the resistance of the film after this initial heating was approximately 5% lower than before heating. Subsequent heating of the films showed linear behavior with no significant change in the room temperature resistance. Thus, prior to making the actual calibration runs, the samples were annealed at a temperature of approximately 260 C for 3 to

5 minutes. In the calibration runs, the samples were heated at a rate of 3 to 4°C per minute. Resistances were measured for each of the three sections of the Al film in cyclic order, i.e., one resistance measurement was made every 2°C, so that each section had an R(T) measured every 6°C. Measurements were made from 24°C to 258 C utilizing a Hewlett-Packard Model 3490A digital multimeter. The thermocouple was read to 0.001 meV, and the resistances in the calibration were read directly in ohms to within 0.001 ohm. There were two primary reasons for using the 3490A in this mode when measuring the calibration resistances, as opposed to applying a .10 mA or 100 mA signal from an external source and measuring the voltage drop along the Al strip. First, as was mentioned earlier, only a few hundred milliamps were needed to heat the Al film to over 100°C. Thus, to insure that the Al strip was not being resistively heated to a different temperature than the thermocouple, as small a current as feasible was desired. The 3490A supplies a one milliamp signal in the 0.1 K resistance mode. The second reason stems from the fact that the 3490A was used to measure all necessary voltages in our experimental arrangement. If an external current were applied, three voltages would have to be measured for each calibration point: the thermocouple voltage, the voltage across the sample, and the voltage across the reference resistor (to find the external current). The current would have to be monitored since the current from the power supply (Hewlett-Packard Model 6214A) was not well regulated. Thus, the changes in resistance of the Al film plus instabilities in the supply would cause changes in current. Since a single instrument was used, all three voltages could not be measured simultaneously. Moreover, since the sample was being heated continuously, all three voltages could not be

determined at the same temperature. On the other hand, two measurements (the thermocouple voltage and the sample resistance) could be made maintaining an essentially isothermal film.

The data were reduced by fitting the points for each section of each sample to their own straight lines of the form $\Delta R/R_i = b\Delta T$ by means of a linear least-squares scheme (8). The slopes of the resulting lines were then averaged to find the desired temperature coefficient of resistance. In our calibration, we obtained data for 24 sections from nine separate samples (in three samples one lead came loose making measurements from one section impossible). In the most unfavorable case, the data from a single section contributed less than 0.5% uncertainty in the slope of its line (one standard deviation) and had a one standard deviation spread about that line of 1.3°C. However, the variation in slopes among sets of data representing different substrates was more significant in that it resulted in a one standard deviation uncertainty of 8% for any given slope compared to the average. The 24 sets of data taken together gave an average temperature coefficient of resistance (b) of 2.16×10^{-3} $(°C)^{-1}$. This corresponds to an α[temperature resistance coefficient for $T_i = 0°C$, see Eq. (1)] of 2.28×10^{-3} $(°C)^{-1}$ for our thin Al films, as compared to the bulk value of 4.29×10^{-3} $(°C)^{-1}$ (5). These results are summarized in Fig. 2. This observed variation in the slopes could be due to a variety of reasons. For example, the rate of evaporation of the Al and the thickness of the Al film varied somewhat from sample to sample, and both of these could affect the properties of the thin films. If better accuracy were needed in the temperature measurements, the fabrication of the junction could be monitored more closely. Moreover, each sample could be calibrated individually up

to approximately 50°C, and its (constant) slope then used. Once the temperature coefficient of resistance has been determined, it may be used to measure the temperature of the resistively heated Al film according to Eq. (2). It should be noted that since this coefficient appears to depend on the exact details of the junction fabrication, each research group should perform its own calibration experiments.

The efficiency of the resistance heating depends on how efficiently heat is dissipated from the Al film. For example, we found that when the glass support is in intimate thermal contact with the copper block (as when using the Dow Corning 11 compound, discussed above), and 100 μ of gas is present in the vacuum chamber, approximately 1 watt (∿300 mA across 10Ω) is needed to reach a temperature of 100°C. However, when a mechanical clamp alone is used to hold the glass support (poorer thermal contact with the copper block, but 100 μ of gas still present) only about 0.225 watt (∿150 mA across 10 Ω) is needed to reach the same temperature, and only about 0.6 watt is necessary to reach 200°C.

Fig. 3 illustrates how our simultaneous heating and temperature measurement scheme has been used successfully to investigate the IET spectra of clean Al-Al_2O_3-Pb tunnel junctions formed at several elevated temperatures, using an H_2O plasma discharge. As discussed in detail elsewhere (9), our ability to heat the insulating barrier has resulted in the discovery that the character of the barrier changes from an aluminum hydroxide to an aluminum oxide as the temperature at which the oxide is formed is increased.

In summary, a method has been presented which permits the rapid and efficient resistive heating of IETS samples with the simultaneous

monitoring of the sample temperature through the temperature dependent behavior of the resistance of the Al substrate. This capability is required if IETS is to prove useful in studying such surface phenomena as the rates of chemisorption and/or heterogeneously catalyzed surface reactions.

References

1. R. C. Jakevic and J. Lambe, Phys. Rev. Letters 17, 1139 (1966); and J. Lambe and R. C. Jaklevic, Phys. Rev. 165, 821 (1968).

2. J. Klein, A. Léger, M. Belin, D. Défourneau and M. J. L. Sangster, Phys. Rev. B 7, 2336 (1973).

3. M. G. Simonsen, R. V. Coleman and P. K. Hansma, J. Chem. Phys. 61, 3789 (1974).

4. B. F. Lewis, M. Mosesman and W. H. Weinberg, Surface Sci. 41, 142 (1974); B. F. Lewis, W. M. Bowser, J. L. Horn, Jr., T. Luu and W. H. Weinberg, J. Vac. Sci. Technol. 11, 262 (1974); and W. H. Weinberg, W. M. Bowser and B. F. Lewis, Japan. J. Appl. Phys. Suppl. 2, Pt. 2, 863 (1974).

5. R. C. Weast, Handbook of Chemistry and Physics, 52nd ed., The Chemical Rubber Co., Cleveland, 1971.

6. A. S. Grove, Physics and Technology of Semiconductor Devices, John Wiley, New York, 1967.

7. K. L. Chopra, Thin Film Phenomena, McGraw-Hill, San Francisco, 1969.

8. P. R. Bevington, Data Reduction and Error Analysis for the Physical Sciences, McGraw-Hill, New York, 1969.

9. W. M. Bowser and W. H. Weinberg, Surface Sci., to appear.

Figure Captions

Figure 1: The steps followed in the preparation of IETS junctions: (a) Wire leads are attached to the glass support with In solder or Ag paint; (b) A 1000 Å Al film is evaporated, making contack with the pre-attached leads. The Al is then oxidized. Heating current is supplied through leads A and B while voltage drops are measured between leads 1-2, 2-3, or 3-4; (c) Pb cross strips are then deposited to complete the junction.

Figure 2: A plot of $\Delta R/R_i$ as a function of T using the slope found by averaging the results of 24 sets of data. The dashed lines represent one standard deviation uncertainty in slope (8%) expected for any given sample. T_i is taken to be 24°C, R_i ranges from 3.0 to 3.5 ohms.

Figure 3: IET spectra of clean junctions with the insulators formed (a) in an O_2 plasma discharge at 50°C, and in an H_2O vapor discharge at (b) room temperature (c) 50°C (d) 100°C (e) 150°C (f) 200°C and (g) 250°C. This illustrates the decrease in hydroxylation of insulating barriers formed in H_2O as the temperature of oxidation is increased. Structure at 75, 90, 165-230 and 447 meV is associated with hydroxyl groups adsorbed on or incorporated in the oxide barrier (9).

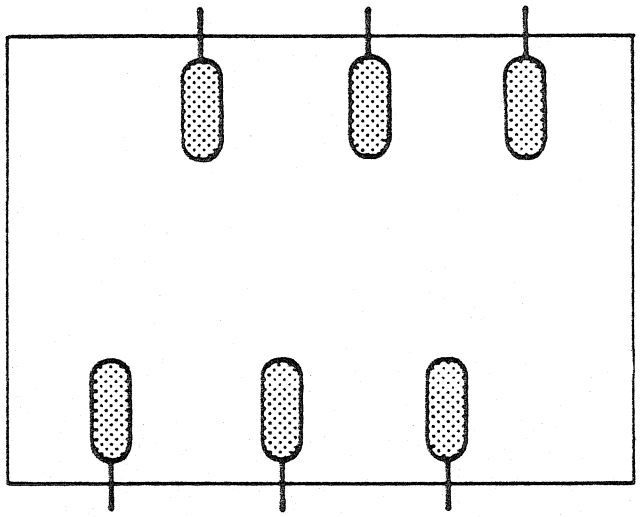

a.

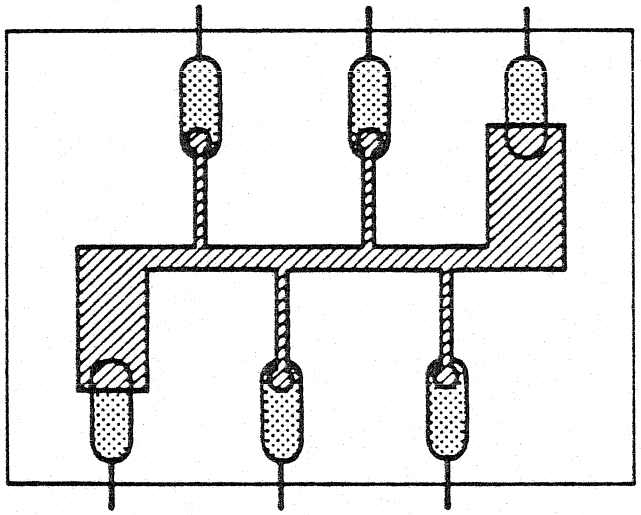

b.

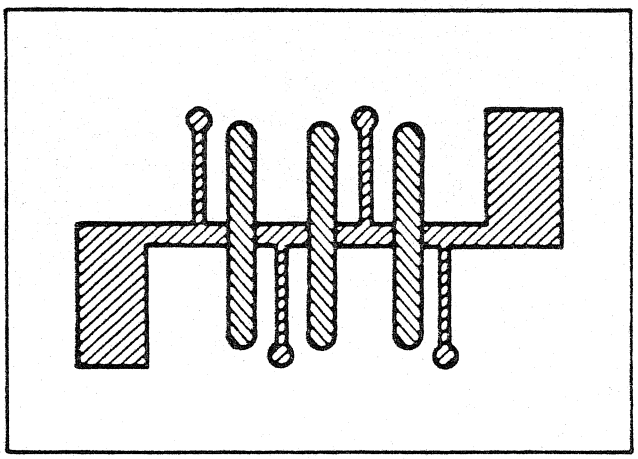

c.

In Al Pb

Fig. 1

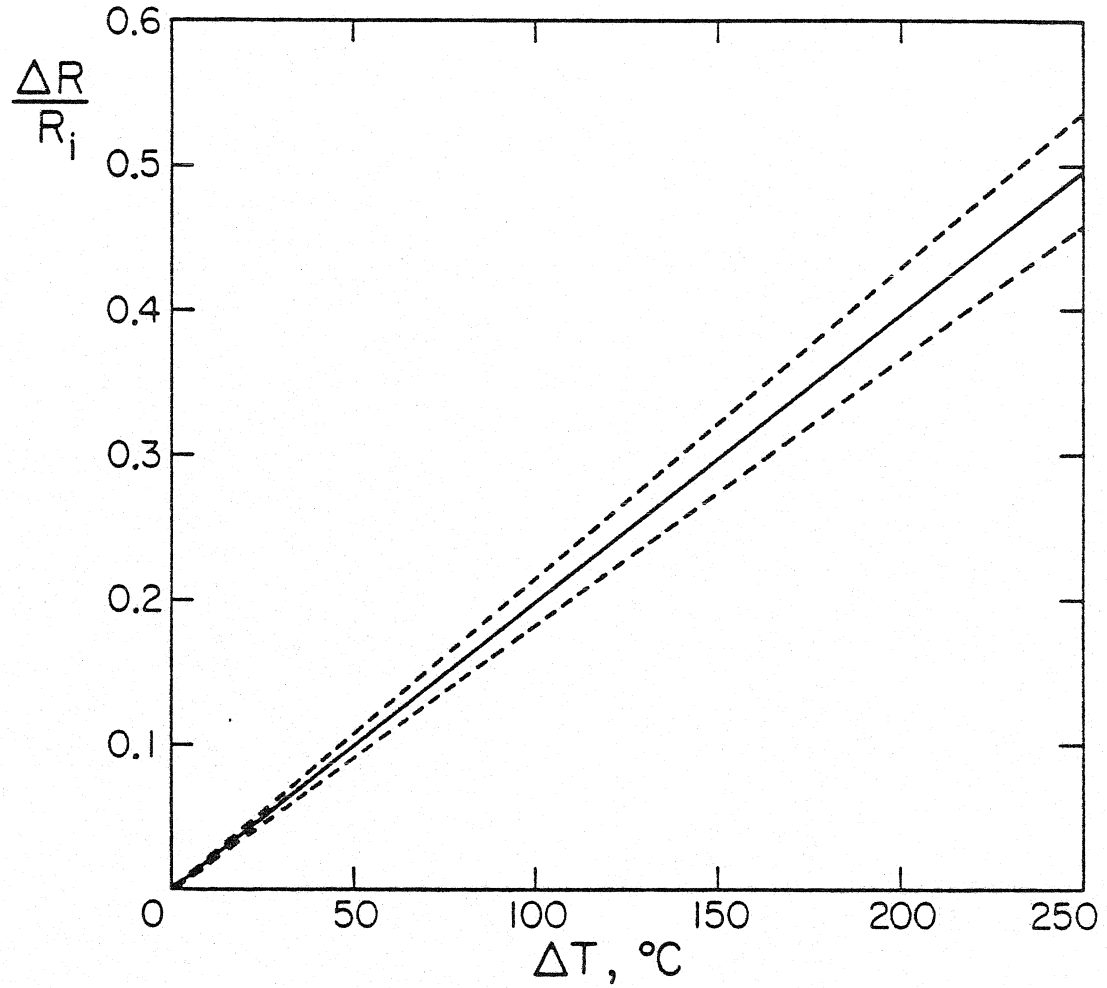

Fig. 2

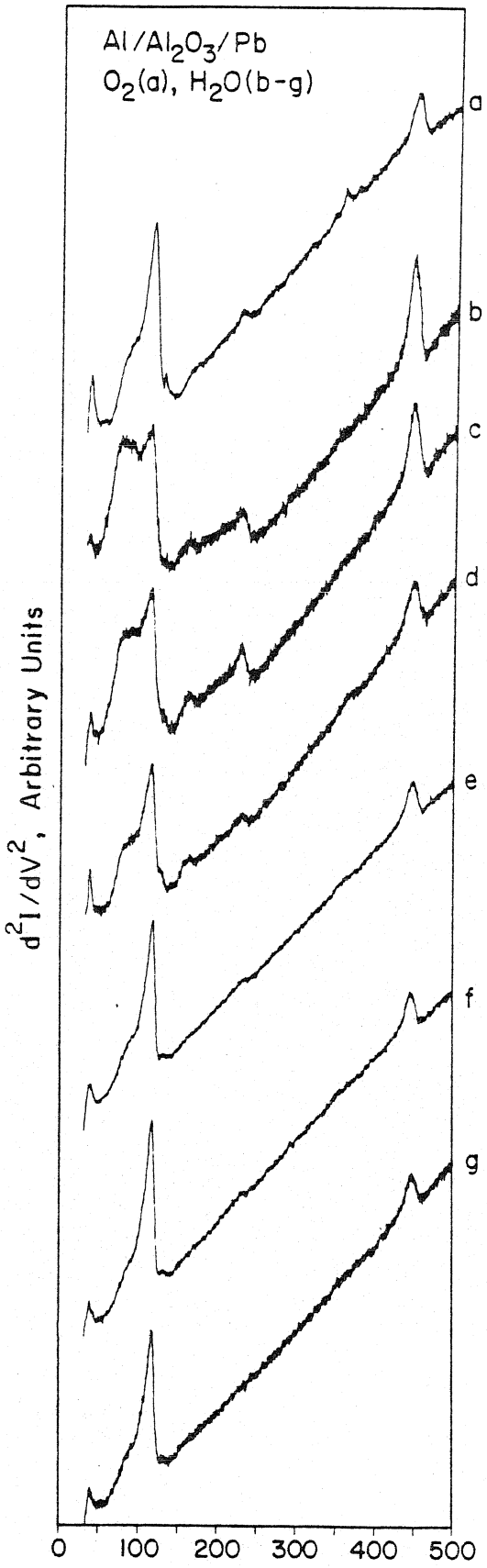
Al/Al2O3/Pb
O2(a), H2O(b-g)
a
b
c
d
e
f
g
d2I/dV2, Arbitrary Units
0
100
200
300
400
500
V, meV

Fig. 3

Chapter III

The Nature of the Oxide Barrier in Inelastic Electron Tunneling Spectroscopy

Surface Science 64 (1977) 377–392

THE NATURE OF THE OXIDE BARRIER IN INELASTIC ELECTRON TUNNELING SPECTROSCOPY †

W.M. BOWSER * and W.H. WEINBERG **

Division of Chemistry and Chemical Engineering, California Institute of Technology, Pasadena, California 91125, USA

Received 4 October 1976; manuscript received in final form 18 January 1977

We have investigated the insulating barrier of Al-oxidized Al–Pb tunnel junctions. This study was effected by measuring the inelastic electron tunneling (IET) spectra of various junctions in which the insulator was formed by oxidizing the aluminum either in an O_2, H_2O or D_2O plasma discharge at various temperatures between room temperature and 250°C. We found that those insulators formed at all temperatures in O_2 and those formed at high temperatures ($\gtrsim$150°C) in H_2O and D_2O are aluminum oxide with no evidence for any appreciable bulk hydroxide. The surfaces of these insulators do have adsorbed hydroxyl groups present, however. The insulators made at lower temperatures (<100°C) are also primarily aluminum oxide, but there is evidence for some bulk hydroxide. These "oxides" have a high concentration of surface hydroxyl groups with indications of two types of surface hydroxyls.

1. Introduction

Since its discovery and interpretation by Jaklevic and Lambe [1] and subsequent theoretical confirmation by Scalapino and Marcus [2], inelastic electron tunneling spectroscopy (IETS) has become a useful tool for the study of vibrational modes of molecules. In this technique, a metal–insulator–metal (M_1–I–M_2) tunnel junction is used. In our work, the first electrode film (M_1) is aluminum, the surface of which is oxidized to form the insulating barrier. It is on the surface of this insulator that we adsorb the molecular species to be studied. The top electrode is generally lead, but other metals have been used [3]. When a potential is applied across the junction, electrons can tunnel elastically (without losing energy) from filled states in one electrode through the insulating barrier into empty electronic states in the opposite electrode. As the applied potential is increased past the vibrational excitation energy, $\hbar\omega$, of a molecular species in or near the barrier, a new channel for tunneling is opened. In this case, the electron, as it traverses the barrier, loses $\hbar\omega$ of

† Research supported by the National Science Foundation under Grant No. GK-43433.
* NSF Energy-related Trainee and American Vacuum Society Graduate Fellow.
** Alfred P. Sloan Foundation Fellow.

its energy to this molecular vibration. This causes a slight increase in the conductivity of the junction which appears as a peak in the derivative of the conductivity, $d\sigma/dV$ or d^2I/dV^2. Thus, by plotting d^2I/dV^2 as a function of the applied bias potential eV, one obtains a series of peaks occurring at the energies of both the infrared and Raman active modes [2,4] of molecular species adsorbed on or occluded in the insulating layer.

Applications of IETS have been found in a variety of fields ranging from the study of the vibrational structure of large molecules of biological interest, such as amino acids [5,6], to the degradation of molecules exposed to the electron beam of an electron microscope [7]. However, the sensitivity of this technique to molecules adsorbed on the surface of the insulator has made IETS a most attractive tool for the study of chemisorption and catalysis. Specific examples of the utility of IETS in this arena of research are shown in table 1. In each of these cases, the aluminum–oxidized aluminum–metal tunnel junction was employed. Since the way in which a molecule reacts with a surface depends upon the properties of that surface, in order to carry out significant chemisorption and catalysis studies with IETS, the character of the insulating layer and its surface must be known. One major question has been whether this insulator is an aluminum oxide as contended by Lewis et al. [8], or an aluminum trihydroxide as reported by Geiger et al. [13] and Lambe and

Table 1
Information that can be gained from IETS: applications to chemisorption.

Information	Example
Adsorbate molecular structure	Acetic acid was observed to adsorb on aluminum oxide as an acetate ion as judged by absence of OH stretching and bending modes in surface–adsorbate complex [8]
Adsorption kinetics	Empirical sticking probability was measured as a function of coverage for formic acid on aluminum oxide [8]
Surface concentrations	Intensities of peaks in IET spectra were confirmed to be a direct function of adsorbate surface concentrations [9]
Adsorbate orientations	Benzene was observed to adsorb with its ring parallel to aluminum oxide surface [10]
Adsorbate–adsorbate interactions	Hydrogen bonding was observed between adsorbed phenol and surface hydroxyl groups on aluminum oxide [11]
Surface reactions	Benzoyl chloride was observed to react with aluminum oxide surface to form aluminum benzoate and HCl [12]

Jaklevic [4]. Thus, we felt that an important task to consider would be to gain further information on the insulator formed in these Al–insulator–Pb tunnel junctions with particular emphasis on the role of O and OH in the barrier region. One way to approach this problem is to form the insulator in the three different oxidizing gases O_2, H_2O and D_2O to determine any variation in the IET spectra of the resulting junctions. Also, by carrying out the oxidation in these three gases while the aluminum is held at an elevated temperature, we may ascertain how the composition of the insulator depends upon the temperature at which it is formed. In particular, we may determine whether a significantly "drier" oxide can be formed at an elevated temperature as compared with room temperature.

In the following section, we will describe the experimental procedures followed in this study. In section 3, we will present our results which will then be discussed in section 4. The major conclusions concerning the composition of the insulating barrier will be given in the final section.

2. Experimental

The general procedure followed in the fabrication of IETS junctions at room temperature in an oxygen plasma discharge has been discussed elsewhere [4,8]. Some modifications to this procedure are necessary, however, if the oxidation is carried out at elevated temperatures. The heating and temperature measurement scheme used in this experiment are described in detail elsewhere [14], so we will only briefly review the technique and discuss how it is used. We will then outline the general procedure followed in the junction preparation.

For the elevated temperature work, the Al film was resistively heated and its temperature-dependent change in resistance used to determine the temperature. This method selectively heats the Al strip, thus minimizing the thermal desorption of possible contaminants from surfaces inside the vacuum chamber. Moreover, since large masses are not heated, the temperature can be varied quite quickly. The temperature dependence of the resistance of a metal film can be described by the relation $R = R_i[1 + b(T - T_i)]$, where R is the resistance of the film at a temperature T, b is the temperature coefficient of resistance and R_i is the resistance of the metal film at an initial temperature T_i. By rearranging terms in the above equation, one obtains $T = T_i + (R - R_i)/bR_i$. Thus, if b, R_i and T_i are known, and if R can be measured, the temperature of the Al film can be determined. R_i is measured directly at room temperature using a Hewlett-Packard Model 3490A Digital Multimeter. During the resistive heating, R is determined by monitoring the heating current and measuring the voltage drop along the Al strip by means of a four-point probe technique. The temperature coefficient of resistance, b, is determined separately to an accuracy of 8% (one standard deviation) for any given sample [14]. It was found that in order to obtain a linear change in $\Delta R/R_i$ with tempera-

ture, the aluminum film must first be annealed at a temperature greater than that which will subsequently be used.

This technique was easily adapted to the heating of the Al film during oxidation. However, it is necessary to consider the following two points. First, the pressure in the vacuum chamber greatly affects the heating rate and the temperature at which the Al strip stabilizes for a given heating current. This means that the oxidizing gas has to be introduced into the vacuum system before the Al film is brought to the desired temperature. Second, the temperature of the Al film continues to rise during the oxidation due to the exothermic nature of the chemical reaction. This requires that the temperature be monitored and the heating current adjusted during the oxidation to prevent any large ($\gtrsim$5°C) variations in temperature. Since the effects we are viewing occur in part at the surface of the insulator, we stipulated that the insulator–lead interface be consistent among samples. Thus, prior to the evaporation of the lead overlayer, we allowed the Al film and glass support to cool to less than 35°C. This minimized spurious effects due either to diffusion of the lead into the barrier or to the aggregation of the lead into islands upon condensation [15].

Only minor modifications in our procedure were needed when using H_2O and D_2O as the oxidizing gas. The Al film is still oxidized in a plasma discharge. In O_2, this discharge occurs between an Al wire cathode at −700 V and ground. At a pressure of approximately 100 μm of O_2, we obtain a discharge current of 20 mA. The Al film is biased a few volts positively with respect to ground. We found that with H_2O and D_2O, in order to obtain discharge currents at pressures comparable to those used with O_2, the wire electrode must be held at +350 to 400 V. Also, the oxidation proceeded more rapidly if the Al film was biased a few volts negatively with respect to ground. In O_2, the oxidation times were on the order of 10 min, while in H_2O and D_2O, they were about 20 min.

We are now in a position to outline the procedure followed in the fabrication of our junctions. The steps followed are illustrated schematically in fig. 1. First, an aluminum strip the dimensions of which are 20 mm × 1.3 mm × 1000 Å is evaporated onto a glass support and annealed (by resistive heating) for one to two minutes at a temperature above that at which the oxidation is to be carried out. After the Al strip has returned to room temperature, T_i and R_i are measured, and approximately 100 μm of oxidizing gas is introduced into the vacuum system. The Al film is then heated to the desired temperature, and the plasma discharge is initiated. The temperature is monitored periodically, and the heating current is adjusted when necessary. At the conclusion of the oxidation, the discharge is quenched, the heating current is discontinued, and the oxidizing gas is pumped away. When the sample has cooled to approximately 30°C and the vacuum chamber has been evacuated to $\lesssim 5 \times 10^{-5}$ Torr, the lead cross strips are evaporated. These completed junctions are then removed from the vacuum system, and their resistances are measured. Those junctions with resistivities between 0.5 and 2.5 ohm-cm^2 (34 to 170 ohm across a 1.5 mm^2 junction) are stored in liquid N_2 awaiting

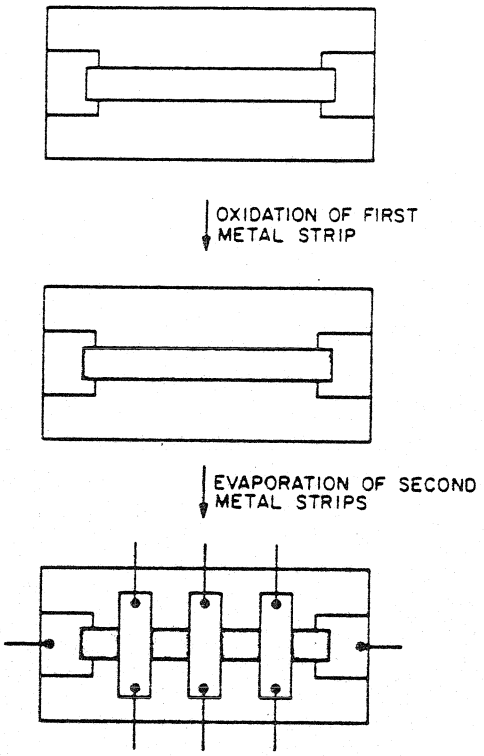

Fig. 1. Schematic illustration of the steps followed in sample preparation: a thin Al strip is evaporated; the strip is brought to temperature and oxidized; after allowing the oxidized Al film to cool, Pb cross-strips are evaporated.

subsequent measurement. We found that storage in liquid N_2 was necessary since the junctions tend to degrade with time at room temperature (probably due to the oxidation of the lead).

The IET spectra were all measured with the samples at 4.2 K in a liquid He dewar. The second derivative of the applied bias voltage with respect to tunneling current, d^2V/dI^2 (proportional to d^2I/dV^2 at these low voltages) is detected by measuring the second harmonic of a small modulation voltage which is superposed on the applied potential. This technique is described in detail by Lewis et al. [8]. The applied modulation voltage must be small enough not to degrade the measured spectrum, i.e., it must be less than the peak separation and intrinsic peak width, and yet it must be large enough to give an acceptable signal-to-noise ratio. For this experiment, a modulation of 4 meV peak-to-peak satisfied these requirements.

3. Results

In this section we will describe that which we observed in the measured IET spectra, first for the junctions prepared in O_2 and then for those prepared with H_2O and D_2O. We will also describe the variations in the IET spectra among junctions fabricated at various temperatures.

All samples prepared in O_2 plasma discharges at room temperature, 60 and 116°C yielded IET spectra essentially identical to those spectra previously published for clean tunnel junctions fabricated at room temperature [4,8]. There was no noticeable dependence on the temperature at which the Al was oxidized over this range of temperatures. A spectrum of a sample prepared at 60°C is shown in fig. 2a. In this spectrum we note the following: (1) a peak at 37 meV, which is present in all our spectra; (2) an intense, sharp peak at 117 meV, asymmetrically broadened on the low energy side with a shoulder at 80 meV; (3) a small peak at 230 meV; (4) another small peak at 358 meV; and (5) a broad peak at 447 meV of medium intensity.

Tunnel junctions with the insulator formed in an H_2O discharge were prepared over a wider range of temperatures. The IET spectra of samples prepared at room temperature, 56, 104, 157, 203, and 257°C are shown in fig. 2b–g. The following three points should be noted. First, those junctions prepared in H_2O at low temperatures ($\lesssim$100°C) have spectra quite different from those junctions prepared in O_2. Second, the spectra show a marked dependence upon the temperature at which the oxide is formed. Third, the spectra of those samples prepared in H_2O at higher temperatures ($\gtrsim$150°C) are identical to the spectra of samples prepared in O_2.

Comparing fig. 2b with fig. 2a, we note several differences between the spectrum of a junction prepared at room temperature in an H_2O discharge and the spectrum of a sample prepared in O_2. What was an 80 meV shoulder on the 117 meV peak in the junction prepared in O_2 appears as two intense, broad peaks at 76 and 90 meV in the junction prepared in H_2O. The 117 meV peak is broadened and shifted to 114 meV in the junction prepared in H_2O. Moreover, a new peak is present at 165 meV, and the 230 and 447 meV peaks are more intense than in the spectrum of the sample prepared in O_2.

As one increases the temperature at which the Al is oxidized, the IET spectra of the junctions prepared in H_2O change. At 56°C (fig. 2c), the structure at 76, 90, 165, 230, and 447 meV has all decreased in intensity relative to the strong peak near 117 meV. By 104°C (fig. 2d), the 76 and 90 meV peaks are no longer distinct but appear as a single rather strong shoulder on the 117 meV peak which is no longer shifted. The 165, 230, and 447 meV peaks have also decreased further in relative intensity. By 157°C, (fig. 2e), the spectrum appears very much like the spectrum of a sample prepared in oxygen. The shoulder at 80 meV is small, the 165 meV peak is barely visible, and the 230 meV peak is decreased further. There are no prominent changes in the spectrum upon increasing the oxidation temperature

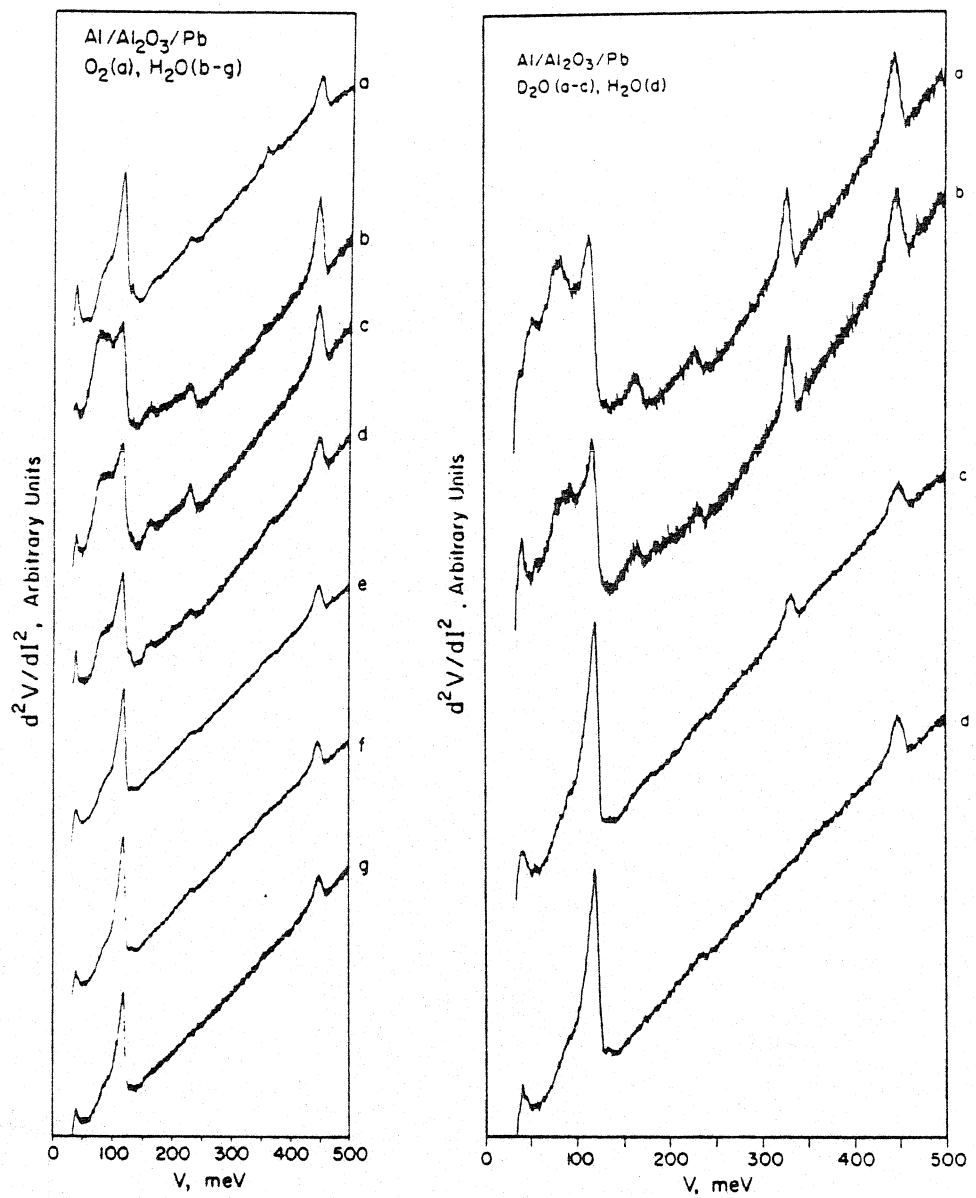

Fig. 2. IET spectra of samples in which the insulator was prepared (a) in an O_2 plasma discharge at 60°C, and in H_2O plasma discharges at (b) room temperature, (c) 56°C, (d) 104°C, (e) 157°C, (f) 203°C and (g) 257°C.

Fig. 3. IET spectra of samples prepared in a D_2O plasma discharge at (a) room temperature, (b) 107°C, and (c) 203°C. For comparison, the IET spectrum for the 203°C H_2O sample is shown in (d).

to 200°C (fig. 2f) or 250°C (fig. 2g). The 165 meV peak is no longer visible, and both the 80 meV shoulder and the 230 meV peak are very weak.

The samples prepared in D_2O yielded spectra which were similar to those for samples fabricated in H_2O. Fig. 3(a–c) show IET spectra for junctions prepared at room temperature, 107 and 203°C in a D_2O plasma discharge. In the spectrum of the sample prepared at room temperature (fig. 3a), we observe (as in the case of the room temprature H_2O sample) peaks at 76, 115 meV (the shifted 117 meV peak), 165, 230 and 447 meV. The 90 meV peak is not easily visible but may simply be buried at the background. In addition to this structure, we note new peaks at 54 and 65 meV (very weak but reproducible), structure at 80 to 85 meV, and a peak at 334 meV. As in the case of those samples prepared in H_2O, the intensity of much of this structure decreases (with respect to the intensity of the 117 meV peak) as the temperature at which the Al is oxidized is increased. By 203°C, the spectrum appears identical to the spectrum of the sample prepared in H_2O at 203°C except for a small peak at 54 meV and a larger peak at 334 meV.

4. Discussion

In this section we will make specific assignments for the various peaks making use of the results presented in this paper as well as results of previous infrared and tunneling work. We will then determine the composition of the barrier region based on these peak assignments. Since the IET spectra of those samples prepared in O_2 at all temperatures and of those prepared in H_2O (and D_2O) at high temperatures are all essentially identical, it is reasonable to assume that the composition of the barrier in these junctions is also identical. Thus, conclusions drawn about those samples prepared at 200°C in H_2O and D_2O will also apply to a sample prepared at 60°C in O_2, for example.

There are two peaks in the spectra which are not related directly to our investigation. First, the peak present at 37 meV is very close to where an aluminum phonon mode is expected [16]. The second peak appears at 358 meV and is due to the C–H stretching mode of hydrocarbon contamination [4,8]. The fact that this latter peak is very small, if visible at all, indicates that our tunnel junctions are all quite clean.

There are several peaks present in our spectra which can be ascribed directly to hydroxyl vibrational modes. These are the peaks visible at 75, 90, and 447 meV which are most pronounced in the spectra of the insulators formed in H_2O at room temperature (fig. 2b). The association of these peaks with hydrogen linkages is confirmed by the presence of the 54 meV ($\sim 75/\sqrt{2}$), 65 meV ($\sim 90/\sqrt{2}$) and 330 meV ($\sim 447/\sqrt{2}$) peaks observed in the spectra of samples prepared at room temperature in D_2O. The absence of a peak near 198 meV (1600 cm^{-1}) excludes the possibility of their being associated with molecularly adsorbed water [17]. Furthermore, we conclude that the hydroxyl groups responsible for these modes

are located on the surface of the insulator as opposed to being incorporated in the bulk as aluminum hydroxide. According to Dorsey [18], the bending modes of bulk aluminum hydroxide occur at energies greater than 112 meV (900 cm^{-1}), whereas surface hydroxyl modes are expected at lower energies. It has been noted that the position and full-width at half-maximum (the half-width) of the 447 meV peak depend upon the metal used for the top electrode [3]. Also, the exchange reaction between these hydroxyl groups and gaseous D_2O has been observed on these insulators [19]. Both these observations demonstrate unequivocally that those hydroxyl groups responsible for the 447 meV stretching mode are present on the insulator surface. No modes are observed which may be interpreted as stretching frequencies of bulk hydroxyls.

By comparing the intensities of those peaks at 75, 90, and 447 meV, we see that the surface concentration of OH groups does not depend critically on the temperature of oxidation for those insulators formed in O_2 at any temperature (fig. 2a), and those prepared in H_2O and D_2O above 150°C (figs. 2e–g and 3c). However, those insulators prepared at lower temperatures in H_2O (D_2O) show a strong temperature dependence which indicates a higher concentration of surface OH groups for room temperature oxidation and a decreasing surface concentration with increasing oxidation temperature up to approximately 150°C where, as mentioned above, the concentration seems to reach a plateau. We should emphasize that the insulator surfaces formed by oxidation in H_2O at a temperature between 150 and 250°C still have a rather high concentration of surface OH groups. We expect further dehydroxylation to occur at higher preparation temperatures, e.g., $\gtrsim$400°C [19].

The presence of two bending modes at 75 and 90 meV observed on those insulator surfaces prepared by H_2O oxidation at temperatures below approximately 150°C raises a new question: Do these two peaks represent two modes of the same type of hydroxyl group, or do they represent two types of surface hydroxyl groups? The former would imply that the *relative* intensities of the two peaks should remain constant with variable surface OH concentration. However, this is not the case as seen in the spectrum of the sample prepared at room temperature in D_2O where the 75 meV peak is still quite prominent, but the 90 meV peak is not easily visible (figs. 3a and 4b). Also, absorption infrared spectra of various forms of high surface area transition aluminas often show evidence for more than one type of surface hydroxyl [20,21]. The evidence is generally in the form of several OH stretching peaks since the bending modes occur in a spectral region where the alumina itself is strongly absorbing [17]. This raises the question that if the two bending modes do indeed represent two fundamentally different types of hydroxyl groups, why is there only a single OH stretching peak? The answer may well be that there are indeed two stretching modes present, but hydrogen bonding and surface electrode effects [3] have broadened them sufficiently to make them indistinguishable. In absorption infrared work, the alumina must be dehydrated at 400 to 600°C before hydrogen bonding is reduced sufficiently to allow all the surface hydroxyl

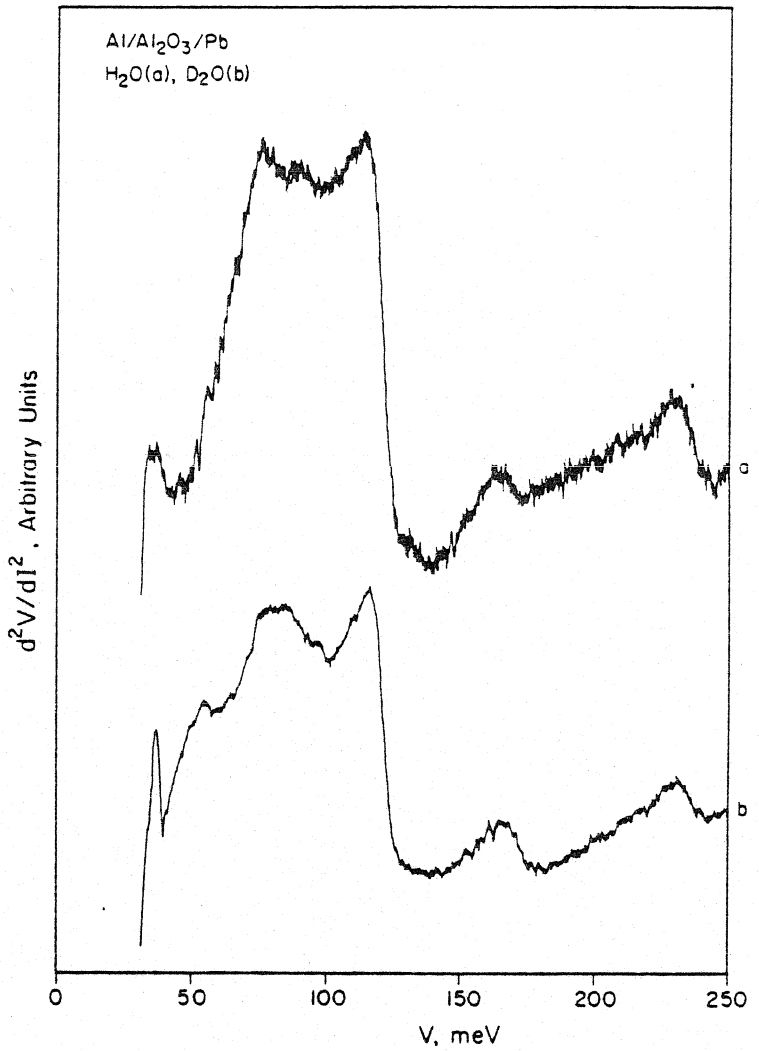

Fig. 4. Expanded IET spectra of samples prepared at room temperature in (a) H_2O and (b) D_2O plasma discharges.

stretching modes to be visible [21]. Moreover, the half-width of our 447 meV peak, 15 meV (120 cm^{-1}), is not inconsistent with the half-width of a strong doublet observed by Peri on γ-alumina [21] in the OH stretching region of the infrared spectrum. A second possibility that should be considered is that the 447 meV peak does represent a single type of hydroxyl group, but through orientation-dependent selection rules [2,4] the second mode does not couple effectively with the tunneling electron. Such a uniform alignment of the OH groups with respect to the plane of the junction interface does not seem likely on an amorphous surface,

however. Since these modes are apparent in the IET spectra of *all* our junctions, we conclude that some hydroxyl groups are always adsorbed on the surface of the insulator formed in our tunnel junctions. Furthermore, the concentration of these hydroxyl groups depends on the composition of the oxidizing gas and on the temperature at which the oxidation takes place.

At this point we need to consider two additional questions concerning our observed IET spectra. First, from where does the OH come in those insulators formed in an oxygen plasma discharge? The answer evidently lies in the fact that much of the residual gas in the vacuum system at our base pressure ($\sim 10^{-6}$ Torr) is water vapor [15]. When the plasma discharge is initiated, even more water is desorbed from the walls of the vacuum chamber. This H_2O is excited in the plasma, and these excited molecules or molecular ions can then adsorb on the insulator. The second question is why are the OH modes so intense in the spectra of those insulators formed in D_2O vapor? At the time of evaporation of the Al film, much of the ambient gas consists of water vapor, and hence it is plausible that the Al surface may dissociatively chemisorb water in the form of H atoms and OH groups prior to the plasma oxidation. These OH groups are not expected to survive the subsequent oxidation of the near surface region, however, when the junction barrier is formed. A more cogent explanation of the observed intensity of the OH modes is due to the isotopic differences between H_2O and D_2O. First, the vapor was introduced into the vacuum chamber by evaporation from 99.8% D_2O liquid in an external container. Since H_2O has a 15% higher vapor pressure than D_2O [22], the oxidizing gas will contain a correspondingly higher percentage of H_2O. A more important effect is that due to a difference in the zero point energy. Using the procedure outlined by Melander [23], a crude calculation was performed to estimate the ratio of rates at which OH and OD would adsorb onto a surface from gaseous H_2O and D_2O. It was found that $R_{OH}/R_{OD} \gtrsim 25$. Since a plasma discharge was used in the actual experiments, several additional effects must be considered such as relative rates of ionization, rates of quenching, and the acceleration of the relative ions to the surface due to Coulombic attraction, all of which will exhibit an isotopic dependence. Finally, the cross section for vibrational excitation by the tunneling electrons may differ for hydroxyl and deuteroxyl groups. When all of these factors are considered, it is possible to appreciate that the small amount of H_2O present in the liquid D_2O could result in an appreciable surface hydroxyl concentration as measured in the IET spectra.

There has been a controversy over the assignment of the 117 meV peak which is prominent in the IET spectra of all our Al-oxidized Al–Pb tunnel junctions. According to Geiger et al. [13] and Lambe and Jaklevic [4], this peak corresponds to the AlO–H bending mode of an aluminum trihydroxide. On the other hand, Lewis et al. [8] suggest that this peak represents the Al–O stretching mode of an aluminum oxide. If the insulator were an aluminum trihydroxide, then in the spectrum of every sample prepared in D_2O, there should be a peak occurring at $2^{-1/2} \times 117$ meV (=83 meV) due to the bulk AlO–D bending mode. However, as

may be seen in fig. 3(c), in the spectrum of a sample prepared at 203°C in a D_2O plasma discharge, there is no significant peak below 100 meV. In fact, except for a small peak at 54 meV and a peak at 330 meV, this spectrum is identical to the spectra observed for junctions prepared either in O_2 or at higher temperatures in H_2O. It is unlikely that Al reacts exclusively with H_2O in forming a bulk hydroxide while still adsorbing deuteroxyl groups on the surface. Thus, we conclude that those insulators formed by oxidizing Al in a plasma discharge of O_2 at all temperatures and a discharge of H_2O or D_2O at high temperatures ($\gtrsim$150°C) are aluminum oxide.

However, there is some evidence for bulk aluminum hydroxide incorporation in those insulators formed in H_2O and D_2O at lower temperatures ($\lesssim$150°C). This evidence takes the form of a peak at 80–85 meV in our IET spectra of the samples prepared at room temperature in a D_2O plasma discharge. This is at the correct energy to be the AlO–D bending mode of aluminum deuteroxide as reported by Lambe and Jaklevic [4] and Geiger et al. [13]. Also, the broadening and shift of the 117 meV peak noted in these lower temperature H_2O and D_2O samples may be partially a manifestation of the presence of a nearly coincident AlO–H mode. As discussed by Geiger et al. [13], the strong hydrogen bonding that would be present in this bulk hydroxide could broaden the AlO–H stretching mode sufficiently to make it unobservable. This would explain the reason a second peak is not seen in the region 400–450 meV. Nevertheless, we conclude that the insulator is still primarily an aluminum oxide since the Al–O stretching mode remains quite strong. It should be noted that even though we refer to this mode as an Al–O stretch, the vibrations are actually optical phonons of the oxide as opposed to vibrations of individual molecules. The selection rules for excitation of phonons by electrons are different from those for excitation by IR photons since electrons can transfer a finite momentum to the oxide, creating phonons with an appreciable wavevector, k. However, since the oxide is amorphous, it is appropriate only to consider phonons with small k. Moreover, even in ordered systems the probability of exciting a phonon decreases rapidly with increasing phonon wavevector. Thus, even though a technique such as inelastic neutron scattering may be a closer analogy to IETS due to the ability of the former to transfer momentum, the fact that most of the intensity comes from small wavevector phonons makes the comparison between IET spectra and IR spectra valid.

The structure which occurs between 165 and 230 meV may be attributed to overtone and combination bands of those modes present at 75–117 meV. The 165 meV peak would correspond to a combination of the 75 and 90 meV bending modes with possible contributions from the first overtones of these two fundamental modes. The 230 meV peak is the first overtone of the 117 meV mode. The intensity of the 165 meV peak depends upon the temperature at which the insulator is formed in the H_2O samples, i.e., the intensity decreases as the temperature of oxidation increases. This reflects correctly the behavior of the two fundamental modes. The intensity of the 230 meV peak also shows this same dependence upon

the temperature at which the oxidation is performed even though the 117 meV peak remains prominent. This result may be explained within the context of that which has already been discussed. The intensity of an overtone or combination band depends upon the anharmonicity of the bonds involved in the vibration, i.e., the more anharmonic the bond, the greater the intensity of the overtone or combination band [24]. Also, as noted by Herzberg for diatomic molecules, bonds containing hydrogen are more anharmonic than those which contain other atoms [24].

Table 2
Observed peaks and their assignments for various types of clean Al–oxidized Al–Pb tunnel junctions

Peak position (meV)	Discharge gas/temperature of oxidation	Peak assignment	Comments
37	All [a]	Al phonon	
358		C–H stretch	Hydrocarbon contamination; very weak if visible at all
75, 90	All [a]	Surface OH bend	Intensity decreases from strong for low T oxidation in H_2O to very weak for high T oxidation in H_2O; two peaks resolved only for low T oxidation in H_2O and D_2O; shoulder on 117 meV peak for others; two peaks indicate two types of surface OH groups
54, 65	D_2O/low T	Surface OD bend	
447	All [a]	Surface OH stretch	Strong to medium intensity; strongest intensity for low T oxidation in H_2O and D_2O
330	D_2O/all T	Surface OD stretch	
117	All [a]	Al–O stretch	Always strong
117	H_2O and D_2O/low T	AlO–H bend (bulk)	Some contribution to the 117 meV peak at low T oxidation in H_2O (D_2O); not evident for higher T oxidations
80–85	D_2O/low T	AlO–D bend (bulk)	
165	H_2O and D_2O/low T	Combination and overtone peaks from 75 and 90 meV fundamental peaks	Medium intensity for low T oxidations in H_2O and D_2O; not visible for oxidation at $\gtrsim 150°C$
230	All [a]	Overtone of 117 meV	Medium intensity for low T oxidation in H_2O and D_2O; very weak for others

[a] "All" signifies oxidation in either O_2, H_2O or D_2O plasmas at all surface temperatures studied ($20 < T < 250°C$).

Thus, the AlO–H bending mode of the hydroxide which is present in the insulators formed in H_2O vapor at room temperature will contribute proportionally more to the overtone (230 meV) peak than will the Al–O stretching mode. As the temperature of oxidation increases, the concentration of bulk hydroxide decreases. This decreases the contribution from the AlO–H bending mode to the 117 meV peak, and this in turn decreases the intensity of the 230 meV overtone.

Two final comments concerning our interpretation of the IET spectra should be mentioned for completeness. As occurs in some chemically anodized aluminum films [18], it is possible that A=O bonds may have been formed in the H_2O discharge at lower temperatures. This species has a stretching mode in the region 166–210 meV (1345–1696 cm^{-1}) [18], and this could be the mode associated with the 165 meV peak. However, it is not clear why this species would not also be present in the insulators formed in an oxygen discharge so we tend to reject this interpretation of the observed 165 meV peak. A second consideration is that some *molecular* water may be present in the junction. Water has a deformation mode near 200 meV (1600 cm^{-1}) [17], but, as noted earlier, there are no modes at higher energy that can be attributed to the O–H stretching mode of the molecule. Therefore, we also reject the possibility that molecular water is incorporated into our insulating films. The peak assignments of all the types of insulators which we have examined are summarized in table 2.

5. Conclusions

Our conclusions concerning the composition of the barrier region of clean (no intentional adsorbate) tunnel junctions are illustrated schematically in fig. 5. We include the cases where the insulator is formed in either an O_2, H_2O or D_2O plasma discharge at various temperatures. Those insulators formed in O_2 at all temperatures and those formed in H_2O and D_2O at high temperatures ($\gtrsim$150°C) (fig. 5a) are composed of aluminum oxide with no evidence for any appreciable bulk hydroxide. The surfaces of these insulators do have adsorbed hydroxyl groups present, however. Those insulators formed at lower temperatures (<160°C) in H_2O (fig. 5b) and D_2O (fig. 5c) are also primarily aluminum oxide, but they show evidence for the presence of some bulk aluminum hydroxide. The concentration of surface hydroxyl groups is greater on the lower temperature than on the higher temperature H_2O and D_2O samples. Those junctions prepared in H_2O and D_2O plasmas at the lower temperatures show two surface OH bending modes indicating the presence of two different types of surface hydroxyl groups. Although we detect only one peak corresponding to an OH stretching mode on surfaces such as are shown schematically in figs. 5b–c which yield two bending modes, this may be attributed to the fact that the half-width of the measured surface OH stretching mode is consistent with

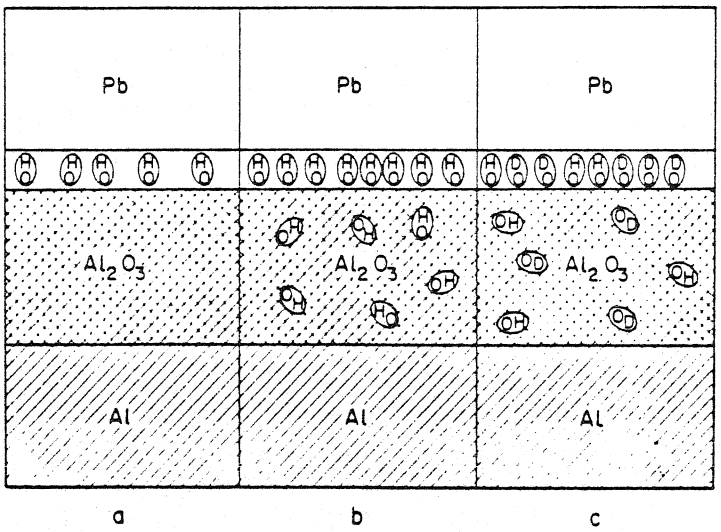

Fig. 5. Schematic illustration of the composition of the barrier region of tunnel junctions prepared under various conditions: (a) insulators formed in O_2 at all temperatures and in H_2O (and D_2O) at high temperatures (>150°C), (b) insulators formed at low temperatures (<150°C) in H_2O, and (c) insulators formed at low temperatures in D_2O.

the idea that two modes are present. These two modes may simply be rendered indistinguishable from broadening due both to hydrogen bonding and surface (top metal) electrode effects.

Acknowledgment

We acknowledge the support of this research by the National Science Foundation and the American Vacuum Society.

References

[1] R.C. Jaklevic and J. Lambe, Phys. Rev. Letters 17 (1966) 1139.
[2] D.J. Scalapino and S.M. Marcus, Phys. Rev. Letters 18 (1967) 459.
[3] J.R. Kirtley and P.K. Hansma, Phys. Rev. B12 (1975) 531.
[4] J. Lambe and R.C. Jaklevic, Phys. Rev. 165 (1968) 821.
[5] M.G. Simonson and R.V. Coleman, Nature 244 (1973) 218.
[6] M.G. Simonson and R.V. Coleman, Phys. Rev. B8 (1973) 5875.
[7] P.K. Hansma and M. Parikh, Science 188 (1975) 1304.
[8] B.F. Lewis, M. Mosesman and W.H. Weinberg, Surface Sci. 41 (1974) 142.
[9] J.D. Langan and P.K. Hansma, Surface Sci. 52 (1975) 211.
[10] N.I. Bogatina, Opt. Spectrosc. 38 (1975) 43.
[11] B.F. Lewis, W.M. Bowser, J.L. Horn, Jr., T. Luu and W.H. Weinberg, J. Vacuum Sci. Technol. 11 (1974) 262;
W.H. Weinberg, W.M. Bowser and B.F. Lewis, Japan. J. Appl. Phys., Suppl. 2, Pt. 2 (1974) 863.

[12] D.G. Walmsley, I.W.N. McMorris and N.M.D. Brown, Solid State Commun. 16 (1975) 663.
[13] A.L. Geiger, B.S. Chandrasekhar and J.G. Adler, Phys. Rev. 188 (1969) 1130.
[14] W.M. Bowser and W.H. Weinberg, Rev. Sci. Instr. 47 (1976) 583.
[15] K.L. Chopra, Thin Film Phenomena (McGraw-Hill, San Francisco, 1969).
[16] J. Klein and A. Leger, Phys. Letters 28A (1968) 134.
[17] L.H. Little, Infrared Spectra of Adsorbed Species (Academic Press, New York, 1966).
[18] G.A. Dorsey, Jr., J. Electrochem. Soc. 113 (1966) 169.
[19] H.E. Evans and W.H. Weinberg, unpublished results.
[20] J.B. Peri and R.B. Hannan, J. Phys. Chem. 64 (1960) 1526.
[21] J.B. Peri, J. Phys. Chem. 69 (1965) 211.
[22] A. Farkas, Orthohydrogen, Parahydrogen, and Heavy Hydrogen (Cambridge Univ. Press, London, 1935).
[23] L. Melander, Isotope Effects on Reaction Rates (Ronald Press, New York, 1960).
[24] G. Herzberg, Molecular Spectra and Molecular Structure. II. Infrared and Raman Spectra of Polyatomic Molecules (Van Nostrand, New York, 1945).

Chapter IV

Inelastic Electron Tunneling Spectroscopy of Phenol and Hydroquinone Chemisorbed on Alumina

Abstract

Inelastic electron tunneling spectroscopy has been used to probe the irreversible chemisorption of C_6H_5OH and 1,4-$C_6H_4(OH)_2$ on a thin amorphous film of Al_2O_3. This spectroscopy yields a representation of the vibronic excitations of the chemical bonds in the adspecies, i.e. the tunneling spectra are analogous to IR spectra. The C_6H_5OH is found to adsorb predominately as $C_6H_5O^-$ with a small amount of adsorption as C_6H_5OH. The 1,4-$C_6H_4(OH)_2$ is found to adsorb predominately as $C_6H_4(OH)O^-$ and perhaps to a smaller extent as $C_6H_4O_2^{-2}$. Extensive hydrogen bonding is observed among adsorbates and between adsorbates and the hydroxylated alumina surface.

Introduction

The irreversible chemisorption of phenol, C_6H_5OH, and hydroquinone, 1,4-$C_6H_4(OH)_2$, on amorphous alumina has been investigated using inelastic electron tunneling spectroscopy. The inelastic electron tunneling phenomena which will be discussed involve the tunneling of electrons through an insulating oxide barrier between two metal electrodes and the interaction of these electrons with adsorbates at the oxide-metal interface.

In pioneering work, Lambe and Jakelvic (1,2) have shown that the second derivative of the characteristic current-voltage (I-V) function of a tunneling junction is analogous to an infrared absorption spectrum. In the case of molecular adsorbates on the insulator surface of tunneling junctions, the molecular symmetry is ordinarily broken so that both Raman and IR vibrational modes are observed. Thus inelastic tunneling spectroscopy is a potentially powerful experimental probe of the chemical interaction of molecules adsorbed on insulating surfaces.

In the present work, inelastic tunneling spectra of phenol and hydroquinone have been measured and compared to Raman and IR spectroscopy for the same adsorbate-adsorbent systems.

Theory

The theory of inelastic tunneling spectroscopy has been discussed in detail previously (2 - 5) and will be very briefly reviewed here as it applies to the metal-metal oxide-superconductor junctions used in the present work. Vibronic excitations can occur within the adsorbed molecules present at the oxide insulator surface if $eV \geq \hbar\omega_0 + \Delta_2$, where eV is the

bias voltage applied across the vibrational excitation in the adsorbate, and $2\Delta_2$ is the energy gap of the superconductor. The tunneling spectra are measured at temperatures low enough (4.2 K) to insure that all vibrational modes of the adsorbate are in their ground states. An energy diagram describing this physical situation is shown in Fig. 1. Horizontal transitions from energy level E_1 of metal 1 correspond to elastic tunneling, whereas inelastic transitions correspond to an energy loss of $\hbar\omega_0$.

It has been shown that the derivative of the junction conductance, d^2I/dV^2, is analogous to the IR absorption spectrum of the adsorbate (2). Thus, inelastic electron tunneling spectroscopy may be used to study chemisorption and heterogeneously catalyzed surface reactions in much the same way absorption IR spectroscopy has been employed previously. The d^2I/dV^2 peak intensities are proportional to the surface coverage; and the observed peaks and peak positions reveal which bonds are broken and formed during chemisorption and/or surface reaction. Shifts in peak positions give information about both adsorbate-adsorbent and adsorbate-adsorbate interactions.

Experimental

The tunneling junctions were made by the techniques developed by Lambe and Jaklevic (1,2) and Geiger et al. (6). Briefly, this consists of evaporating an Al strip onto a glass slide and then oxidizing the surface of the strip in a glow discharge of pure oxygen. After evacuating the oxygen from the high vacuum system, the oxidized Al_2O_3 strip is exposed to approximately six torr-sec of the desired adsorbate. The adsorbate

vapor is then evacuated,and a Pb cross strip is evaporated onto the oxidized strip. These steps are all conducted in a chamber whose base pressure is on the order of 10^{-6} torr. Immediately after the junctions are made, they are stored in liquid N_2 and never again warmed up above 77 K. All adsorption experiments are conducted at room temperature.

The tunneling spectra are obtained by measuring the second derivative of the I-V characteristic of the junction. The bias current is modulated with an ultra-pure 50 kHz sine wave, and the second harmonic voltage generated across the junction is measured with a lock-in detector. The modulation voltage generated across the sample is usually 2 meV peak-to-peak or less, and the second harmonic voltage is less than 1 μeV rms. During such measurements the samples are immersed in liquid He and can be easily cooled to 1.3 K.

Chemisorption of Phenol and Hydroquinone

As described previously, the Al_2O_3 surfaces were given saturation (6 Torr-sec) exposures of both C_6H_5OH and 1,4-$C_6H_4(OH)_2$ at 300 K. The inelastic electron tunneling spectra of the C_6H_5OH and the 1,4-$C_6H_4(OH)_2$ are shown in Figs. 2 and 3, respectively. The various vibronic transitions in both spectra are listed in Tables I and II. Also shown in Table I are the infrared (IR) transitions in vapor, liquid and solid C_6H_5OH and the Raman transitions of liquid C_6H_5OH (7,8). The IR transitions of solid and liquid 1,4-$C_6H_4(OH)_2$ and the Raman transitions of liquid 1,4-$C_6H_4(OH)_2$ are shown in Table II (9). The assignments of the IR and Raman peaks are also given in both Tables I and II.

From the spectrum shown in Fig. 2, it is concluded that most of the C_6H_5OH chemisorbs on Al_2O_3 as a phenoxide ion by cleaving the OH bond in the adsorbate. In tunneling junctions made with no intentionally introduced adsorbate, the oxide surface is saturated with OH groups (2,6,10,11) and the tunneling spectra show OH stretching vibrations (ca. 448 meV) very similar in intensity and shape to those observed for C_6H_5OH junctions. Thus, the C_6H_5OH must either displace the "clean" surface OH groups, adsorb with its OH group orthogonal to the electric field of the tunneling electrons, or adsorb predominately as a phenoxide ion. In either of the first two cases, the ring stretch with OH-bending-character vibrations at 170.9 and 163.3 meV would be much stronger than is observed. The second case is also unlikely since the oxide is amorphous. There must be a distribution of adsorbate orientations on the surface. Thus most of the C_6H_5OH chemisorbs as a phenoxide ion. However, a small amount of C_6H_5OH evidently chemisorbs on the Al_3O_3 associatively as judged by the weak peaks at 418.8, 170.9 and 163.3 meV. That is, there is a small amount of irreversibly adsorbed molecular C_6H_5OH on the Al_2O_3 after evacuation of the adsorbate from the gas phase at 300 K to a partial pressure $<10^{-5}$ Torr. The strong transition in adsorbed C_6H_5OH present at 118.5 meV is due not only to a CH bending mode of the adsorbate but also to an Al-O stretching mode in the adsorbent (2,6,10,11). All of the other transitions are indicative of an adsorbed phenoxide ion chemisorbed to the Al^{+3} site of the Al_2O_3 surface.

It is also clear from Fig. 2 that there is a considerable amount of hydrogen bonding between the adsorbed $C_6H_5O^-$ and presumably adjacent OH groups on the Al_2O_3 surface; this is apparent from the long asymmetric

tailing of the OH stretching mode to lower energies. Such a tail is present on the "clean" hydroxylated surface, but is much smaller, i.e. there is only a relatively small amount of hydrogen bonding between the OH groups on the otherwise clean Al_2O_3 surface. It should be noted also that Raman modes are evidently active in adsorbed $C_6H_5O^-$ due both to the high intensity of the CH stretching modes and the presence of the 124.4 meV "ring breathing" mode.

The extremely high resolution of IETS is obvious from Fig. 2 and even more apparent when compared with a recent investigation of C_6H_5OH chemisorption on Al_2O_3 using absorption IR spectroscopy (12). The IR results also indicate that C_6H_5OH is chemisorbed as a phenoxide ion on Al_2O_3 at 425 K, but only five transitions are resolved above 150 meV - CH stretching modes at 378 and 374 meV, aromatic ring vibrations at 199 and 185 meV, and a CO stretching mode (i.e. an x-sensitive mode) at 159 meV (9). This is in good agreement with the present results, but the much higher resolution of IETS should be emphasized.

The inelastic electron tunneling spectrum of adsorbed 1,4-$C_6H_4(OH)_2$ is shown in Fig. 3, and the results are similar to those of C_6H_5OH. The high intensity of the 448.1 meV OH stretching mode and its attendant low energy tail and broad peak at 425.0 meV suggests that one of the OH bonds is preserved in adsorbed 1,4-$C_6H_4(OH)_2$, and the adsorption occurs by cleaving the other OH bond analogous to the mode of adsorption of C_6H_5OH (e.g. compare the intensity of the OH stretching to CH stretching modes in 1,4-$C_6H_4(OH)_2$ to those in $C_6H_5(OH)$).

The possibility of adsorption without cleaving either OH bond cannot be ruled out entirely. Analysis of the data is not yet sufficiently refined to determine whether the OH bending vibrations observed at 170.0 and 156.9 meV are indicative of one or two OH groups per adsorbed molecule. Indeed, there may be di-adsorbed ions (cleaving both OH bonds), especially at low surface coverage. In view of the results for C_6H_5OH, however, it is most probable that adsorption occurs predominately by cleaving one of the OH bonds. There is a considerable amount of hydrogen bonding apparent for the adsorbed 1,4-$C_6H_4(OH)_2$, even more than in the case of adsorbed C_6H_5OH. This is to be expected in view of the additional OH group present in 1,4-$C_6H_4(OH)_2$. As noted above for the case of C_6H_5OH, the transitions at 448.1 and 115.6 meV in Fig. 3 and Table II are indicative to some extent of the Al_2O_3 adsorbent in the absence of any adsorbate.

Summary

Inelastic electron tunneling spectroscopy has been used to probe the chemisorption of phenol and hydroquinone on the surface of an Al_2O_3 film in an $Al/Al_2O_3/Pb$ tunnel junction. The measurement temperature was 4.2 K, and thus the junction was of the type NS with normal Al and superconducting Pb.

Both C_6H_5OH and 1,4-$C_6H_4(OH)_2$ chemisorb irreversibly on the Al^{+3} sites of the Al_2O_3 surface at room temperature. The C_6H_5OH adsorbs predominantly as a $C_6H_5O^-$, and the 1,4-$C_6H_4(OH)_2$ predominantly as a $C_6H_4(OH)O^-$. There is also a small fraction of the Al_2O_3 which chemisorbs associated C_6H_5OH at a room temperature exposure of 6 torr-sec. The 1,4-$C_6H_4(OH)_2$ may adsorb to a

very small extent both in the associated form and also as the di-ion $C_6H_4O_2^{-2}$. There is extensive hydrogen bonding between both the adsorbates, and the adsorbate and the OH groups present on the Al_2O_3 surface as witnessed by the long low energy tail observed on the OH stretching mode. This occurs for both chemisorbed phenol and hydroquinone to a much greater extent than the hydrogen bonding which exists between the OH groups on the clean, but hydroxylated, Al_2O_3 surface. The high resolution of inelastic electron tunneling spectroscopy is especially evident when compared with absorption IR data for C_6H_5OH adsorbed on Al_2O_3 (12).

Acknowledgment

The support of this research by the President's Fund of the California Institute of Technology (Grant No. PF-047) is gratefully acknowledged. We have benefited from the facilities of the Jet Propulsion Laboratory of the California Institute of Technology. JLH and TL wish to thank the Esso Corporation for partial support as participants in the undergraduate research program in the Division of Chemistry and Chemical Engineering at the California Institute of Technology.

References

1. R. C. Jaklevic and J. Lambe, Phys. Rev. Lett. 17, 1139 (1966).
2. J. Lambe and R. C. Jaklevic, Phys. Rev. 165, 821 (1968).
3. D. J. Scalapino and S. M. Marcus, Phys. Rev. Lett. 18, 459 (1967).
4. C. B. Duke, Tunneling in Solids (Academic, New York, 1969).
5. Tunneling Phenomena in Solids, edited by E. Burstein and S. Lundquist (Plenum, New York, 1969).
6. A. L. Geiger, B. S. Chandrasekhar and J. G. Adler, Phys. Rev. 188, 1130 (1969).
7. J. C. Evans, Spectro. Acta 16, 1382 (1960).
8. J. H. S. Green, J. Chem. Soc. 2236 (1961).
9. A. Hidalgo and O. Otero, Spectro. Acta 16, 518 (1960).
10. J. Klein, A. Leger, M. Belin, D. Defourneau and M. J. L. Sangster, Phys. Rev. B. 7, 2336 (1973).
11. B. F. Lewis, M. Mosesman and W. H. Weinberg, Surface Sci. 41, 142 (1974).
12. D. R. Taylor and K. H. Ludlum, J. Phys. Chem. 76, 2882 (1972).

TABLE I. Infrared and Raman transitions in phenol and inelastic electron tunneling transitions in phenol adsorbed on an alumina film.[a]

Infrared			Raman	IETS	
Vapor	Liquid	Solid	Liquid	Adsorbate	Assignment
453.9				448.9 (s, b)	
452.9	433.9 (sh)		433.9 (w, b)	418.8 (b)	OH stretch
452.3	415.3 (vs, b)	399.8	415.3 (w)		
381.6	380.6 (w)	380.6 (sh)		382.5 (sh)	
			379.5 (s)	378.1 (s)	
	378.1 (sh)			372.2 (s)	CH stretch
378.1	377.4 (m)	377.3		359.8 (s)	
	374.4 (w)	374.3	374.8	350.6 (sh)	
	198.9 (s)	199.0	199.0 (m)	209.8 (m)	
199.0	198.0 (vs)	198.1	197.8 (m)	197.6 (s)	
186.8					
186.1	186.0 (vs)	186.1	186.0 (w)	184.2 (m)	Ring stretch
185.1					
183.2					
182.3	187.2 (vs)	182.6	182.4 (w)	179.3 (s)	
181.3					
	168.9 (m)	169.9		170.9 (vw)	
167.3					Ring stretch with OH bending character
166.5	166.5 (w)			163.3 (vw)	
165.5					
	160.2 (vvw)	160.2			CH bend
157.2					
156.2		155.2	155.3 (m)	158.4 (s)	X-sensitive
155.3					
	152.2 (vs)	152.5	151.3 (b, w)	154.7 (vw, sh)	
	148.5 (sh)		148.3 (w)		
146.5					OH bending with ring stretch character
145.9					
144.8					
	144.8 (w)	144.9	145.1 (m)	143.1 (m)	
143.6					
142.6	142.8 (w)	142.8	143.2 (m)		
141.6					CH bend
132.9	132.9 (m)	132.9	132.9 (w)	132.7 (m)	
127.9					
127.2	127.1 (w)	127.0	127.0 (m)	127.2 (w)	
126.2					
			124.0 (s)	124.4 (w)	Ring breathing

	121.3 (vvw)	121.6			
		120.8		118.5 (vs)	(Al–O stretch) CH bend
	118.8 (vvw)	119.3			
109.2	110.1 (w)	110.1			
		109.4			
102.0	102.7 (w)	102.7	102.7 (m)	102.7 (s)	
100.9	100.7 (s)	100.7	100.9 (m)		X-sensitive
93.0	93.2 (vs)	93.5	93.6 (w)	94.8 (m)	CH bend
85.1	85.5 (vs)			87.0 (s)	
76.9	76.6 (vw)	76.6	76.5 (m)	76.6 (m)	Ring deformation
66.1					
65.3	65.8	66.3	65.8 (m)	65.3 (m)	
64.2					X-sensitive
62.4	63.0 (m)	62.9	63.1 (w)	60.4 (w)	
		62.2			
	50.8 (b)	51.5	51.5 (b, w)	52.8 (s)	Ring deformation
49.3		56.4		43.5 (w)	X-sensitive

[a] ir and Raman data are taken from Evans (Ref. 7) and Green (Ref. 8). The symbols are defined as follows: b = broad, m = medium, s = strong, sh = shoulder, w = weak, v = very, X = substituent on the aromatic ring.

TABLE II. Infrared and Raman transitions in hydroquinone and inelastic electron tunneling transitions in hydroquinone adsorbed on an alumina film.[a]

Infrared Solid	Infrared Liquid	Raman Liquid	IETS Adsorbate	Assignment
			448.1 (s, b)	OH stretch
406.4	420.8		425.0 (w, b)	
375.7	375.2		388.1 (w)	CH stretch
364.4	367.1		375.6 (m)	
363.5	357.3		360.3 (s)	
353.6	350.6		352.5 (sh)	
337.5	337.5		337.5 (sh)	
230.2	230.2		231.9 (w)	Ring stretch
226.9	226.9		207.5 (w)	
201.6	202.1	199.7	197.5 (m)	
187.5	187.5		186.2 (sh)	
181.9	180.4		181.2 (m)	
166.4	165.5		170.0 (sh)	OH bend
161.8	163.3			CH bend
155.0	154.4	156.7	156.8 (m)	OH bend
153.1	152.1	153.2		
149.2	149.6			
147.3	148.2			CH bend
144.1	144.1	143.6	143.1 (w)	
138.4	138.2		135.0 (sh)	
136.0	136.4		131.2 (m)	
125.2	125.3		123.8 (sh)	
116.5	116.2		115.6 (vs)	
114.1	113.9			
110.3	111.3			
102.8	103.2	105.8	105.0 (m)	
100.4	98.9	102.8	100.8 (m)	
94.2	94.5		97.2 (sh)	Ring deformation
	93.2		89.0 (m)	CH bend
84.2	83.9		86.0 (sh)	Ring deformation
75.5	75.6	80.7	80.4 (w)	
67.6	67.4		72.0 (w)	
64.3	64.1	65.8	66.8 (w)	
56.9	56.8	58.0	59.8 (m)	
	51.1		53.2 (m)	
	47.7		47.1 (m)	

[a] ir and Raman data taken from Hidalgo and Otero (Ref. 9). Symbols are defined in Table I.

Figure Captions

Figure 1. Schematic diagram for the inelastic electron tunneling between energy level E_1 in a normal metal and energy level E_2 in a superconducting metal of energy gap $2\Delta_2$. The Fermi level of the normal metal is $E_{F1} = 0$, while that of the superconducting metal is $E_{F2} = -eV$ where eV is the applied bias voltage. Elastic tunneling is represented by the horizontal dashed line, while inelastic tunneling is represented by the oblique dashed line, resulting in a vibronic excitation of energy $\hbar\omega_0$. The width of the insulating barrier is given by ℓ.

Figure 2. Inelastic electron tunneling spectrum of C_6H_5OH adsorbed on Al_2O_3 in an $Al/Al_2O_3/Pb$ junction. T = 4.2 K; junction impedance = 82 Ω; modulation voltage = 2 meV peak-to-peak; oscillator frequency = 46 kHz.

Figure 3. Inelastic electron tunneling spectrum of 1,4-$C_6H_4(OH)_2$ adsorbed on Al_2O_3 in an Al/Al_2O_3Pb junction. T = 4.2 K; junction impedance = 36 Ω; modulation voltage = 2 meV peak-to-peak; oscillator frequency = 47 kHz.

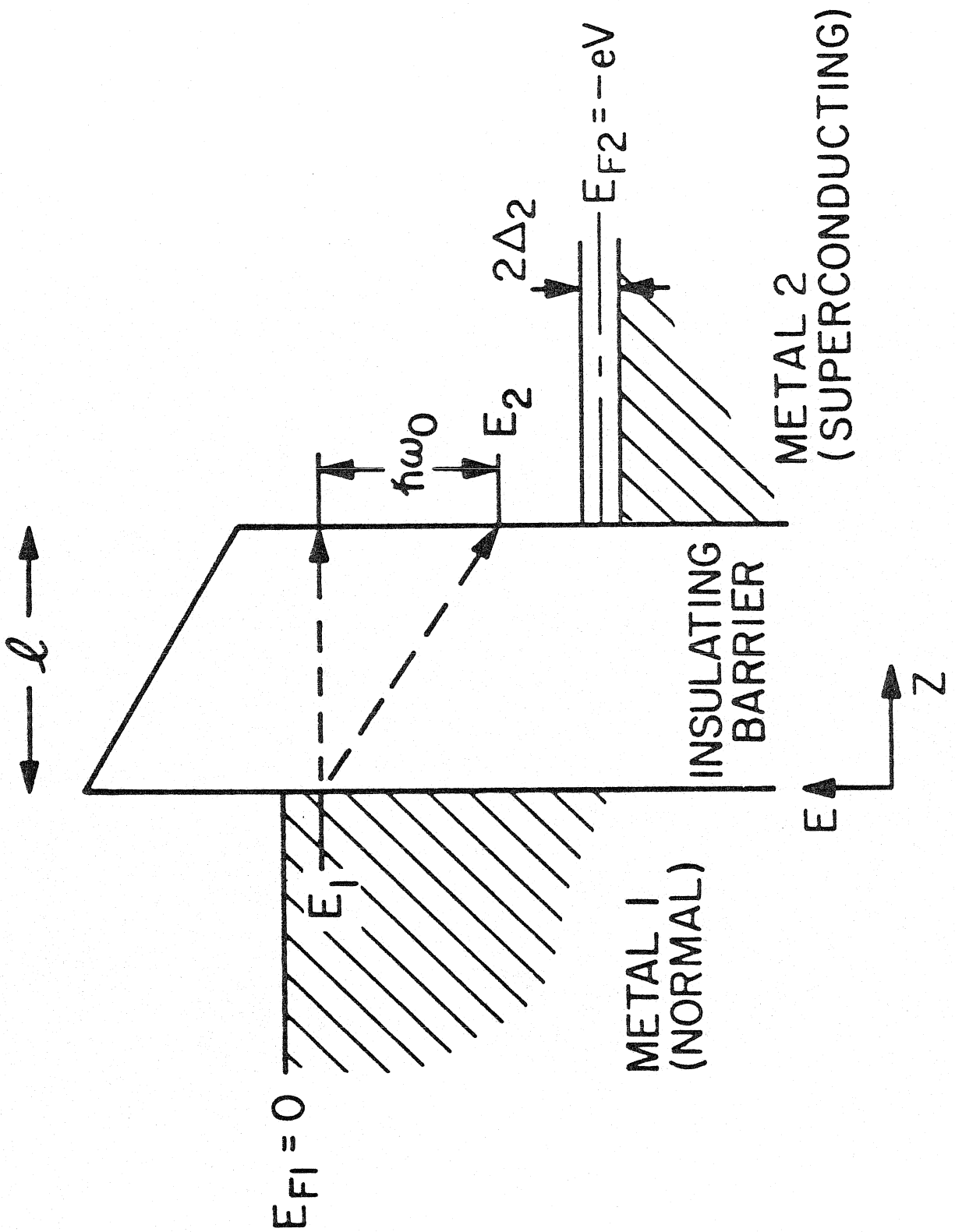
$E_{F1} = 0$
E_1
METAL 1
(NORMAL)
INSULATING
BARRIER
METAL 2
(SUPERCONDUCTING)
E_2
$\hbar\omega_0$
$2\Delta_2$
$E_{F2} = -eV$
ℓ
E
Z

Fig. 1

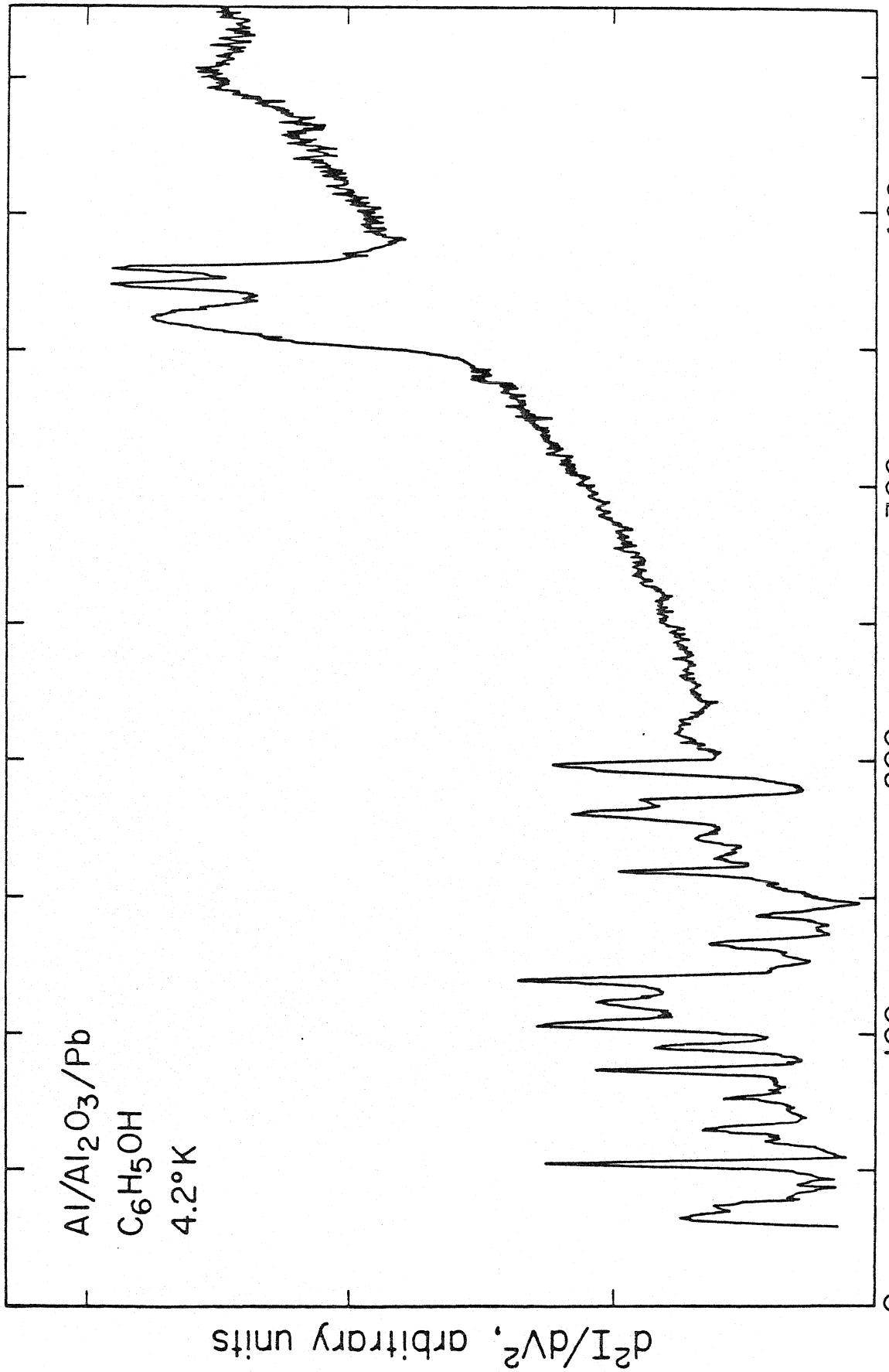
Al/Al2O3/Pb
C6H5OH
4.2°K
d2I/dV2, arbitrary units
0
100
200
300
400
V, meV

Fig. 2

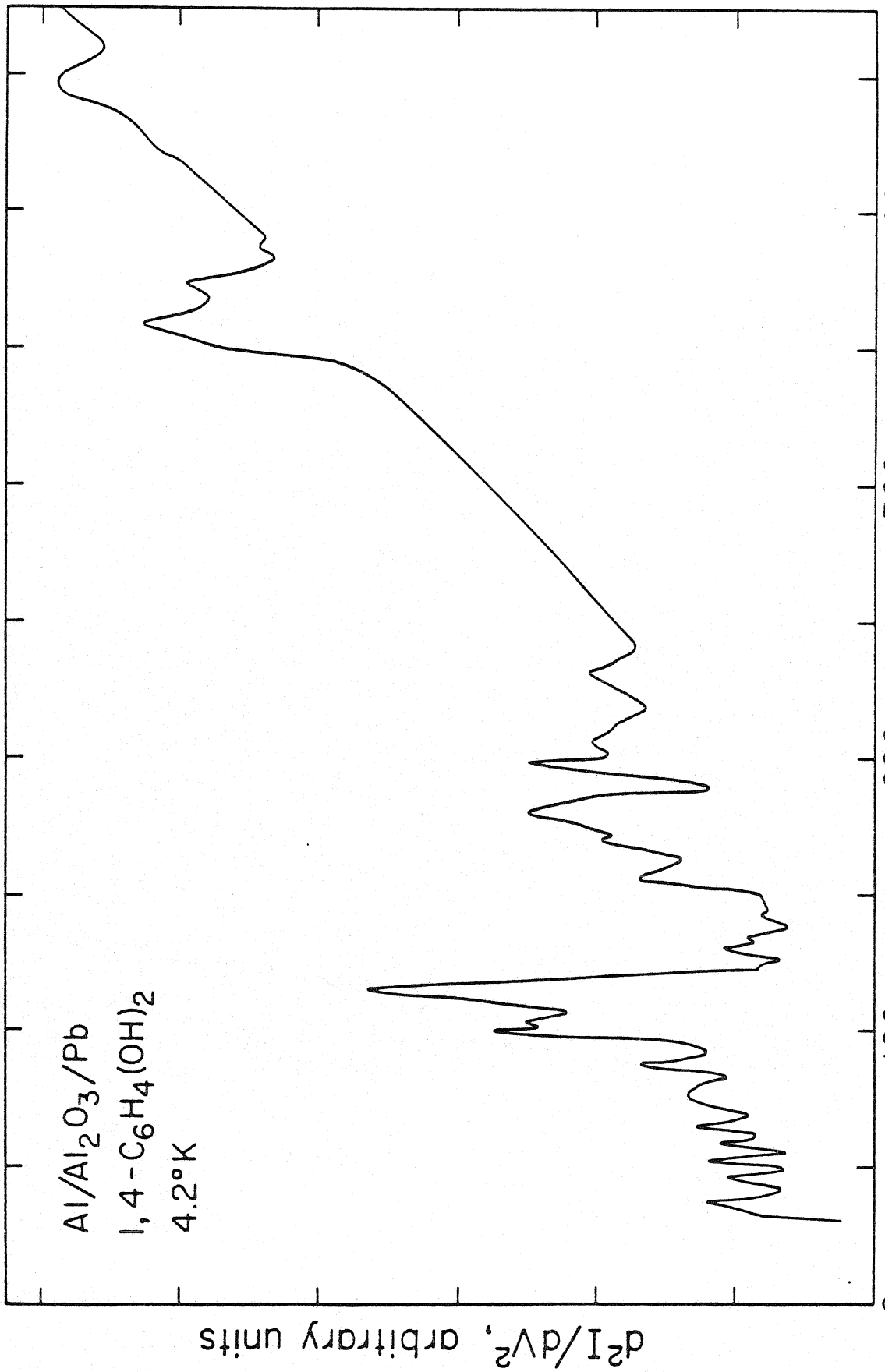
Al/Al2O3/Pb
1,4-C6H4(OH)2
4.2°K
d2I/dV2, arbitrary units
0
100
200
300
400
V, meV

Fig. 3

Chapter V

Inelastic Electron Tunneling Spectroscopy of Phenol, Catechol, Resorcinol and Hydroquinone Chemisorbed on Alumina

Synopsis

Inelastic electron tunneling spectroscopy has been used to probe the irreversible chemisorption at 300 K of phenol, catechol, resorcinol and hydroquinone on thin amorphous alumina films in $Al/Al_2O_3/Pb$ sandwich structure tunneling junctions. This spectroscopy yields a representation of the vibronic excitations of the chemical bonds in the adspecies. Phenol chemisorbs predominantly as $C_6H_5O^-$ on Al^{+3} sites with a very small amount of associative chemisorption at high coverages. Catechol and resorcinol both adsorb predominantly as the di-ion $C_6H_4O_2^{-2}$, whereas hydroquinone chemisorbs both as the di-ion and as the single ion 1,4-$C_6H_4(OH)O^-$ at high surface coverages. Hydrogen bonding is observed among the adsorbates and between the adsorbates and the OH groups on the partially hydroxylated Al_2O_3 surface. The experimental results are explicable in terms of the geometry and chemical properties of the adsorbates and the oxide surface.

Introduction

The experimental technique of inelastic electron tunneling spectroscopy (IETS) may be used to investigate the vibrational structure of species adsorbed on solid surfaces by utilizing a metal-oxide-metal tunneling junction sandwich structure. The method has been used extensively to determine the structure of various adsorbates chemisorbed on Al_2O_3 surfaces, usually in $Al/Al_2O_3/Pb$ junctions (1 - 3). All tunneling measurements reported herein have been conducted at $1.3 < T < 4.2$ K; at this temperature the Al electrode is normal and the Pb is superconducting. When a bias voltage is applied between the two metal electrodes tunneling (both elastic and inelastic) occurs through the thin ($\sim$ 25 Å) oxide barrier. When the applied voltage is equal to one of the vibrational excitation energies of the adsorbed molecule, an additional inelastic channel for tunneling is allowed, and this is reflected in an increase in the measured tunneling current. Thus the junction I-V curve is piecewise continuous with breaks (and concomitant increases in the slope of the curve) at the frequencies of the vibronic excitations; the $\frac{dI}{dV}$ - V (or σ - V function where σ is the junction conductance) is a step function at the excitation energies; and the $\frac{d^2I}{dV^2}$ - V function is a δ-function at the excitation energies which can be shown to be analogous to either IR or Raman spectroscopy of adsorbed species (1 - 3).

2. Experimental Procedures and Results

The method of junction preparation has been described in detail previously (2,3). Briefly, it involves evaporation and oxidation techniques

in an oil diffusion pumped bell jar with a base pressure of $\lesssim 10^{-6}$ torr.* An Al strip 1 mm x 25 mm is evaporated to a thickness of ca. 5000 A, and this strip is oxidized in a glow discharge of pure O_2 (at a pressure of 50 μ) to form an amorphous Al_2O_3 film with a thickness of 25 - 30 Å. After the oxidation of the Al and evacuation of the bell jar, the adsorbate is then introduced into the vacuum system. All exposures reported herein represent a saturation exposure of the various adsorbates on the 295 K Al_2O_3 surface, i.e. full monolayer coverage (as judged by a saturation of the adsorbate vibrational excitation peaks with respect to the vibrational modes of the Al_2O_3 lattice). The saturation exposures are 10 torr-sec, i.e. an adsorbate partial pressure of 10^{-2} to 10^{-1} torr with an exposure time of 100 to 1000 seconds. After the adsorption has occurred and evacuation of the adsorbate from the bell jar, several cross strips of Pb are slowly evaporated onto the oxide. The Pb strips are 1 mm x 15 mm and approximately 1 μ in thickness. Thus the number of different tunneling junctions is determined by the number of Pb cross strips (generally three), and the "surface area" of the adsorbent is the area of intersection of the Pb with the Al_2O_3, namely 1 mm^2. The impedance of the junctions is a sensitive function of the oxide thickness, and in this work the junction impedance is on the order of 25 - 100 Ω corresponding to an oxide thickness of ca. 25 - 30 Å.

Pb is chosen for the upper electrode for three reasons. First, it has a relatively large ionic radius and does not tend to diffuse into the

*An ultra-high vacuum (UHV) environment ($p < 10^{-9}$ torr) is not required when conducting chemisorption experiments on Al_2O_3 surfaces at room temperature since the sticking probability of background gases is very low on this oxide surface (2,3).

oxide lattice even under the influence of an applied potential. Such diffusion would cause irreproducibility in the tunneling measurements. In addition, the Pb is superconducting below 7.2 K, so even at 4.2 K, one of the metal electrodes is superconducting; and this enhances the resolution of IETS (1 - 3). Finally, the Pb is chemically inert and does not interact except physically with any of the adsorbates. In this respect IETS is rather similar to matrix isolation IR spectroscopy (2).

Since the $\frac{d^2I}{dV^2}$ -V function is analogous to the vibrational spectrum, this desired second derivative of the tunneling current is measured electronically by measuring the second harmonic of a small modulation voltage applied across the metal electrodes (2,3). This technique is quite standard in very many different kinds of modulation spectroscopy, e.g. Auger electron spectroscopy.

Phenol and the three dihydroxy substituted phenols catechol [1,2-$C_6H_4(OH)_2$], resorcinol [1,3-$C_6H_4(OH)_2$] and hydroquinone [1,4-$C_6H_4(OH)_2$] were all adsorbed on the Al_2O_3 films at room temperature, and the tunneling spectra of these adsorbates were measured at 4.2 K in Al/Al_2O_3/Pb junctions as described previously. The measured spectra for the phenol, catechol, resorcinol and hydroquinone are shown in Figs. 1, 2, 3 and 4, respectively. Tentative peak assignments are given in Table I by making comparisons with IR spectroscopy of molecular phenol and the phenol derivatives (4 - 6).

3. Discussion and Conclusions

Perhaps the most striking feature to note in Table I is the close similarity between the molecular IR spectra of phenol and the phenol

derivatives and the IETS results for the corresponding chemisorbed phenol and phenol derivatives. The assignments given in Table I have been confirmed for the molecular species (4 - 6), but the assignments for the adspecies should be viewed as tentative. Obviously, the IETS assignments can be verified using isotopically labeled phenol derivatives, but the salient point to note is the ability of IETS to elucidate with high resolution and high sensitivity the vibrational structure of these adspecies. The nature of the excitation (the longitudinal electric field of the tunneling electron) allows vibrational excitations to be observed even at very low energies, e.g. the ca. 52 meV (419 cm^{-1}) phonon mode of the Al_2O_3 lattice. This is in contradistinction to the usual case of absorption IR spectroscopy of adsorbed species where transmission of the transverse electromagnetic radiation becomes a serious problem at the lower energies. For example, a recent absorption IR investigation of phenol adsorbed on Al_2O_3 resolved four transitions (all above 150 meV) (7), as opposed to the 26 transitions resolved by IETS and shown in Fig. 1.

The shifts in the vibrational spectra of the adsorbed species are rather small in comparison to the molecular IR spectra. This indicates that the adsorbate molecule is not radically perturbed by chemisorption. It should be noted also that the OH vibrational modes of adsorbed phenol, catechol and resorcinol are not present, and only a rather small contribution is observed in adsorbed hydroquinone. The transition near 450 meV is due to a partially hydroxylated Al_2O_3 surface (1 - 3); if the Al_2O_3 surface were made more acidic through further hydroxylation, it is likely that this 450 meV transition due to an OH stretching mode would intensify and split into more than a single peak (8). The shifts in frequency of the

surface OH mode are due to a varying degree and type of interaction with the adsorbate, e.g. a hydrogen bonding "through-space" and collective electronic "through-bond" interaction. In the case of phenol, adsorption occurs as a phenoxide ion; and both catechol and resorcinol chemisorb almost exclusively as the di-ion. However, since hydroquinone can adsorb only as the di-ion with the ring parallel to the surface, and this is sterically forbidden for many of the pairs of Lewis acid sites, there is chemisorption of the hydroquinone both as the di-ion and as the mono-ion.

In conclusion, it should be emphasized that the high resolution and sensitivity of IETS has again been graphically demonstrated. The resolution is sufficient to identify all the vibrational modes in the adsorbed phenols and to easily distinguish among the four very similar adsorbates investigated. The sensitivity of IETS is also quite impressive. Based on the known Al_2O_3 surface area and the molecular dimensions of the phenols, the number of adspecies which yield the spectra shown in Figs. 1-4 can be calculated; it is estimated that the number of adsorbed species lies between 2×10^{12} mm^{-2} (phenol) and 4×10^{11} mm^{-2} (hydroquinone). With the signal-to-noise ratio for the hydroquinone spectrum >200, it is inferred that even with no signal averaging techniques, $\lesssim 2 \times 10^{9}$ molecules of adsorbed hydroquinone can be detected on the 1 mm^2 Al_2O_3 surface.

The importance of IETS in surface chemistry and chemical catalysis research lies in the fact it probes the vibrational structure of adsorbates or reaction intermediates. Thus, it is a complementary probe to the other modern electron spectroscopies which can be applied to surface chemical problems, e.g. Auger electron spectroscopy, and X-ray and UV-photoelectron spectroscopy since the latter probe the electronic levels

of adspecies. IETS is of great importance also because it gives information concerning the nature of H on solid surface, a feature lacking in the other electron spectroscopies mentioned above. This is obviously vital information when investigating, e.g.,elementary surface reactions in the catalytic conversion of hydrocarbons.

Acknowledgment

The support of this research by the President's Fund of the California Institute of Technology (Grant No. PF-047) is gratefully acknowleged.

References

1. J. Lambe and R. C. Jaklevic, Phys. Rev. 165 (1968) 821.

2. B. F. Lewis, M. Mosesman and W. H. Weinberg, Surface Sci. 41 (1973).

3. B. F. Lewis, W. M. Bowser, J. L. Horn, Jr., T. Luu and W. H. Weinberg, J. Vac. Sci. Technol. 11,262 (1974).

4. A. Hidalgo and C. Otero, Spectro. Acta 16 (1960) 528.

5. J. C. Evans, Spectro Acta 16 (1960) 1382.

6. J. H. S. Green, J. Chem. Soc. (1961) 2236.

7. D. R. Taylor and K. H. Ludlum, J. Phys. Chem. 76 (1972) 2882.

8. W. K. Hall, private communication.

Table I. Vibrational frequencies in meV of molecular phenol, catechol, resorcinol and hydroquinone and these molecules chemisorbed on amorphous alumina films.[a]

Phenol (IR)[b]	Phenol on Alumina (IETS)	Catechol (IR)[b]	Catechol on Alumina (IETS)	Resorcinol (IR)[b]	Resorcinol on Alumina (IETS)	Hydroquinone (IR)[b]	Hydroquinone on Alumina (IETS)	Tentative Assignment
	448.9(s,b)[c]		450.1(s,b)[c]		450.0(s,b)[c]		448.1(s,b)[c]	
401.1	418.8(vw,b)	416.6		420.8		420.8	425.0(w,b)	OH stretch
		414.3						
383.7	382.5(sh)						388.1(w)	
381.9	378.1(s)		371.2(m)		366.2(sh)		375.6(m)	
377.9	372.2(s)	377.5	360.4(s)	377.5	359.9(s)	375.2	360.3(s)	CH Stretch
374.9	359.8(s)	370.0	352.2(sh)	371.0	351.4(sh)		352.5(sh)	
	350.6(sh)						337.5(sh)	
			230.6(w)[d]				231.9(w)[d]	
207.9	209.8(m)	210.4	209.4(m)	207.3	208.8(m,b)		207.5(w)	
198.6	197.6(s)	201.5	197.0(s)	200.9	200.0(m,b)	201.6	197.5(m)	
198.0		199.4		199.1		199.7		CC stretch
185.4	184.2(m)	187.8		184.7		187.5	186.2(sh)	
182.3	179.3(s)	182.1	181.0(s)	181.0	179.4(s)	181.9	181.2(m)	
124.2		125.6	127.8(w)	124.1				
155.0	163.3(w)	154.1	158.4(w)	160.0	163.4(sh)	161.8	156.9(m)	
144.1	158.4(s)	144.1	149.9(w)	144.1	154.8(sh)	147.3	143.1(w)	
142.6	143.1(m)	142.6	142.4(m)	142.2	138.1(m)	138.4	135.0(sh)	CH in-
132.7	132.7(m)	135.1	136.5(w)	133.3	131.2(m)	136.0	131.2(m)	plane
126.8	127.2(w)	128.9	130.2(w)			125.2	123.8(sh)	deforma-
		41.4				47.7		tion
121.5	124.4(w)	120.0		113.1		114.1		
115.6	118.5(s)[e]	116.3	116.2(s)[e]	119.3	116.8(s)[e]	116.5	115.6(s)[e]	OH out-of-
109.2		106.5	106.9(sh)	105.4	107.9(sh)	110.3	105.0(m)	plane
102.7	102.7(s)	105.4		100.8	97.4(sh)	102.8	100.8(m)	deforma-
93.0	87.0(s)	92.4	92.4(s)	91.6		94.2	89.0(m)	tion
100.4	94.8(m)	96.0		99.2	88.5(w)	100.4	97.2(sh)	in-plane
76.2	76.6(m)	79.7	76.9(w)	75.6	80.0(w)	75.5	80.4(w)	ring vibra-
65.7	65.3(m)	67.9	71.5(m)	67.2	71.2(w)	67.6	72.0(w)	tion
84.9				84.6		84.2	86.0(sh)	out-of-
62.6	60.4(w)	62.2	56.9(m)	64.3	59.4(m)	64.3	59.8(m)	plane ring
56.0	52.8(s)	55.5	52.4(sh)	56.8	52.2(w)	51.1	53.2(m)	vibration
169.0	170.9(w)	168.0	166.5(m)	171.2	170.4(m)	166.4	170.0(sh)	CO stretch

a. To convert from meV to cm^{-1}, multiply the former by 8.0657.

b. IR data taken from refs. 4, 5 and 6.

c. Nomenclature: s=strong, m=medium, w=weak, sh=shoulder, v=very, b=broad. The highest energy OH stretching frequencies for the adsorbate-adsorbent system are due to a partially hydroxylated Al_2O_3 surface.

d. Second harmonic.

e. The preponderance of this peak is due to the Al-O stretching frequency.

Figure Captions

Fig. 1: Inelastic electron tunneling spectrum of phenol chemisorbed on alumina. Phenol exposure of 10 torr-sec (saturation coverage) at room temperature. Junction impedance - 82 Ω; measurement temperature - 4.2 K; modulation frequency = 46 kHz; modulation voltage = 0.7 meV rms; lock-in time constant = 3 sec; sweep speed = 20,000 sec/volt.

Fig. 2: Inelastic electron tunneling spectrum of catechol chemisorbed on alumina. Catechol exposure of 10 torr-sec (saturation coverage) at room temperature. Junction impedance = 33 Ω; measurement temperature = 4.2 K; modulation frequency = 47 kHz; modulation voltage = 0.7 meV rms; lock-in time constant = 1 sec; sweep speed = 4,000 sec/volt.

Fig. 3: Inelastic electron tunneling spectrum of resorcinol chemisorbed on alumina. Resorcinol exposure of 10 torr-sec (saturation coverage) at room temperature. Junction impedance = 31 Ω; other conditions as in Fig. 2.

Fig. 4: Inelastic electron tunneling spectrum of hydroquinone chemisorbed on alumina. Hydroquinone exposure of 10 torr-sec (saturation coverage) at room temperature. Junction impedance = 36 Ω; other conditions as in Fig. 2.

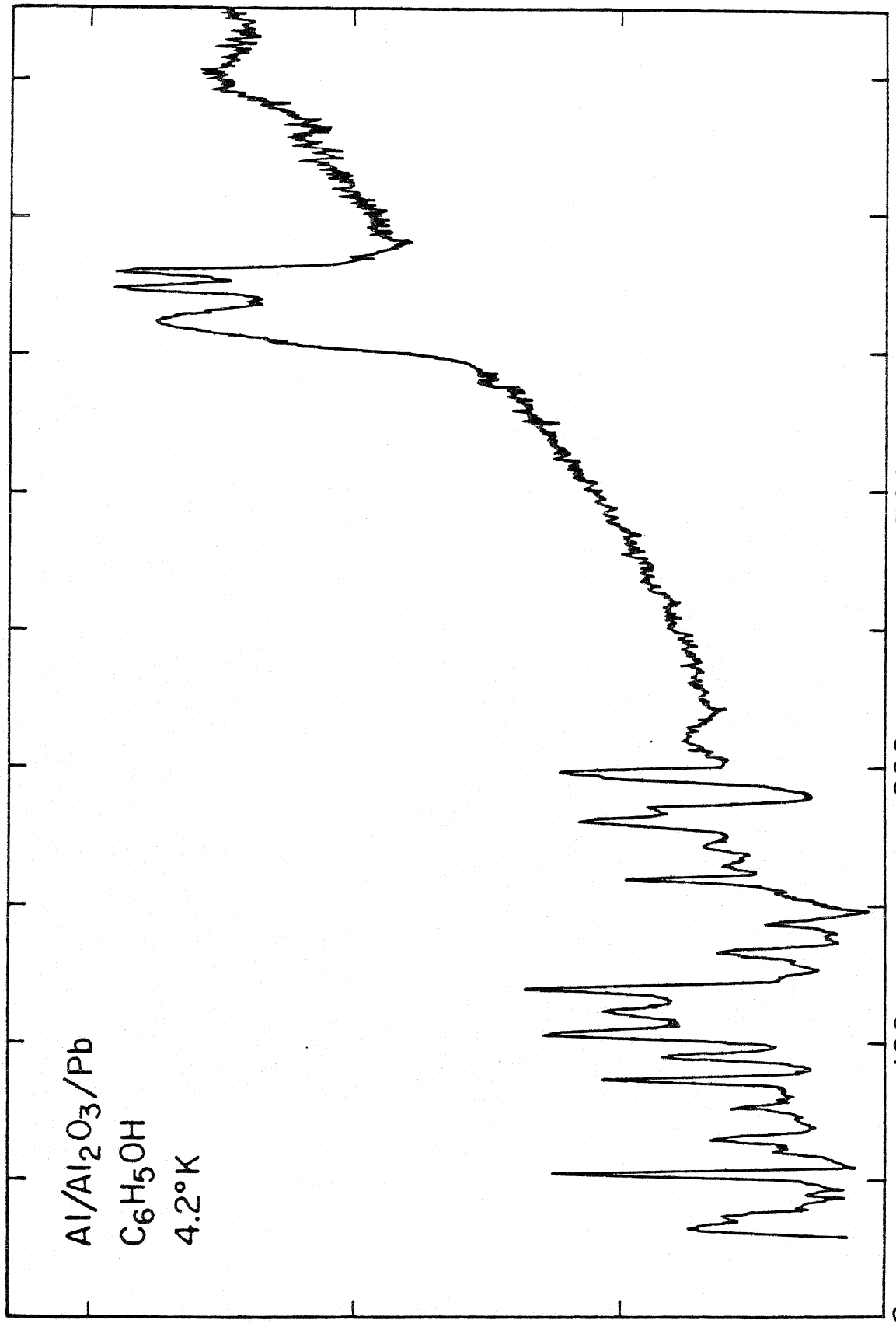
Al/Al2O3/Pb
C6H5OH
4.2°K
0
100
200
300
400
V, meV
d2I/dV2, arbitrary units

Fig. 1

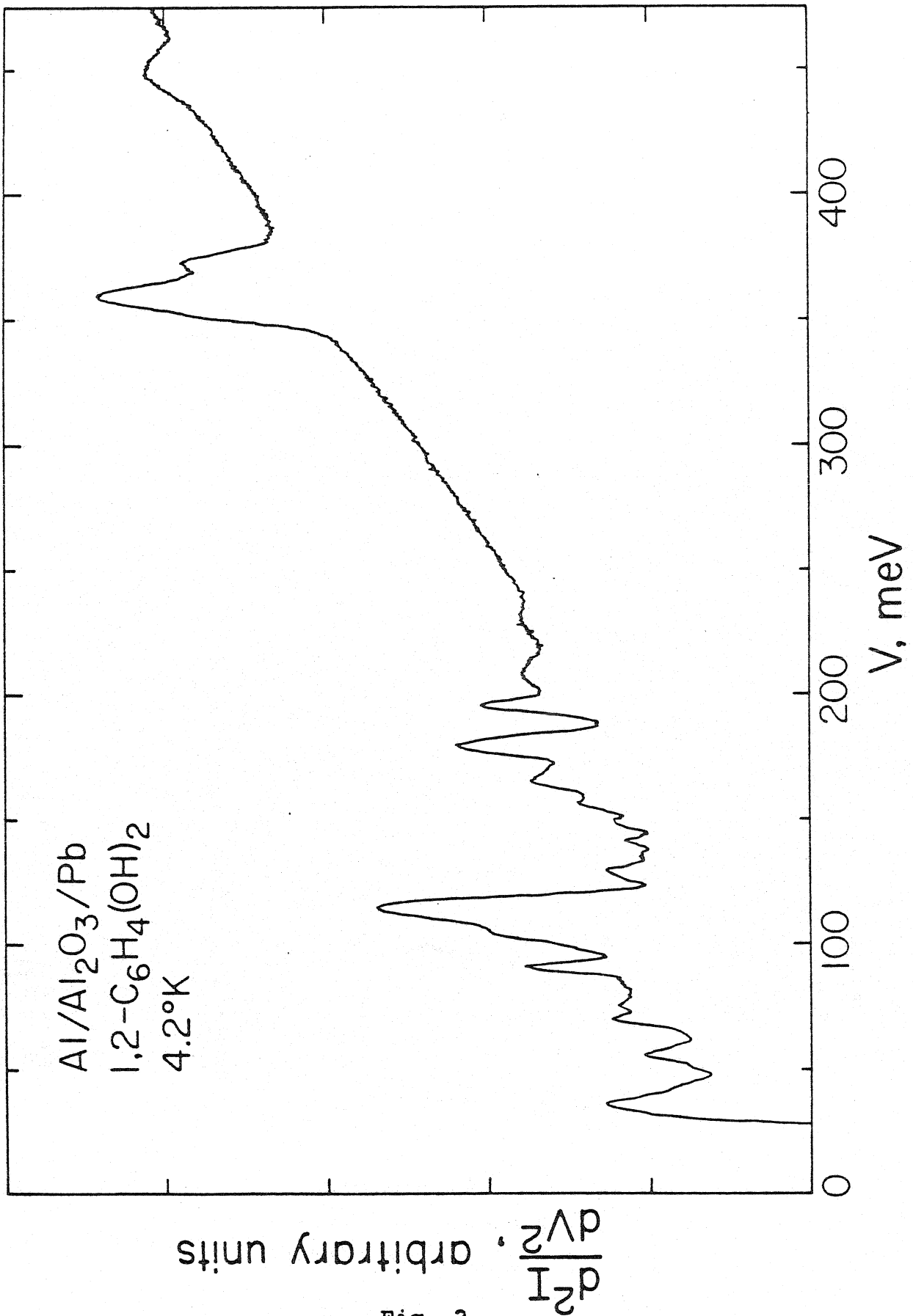
Al/Al2O3/Pb
1,2-C6H4(OH)2
4.2°K
0
100
200
300
400
V, meV
d2I/dV2, arbitrary units

Fig. 2

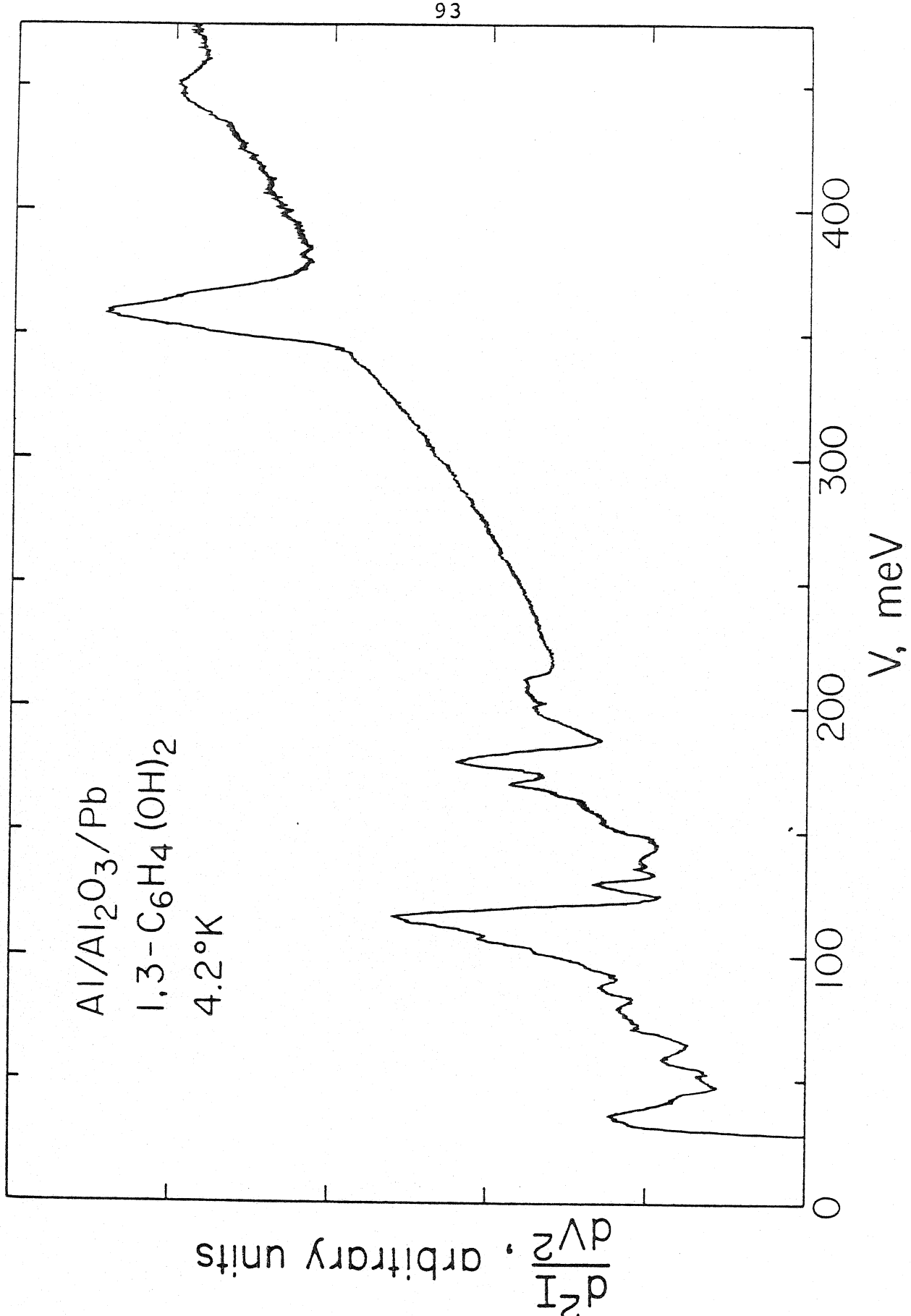
Al/Al2O3/Pb
1,3-C6H4(OH)2
4.2°K
d²I/dV², arbitrary units
V, meV
0
100
200
300
400

Fig. 3

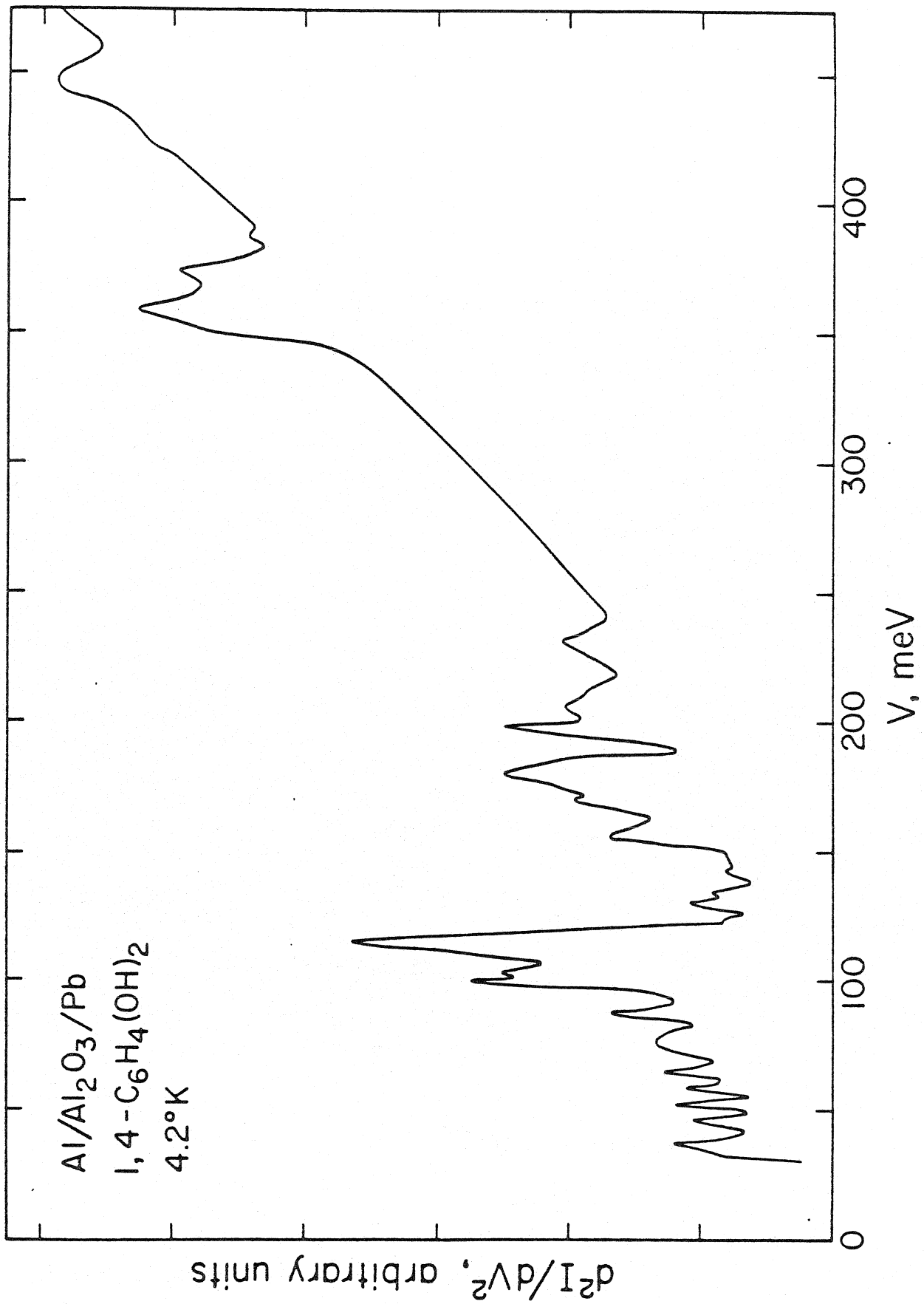
Al/Al2O3/Pb
1,4-C6H4(OH)2
4.2°K
d2I/dV2, arbitrary units
0
100
200
300
400
V, meV

Fig. 4

Chapter VI

An Inelastic Electron Tunneling Spectroscopic Study of the Interaction of $[Rh\ Cl\ (CO)_2]_2$ with an Aluminum Oxide Surface

Abstract

The interaction of the chlorodicarbonyl rhodium dimer, $[RhCl(CO)_2]_2$, with aluminum oxide as a function of surface temperature was studied by means of inelastic electron tunneling spectroscopy. The complex was found to adsorb dissociatively via an interaction with surface hydroxyl groups, losing chlorine through HCl liberation, and bonding to the surface via Rh-O bonds. At room temperature, one monolayer, or less, of the dimer adsorbs strongly. Below room temperature, multilayers of $[RhCl(CO_2)]_2$ condense physically. Evaporation of the Pb counter electrode on this physically adsorbed complex promotes further chemisorption. Thus, the Pb plays an active role in this interaction. Higher dispersion of the rhodium was attained than when rhodium is evaporated onto the surface in its zero valent state.

1. Introduction

Although the importance of supported metal catalysts for industrial applications is unquestionable, a full understanding of how these catalysts function on a molecular level is still lacking. A rather new technique that has been applied recently to this problem is inelastic electron tunneling spectroscopy (IETS) (1 - 6). Like infrared (IR) spectroscopy, IETS provides vibrational information concerning the support-supported metal-adsorbate system. However, IETS has several advantages over IR spectroscopy: (1) The IETS sample is planar and of small surface area (approximately one mm^2), so uniformity over the surface is more probable; (2) Vibrational frequencies as low as 240 cm^{-1} can be probed without serious interference from the support, allowing low frequency vibrations such as metal-ligand stretching and bending modes to be observed; and (3) The entire sample fabrication may be carried out within a vacuum system, so the history of the surface may be controlled rather carefully.

A technique for making supported metal catalysts which has gained much attention recently is the anchoring of transition metal carbonyl complexes or organometallic complexes to solid supports (7 - 15). These supported complexes may then either be calcined to yield bare metallic catalysts (e.g., 10 - 12) or left with some fraction of the original number of their ligands attached (e.g., 14). This procedure has certain advantages over the more standard method of forming the metal catalyst by reduction of a metal salt which had been impregnated into the support material. In many cases, higher dispersion is attained (10 - 11), as well as increases in reactivity (13) and modifications in the selectivity of

the catalyst (12,14). Recently, IETS investigations in this area have been carried out in our laboratory with the study of the polymerization catalyst, $Zr(BH_4)_4$ on Al_2O_3 (6). However, no one has heretofore published a successful tunneling investigation of a transition metal carbonyl complex adsorbed onto an oxide support.

In this paper, we present an IETS investigation of the interaction of the chlorodicarbonyl rhodium dimer with alumina. This compound was selected for a number of reasons. First, supported rhodium metal has been studied extensively both by IR (16 - 20) as well as by IET spectroscopy (1 - 4), so a direct comparison with our findings could profitably be made. Second, this complex sublimes readily in vacuum without decomposing and has been observed to adsorb from solution on γ-alumina (20). Finally, it is more likely to form a very highly dispersed catalyst than larger rhodium carbonyl complexes which have three or more metal atoms bound together within the molecular complex. This is of interest since significant increases in the activity of some reactions have been related to high dispersion of the metal catalyst (13,21).

The next section of this paper will describe the experimental procedures followed in the preparation of the tunnel junctions. The third section will present the results obtained and discuss their interpretation. Our conclusions are summarized in the final section.

2. Experimental Procedures

The fabrication of the tunnel junctions was carried out in an oil diffusion pumped vacuum system with a base pressure below 5×10^{-7} torr.

Three samples, each containing three independent tunnel junctions, were made simultaneously. The sample substrates (cleaned glass microscope slides) were mounted on individual copper sample holders. To each of the three sample holders was silver soldered an independent cooling line through which liquid nitrogen could be flowed. With this arrangement, the samples could be cooled to below 170 K in vacuum. By varying the flow rate of the liquid nitrogen through these lines, each of the three samples could be cooled individually to a different temperature. These temperatures were monitored by means of iron-constantan thermocouples which were indium soldered to the sample substrates.

The rhodium chlorodicarbonyl dimer ($[RhCl(CO)_2]_2$, 95% purity) was obtained from Alpha Division of Ventron. This complex is a red crystalline solid at room temperature and sublines readily at 353 to 363 K. This complex is described as air sensitive and will decompose above 398 K (22). The structure of the dimer, as determined by Dahl et al. (23) from X-ray diffraction, is shown in Fig. 1.

For each experiment, approximately 25 mg of $[RhCl(CO)_2]_2$ was placed in a glass ampule mounted within the vacuum system. This ampule was sealed by means of a ground glass ball-and-socket joint. This arrangement was effective both in inhibiting the undesirable loss of the $[RhCl(CO)_2]_2$ via room temperature sublimation, as well as in protecting the complex from the oxygen plasma present in the vacuum system during the oxidation of the evaporated aluminum film. Moreover, this type of ampule is much more convenient to use than breakable presealed ampules which can be used only once. This ampule is mounted on an arm which in turn is attached to a high vacuum rotary and linear feedthrough. The stopper of the ampule

is mounted on a stationary support. With this arrangement, the ampule could be opened and moved into position approximately 30 cm below the samples during the exposures. Line-of-sight between the positioned ampule and the samples could be blocked with a rotatable shutter. Attached to the base of the ampule are a tungsten heating wire and an iron-constantan thermocouple, which permits heating of the ampule to the correct temperature to sublime the complex without risk of overheating and possibly decomposing the complex.

One problem which was encountered while working with this complex was that during sublimation the pressure within the vacuum system did not rise significantly, and no change in the frequency of the quartz crystal microbalance (which was held at room temperature) could be detected. Thus, no direct measure of the exposure of the sample to the complex could be determined. However, the parameters during exposure (sublimation temperature and exposure time) were held constant insuring that the exposures from experiment to experiment are comparable.

The "standard" procedure used to produce tunneling junctions of optimum quality is very similar to the procedure developed for other adsorbate systems. First, an aluminum strip, approximately two mm in width by twenty mm in length by 800 Å in thickness is evaporated onto a clean glass microscope slide. This aluminum is then exposed to an oxygen plasma discharge in 0.12 to 0.16 torr of high purity oxygen. The pressure of the oxygen is adjusted to stabilize the discharge at 20 mA and 1135 V. Oxidation times, which varied from 13 to 20 minutes depending upon the subsequent adsorbate exposure conditions, were chosen so that the resistance of the completed junction fell in the range 20 to 200 ohms.

This corresponds to an oxide layer 20 to 30 Å in thickness on the aluminum. The system was then evacuated and a flow of liquid nitrogen was initiated through the cooling lines of the sample holder. When the samples had cooled to the desired temperature, the ampule containing the $[RhCl(CO)_2]_2$ was moved into position 30 cm below the samples, and the ampule was heated. At this point, line-of-sight between the ampule and the samples was blocked by the shutter. The ampule was heated for one to two minutes to allow evaporation of high vapor pressure contaminants in the complex before the shutter was opened and the samples exposed. Exposures were all for 20 minutes with the ampule held at 353 to 368 K. At the completion of the exposure, the ampule was cooled and reclosed, and the Pb top electrode was evaporated immediately with the samples cold. The completed junctions were then allowed to warm to room temperature under vacuum before being removed and mounted on the measurement supports. This warming was necessary to prevent condensation of atmospheric water onto the samples, since liquid water oxidizes the thin Pb films thus destroying the junctions. The resistances of the junctions were measured and those with resistances between 20 and 200 Ω were stored under liquid nitrogen until the tunneling measurements could be made (as described below).

Several variations on this basic preparation procedure were attempted, the rationale for which will be explained in the next section. For some samples, surface hydroxyls on the oxide were exchanged with D_2O before cooling and exposing to the $[RhCl(CO)_2]_2$. Samples were prepared also by exposing the oxide to the complex at low temperature and then warming to room temperature, either in vacuum or in a background of CO, before the

Pb overlayer was evaporated. Other samples were exposed to the complex at low temperature followed by exposure to a hot tungsten filament (to test for radiative heating) before warming to room temperature and evaporating the Pb. Finally, samples were cooled, exposed to the $[RhCl(CO)_2]_2$ and then exposed to low coverages of Pb (50, 10 or 3 Å) before warming to room temperature and completing the Pb evaporation. The final Pb electrodes were 2500 to 3000 Å in thickness.

The IET spectra were measured with the samples immersed in liquid helium at 4.2 K. The desired acquisition of the data (d^2V/dI^2 as a function of V) was obtained by a modulation and harmonic detection scheme (24), using a modulation frequency of about 50 kHz (25). The electronics were controlled, and spectra were recorded in digital form, by a PDP-11/10 laboratory minicomputer as described elsewhere (26). The modulation voltages used in the measurement were between 1.0 and 2.0 meV rms, depending on the resolution desired and the signal-to-noise characteristics of the junctions.

3. Results and Discussion

In our inelastic electron tunneling spectroscopic study of the interaction of $[RhCl(CO)_2]_2$ with aluminum oxide, we found that the intensity of the spectral features associated with the complex depended strongly on the procedure followed in junction preparation, even for constant exposures. The peak positions did not vary, however, and they correspond well with the peak positions seen in IETS investigations of CO adsorbed on evaporated rhodium islands (1 - 3). In our study, no spectral features

were seen that could be ascribed either to Rh-Cl, to Al-Cl or to O-Cl vibrations. This leads us to conclude that the $[RhCl(CO)_2]_2$ decomposes to form $Rh_n(CO)_m$ species bound to the alumina surface.

For reference, curve (a) of Figs. 2 and 3 illustrates the IET spectrum of a sample not exposed to the $[RhCl(CO)_2]_2$. The peaks seen are characteristic of a "clean" tunnel junction. The small peak near 280 cm^{-1} is a phonon mode of the Al metal electrode. The large peak at 945 cm^{-1} and the weak feature at 1880 cm^{-1} are due, respectively, to the Al-O stretching vibration of the bulk oxide and to the first overtone of that oxide mode. The low energy shoulder on the 945 cm^{-1} peak and the peak at 3630 cm^{-1} are due to bending and stretching vibrations, respectively, of surface OH groups. Finally, the small peak at 1089 cm^{-1} and the structure around 2900 cm^{-1} are due to CH vibrations of a small amount of hydrocarbon contamination.

For those junctions prepared using the "standard" procedure, i.e., cooling the oxidized aluminum strip, exposing to the complex and evaporating the Pb while cold, the intensity of the IET spectrum depends on the temperature to which the sample was cooled during preparation, as illustrated in Fig. 2. For those samples prepared at room temperature, the tunneling spectra show only two features that can be ascribed to the $[RhCl(CO)_2]_2$ interaction with the oxide: a small but sharp peak at 427 cm^{-1} and a broad weak feature at 1968 cm^{-1}. As the fabrication temperature is decreased, the peak at low frequency splits into two peaks at 406 and 443 cm^{-1}. The 406 cm^{-1} peak is very sharp and is always the more intense of the two. Also, this lower frequency peak appears to increase in intensity with coverage more rapidly than the 443 cm^{-1} peak. A third low

frequency mode is seen at 561 cm^{-1}. At higher frequencies, the 1968 cm^{-1} peak increased in intensity and, in some cases, a very broad weak mode can be distinguished at approximately 1726 cm^{-1}.

The frequencies of these five features, listed in Table 1, agree very favorably with the five peaks reported in the IETS studies by Kroeker et al. (2) and Klein et al. (3) for carbon monoxide adsorbed on rhodium which was deposited by evaporation onto the aluminum oxide surface. Also, no features are present in the spectra which can be ascribed to a rhodium-chlorine vibration which would be expected in the range 260 to 280 cm^{-1} for bridging Cl (27) or between 285 and 358 cm^{-1} for terminal Cl (27). These results lead us to conclude that, upon adsorption on the alumina, the $[RhCl(CO)_2]_2$ partially decomposes, losing the chlorine and leaving rhodium-CO species bound to the surface. This is consistent with the results obtained by Smith et al. (20) for $[RhCl(CO)_2]_2$ adsorption on γ-alumina. There is some question, however, concerning the assignment of the five modes associated with these Rh-CO species. There are three types of RhCO bonding geometries present on dispersed rhodium, as deduced from infrared studies (19 - 21). Two of these species are classified as linearly bonded CO, one consisting of two CO molecules bound to an isolated rhodium atom, $Rh(CO)_2$, and the other having a single CO bound to one rhodium, RhCO. The third species is bridge bonded CO, i.e., a single CO bound to two rhodium atoms, Rh_2CO. Infrared studies of the carbonyl stretching region of Rh-CO systems indicate that the peaks associated with the two linear CO species occur between 2030 and 2100 cm^{-1} (19), whereas the bridged species should produce a peak between 1860 cm^{-1} (20,21) and 1925 cm^{-1} (19). In tunnel junctions, the top metal electrode has the

effect of downshifting the frequencies of these highly polarizable bonds approximately 120 cm^{-1} (2). Thus, the linearly bound CO stretching frequency appears at 1968 cm^{-1}, while the bridging CO stretching frequency occurs at 1726 cm^{-1}. The three modes of the two linearly bound CO species lie close together in energy [all three lie within 80 cm^{-1} as shown by IR studies (19 - 21)]. In IETS, the presence of the top Pb electrode will broaden these modes (2), and since the CO stretching mode depends sensitively on the environment of the metal-CO entity, any variations in binding will tend to broaden the peaks further. Thus, the contributions of the two linearly bound CO species to the CO stretching region cannot be resolved. There is some dispute as to the assignment of the low frequency structure. This region of the spectrum is not available to transmission IR studies of dispersed metal systems due to the strong absorption of the radiation by the oxide support. Thus, little work had been concerned with these modes before the advent of IETS (this region can be studied with EELS but only with lower resolution). This low frequency region includes contributions from Rh-CO stretching and bending modes as well as Rh-C and Rh-O stretching vibrations of possibly dissociated CO. The two IETS studies which have been published concerning the interaction of CO with supported Rh (2,3) disagree as to the assignment of these modes. Kroeker et al. (2) assign their 416 cm^{-1} peak to (primarily) the bending mode of $Rh(CO)_2$, the 469 cm^{-1} peak to (primarily) the bending mode of RhCO and the 605 cm^{-1} peak to either a bending or a stretching mode of Rh_2CO. On the other hand, Klein et al. (3) assign the same three peaks, respectively, to the Rh-C stretching mode of dissociated CO, the Rh-CO stretching mode or the symmetric Rh_2-CO stretching mode, and the asymmetric Rh_2-CO stretching

mode. In our work, the $[RhCl(CO)_2]_2$ molecular complex possesses the $Rh(CO)_2$ structure (as seen in Fig. 1), and since adsorption is carried out at room temperature and below, we would expect $Rh(CO)_2$ to be a major surface constituent. Also, we would not expect to observe decomposition of the CO at these low temperatures (18,28). Thus, the fact that the 406 cm^{-1} peak is by far the dominant feature in our spectra would support the assignment of this peak to the $Rh(CO)_2$ species. Also, in our spectra, the relative intensities of the 443 and 561 cm^{-1} features are not constant and, thus, are probably not associated with the same species on the surface. Therefore, we correlate our 443 cm^{-1} peak with RhCO and the 561 cm^{-1} peak with $Rh_2(CO)$. However, from our data we cannot ascertain whether they are bending or stretching in character.

Due to the selection rules for IETS, as well as the lack in certainty as to the exact vibrations which produce our observed spectra, we cannot make any statement as to the concentration of $Rh(CO)_2$ relative to RhCO and Rh_2CO on our oxide surface. However, by comparing our spectra to those seen for low coverages of evaporated Rh on alumina (1), and assuming that the cross sections for excitation of the respective vibrations are the same in the two studies, we can say qualitatively that there is a higher proportion of $Rh(CO)_2$ in our junctions. Since this species is associated with isolated Rh atoms (16,18), we conclude that the rhodium deposited on alumina at low temperature through decomposition of $[RhCl(CO)_2]_2$ is more highly dispersed than rhodium deposited by evaporation. This is supported by the very low intensity of the CO stretching mode associated with Rh_2CO, which we would expect to be prominent if a significant fraction of the metal atoms were coalesced into islands or rafts.

In addition to the features which can be ascribed directly to surface rhodium-CO species, we note that the feature associated with free hydroxyl groups on the alumina surface is perturbed strongly by the adsorption of the rhodium complex, as shown in Fig. 3. The peak at 3646 cm^{-1} is broadened significantly toward low frequency. It appears that a second OH mode at approximately 3525 cm^{-1} appears in addition to the original peak near 3630 cm^{-1}. If these surface hydroxyls are exchanged partially with deuteroxyl groups (by exposure to D_2O at room temperature before cooling and exposure to the $[RhCl(CO)_2]_2$), the same perturbation of the OD mode is seen. It is impossible to ascertain whether the actual number of hydroxyls is decreased due to the adsorption of the complex. It should be noted, however, that no new peaks were seen in the low frequency region which could be ascribed to Rh-D [seen near 1450 - 1500 cm^{-1} for complexes with Rh-D bonds (29)].

The most plausible mechanism for the adsorption of $[RhCl(CO)_2]_2$ on hydroxylated alumina which is consistent with all our measured spectra is illustrated in Fig. 4. The dimer first adsorbs weakly (or physically adsorbs) on the alumina. The temperature dependence of the spectra implies that the number of dimers which adsorb physically and subsequently chemisorb is a strong function of the temperature. The dimer dissociates, and the monomer reacts with a surface hydroxyl. The hydrogen is transferred from the oxygen to the rhodium resulting in the formation of a Rh-O bond. The hydrogen then combines with the chlorine forming HCl which desorbs immediately. This mechanism is consistent also with the bonding seen for organometallic compounds on hydroxylated oxide surfaces (7 - 9). The rhodium of this $Rh(CO)_2$ group may now interact with the oxygen of an

adjacent hydroxyl forming a coordination bond. This downshifts the OH stretching frequency of that hydroxyl strongly and results in the predominant species on the alumina surface. Some of these $Rh(CO)_2$ groups may interact further with the oxide desorbing one CO and forming another surface bond, yielding RhCO. Also, if a second Rh atom is on an adjacent site (which is not unlikely since the metal atoms arrive at the surface as a dimer), the two rhodium atoms may interact allowing a bridge bonding, Rh_2CO, species to form. For this type of chemisorption at room temperature and below, it would seem unlikely that extensive surface migration of the rhodium would occur. Thus we would not expect significant island formation, a fact which is consistent with our data.

This mechanism, however, does not yet explain all the data. New questions were raised by the spectra of junctions formed by variations on the "standard" procedure. If, in the fabrication, the oxidized aluminum is cooled and exposed to the $[RhCl(CO)_2]_2$ but then allowed to warm to room temperature before the Pb is evaporated, the resulting IET spectra show much weaker $Rh(CO)_n$ structure than would have been obtained if the Pb had been evaporated on the cold sample.

One possible explanation is that the supported rhodium is decarbonylating as the surface is warmed. Desorption of CO from supported rhodium at room temperature was seen in a recent infrared study of Rh dispersed on Al_2O_3 (18). However, this difference in adsorbed CO concentration was seen in going from a background of 50 torr of CO to vacuum; once under vacuum little additional loss was observed without heating (18). Several experiments were carried out to determine whether this process was occurring with our samples. Warming in a background of CO should inhibit the

desorption of CO, so samples were prepared by adsorbing the $[RhCl(CO)_2]_2$ on a surface at 180 K and then warming to room temperature in 10^{-4} torr of flowing CO before evacuating and evaporating the Pb. The resulting spectra were identical to those of samples warmed in vacuum. Samples were also made by exposing the alumina to the rhodium complex at room temperature, then cooling to 180 K in a background of 10^{-4} torr CO before evaporating the Pb. Others were made by cooling the alumina to 180 K, exposing it to the complex, then heating the surface resistively (30) to 395 K in 50 microns of CO or to 475 K in 25 microns of CO. The samples were then allowed to cool to 240 K in CO before evacuating and evaporating the Pb. The resulting spectra for all these fabrication procedures were very similar showing only weak features from $Rh(CO)_n$. It should be noted that in the experiments where samples were heated resistively, one set of control samples was left cold. In all cases, the unheated samples had much higher resistances (an order of magnitude or more) indicative of higher adsorbate concentrations. Also, the physical appearance of the Pb electrodes differed; the Pb on the heated samples was smooth and bright, while on the unheated controls, the Pb was dull and dark. Thus, while desorption of CO from the supported rhodium may contribute to the loss of spectral intensity, it does not appear to be the only cause.

An alternate mechanism could explain our observations, however. As the $[RhCl(CO)_2]_2$ impinges on the cold alumina, the dimers adhere to but do not dissociate on the surface immediately. Rather, a multilayer of physically adosrbed $[RhCl(CO)_2]_2$ forms with only the first monolayer adsorbing as $Rh(CO)_n$. If the surface is allowed to warm, the outer, physically adsorbed layers desorb leaving only a small statistical coverage

of rhodium. If, however, the Pb is evaporated on the cold multilayer, sufficient energy is presented to the surface region, either through radiation or heat of condensation, to initiate the schism of the dimers, allowing the adsorption and loss of the Cl through HCl formation.

As a test of the plausability of this mechanism, some rather crude calculations were carried out. From the structure of the complex as determined by X-ray diffraction (23) (cf., Fig. 1), it was determined that the dimer would occupy approximately 37 $\mathring{A}^2$ on the surface. This corresponds to a monolayer consisting of 2.7×10^{14} dimers, or 5.4×10^{14} Rh atoms per cm^2. If we assume bulk spacing for Rh at full monolayer coverage, we find that a monolayer of Rh consists of 1.6×10^{15} atoms/cm^2, and a thickness of 2.16 Å. Thus, one monolayer of $[RhCl(CO)_2]_2$ decomposed on the surface yields one-third of a monolayer of Rh metal, or a statistical thickness of 0.7 Å of Rh. Thus, we can compare our IET spectra for samples prepared by adsorbing the complex at low temperature and warming (to desorb the physically adsorbed multilayers) before evaporating the Pb, to the spectra of samples prepared by Hansma et al. (1) after evaporation of 0.5 to 1 statistical Å of Rh metal and exposing that to CO. The qualitative agreement is quite good.

We now address the question of what occurs when Pb is evaporated onto the cold surface with the multilayer present. Since there is no evidence that the $[RhCl(CO)_2]_2$ remains intact within the junction, it evidently decomposes during the Pb evaporation. As noted earlier, this complex is heat sensitive and has been found to decompose at 400 K (22), or at kT of only 34 meV. During the Pb evaporation, energy must be dissipated across the adsorbate-alumina interface. Thus, it is quite probable that

the multilayer may gain enough energy sufficiently rapidly to decompose before it has a chance to desorb. It is possible to calculate the flux of energy reaching the samples due to radiation from the Pb evaporation source. If we assume that the source is a one cm diameter sphere at 770 K with an emissivity of 0.1 [approximate for Pb at 775 K (31)], then the amount of radiant energy incident on the samples 40 cm away is approximately 20 meV/A^2-sec, or approximately 740 meV per dimer per second. Not all of this radiation will be absorbed by the adsorbate. On the timescale of molecular vibrations (10^{-13} sec), the dimer will undergo 10^{10} vibrations before even one meV of radiant energy is absorbed. Thus, even if the dimer is only weakly coupled to the surface, it should be able to transfer this energy to the alumina at an adequate rate not to heat appreciably more than the oxide itself. Even if all the incident radiant energy were trapped in the first 10 Å of the alumina film, the surface would only be heated by approximately 0.2 K/sec at 200 K. Thus, radiant heating is not causing the breakup of the dimers on the surface.

A much more likely cause of the dissociation is the energy released in the condensation of the Pb atoms. The heat of condensation of Pb (in going from a gas to a solid) is 43.64 kcal/mole (32), or, in other words, each Pb atom striking the surface must release 1.9 eV on the timescale of many molecular vibrations (perhaps 10^{-9} sec). Each dimer will encounter an average of 1.8 Pb atoms before the first monolayer of lead is evaporated. Since the adsorbate is thermally unstable, and since it is not coupled strongly to the surface, enough of this energy could reasonably be trapped in the $[RhCl(CO)_2]_2$ sufficiently long to result in the dissociation of the dimer, thus allowing the monomers to adsorb on the alumina via the mechanism described above. A similar effect has been observed by Lindau et al.

(33), where the heat of condensation of gold deposited on III-V semiconductors is postulated to initiate the decomposition of the semiconductor surface.

To test these hypotheses, two final experiments were performed. In the first, a set of junctions was prepared by adsorbing the $[RhCl(CO)_2]_2$ on alumina (below 180 K) and exposing this cold surface to a hot tungsten filament (much hotter than the Pb source) for 25 sec. The samples were then warmed to room temperature before the Pb was evaporated. The junction resistances were comparable to those of junctions fabricated by the same procedure but without exposure to the hot filament, and the resulting IET spectra showed no significant enhancement of the spectral features due to $Rh(CO)_n$. In the final experiment, several sets of junctions were prepared by the following procedure. The $[RhCl(CO)_2]_2$ was again adsorbed on alumina below 190 K. Following this, varying amounts of Pb were evaporated on the three samples while they were still cold. One was covered with approximately 50 Å of Pb, enough to cover the surface completely. The second was exposed to approximately 10 Å of Pb, on the order of three or four monolayers. The third was exposed only to approximately 3 Å of Pb, approximately one monolayer, which is not enough to bury the surface region physically but which should be enough to cause decomposition of some of the $[RhCl(CO)_2]_2$ layer. The samples were then warmed to room temperature, and the remainder of the Pb overlayer was evaporated. In all instances, the resulting junction resistances of the three samples were comparable to each other and were approximately two orders of magnitude greater than for junctions prepared without any Pb evaporation at low temperatures. This is indicative of a higher adsorbate concentration. Unfortunately,

the resulting IET spectra were too noisy to give useful spectra.

It has been assumed in the past that the Pb overlayer in IETS tunnel junctions plays no direct role in the interaction of an adsorbed species with the aluminum oxide surface [apart from downshifting the observed frequencies somewhat (34)]. This appears to be valid for stable species chemisorbed on the oxide surface. However, we have seen in this study that for weakly bound multilayers of unstable molecules, the energy released in the condensation of the Pb may be sufficient to initiate further chemical reaction. Thus, the lead may play an active role in the chemistry of the interfacial region.

4. Conclusions

We have studied by means of inelastic electron tunneling spectroscopy the interaction of the chlorodicarbonyl rhodium dimer, $[RhCl(CO)_2]_2$, with aluminum oxide films during the formation of Al-Al_2O_3-complex-Pb tunnel junctions. We believe this to be the first published IETS study of a transition metal carbonyl complex.

The postulated reaction pathway is illustrated in Fig. 4. The dimer adsorbs physically on the surface, but it must dissociate before chemisorption can occur. When the dimer dissociates, the monomers react with surface hydroxyl groups resulting in the formation of HCl gas and allowing the rhodium atom to bond to the resulting surface oxygen. The metal atom can interact further with a neighboring hydroxyl, possibly coordinating with the lone pair of electrons on the oxygen. This is the predominant surface species, consisting of an isolated rhodium atom binding two carbonyl ligands, $Rh(CO)_2$. Some of these groups may lose one of their

carbonyls, or, if two rhodium atoms are on adjacent sites, a CO may form a bridge bond between the two. These result in RhCO and Rh_2CO species, respectively. The schism of the dimer appears to be the rate limiting step. Adsorption at low temperatures results in a multilayer of physically adsorbed $[RhCl(CO)_2]_2$. If this surface is allowed to warm to room temperature, the multilayers desorb, leaving only the chemisorbed monolayer. If, however, Pb is evaporated on the cold surface, the energy released by the condensing Pb is sufficient to dissociate the dimers present in the multilayer. These monomers then lose their chlorine and bind to the surface.

Our spectra indicate that, compared with evaporated Rh, a large proportion of the Rh present on the surface is in the form of $Rh(CO)_2$ indicating almost atomic dispersion of the metal.

Acknowledgments

We wish to thank Dr. John Yates, Jr. for suggesting this study and for valuable discussions and encouragement. We would like to thank also Prof. R. H. Grubbs for very helpful discussions on probable surface reactions. We gratefully acknowledge the financial support of the National Science Foundation under Grant Number ENG78-16927.

References

1. P. K. Hansma, W. C. Kaska and R. M. Laine, J. Am. Chem. Soc. 98, 6064 (1976).
2. R. M. Kroeker, W. C. Kaska and P. K. Hansma, J. Catal. 57, 72 (1979).
3. J. Klein, A. Léger, S. DeCheveigné, C. Guinet, M. Belin and D. Defourneau, Surface Sci. 82, L288 (1979).
4. H. E. Evans, W. M. Bowser and W. H. Weinberg, Surface Sci. 85, L497 (1979).
5. H. E. Evans and W. H. Weinberg, J. Am. Chem. Soc. (in press).
6. H. E. Evans and W. H. Weinberg, J. Am Chem. Soc. (in press).
7. D. G. H. Ballard, J. Polymer Sci. 13, 2191 (1975).
8. V. A. Zakharov and Yu. I. Yermakov, Catal. Rev.-Sci. Eng. 19, 67 (1979).
9. J. M. Basset and A. K. Smith, Fundamental Research in Homogeneous Catalysis, Ed., M. Tsutsui and R. Ugo, Plenum Press, New York, 1976, p. 69.
10. A. Brenner, J. C. S. Chem. Comm. 251 (1979).
11. J. R. Anderson, P. S. Elmes, R. F. Howe and D. E. Mainwaring, J. Catal. 50, 508 (1977).
12. M. Ichikawa, Bull. Chem. Soc. Japan 51, 2268 (1978).
    M. Ichikawa, Bull. Chem. Soc. Japan 51, 2273 (1978).
13. G. Carturan and G. Strukul, J. Catal. 57, 516 (1979).
14. H. Knözinger, E. W. Thornton and M. Wolf, J. C. S. Faraday I 75, 1888 (1979).
15. V. L. Kuznetsov, B. N. Kuznetsov and Yu. I. Ermakov, Kinet. Catal. 19, 272 (1978).

16. A. C. Yang and C. W. Garland, J. Phys. Chem. 61, 1504 (1957).

17. H . Arai and H. Tominga, J. Catal. 43, 131 (1976).

18. J. T. Yates, Jr., T. M. Duncan, S. D. Worley and R. W. Vaughan, J. Chem. Phys. 70, 1219 (1979).

19. D. J. C. Yates, L. L. Murrell and E. B. Prestridge, J. Catal. 57, 41 (1979).

20. G. C. Smith, T. P. Chojnacki, S. R. Dasgupta, K. Iwatate and K. L. Watters, Inorg. Chem. 14, 1419 (1975).

21. J. F. Hamilton and R. C. Baetzold, Science 205, 1213 (1979).

22. C. W. Garland and J. R. Wilt, J. Chem. Phys. 50, 1044 (1962).

23. L. F. Dahl, C. Martell and D. L. Wampler, J. Am. Chem. Soc. 83, 1761 (1961).

24. W. H. Weinberg, Ann. Rev. Phys. Chem. 29, 115 (1978).

25. B. F. Lewis, M. Mosesman and W. H. Weinberg, Surface Sci. 41, 142 (1974).

26. W. M. Bowser, PhD Thesis, California Institute of Technology, Pasadena, CA (1980).

27. D. M. Adams, Metal-Ligand and Related Vibrations, Edward Arnold Ltd, London, 1967, pp. 65-71.

28. J. T. Yates, Jr., E. D. Williams and W. H. Weinberg, Surface Sci. (in press).

29. Adams, op. cit. (ref. 27), p.176.

30. W. M. Bowser and W. H. Weinberg, Rev. Sci. Instrum. 47, 583 (1976).

31. R. C. Weast, Ed., Handbook of Chemistry and Physics, CRC Press, Cleveland (1973), p. E-225.

32. Ibid., p. D-57.

33. I. Lindau, P. W. Chye, C. M. Garner, P. Pianetta, C. Y. Su and W. E. Spicer, J. Vacuum Sci. Technol. 15, 1332 (1978).

34. J. R. Kirtley and P. K. Hansma, Phys. Rev. B 12, 531 (1975).

J. R. Kirtley and P. K. Hansma, Phys. Rev. B 13, 2910 (1976).

Table 1

Vibrational modes resulting from $[RhCl(CO)_2]_2$ adsorption on alumina.

Frequency, cm^{-1}*	Surface Specie	(Type of Mode)
406	$Rh(CO)_2$	(M-C-O bending)
443	RhCO	(M-C-O bending)
561	Rh_2CO	(M-C-O bending or M-CO stretching)
1726	Rh_2CO	(CO stretching)
1968	$Rh(CO)_2$ + RhCO	(CO stretching)
2621	Coordinated OD	(OD stretching)
2710	Free OD	(OD stretching)
3525	Coordinated OH	(OH stretching)
3629	Free OH	(OH stretching)

*After subtracting 8.15 cm^{-1} to correct for the effect of the Pb superconducting gap (34).

Figure Captions

Fig. 1: The structure of the $[RhCl(CO)_2]_2$ dimer as determined from X-ray crystallography (23).

Fig. 2: IET spectra of alumina cooled to various temperatures and exposed to $[RhCl(CO)_2]_2$ from the gas phase. A clean surface spectrum is shown in (a), the other spectra represent the surface exposed to the complex at (b) room temperature (295 K), (c) 240 K, (d) 210 K, (e) 190 K, and (f) 180 K. The lead was evaporated on the cold surface.

Fig. 3: IET spectra showing the OH and OD vibrational region. The spectra are for (a) a clean sample, (b) alumina exposed to $[RhCl(CO)_2]_2$ at 210 K [corresponds to spectrum (d) of Fig. 2], (c) clean surface partially deuterated, and (d) deuterated surface exposed to $[RhCl(CO)_2]_2$ at 200 K.

Fig. 4: Postulated adsorption mechanism for $[RhCl(CO)_2]_2$ on a hydroxylated alumina surface.

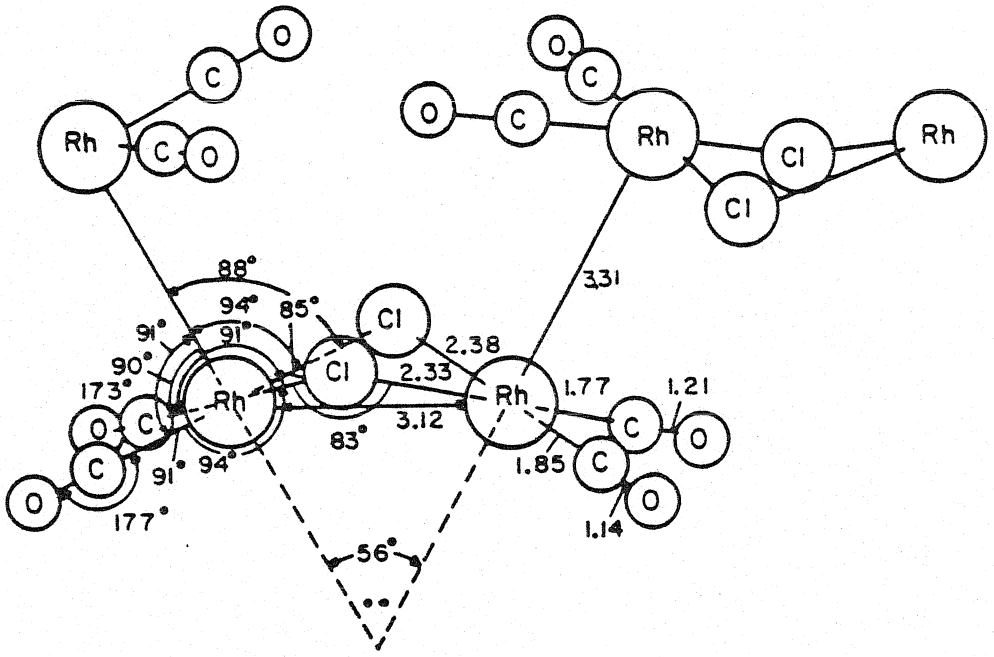
O
C
Rh
C
O
O
C
O
C
Rh
Cl
Rh
Cl
88°
94°
85°
91°
91°
90°
173°
Cl
2.38
2.33
3.31
Rh
1.77
1.21
O
C
3.12
83°
C
O
C
91°
94°
1.85
O
177°
1.14
56°

Fig. 1

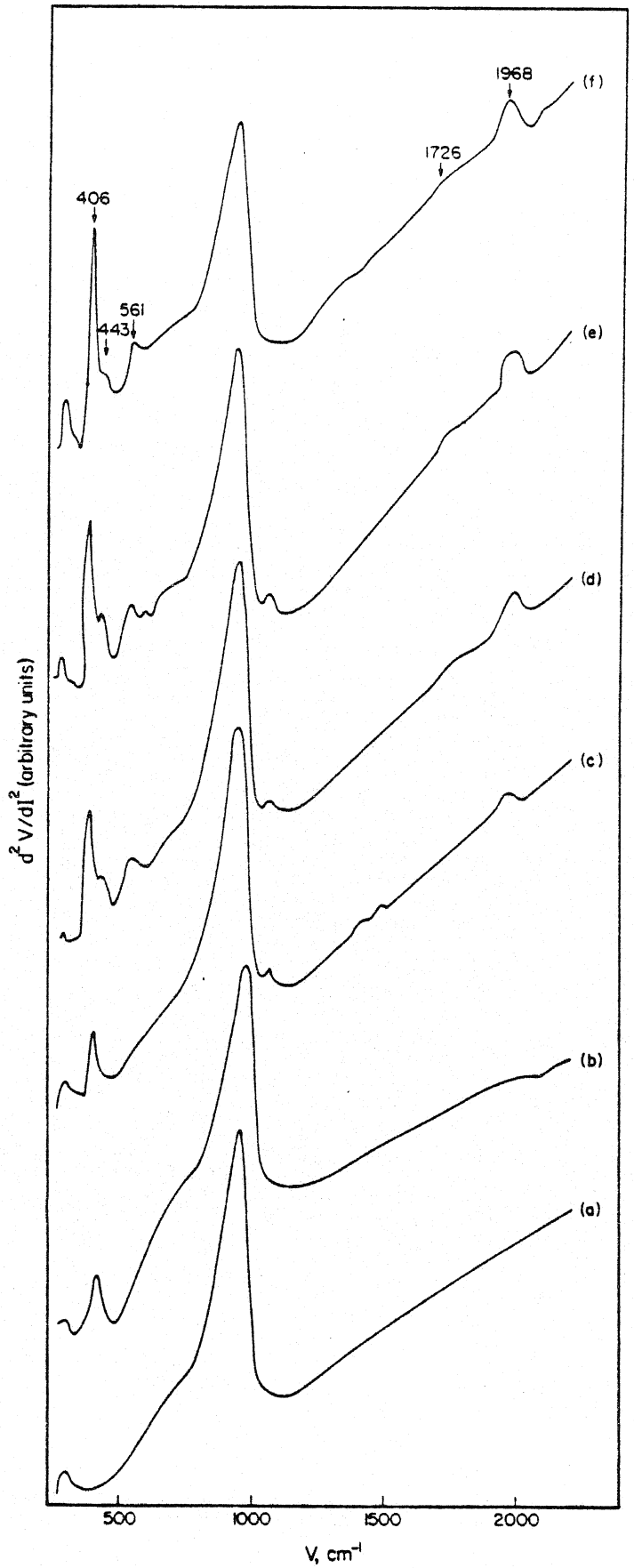
1968
(f)
1726
406
561
443
(e)
(d)
(c)
(b)
(a)
d^2V/dI^2 (arbitrary units)
500
1000
1500
2000
V, cm^{-1}

Fig. 2

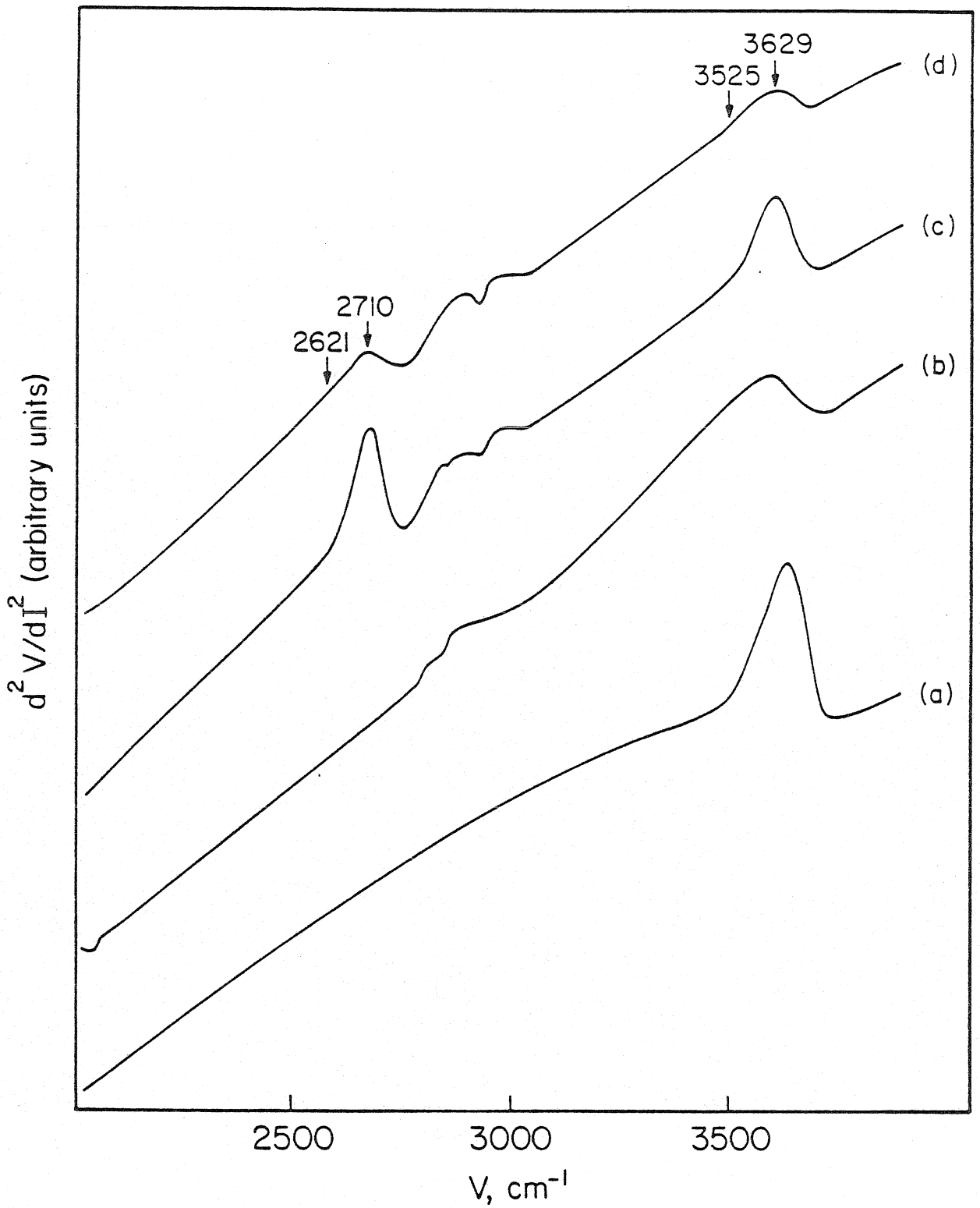
3629
3525
(d)
(c)
2710
2621
(b)
(a)
d^2V/dI^2 (arbitrary units)
2500
3000
3500
V, cm^{-1}

Fig. 3

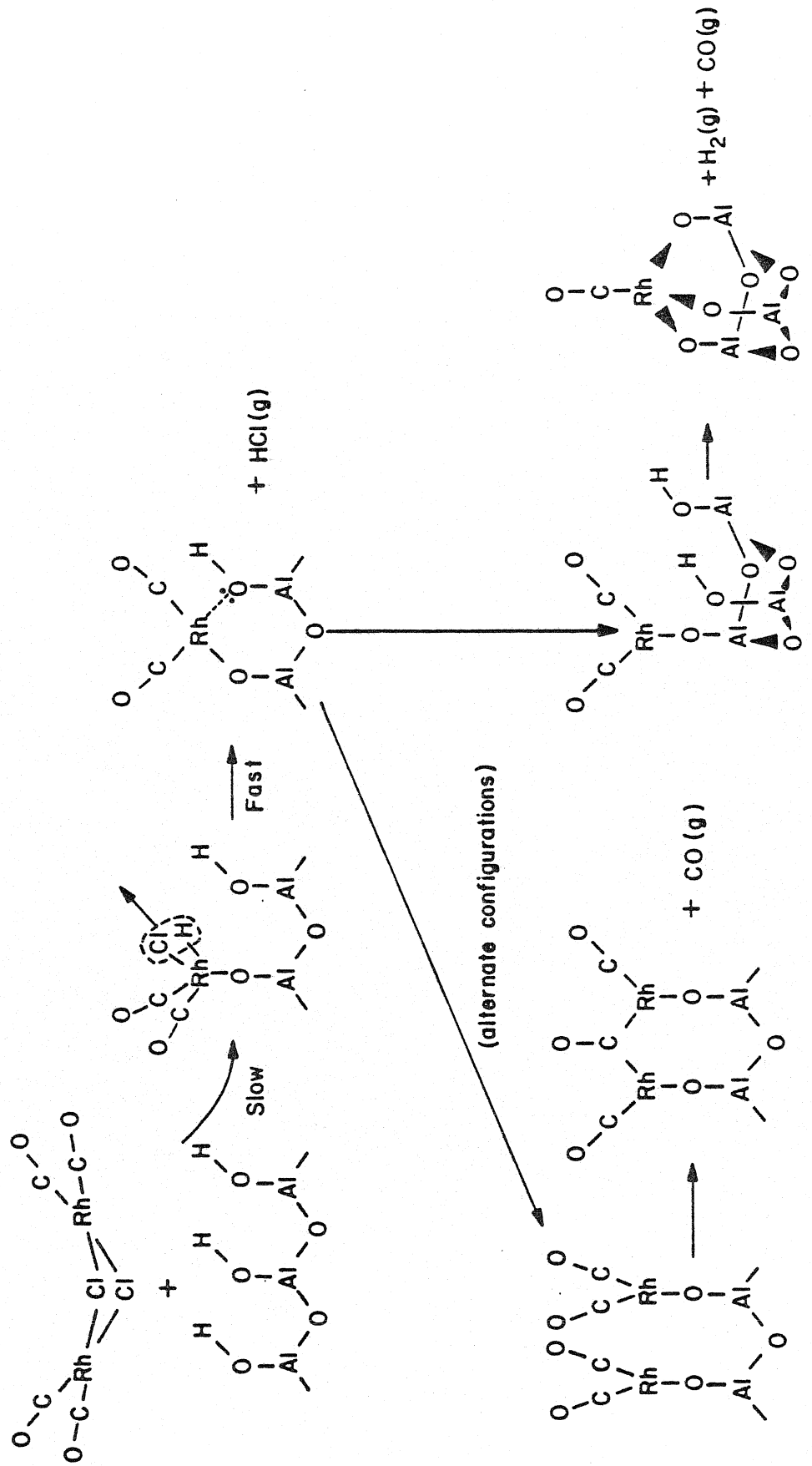

Fig. 4

Chapter VII

An Inelastic Electron Tunneling Spectroscopic Study of $Ru_3(CO)_{12}$ Adsorbed on an Aluminum Oxide Surface

"An Inelastic Electron Tunneling Spectroscopic Study of $Ru_3(CO)_{12}$ Adsorbed on an Aluminum Oxide Surface"

by

W. M. Bowser and W. H. Weinberg*
Division of Chemistry and Chemical Engineering
California Institute of Technology
Pasadena, California 91125

February 1980

To be Submitted to *The Journal of the American Chemical Society*

Abstract

The adsorption of $Ru_3(CO)_{12}$ on aluminum oxide has been studied by means of inelastic electron tunneling spectroscopy. The complex was found to retain its molecular structure when adsorbed on a hydroxylated alumina surface at low temperature. Upon heating to 470 K in 0.1 torr of O_2, the $Ru_3(CO)_{12}$ is lost from the surface through desorption and possible oxidation of the complex.

1. Introduction

In the area of chemisorption and heterogeneous catalysis, one of the more technologically important fields of study is research aimed at understanding the properties of supported metal catalysts on a molecular level. A rather new technique, ideally suited for the investigation of such systems, is inelastic electron tunneling spectroscopy (IETS) (1 - 3). IETS provides vibrational information concerning the support-supported metal-adsorbate system. In this sense, IETS is analogous to IR spectroscopy. Tunneling spectroscopy, however, has several advantages over IR spectroscopy; for example: (1) IETS is sensitive to both infrared (dipolar) as well as Raman (induced dipolar) active excitations; (2) The IETS sample is a planar surface with an area on the order of one mm^2, making uniformity over the sample more probable; (3) Vibrational modes as low as 240 cm^{-1} are visible, allowing metal-ligand stretching and bending modes to be seen; and (4) Since the sample preparation is carried out entirely in a well-controlled environment (a high vacuum system), the history of the sample is known.

Recently, IETS has been shown to be useful in several studies of supported metals which have been evaporated onto an alumina surface (4 - 7). The standard commercial approach to making supported metal catalysts is to reduce metallic salts which have been impregnated into high surface area oxides. The synthesis of tunnel junctions in this manner, however, has not been reported. A third approach in forming supported metal catalysts, which is receiving much attention, is the attachment of homogeneous catalysts onto solid supports (8 - 19). The supported complex may be

calcined to bare metal (11,12) or left with some fraction of its original ligands attached (13,14). This technique provides several advantages over the use of calcined metallic salts; for example: (1) Higher dispersion (11,12); (2) An increase in activity (15); and (3) A modification in the selectivity for some reactions (16,17). Investigations in this area utilizing IETS were begun in our laboratory when studies of the polymerization catalyst, $Zr(BH_4)_4$ supported on Al_2O_3, were carried out successfully (18). Also, the interaction of $[RhCl(CO)_2]_2$ with the hydroxylated alumina surface has been studied using IETS (19).

In this paper, we extend our investigations in this area by considering $Ru_3(CO)_{12}$ adsorbed on Al_2O_3. This complex was selected for a number of reasons. First, the vibrational spectra of several small molecules adsorbed on the (001) surface of single crystalline Ru have been measured in our laboratory using high resolution electron energy loss spectroscopy (EELS) (20), and a comparison with the vibrations associated with the supported metal and supported complex is of interest. Second, since $Ru_3(CO)_{12}$ is thermally quite stable, the prospects of subliming the molecular complex successfully were good. Third, since the molecule is stable, the possibility of adsorbing the complex on the alumina surface without decomposition was good. This would allow us subsequently to study its decomposition on the surface more easily than if decomposition occurred already at low temperatures. Finally, $Ru_3(CO)_{12}$ has been attached successfully to commercial (high surface area) oxide supports (12,13,16).

This work examines the adsorption of $Ru_3(CO)_{12}$ onto hydroxylated Al_2O_3 and the interaction of the supported complex with oxygen at elevated temperature. The next section of the paper will discuss the experimental

details of the work. Section three will present the results and discuss their interpretation, and the final section will delineate the important conclusions.

2. Experimental Procedures

The sample preparation procedures used in the adsorption of the $Ru_3(CO)_{12}$ complex were very similar to those used in the study of $[RhCl(CO)_2]_2$ and are described in detail elsewhere (19).

The $Ru_3(CO)_{12}$ was obtained from Strem Chemicals. This complex is an orange crystalline solid described as air stable but does decompose at 423 K. The structure of the complex, as determined by Churchill et al. (21), is illustrated in Fig. 1. The complex consists of an equilateral triangle of Ru atoms, each metal atom being bound directly to the other two metal atoms. Attached to each Ru atom are four terminal CO groups, two of which are axial, aligned perpendicular to the Ru triangle, and the other two are radial, lying in the plane of the Ru triangle.

The $Ru_3(CO)_{12}$ was introduced into the vacuum system via a sealed glass ampule with a ground glass ball-and-socket joint, as described elsewhere (19). In order to effect the exposure of the complex to the alumina surface, the ampule was moved into position approximately 30 cm below the samples, and the ampule was heated to approximately 408 K to sublime the complex.

As with the $[RhCl(CO)_2]_2$, there was no direct method of determining the number of molecules of the complex which actually impinged on the sample surface during exposure. Hence, the parameters associated with the exposure were kept constant from run to run to assure consistency

between samples.

It was found that $Ru_3(CO)_{12}$ adsorbs well on a fully hydroxylated alumina surface. Hence, the tunnel junction fabrication procedure was modified slightly from the procedure followed for $[RhCl(CO)_2]_2$. First, an Al film approximately 2 mm in width by 20 mm in length by 800 Å in thickness was evaporated onto a cleaned glass substrate. This Al strip was then oxidized in a plasma discharge initiated in 0.12 to 0.16 torr of high purity oxygen. The discharge current was kept at 20 mA at 1135 volts for 6 to 8 minutes. The oxygen was then evacuated from the system and 0.3 to 0.6 torr of H_2O vapor admitted, exposing the samples to this vapor for approximately 8 to 10 minutes. This was done to ensure that the surface was fully hydroxylated. Deuterium oxide was substituted for water when a partially deuteroxylated surface was desired. The system was then evacuated to below 1×10^{-5} torr. At this point, a flow of liquid nitrogen was initiated through the sample holder cooling lines (19), and the samples were allowed to reach the desired temperature of exposure as measured by an iron-constantan thermocouple (In soldered to the sample substrate). This temperature was generally in the range 175 to 195 K. The ampule was then moved into position 30 cm below the samples, and the ampule (and complex) was heated to approximately 408 K. After 1 to 2 minutes of heating, the shutter blocking line-of-sight between the ampule and the samples was removed, and the samples were exposed to the complex for 20 minutes. The ampule heating was then terminated and the ampule re-sealed.

The preparation procedure followed subsequent to this point was varied. For some samples, the top Pb electrode was evaporated onto the cold samples

immediately after the exposure to the $Ru_3(CO)_{12}$.

For the second type of sample, at the conclusion of the $Ru_3(CO)_{12}$ exposure, 0.1 torr of high purity oxygen was introduced into the system. The samples were then heated resistively [by a technique described elsewhere (22)] to approximately 473 K for 250 seconds. The samples were then allowed to cool in oxygen. The vacuum system was then evacuated and the Pb evaporated.

In the final variation, the sample was heated in oxygen, as described above. However, after evacuation, 0.1 torr of CO was introduced, and the samples were reheated to approximately 473 K for an additional 250 seconds. The samples were allowed to cool in CO. The system was evacuated once more, and the Pb electrode was deposited.

The flow of liquid nitrogen to the sample holders was terminated during the $Ru_3(CO)_{12}$ exposure stage of the preparation to prevent the freezing of the O-ring sealing the LN_2 feedthrough. Thus, the temperatures reached by the samples after heating in O_2 and in CO were generally on the order of 250 K and 275 K, respectively.

After evaporating the Pb, the samples were allowed to warm to room temperature under vacuum. This warming was necessary to prevent the condensation of water from the air onto the samples. Condensed water quickly oxidizes the thin (3500 Å) lead films, destroying the junctions. The samples were then removed from the system and their resistances measured. Those junctions with resistances between 20 and 200 ohms were stored under liquid nitrogen to avoid the occurrence of slow structural changes and to ensure junction stability until the IETS measurements could be made.

The IET spectra were measured with the samples immersed in liquid He

at 4.2 K. The desired derivative (d^2V/dI^2 as a function of V) was obtained by a modulation and harmonic detection scheme (1), using a modulation frequency of 50 kHz (23). The electronics were controlled, and the spectra were recorded in digital form, by a PDP 11/10 laboratory minicomputer (24). The modulation amplitudes used in the measurement were between 1.0 and 2.0 meV rms (as measured at a bias voltage of 250 meV), depending on the resolution desired and the signal-to-noise characteristics of the junction.

Since data were collected in digital form, differences between spectra could be made more obvious by digital subtraction of the individual spectra. This proved to be of some aid in the analysis.

3. Results and Discussion

An unfortunate property of the tunnel junctions prepared with $Ru_3(CO)_{12}$ as an adsorbate was that the features present in the resulting spectra were quite weak. This may be either a consequence of a low coverage of the complex or a consequence of weak coupling between the tunneling electrons and the vibrational modes of the complex, or a combination of both effects. In a study of the adsorption of $Ru_3(CO)_{12}$ from solution on high surface area γ-alumina and silica, it was found that the extent of adsorption of the Ru complex was quite low (12). There is some indirect evidence, however, that the coverage on the oxide of the tunnel junction was not extremely low. In order for those junctions exposed to the complex to have a resistance below 200 Ω, the Al strip had to be oxidized for on the order of 400 seconds. As a comparison, junctions with no adsorbate present require an oxidation time of 800 to 1000 seconds to yield

acceptable resistances (over 20 Ω). Also, those samples exposed to $[RhCl(CO)_2]_2$ showing intense spectral features still required 700 seconds to oxidize the Al sufficiently (19).

It has been shown recently that adsorbates may present an additional effective barrier of significant height and width to the tunneling electrons (25). It may be that the Ru surface species present a barrier of unusual height or width, resulting simply from the physical size of the complex. Assuming it adsorbs molecularly (as will be discussed later), the $Ru_3(CO)_{12}$, from the outside of the van der Waals radii of the oxygen on opposing axial CO groups, is over 9 Å in width (21) which is quite significant compared to the width of the oxide (15 to 20 Å). The electrons would then show a large preference for tunneling through those regions where no adsorbate is present. This would increase the average distance between the tunneling electrons and adsorbed molecules, reducing the coupling between the electrons and the complex, resulting in a weak spectral intensity. This explanation has been proposed also to explain the nonlinear peak intensity as a function of coverage seen with tritiated benzoic acid (26). Thus, the weak signals observed are evidently due to a combination of less than monolayer coverage and weak coupling of the tunneling electrons to the vibrational modes.

In order to enhance the visibility of those features due to adsorbed $Ru_3(CO)_{12}$, a digital background subtraction technique was employed in some cases, as illustrated in Fig. 2. Figure 2(a) shows the spectrum in the range 240 to 2250 cm^{-1} obtained by averaging the IET spectra from four separate junctions, each exposed to the $Ru_3(CO)_{12}$. Fig. 2(b) shows the spectrum of a clean junction in the same frequency range. The intensities

of the aluminum oxide vibrational modes at 940 cm^{-1} in the two spectra are matched visually, and the clean spectrum is then subtracted from the spectrum with the adsorbate present. The result is shown in Fig. 2(c), expanded vertically by a factor of three. The region between approximately 800 and 1150 cm^{-1} has been omitted for clarity. Sharp spurious features appear in this region due to a slight mismatch in the shape of the sharp aluminum oxide modes.

The strongest, most reproducible spectra were obtained by heavily hydroxylating (or deuteroxylating) the aluminum oxide surface before cooling and exposing the sample to $Ru_3(CO)_{12}$. This is consistent with the results of Anderson et al. (12) which showed that $Ru_3(CO)_{12}$ did not adsorb on silica or γ-alumina if the oxides were dried at high temperature (630 K) in vacuum.

Several features can be identified clearly in the IET spectra obtained from junctions prepared by adsorbing $Ru_3(CO)_{12}$ on cooled, hydroxylated aluminum oxide, followed by Pb evaporation on the cold sample. Figs. 2(a) and (c) show the normal and difference spectra, respectively, obtained from such junctions. At low-frequency, there is a weak feature at 389 cm^{-1}, next a prominent doublet at 456 and 488 cm^{-1}, followed by two peaks at 547 and 614 cm^{-1}. At the high-frequency end of the spectrum, two features are seen: a broad peak centered at approximately 1919 cm^{-1} and a somewhat sharper peak at 2136 cm^{-1}. The three remaining features, a sharp peak at 1052 cm^{-1} and two broad peaks at 1395 and 1580 cm^{-1}, are due to hydrocarbon contaminants present in the junction. For junctions prepared following the same procedure except that the oxide surface is partially deuteroxylated by exposure to D_2O before cooling and adsorbing the $Ru_3(CO)_{12}$,

the resulting low-frequency spectra are identical to those described above, as shown in Fig. 2(d). The features ascribed to the adsorption of $Ru_3(CO)_{12}$ are listed in Table 1.

In the spectral region between 2200 and 4000 cm^{-1} no features are seen that may be attributed to $Ru_3(CO)_{12}$ adsorption. Broad features are located at approximately 3630 and (for deuteroxylated samples) 2710 cm^{-1} which are due to surface OH and OD stretching vibrations, respectively. Peaks are also seen at approximately 2900 and 3030 cm^{-1} which are attributed to CH stretching modes of hydrocarbon contamination.

It has been reported that $Ru_3(CO)_{12}$, when adsorbed on silica (12,13) and γ-alumina (12) at room temperature, retains its molecular structure. Thus, it would be reasonable to expect that $Ru_3(CO)_{12}$ would also adsorb molecularly on the cooled alumina surface of a tunnel junction. This hypothesis is supported by the close agreement between the observed IET spectral features and observed infrared and Raman features found in solid $Ru_3(CO)_{12}$ (27). These IR and Raman peak locations are listed in Table 1. Also listed in Table 1 are the CO stretching frequencies seen in an IR study of $Ru_3(CO)_{12}$ molecularly adsorbed on silica. Mode assignments for the IR and Raman Bands are also listed.

In the CO stretching frequency region, for the optical spectra we see a strong Raman active mode located at 2127 cm^{-1} and, at lower frequency, a number of closely spaced peaks centered at approximately 2020 cm^{-1}. Although this correlates rather well with the IET spectra, there is one significant question. In IETS, the top Pb electrode has the effect of downshifting the frequencies of vibrational modes and broadening the peaks

(28). This effect is generally significant for chemisorbed CO (4 - 6). Why, then, is the 2136 cm^{-1} IETS peak, in fact, shifted up in frequency over the corresponding 2127 cm^{-1} Raman mode? This can be explained easily. The small upshift in frequency (9 cm^{-1}) is due simply to a change in the electronic environment of the complex upon adsorption on the alumina surface. Upshifts of similar magnitude are also seen for two of the three IR bands for $Ru_3(CO)_{12}$ adsorbed on silica (13), as noted in Table 1.

If we assume that the $Ru_3(CO)_{12}$ is bound to the oxide surface with the plane of the Ru_3 triangle parallel to the surface, then those axial CO ligands located on the complex adjacent to the oxide will be significantly farther from the Pb interface, approximately 5 Å, than the other CO groups. This will greatly decrease the influence of the Pb on the vibrations associated with these bonds. To estimate the frequency shifts expected, the theory outlined by Kirtley and Hansma (28) may be used. They have shown that the frequency shift is given by

$$\Delta\omega = \frac{-q_1^2}{32\pi\varepsilon_o m\omega_o n_1^2 d^3}\left\{1 + \frac{3}{2}\left(\frac{m\omega_o^2}{2E_D}\right)^{\frac{1}{2}}\frac{q_o d}{q_1}\left[1 - \left(1 + \frac{a}{2d}\right)^{-2}\right]\right\} \qquad (1)$$

where q_o and q_1 are the dipole moment and dipole derivative, respectively, of the bond; ω_o is the unshifted frequency of vibration; m is the reduced mass; d is the distance separating the bond and the Pb image plane; E_D is the dissociation energy of the bond; n_1 is the dielectric constant of the oxide; and ε_o is the permittivity constant. The second term in braces will be much less than one for CO (5), and so will be neglected.

The lower frequency CO stretching mode is seen to be shifted by approximately 100 cm^{-1}. If we assume that this shift is due to the close

proximity of the Pb to those CO groups located on the side of the complex nearest the Pb, we may use this observed shift to estimate the effect of the Pb on the other vibrations. For CO bound to Rh on alumina, Kroeker et al. estimated d to be approximately 0.8 Å (if $n_1^2 = 3$) (5). We would expect d to be the same for the CO ligands nearest the Pb for the $Ru_3(CO)_{12}$ complex. The CO ligands adjacent to the oxide will then be approximately 5.8 Å from the Pb. Assuming the bonds are otherwise the same, the frequency shift expected for the CO stretching vibrations of those axial ligands on the complex adjacent to the oxide is $100(\frac{0.8}{5.8})^3$ or approximately 0.3 cm^{-1}, and this is not observable in our spectra. Since the 2136 cm^{-1} is associated with the stretching of these axial CO groups, it is not surprising that our spectra do not show an observable downward shift in frequency.

The effect of the Pb on the low frequency metal-carbon stretching modes may also be estimated. Ibach has found from electron energy loss spectra that the dipole derivatives of the metal-carbon stretching modes of CO groups terminally bound to Ni and Pt are 0.34 and 0.38, respectively, of the dipole derivatives of the corresponding CO stretching mode (29). Thus, we will assume $q_1(MC) = 0.4\ q_1(CO)$. The d associated with the M-C stretching mode will be taken as approximately 2.9 Å. As a worst case estimate, ω_o will be taken as 389 cm^{-1}. The reduced mass of the Ru-CO mode is approximately 22 amu as compared to 6.9 amu for the CO stretching mode. Thus, the expected mode shift is

$$\Delta\omega(CO)\left(\frac{q_1(MC)}{q_1(CO)}\right)^2\left(\frac{d(CO)}{d(MC)}\right)^3\left(\frac{\omega_o(CO)}{\omega_o(MC)}\right)\left(\frac{m(CO)}{m(MC)}\right) = 100\ (0.4)^2\left(\frac{0.8}{2.9}\right)^3\left(\frac{2020}{389}\right)\left(\frac{6.9}{22}\right)$$

which is approximately 0.5 cm^{-1}. Since this was calculated for the lowest

frequency mode for a Ru-C bond closest to the Pb, the effect on any other Ru-C stretching mode is expected to be even less. If the effect on the MCO bending modes is assumed to be of the same order of magnitude, then the shifts in the frequencies of the low energy features will not be detectable in agreement with our observations.

The locations of the IETS features in the low-frequency region of the spectrum agree quite well with features reported in optical spectra (27), as seen in Table 1. Not all of the features are resolved in the tunneling spectra, due to the fact that the resolution in IETS at 4.2 K using a 1 meV modulation voltage is on the order of 15 cm^{-1}. Thus, modes separated by less than that amount will appear as a broadened feature. Exact assignment of these low frequency modes was not attempted, due to the lack of any isotopic data. However, in general, those bands between 350 and 500 cm^{-1} are ascribed to modes with predominantly metal-carbon stretching character, while those bands between 500 and 650 cm^{-1} are attributed to modes of metal-C-O bending character (27).

Our results can be compared also to the EELS results for CO adsorbed on the close-packed (001) surface of a Ru single crystal (20). In EELS, only two peaks are observed corresponding to the symmetric CO stretching vibration (the frequency of which varies with coverage from 1984 cm^{-1} to 2080 cm^{-1}), and the symmetric Ru-C stretching vibration (445 cm^{-1}) attributed to CO bound linearly on the surface. The frequencies of these modes observed at saturation coverage of CO are listed in Table 1. For specular scattering, only vibrations with a dipole derivative normal to the surface can be observed with EELS. Hence, the Ru-CO bending vibrations are not seen. The Ru-C stretching frequency fits quite well into the general

assignments made for the low-frequency modes of $Ru_3(CO)_{12}$. In the CO stretching region, due to interadsorbate interactions, the frequency of the symmetric CO stretching mode is seen to increase as the density of CO groups on the surface increases (20). At saturation on Ru(001), the CO molecules are still separated by 3.33 Å (20), whereas the axial CO ligands on $Ru_3(CO)_{12}$ are separated by only 2.88 Å. Thus, if this frequency shift with CO coverage continues, we would expect the symmetric stretching frequency for the axial CO groups on $Ru_3(CO)_{12}$ to be higher than the CO stretching frequency for a saturation coverage of carbon monoxide adsorbed on Ru, as observed. Thus, the EELS results for CO bound to the Ru(001) surface are consistent with the IETS results for $Ru_3(CO)_{12}$.

In view of these results, we conclude that when a hydroxylated alumina surface is exposed to $Ru_3(CO)_{12}$ in the vapor phase, this complex will adsorb associatively, retaining its molecular structure.

When the sample with the adsorbed $Ru_3(CO)_{12}$ is heated to approximately 470 K (by heating the Al film resistively) in the presence of 0.1 torr of oxygen (undoubtedly with some H_2O vapor in the background), and recooled prior to evaporation of the Pb, the resulting IET spectrum is altered appreciably. First, all IET spectral features associated with adsorbed molecular $Ru_3(CO)_{12}$ are no longer observed. Second, there is a significant increase in the 1840 cm^{-1} harmonic of the 940 cm^{-1} oxide peak [indicative of an increase in bulk hydroxide in the alumina (30)], as well as an apparent increase in the low frequency shoulder of the 940 cm^{-1} peak usually attributed to OH bending vibrations. This latter effect is seen also in junctions prepared in the same manner without the presence of

adsorbed $Ru_3(CO)_{12}$ and may indicate that when the oxide is heated in the presence of background H_2O vapor with an excess of O_2, additional hydroxyl groups may form on the alumina. These hydroxyls, at elevated temperatures, may then be able to diffuse into the bulk. A similar effect was seen when excess hydroxyl groups were formed by the adsorption of ethanol on alumina at elevated temperatures (31).

Also, the junction resistances of those samples with adsorbed $Ru_3(CO)_{12}$ heated in oxygen were not appreciably lower than the resistances of those junctions with $Ru_3(CO)_{12}$ present, but unheated. Samples prepared following the same heating procedure, without exposure to the complex, required twice the oxidation time to obtain acceptable resistances. This would imply that some contribution from the Ru is still present after the complex is heated in O_2. Robertson and Webb found that if $Ru_3(CO)_{12}$ adsorbed on silica is exposed to air, even at room temperature, the complex is oxidized losing all its CO ligands leaving a catalytically inactive surface species (13). This may be occurring to some extent with the IETS samples. However, no reproducible features are seen in the tunneling spectra which may be attributed to Ru-O vibrations. This would imply that the coverage of Ru oxide species, if it is present, is small, or very weakly coupled to the tunneling electrons. Desorption of the $Ru_3(CO)_{12}$ is likely to occur also, as was seen with $[RhCl(CO)_2]_2$ (19), which would account for at least some of the decrease in intensity.

Reheating this type of sample in 0.1 torr of CO to greater than 470 K did not alter the appearance of the resulting IET spectrum. This does not prove that there is no Ru on the surface. However, if there is

Ru present, it is not in a form which is easily reduced. One experiment which would clearly show the presence of Ru would be to examine the oxides, as prepared above, with X-ray photoelectron spectroscopy (XPS). This may also yield information on the oxidation state of the metal atoms. Plans are being made to conduct this study.

4. Conclusions

This paper presents the results of an IETS investigation of the adsorption of $Ru_3(CO)_{12}$ on aluminum oxide.

It was found that $Ru_3(CO)_{12}$ adsorbs, retaining its molecular structure, when exposed to a cold, hydroxylated alumina surface, as evidenced by the agreement between IET spectra and Raman and IR spectra of solid $Ru_3(CO)_{12}$. If this adsorbed $Ru_3(CO)_{12}$ is subsequently heated to 470 K in O_2, the IETS features due to the complex are no longer observed due to probable desorption and possible oxidation of the complex.

Acknowledgments

We gratefully acknowledge the financial support of the National Science Foundation under Grant No. ENG78-16927. Additional support from the Camille and Henry Dreyfus Foundation in the form of a Teacher-Scholar Award to WHW is also greatly appreciated.

References

1. W. H. Weinberg, Ann. Rev. Phys. Chem. 29, 115 (1978).
2. P. K. Hansma, Phys. Reports (Section C of Phys. Letters) 30, 145 (1977).
3. Inelastic Electron Tunneling Spectroscopy, T. Wolfram, Ed., Springer-Verlag, New York, 1978.
4. H. E. Evans, W. M. Bowser and W. H. Weinberg, Surface Sci. 85, L497 (1979).
5. R. M. Kroeker, W. C. Kaska and P. K. Hansma, J. Catal. 57, 72 (1979).
6. J. Klein, A. Léger, S. DeCheveigné, C. Guinet, M. Belin and D. Defourneau, Surface Sci. 82, L288 (1979).
7. P. K. Hansma, W. C. Kaska and R. M. Laine, J. Am. Chem. Soc. 98, 6064 (1976).
8. D. G. H. Ballard, J. Polymer Sci. 13, 2191 (1975).
9. V. A. Zakharov and Yu. I. Yermakov, Catal. Rev.-Sci. Eng. 19, 67 (1979).
10. J. M. Basset and A. K. Smith, in Fundamental Research in Homogeneous Catalysis, M. Tsutsui and R. Ugo, Eds., Plenum Press, New York, 1976, p. 69.
11. A. Brenner, J. C. S. Chem. Comm., 251 (1979).
12. J. R. Anderson, P. S. Elmes, R. F. Howe and D. E. Mainwaring, J. Catal. 50, 508 (1977).
13. J. Robertson and G. Webb, Proc. Roy. Soc. A 341, 383 (1974).
14. H. Knözinger, E. W. Thornton and M. Wolf, J. C. S. Faraday I 75, 1888 (1979).

15. G. Carturan and G. Strukul, J. Catal. 57, 516 (1979).

16. A. K. Smith, A. Theolier, J. M. Basset, R. Ugo, D. Commereuc and Y. Chauvin, J. Am. Chem. Soc. 100, 2590 (1978).

17. M. Ichikawa, Bull. Chem. Soc. Japan 51, 2268 (1978).
M. Ichikawa, Bull. Chem. Soc. Japan 51, 2273 (1978).

18. H. E. Evans and W. H. Weinberg, J. Am. Chem. Soc., Jan. 16, 1980.
H. E. Evans and W. H. Weinberg, J. Am. Chem. Soc., March, 1980.
H. E. Evans and W. H. Weinberg, J. Am. Chem. Soc., March, 1980.
H. E. Evans and W. H. Weinberg, J. Vacuum Sci. Technol., Jan./Feb., 1980.

19. W. M. Bowser and W. H. Weinberg, J. Am. Chem. Soc. (submitted).

20. G. E. Thomas and W. H. Weinberg, J. Chem. Phys. 69, 3611 (1978).
G. E. Thomas and W. H. Weinberg, Phys. Rev. Letters 41, 1181 (1978).
G. E. Thomas and W. H. Weinberg, J. Chem. Phys. 70, 954 (1979).
G. E. Thomas and W. H. Weinberg, J. Chem. Phys. 70, 1000 (1979).
G. E. Thomas and W. H. Weinberg, J. Chem. Phys. 70, 1437 (1979).
P. A. Thiel, W. H. Weinberg and J. T. Yates, Jr., J. Chem. Phys. 71, 1643 (1979).
P. A. Thiel, W. H. Weinberg and J. T. Yates, Jr., Chem. Phys. Letters 67, 403 (1979).

21. M. R. Churchill, F. J. Hollander and J. P. Hutchinson, Inorg. Chem. 16, 2655 (1977).

22. W. M. Bowser and W. H. Weinberg, Rev. Sci. Instrum. 47, 583 (1976).

23. B. F. Lewis, M. Mosesman and W. H. Weinberg, Surface Sci. 41, 142 (1974).

24. W. M. Bowser, PhD Thesis, California Institute of Technology, Pasadena, CA (1980).

25. M. F. Muldoon, R. A. Dragoret and R. V. Coleman, Phys. Rev. B 20, 416 (1979).

26. J. D. Langan and P. K. Hansma, Surface Sci. 52, 211 (1975).

27. C. O. Quicksall and T. S. Spiro, Inorg. Chem. 7, 2365 (1968).

28. J. R. Kirtley and P. K. Hansma, Phys. Rev. B 13, 2910 (1976).

29. H. Ibach, Surface Sci. 66, 56 (1977).

30. W. M. Bowser and W. H. Weinberg, Surface Sci. 64, 377 (1977).

31. H. E. Evans and W. H. Weinberg, J. Chem. Phys. 71, 1537 (1979).

Captions

Table 1. Vibrational frequencies for $Ru_3(CO)_{12}$, and corresponding mode assignments, as observed by IET, Raman and IR spectroscopies. The bands observed for CO bound to the (001) face of Ru via EELS are included on the far right for comparison.

Figure 1. $Ru_3(CO)_{12}$, viewed from a direction 75° from the normal to the Ru_3 plane (21).

Figure 2. (a) The IET spectrum, from 240 to 2220 cm^{-1}, of $Ru_3(CO)_{12}$ adsorbed on aluminum oxide at approximately 180 K.

(b) The IET spectrum of a clean sample, over the same energy range as spectrum (a).

(c) The spectrum resulting from the digital subtraction of spectrum (b) from spectrum (a), expanded vertically by a factor of three.

(d) The difference spectrum, analogous to spectrum (c), for $Ru_3(CO)_{12}$ adsorbed on a deuteroxylated alumina surface.

Table 1

IETS[a]	Raman[b]	IR[b]	IR[c]	Mode Assignments for $Ru_3(CO)_{12}$ with D_{3h} Symmetry (27)		EELS[d]
2136	2127			A_1'	Symmetric axial CO stretching vibration.	
		2062	2065	A_2''	Antisymmetric axial CO stretching vibration.	2080
		2053				
		2042				
	2034			E"	Axial CO stretching vibrations.	
1919	2028	2026	2035	E'		
	2011			A_1'	Symmetric radial CO stretching vibration.	
	2004	2002	2010	E'	Radial CO stretching vibrations	
	1994			E'		
	1989	1989		A_2'	Antisymmetric radial CO stretching vibration.	
614	607	606			Predominantly Ru-C-O deformation in character (no detailed assignment attempted).	
	596	594				
		574				
547	546	546				
	513	512				
488	489				Predominantly Ru-C stretching in character (no detailed assignment attempted).	444
456	458	466				
	446	448				
		400				
389	392	389				

[a] Inelastic electron tunneling spectrum of molecular $Ru_3(CO)_{12}$ bound to Al_2O_3 (this study).

[b] Raman and IR spectra of solid $Ru_3(CO)_{12}$ (27).

[c] IR spectrum of molecular $Ru_3(CO)_{12}$ bound to silica (13).

[d] Electron energy loss spectrum of CO bound to the (001) plane of Ru (20).

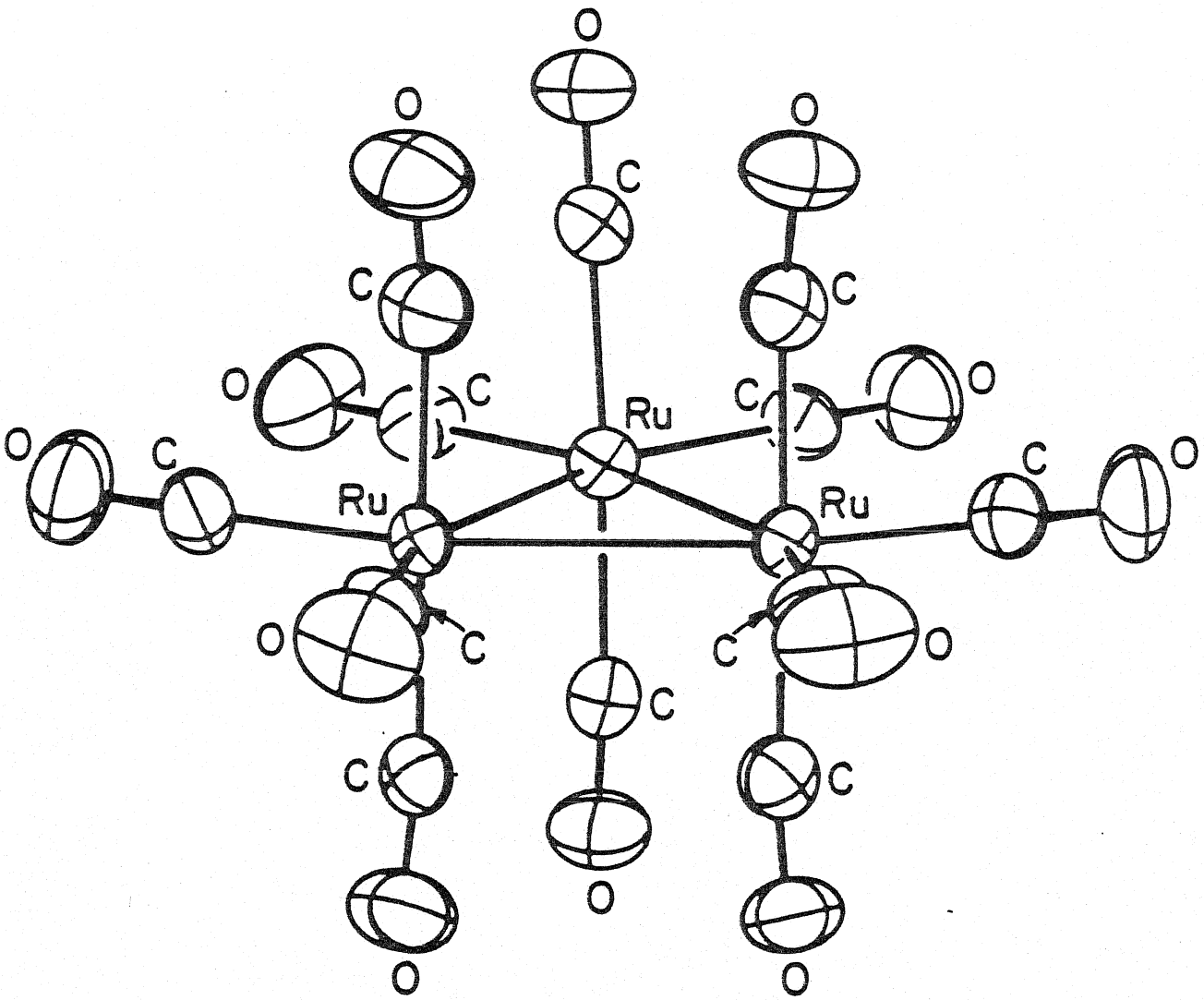

Fig. 1

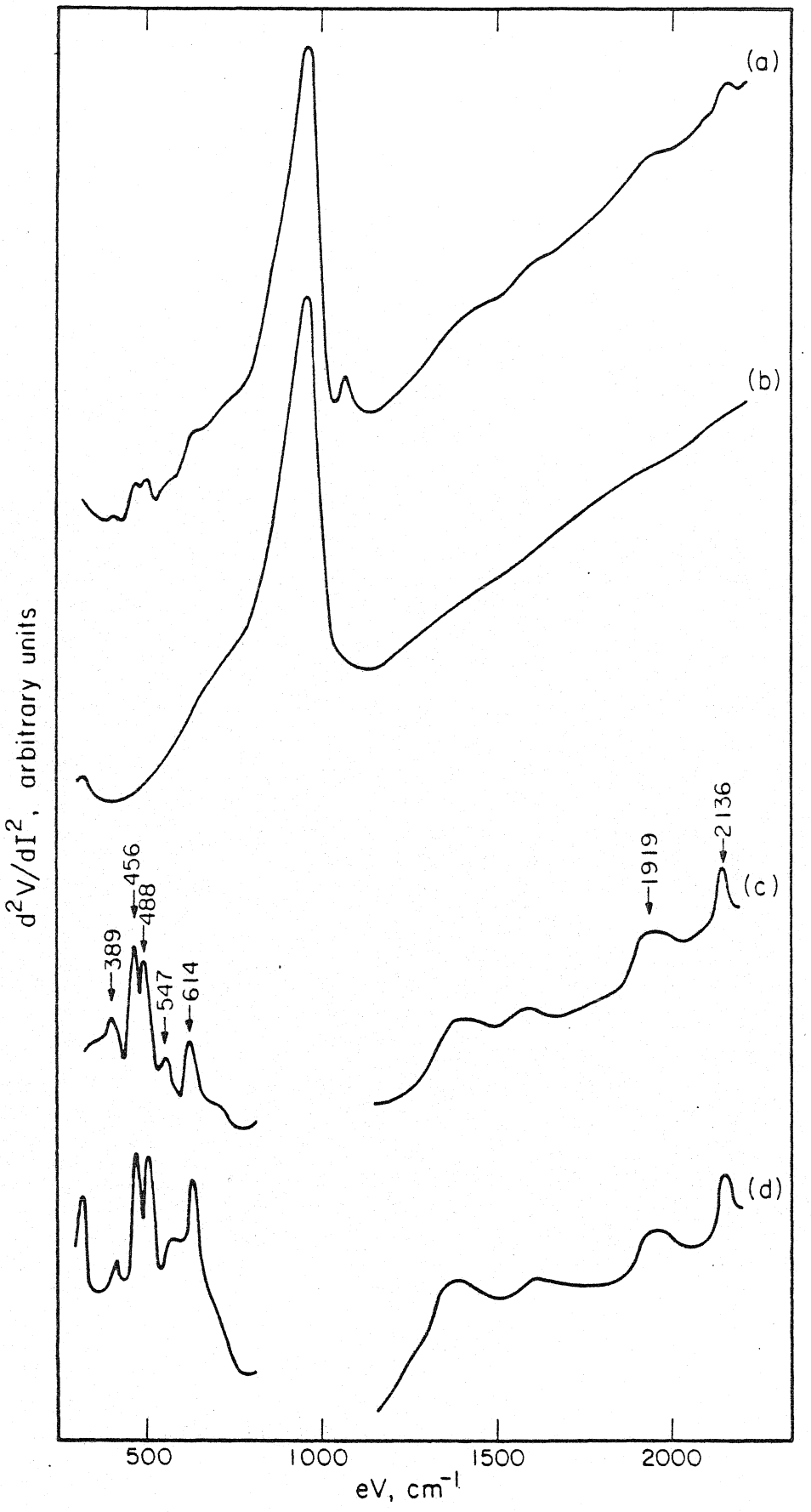
(a)
(b)
(c)
(d)
389
456
488
547
614
1919
2136
d^2V/dI^2, arbitrary units
500
1000
1500
2000
eV, cm^{-1}

Fig. 2

Chapter VIII

Conclusions

The objectives of the work presented in this thesis were aimed at the development and utilization of inelastic electron tunneling spectroscopy (IETS) as a surface sensitive vibrational probe with special emphasis on demonstrating the utility of IETS to the field of chemisorption and heterogeneous catalysis. These objectives were approached through the following steps:

(1) To provide, through an ongoing process of design and development, experimental techniques and hardware to take advantage of the potential of IETS for the study of chemisorption and catalysis.

(2) To contribute to the characterization of the oxide which serves as adsorbent in the IETS samples. This characterization is necessary for the application of IETS results to commercial catalysts.

(3) To demonstrate the utility of IETS for the investigation of chemisorption on alumina through studies of the adsorption of several similar organic compounds on the tunnel junction oxide.

(4) To contribute directly to the field of heterogeneous catalysis through the application of IETS to the investigation of metals and metal complexes bound to the aluminum oxide surface.

A method was presented which permits the rapid and efficient resistive heating of the IETS sample with simultaneous monitoring of the temperature through the temperature dependent behavior of the resistance of the Al thin film substrate. This capability is invaluable in the use of IETS for studying such surface phenomena as temperature dependent chemisorption and heterogeneously catalyzed surface reactions.

This resistive heating technique was successfully utilized in the study of the oxide barrier used in tunnel junctions. This study showed

that when Al is exposed to a water vapor (or D_2O vapor) discharge at elevated temperature (above about 430 K) or an oxygen discharge at any temperature, the insulating layer formed is an aluminum oxide with no evidence for appreciable bulk hydroxide. When Al is exposed to a water vapor discharge at lower temperatures, the insulator is still primarily an oxide but shows evidence for the incorporation of some bulk hydroxide.

The understanding of the oxide films used in IETS was increased by a second study conducted in conjunction with Howard E. Evans (included here as Appendix D). This study was an XPS investigation of the thin oxide layers formed when Al is either heated in air, dipped in liquid water or exposed to a plasma discharge initiated in oxygen or water vapor. It was seen that differentiation between these oxides could be accomplished via analysis of the XPS peak positions. In addition, peak intensities yielded information on the relative amounts of hydration and peak widths indicated relative chemical state distributions. Effects due to halogenating the oxide surface could also be seen. The XPS data were presented in a form which allows ready comparison with comparable studies on commercial aluminas.

The utility of IETS to the investigation of chemisorption on alumina was demonstrated in the two studies presented on the chemisorption on alumina of phenol (C_6H_5OH) and the three phenolic derivatives: catechol ($1,2C_6H_4(OH)_2$), resorcinol ($1,3C_6H_4(OH)_2$) and hydroquinone ($1,4C_6H_4(OH)_2$). It was found that phenol adsorbs by losing its acidic proton and bonding to a surface Al^{3+} ion as a phenoxide ion. Both catechol and resorcinol bond to the surface as the di-ion, that is, by losing the protons from both hydroxyl ligands. For hydroquinone, however, it is sterically more

favorable to bond as the mono-ion. Some di-ion formation cannot be ruled out, however. A small amount of irreversible molecular adsorption is seen for phenol, and is possible for the other species. These studies demonstrated graphically the sensitivity of IETS as well as the high resolution of the technique, easily distinguishing between very similar surface species. These studies demonstrated also that IETS is capable of detecting adsorbate-adsorbate interactions.

One very important area in the field of heterogeneous catalysis is that concerned with metal atoms and clusters dispersed on oxide supports. The final three studies help to demonstrate the utility of IETS in this area of research.

The adsorption of ethanol on silver particles supported on aluminum oxide was studied. This investigation was carried out in conjunction with Howard E. Evans and is included here as Appendix F. This study found that ethanol adsorbs as an ethoxide species on the alumina as well as on the silver metal. The two surface species (Al-ethoxide and Ag-ethoxide) can be distinguished in the IET spectra, thus demonstrating the ability of IETS to differentiate between identical surface species, differing only in binding site.

A method for fabricating heterogeneous catalysts which is of interest is the attaching of metal cluster carbonyl complexes to solid supports. Two studies were done to demonstrate the usefulness of IETS to this area. The interaction of $[RhCl(CO)_2]_2$ with aluminum oxide was studied. It was found that the complex adsorbs physically on the alumina at low temperatures. For chemisorption to occur, the dimer must dissociate. The monomers then interact with surface hydroxyl groups, forming and desorbing HCl, and

leaving the Rh atom bound to a surface oxygen atom. This results in the predominant surface species, a rhodium atom with two carbonyl ligands attached. Evidence for interaction between this metallic species and adjacent hydroxyl groups is seen. Under favorable conditions, this $Rh(CO)_2$ species may further react with the oxide, losing a CO and leaving a Rh with one linear CO attached, or, if a second Rh species is on an adjacent site, the two species may interact losing a CO and forming a CO bridge bond between the two metal atoms. It appears that the dissociation of the dimer is the rate limiting step. If Pb is deposited on the physisorbed complex, the heat of condensation released appears to initiate the dissociation resulting in increased chemisorption. This study demonstrated that the interaction of substituted metal carbonyls with alumina may be studied with IETS. It showed also that the Pb overlayer may, in some cases, play an active role in the surface chemistry.

In contrast to $[RhCl(CO)_2]_2$, with $Ru_3(CO)_{12}$ the close agreement between IET spectra and IR and Raman spectra of solid $Ru_3(CO)_{12}$ indicates that this complex retains its molecular structure when adsorbed on a hydroxylated alumina surface. Upon heating in oxygen, the IET spectral features are lost, probably due, in large part, to desorption of the complex. The formation of Ru-oxide surface species is possible but no direct evidence for this is seen.

Finally, some of the experimental aspects of IETS are covered in Appendices A through C. The electronics and procedures used in measuring IET spectra are described. A description of the calibration of these spectra is also presented. Then, the considerations which must be taken into account when designing a tunnel junction fabrication system are

discussed. Thus, these three appendices, when taken with Appendices A and B of Howard E. Evans' thesis (PhD Thesis, California Institute of Technology, 1980) represent a comprehensive discussion of the practical experimental aspects of inelastic electron tunneling spectroscopy.

Appendix A

Inelastic Electron Tunneling Spectroscopy Measurement Electronics

Appendix A

IETS Measurement Electronics

The Inelastic Tunneling measurement electronics consist of a precision system for measuring and recording the first and second derivatives, $\frac{dV}{dI}$ and $\frac{d^2V}{dI^2}$, of a metal-insulator-metal tunnel junction. The true IET spectrum $\left[\frac{d^2I}{dV^2}(eV)\right]$ may be directly obtained from the above data. However, as mentioned in the text, in most cases where only peak positions and qualitative peak intensities are desired, $\frac{d^2V}{dI^2}$ as a function of applied bias voltage is all that need be measured. In the event that progress is made in IETS theory, calibrated $\frac{d^2I}{dV^2}(V)$ spectra will be desirable, in which case both $\frac{d^2V}{dI^2}$ and $\frac{dV}{dI}$ must be measured.

The electronics, as illustrated in Fig. A1, may be divided into four blocks. The first is the ramp control circuit which provides the DC voltage at the junction and determines the energy scale of the measured spectrum. Second is the modulation source which provides a pure sine wave of frequency ω. This modulation is combined with the ramp voltage and then the sum is applied across the junction. Third is the sample holder which supports the sample and selects which junction is to be measured. Along with this is included the unit used to obtain calibration points for the $\frac{dV}{dI}$ data. Finally, there is the detection circuitry which detects, amplifies and records the component of the voltage across the junction which occurs at a frequency ω or 2ω depending on whether $\frac{dV}{dI}$ or $\frac{d^2V}{dI^2}$ is desired.

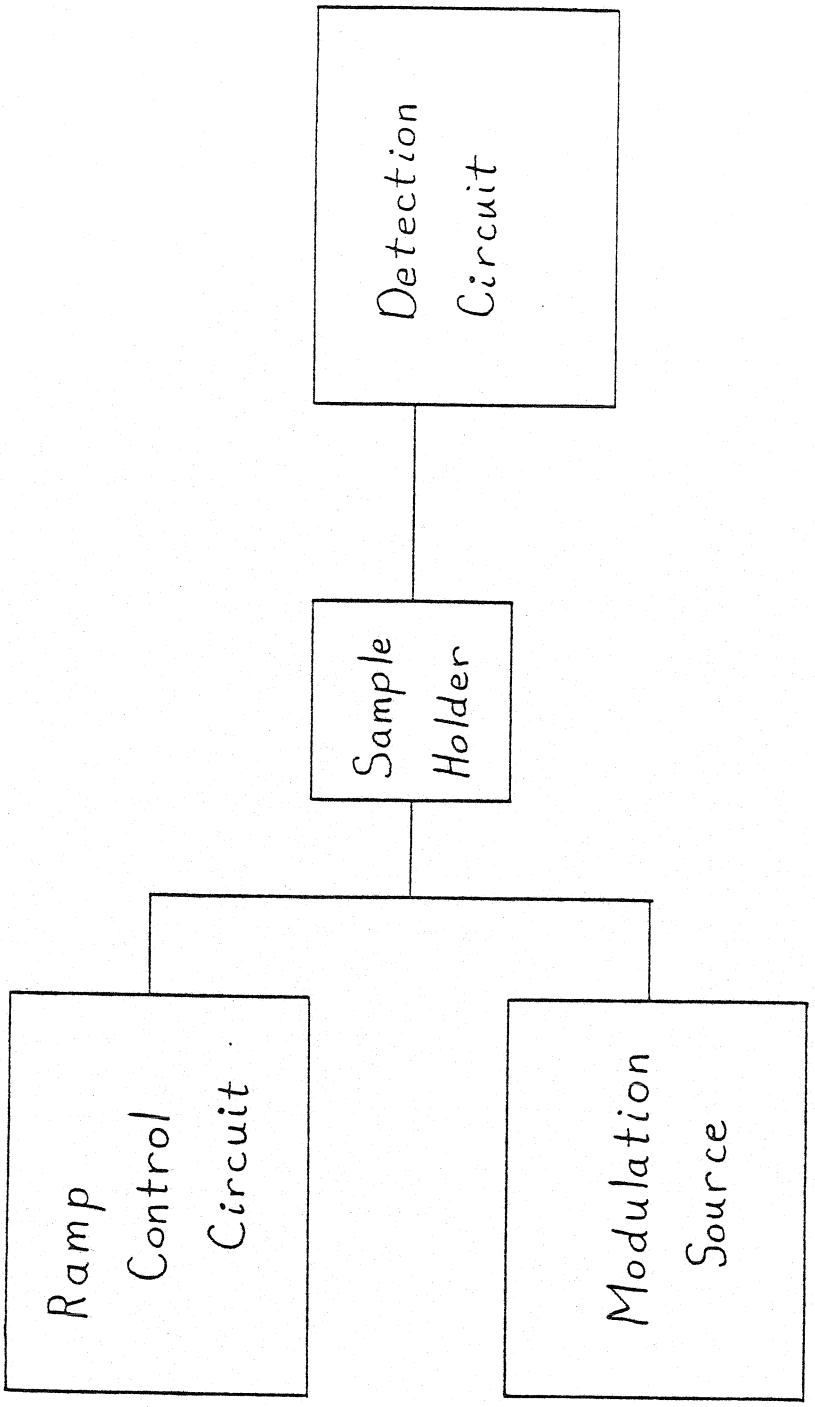
Detection Circuit
Sample Holder
Ramp Control Circuit
Modulation Source

Fig. A1

This appendix will be divided into three sections. The first will be a detailed description of each block of the system. The second section will describe how the system may be tuned to obtain optimum performance, and the third section will contain a step-by-step procedure for using the system to obtain a spectrum.

A. I. System Description

(a) Ramp Control Circuit

The ramp supply will vary somewhat, depending on whether the measurement system is analog or is digitally controlled. There are, however, features common to both.

The basic ramp generator, shown in Fig. A2, consists of a variable voltage source, a series resistor, R_S, and the junction itself, R_J. The junction is not a perfectly linear device, that is, R_J will vary with applied voltage. To minimize any effect this may have, R_S is chosen to be much greater than R_J. Thus, any variations in R_J with voltage will not appreciably alter the load on the voltage supply. In this manner, the current is solely determined by the supply voltage and the series resistance; thus, the junction sees a current source.

There are restrictions on how large R_S can be. The voltage source will have some maximum output, V_{Smax}, and there will also be a maximum voltage drop across the junction that must be reached, V_{Jmax}. With these two constraints, the maximum permissible voltage drop across the series resistor will be $V_{Smax} - V_{Jmax}$. Noting that $I_{max} = \frac{V_{Jmax}}{R_J}$, we find that the maximum allowable R_S is $R_J \left(\frac{V_{Smax}}{V_{Jmax}} - 1 \right)$. In practice, R_S is switch

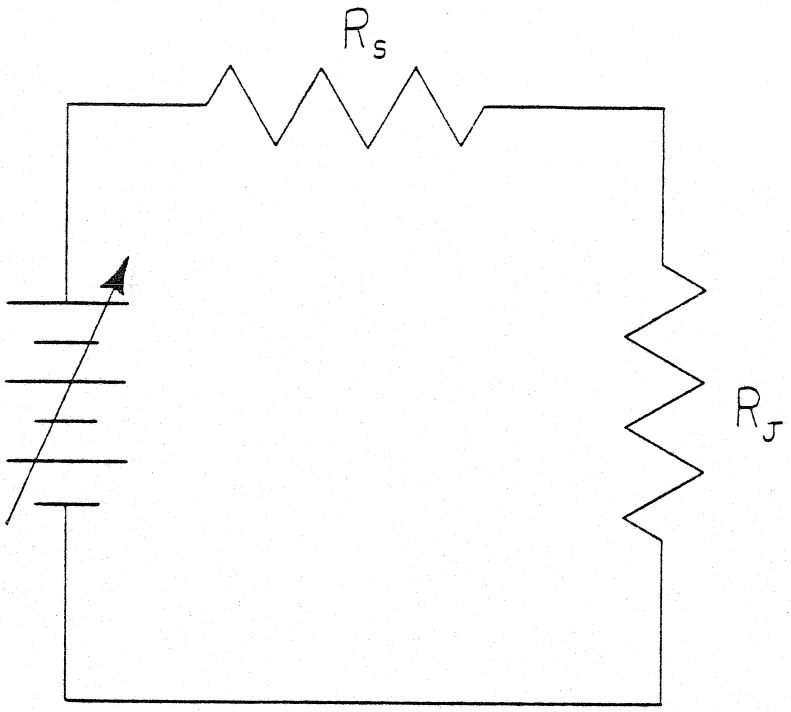

Fig A2

selectable and so has discrete values. Thus, R_S must be chosen to be as large as possible while still permitting the full voltage range at the junction. For example, for a V_{Smax} of 10 V, and V_{Jmax} of 0.5 V and an R_J of 50 Ω, the maximum R_S is 950 Ω. The resistances available for R_S in that range are 500 Ω, 700 Ω and 1.0 KΩ, so the 700 Ω value would be selected.

There have been two types of voltage supply used in our research group. The first was an analog source which was superseded by a digitally controlled unit.

The analog source design (shown in Fig. A3) is quite straightforward. By closing switch S1, a well-regulated constant DC voltage is fed into an integrator. The output of the integrator is then a voltage which varies linearly with time, sweeping from 0 to +10 volts or 0 to -10 volts depending on the polarity of the input. The rate at which the voltage is swept is determined by the resistor-capacitor combination (R_I, C_I), which may be switched manually. The integrator is rezeroed by closing the momentary switch S2, which shorts C_I.

The integrator cannot supply the necessary current to drive the relatively low impedence samples, so a buffer amplifier is added. This buffer is a unity gain amplifier capable of supplying 100 mA at ± 10 volts. The output of the buffer is then applied across the series resistor and sample, as described earlier.

If one wishes to initiate a voltage sweep from a point other than zero, a slight modification is made to the integrator, as shown in the insert to Fig. A3. By adjusting the potentiometer at the + input, the output of the integrator may be set to begin at any point over a wide range of voltages.

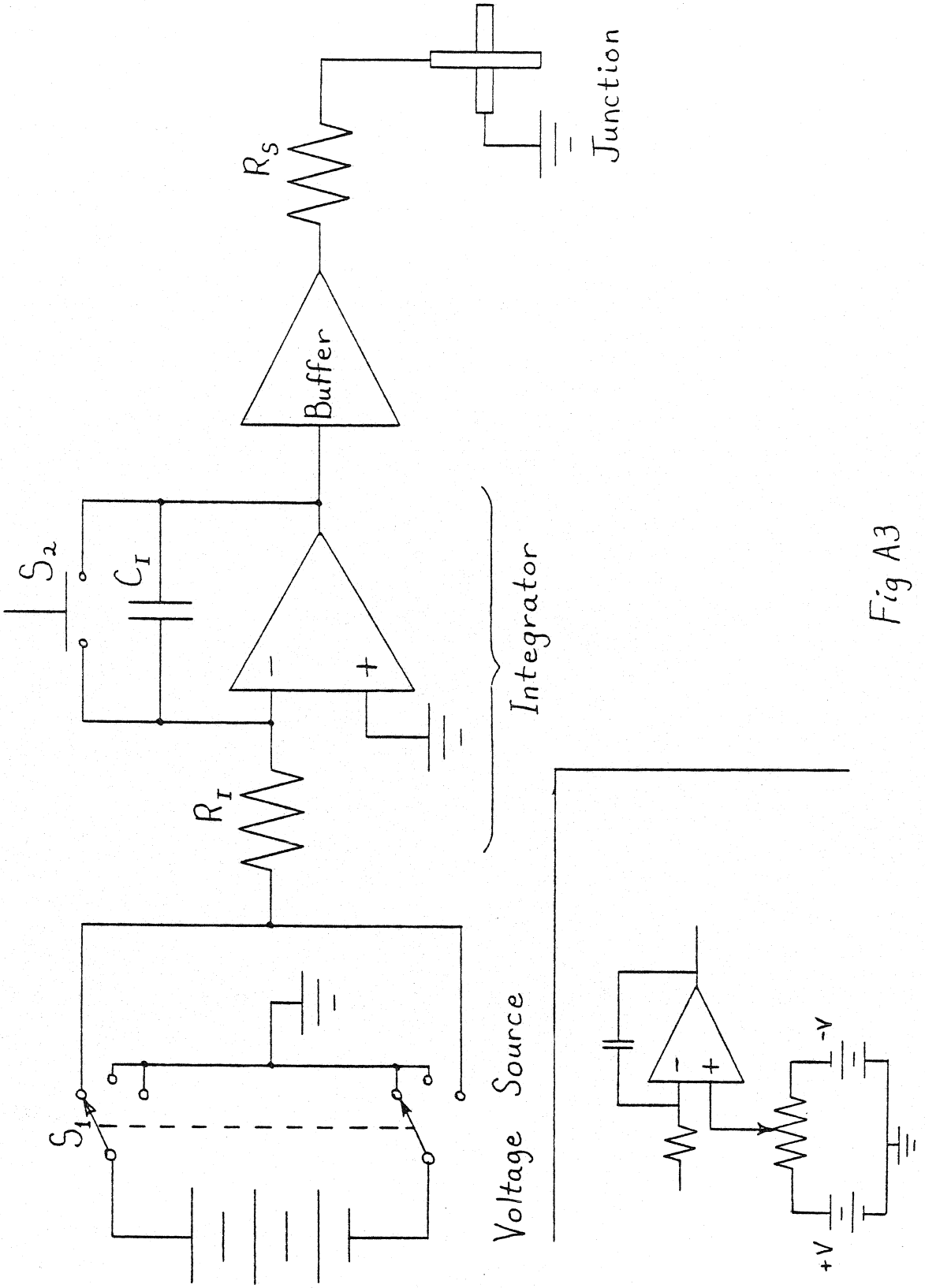

Fig A3

The ramp circuitry presently in use is designed to be digitally controlled by a PDP 11/10 lab computer. The overall system is shown schematically in Fig. A4. The circuit is made up of several parts. Two digital-to-analog converters (DAC's), labeled Wide DAC and Narrow DAC, connect to the input of the ramp control unit through resistors R_W and R_N, respectively. The output of the ramp control unit then goes through the series resistor to the junction and on to ground. The input to two amplifiers, A_H and A_L, connect to either side of the junction and feed back through resistors R_H and R_L, respectively, to the input of the ramp control unit.

Briefly, how this system works is that the computer sets the output of the Wide DAC which in turn determines the initial voltage across the sample. The narrow DAC is then stepped by the computer, incrementing the voltage by discrete amounts at precise time intervals. The control unit uses the voltages from the two DAC's to set its output. The two amplifiers A_H and A_L detect the resulting voltage at either side of the junction and feed this information back to the input of the control unit which, in turn, adjusts its output to ensure that the proper voltage drop across the junction is maintained.

The DAC circuitry is shown in detail in Fig. A5. Both digital-to-analog converters are Analog Devices model 12QZ 12 bit units wired to supply -10 to +10 volts. The DAC's are controlled by the PDP 11 computer via a parallel interface, that is, each bit has its own wire connected directly to the computer interface. The computer is electronically isolated from the measurement electronics by means of a bank of optical isolators, each line having its own isolator. An optical isolator consists

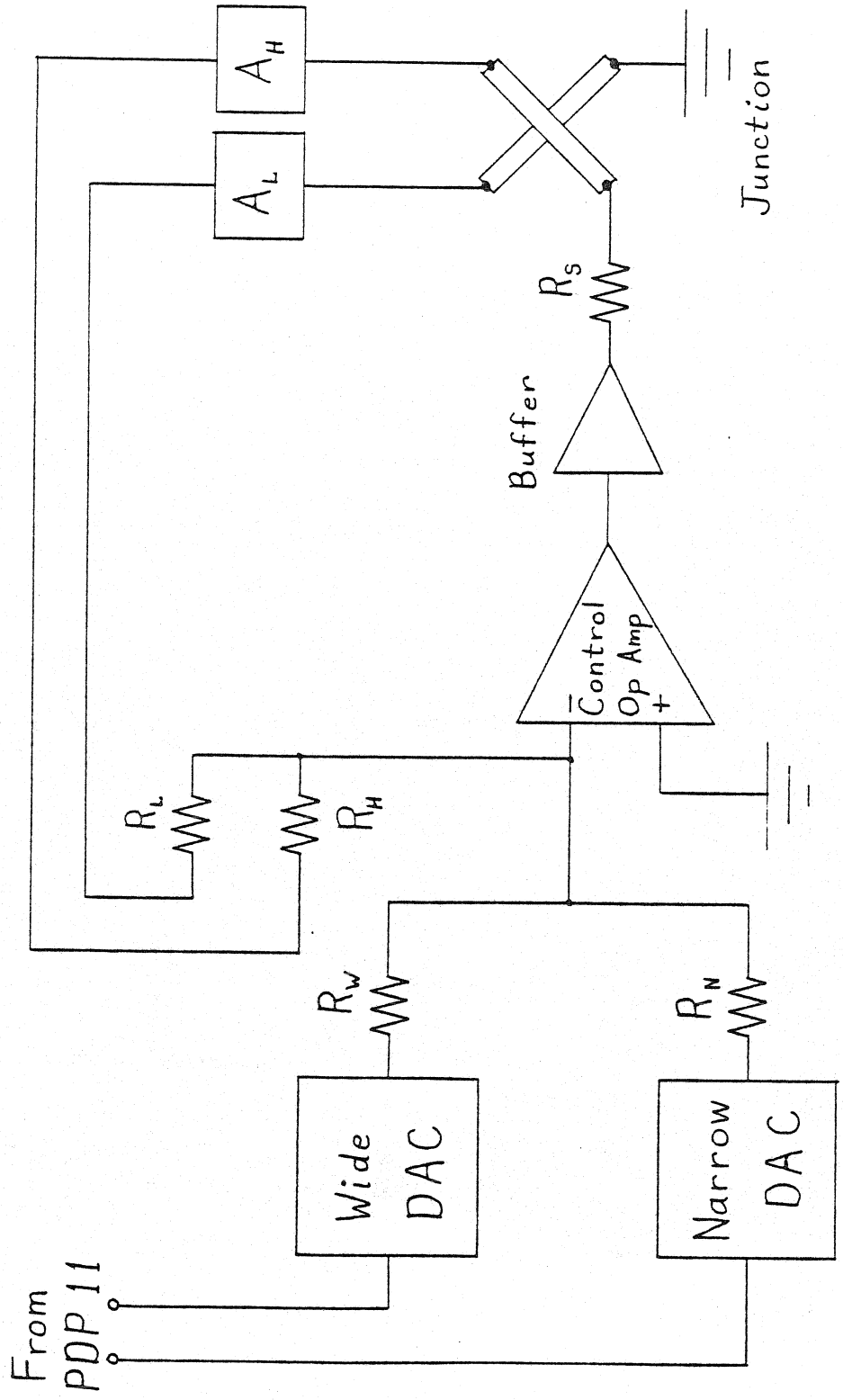
From PDP 11
Wide DAC
Narrow DAC
R_W
R_N
R_L
R_H
Control Op Amp
Buffer
R_S
A_H
A_L
Junction

Fig A4

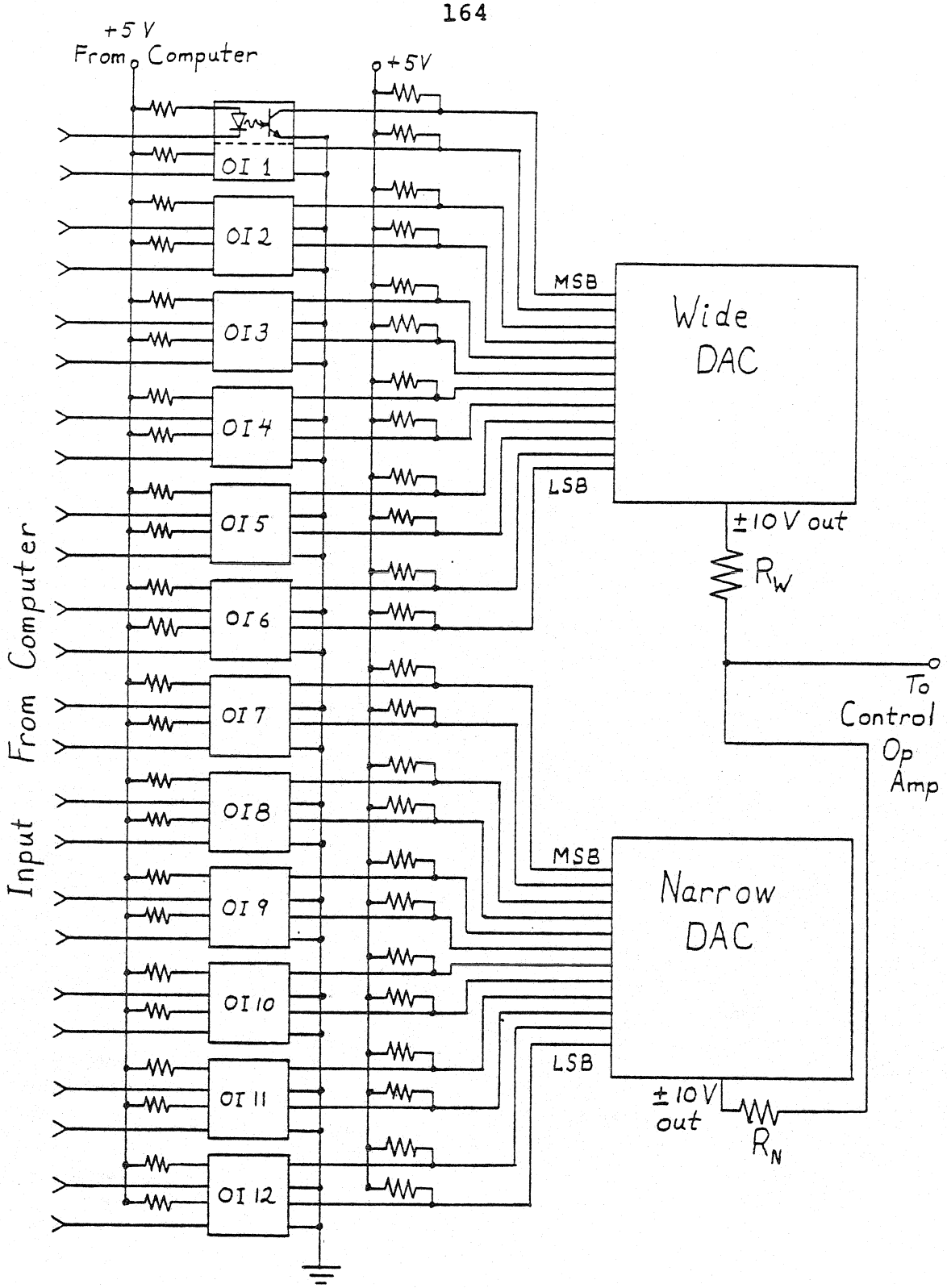
+5 V
From Computer
+5V
OI 1
OI 2
OI 3
OI 4
OI 5
OI 6
OI 7
OI 8
OI 9
OI 10
OI 11
OI 12
Input From Computer
MSB
Wide
DAC
LSB
±10 V out
R_W
To
Control
Op
Amp
MSB
Narrow
DAC
LSB
±10V
out
R_N

Fig A5

of a light emitting diode (LED) optically coupled to, but electronically isolated from, a photosensitive transistor. When a signal is fed to the LED, the diode emits light which is absorbed by, and drives, the photo transistor, which in turn puts out a signal. Thus, the signal is transferred without direct electrical contact. This isolation eliminates the chances of ground loops between the measurement electronics and the computer, which would cause serious noise problems.

As mentioned above, the two DAC's play different roles in the measurement. The output of the wide DAC passes through a fixed 10 KΩ resistor, R_W, to the control circuitry. This DAC is set to the voltage at which the measurement is to begin and retains that value for the duration of the run. The Narrow DAC, on the other hand, begins at zero and is stepped by uniform voltage increments until the desired spectral range is covered. The output of the Narrow DAC goes through a resistor, R_N, to the control circuit. The value of R_N may be set at one of four values: 10 KΩ, 20 KΩ, 50 KΩ and 100 KΩ. The resistance at which R_N is set will determine the range of the Narrow DAC at the sample, as compared to the range of the Wide DAC, i.e., a value of 10 KΩ will set the range of the Narrow DAC equal to the range of the Wide DAC, 20 KΩ gives one half the range, 50 KΩ one fifth the range, and 100 KΩ one tenth the range of the Wide DAC. These resistances are set through the computer by means of a set of reed relays, as shown in Figs. A5 and A6.

The signals from these two DAC's are then combined and fed into the circuitry which controls the actual voltage drop across the tunnel junction. To understand how this circuitry works, one must know something about the characteristics of operational amplifiers (op amps).

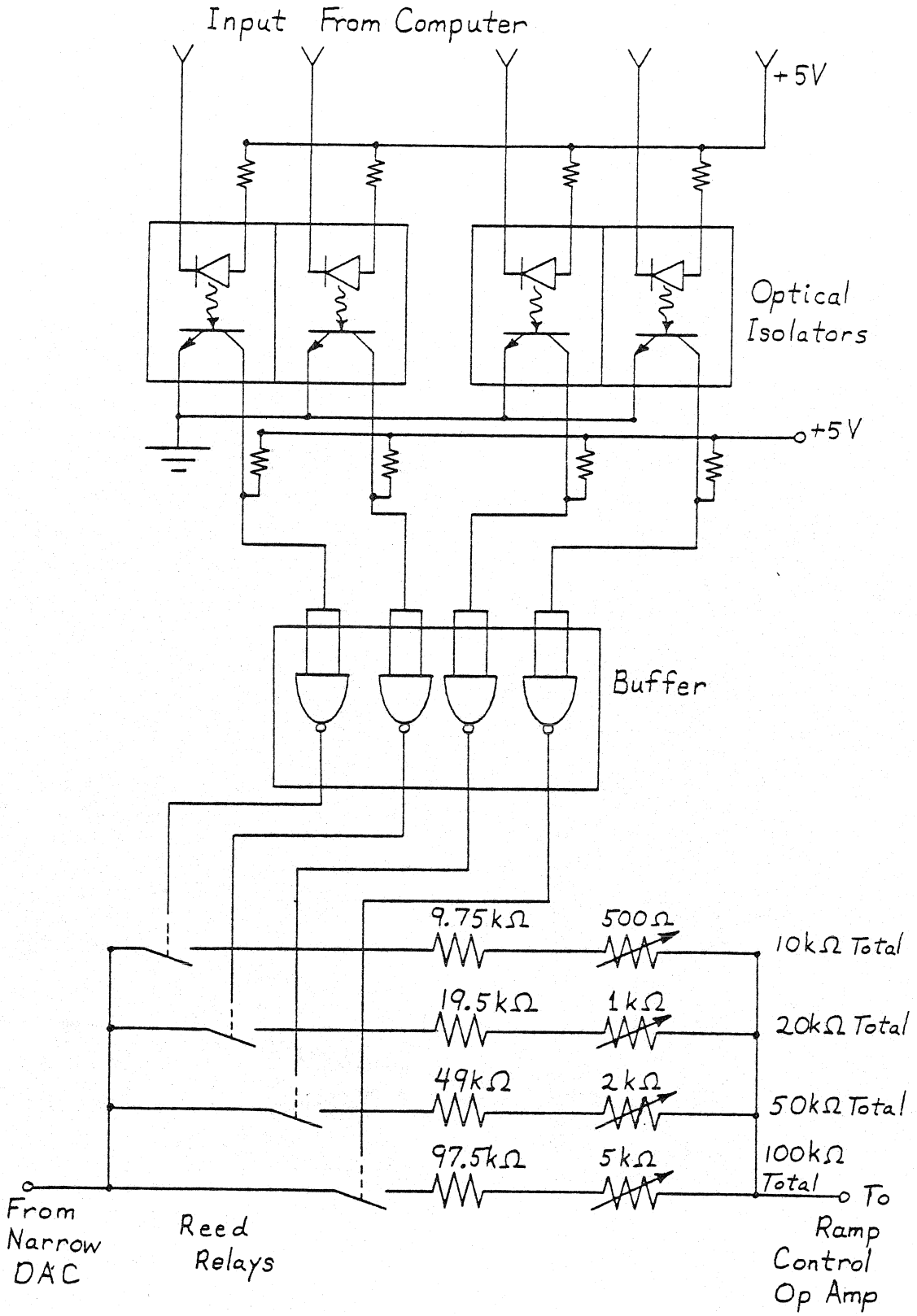
Input From Computer
+5V
Optical Isolators
+5V
Buffer
9.75kΩ
500Ω
10kΩ Total
19.5kΩ
1kΩ
20kΩ Total
49kΩ
2kΩ
50kΩ Total
97.5kΩ
5kΩ
100kΩ Total
To Ramp Control Op Amp
From Narrow DAC
Reed Relays

Fig A 6

An operational amplifier is drawn as a triangle [see Fig. A7(a)] with two inputs, one inverting (-) and the other noninverting (+). The ideal op amp has infinite input impedence (no current flows into its inputs) and infinite gain, A. Also, both inputs are held at the same potential, so if one input is grounded the other input is fixed at zero volts. With these radical characteristics, feedback is almost always necessary to produce a useful circuit. Figure A7(b) shows a simple example of an inverting amplifier which makes use of feedback. The noninverting input is grounded, fixing the inverting input at zero volts. Since no current can flow into the inputs, $\frac{V_{in}}{R_{in}} + \frac{V_{out}}{R_o} = 0$, or rearranging $V_{Out} = - V_{in}\left[\frac{R_o}{R_{in}}\right]$ which gives an amplification of $-(R_o/R_{in})$. The characteristics of real op amps will differ somewhat from ideal. For example, the gain, A, of a typical solid state op amp (a 741) is not infinite but is typically greater than 10^5. Also, the noninverting input for the above-mentioned circuit, is not exactly at zero volts but is at $\frac{V_{out}}{A}$. However, since V_{out} is generally limited to less than 10 volts, V_{out}/A will be less than 10^{-4} volts which is often negligible. With proper tuning of the circuitry (to be described later), the op amp can be made to operate very nearly as ideal, so in the following discussion, we will consider the op amp as an ideal device.

The ramp control circuit shown in Fig. A4 may now be analyzed. The buffer amplifier employed in the circuit serves the same purpose as it did in the analog circuit, that is to provide current at unity voltage gain, and so it will not be discussed further.

The heart of the circuit is the control op amp. Its output can vary from -10 to +10 volts. This drives a current through R_S and the junction

(a)

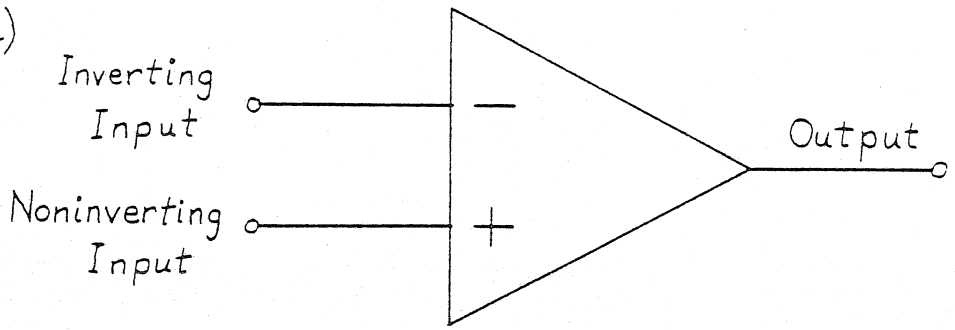

(b)

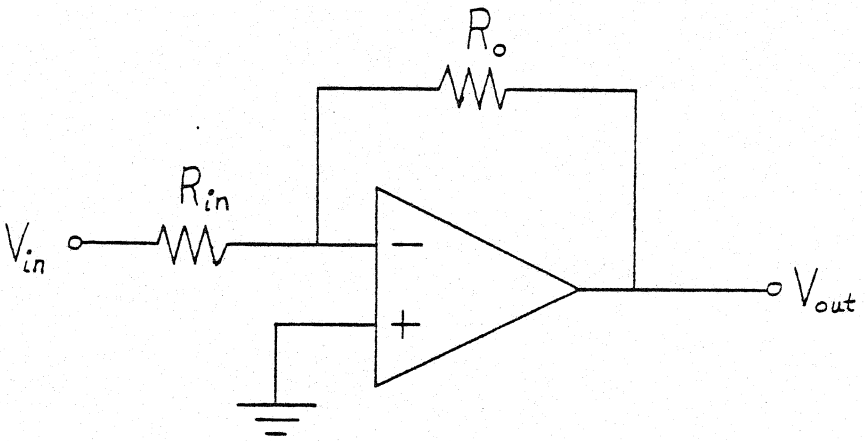

$$V_{out} = A\,V_{in}$$

$$= -\frac{R_o}{R_{in}}\,V_{in}$$

Fig A7

to ground. The resulting voltages at either side of the junction are detected by two high input impedence amplifiers of gain A_H and A_L. These amplifiers take the detected voltages, V_H and V_L, amplify them and feed them, through resistances R_H and R_L, respectively, back to the input of the control op amp.

One may now make use of the characteristics of op amps to analyze the workings of the circuit. The sum of the currents flowing into the input of the control op amp must be zero, and since the input voltage is fixed at zero, each current may be represented as $\frac{V}{R}$. Thus, one has $\frac{V_W}{R_W} + \frac{V_N}{R_N} + \frac{A_H V_H}{R_H} + \frac{A_L V_L}{R_L} = 0$. For simplicity, set V_N to zero. Now A_H, A_L, R_H and R_L are adjusted so that $\frac{A_H}{R_H} = -\frac{A_L}{R_L}$ in which case the above equation reduces to

$$V_H - V_L = -\left(\frac{R_H}{A_H}\frac{1}{R_W}\right) V_W$$

$V_H - V_L$, the true voltage drop across the junction, is now directly related to the output voltage of the DAC. For IETS, three voltage ranges were selected, ± 0.2 volt, ± 1.0 volt and ± 5.0 volts. Since R_W is fixed at 10 KΩ, and V_W has a range of ± 10 volts, the necessary values for $\frac{R_H}{A_H}$ $\left[\text{and } -\left(\frac{R_L}{A_L}\right)\right]$ are 200, 1000 and 5000 Ω. Fixing the values for R_H and R_L at 7.5 KΩ and 30 KΩ, respectively, determines the necessary amplification factors for the two feedback amplifiers. For the 0.2 volt range, A_H must be 37.5 and A_L must be -150; for the 1 volt range, A_H is 7.5 and A_L, -30; for the 5 volt range, A_H is 1.5 and A_L is -6.

The feedback amplifiers themselves utilize operational amplifiers but

in a different configuration. In this case, to obtain maximum input impedence, a noninverting amplifier circuit is used in the input stage. A_H and A_L are shown in Fig. A8. A_H is a basic noninverting amplifier. Since both inputs are held at the same potential and no current can flow into either input, one finds $V_H = (A_H V_H) \frac{R_1}{R_1 + R_2}$, or $A_H = \frac{R_1 + R_2}{R_1}$. R_1 has been fixed at 2.5 KΩ so, in order to obtain A_H's of 37.5, 7.5 and 1.5, the three values for R_2 must be 91.25 KΩ, 16.25 KΩ and 1.25 KΩ.

A_L differs from A_H in that the net amplification A_L must be negative so the noninverting stage is followed by a unity gain inverting amplifier. For A_L, R_3 is fixed at 1.0 KΩ so to obtain amplifications of 150, 30 and 6, R_4 must take on values of 149 KΩ, 29 KΩ and 5 KΩ.

The trim pots shown in Fig. A8 are used to fine tune the amplification factors. Their adjustment is described later in the tuning instructions.

For convenience, an extra circuit, labelled the Phase Lock Test circuit (Fig. A9), was added. This circuit detects the voltage at the input to the control op amp. If this voltage is close to ground potential, then all is well. A voltage significantly different from zero at the input indicates that the feedback control is not able to hold the voltage drop across the junction at the desired value (this usually results from too large an R_S). The operation of this circuit is straightforward. The test circuit feeds the detected voltage to two FET op amps which act as voltage sensitive switches. These two op amps are biased at +100 mV (upper amp) and -100 mV (lower amp). If the absolute value of the input voltage is less than 100 mV, then the output voltage of both op amps is large and positive. This large positive voltage reverse biases the two

01 02

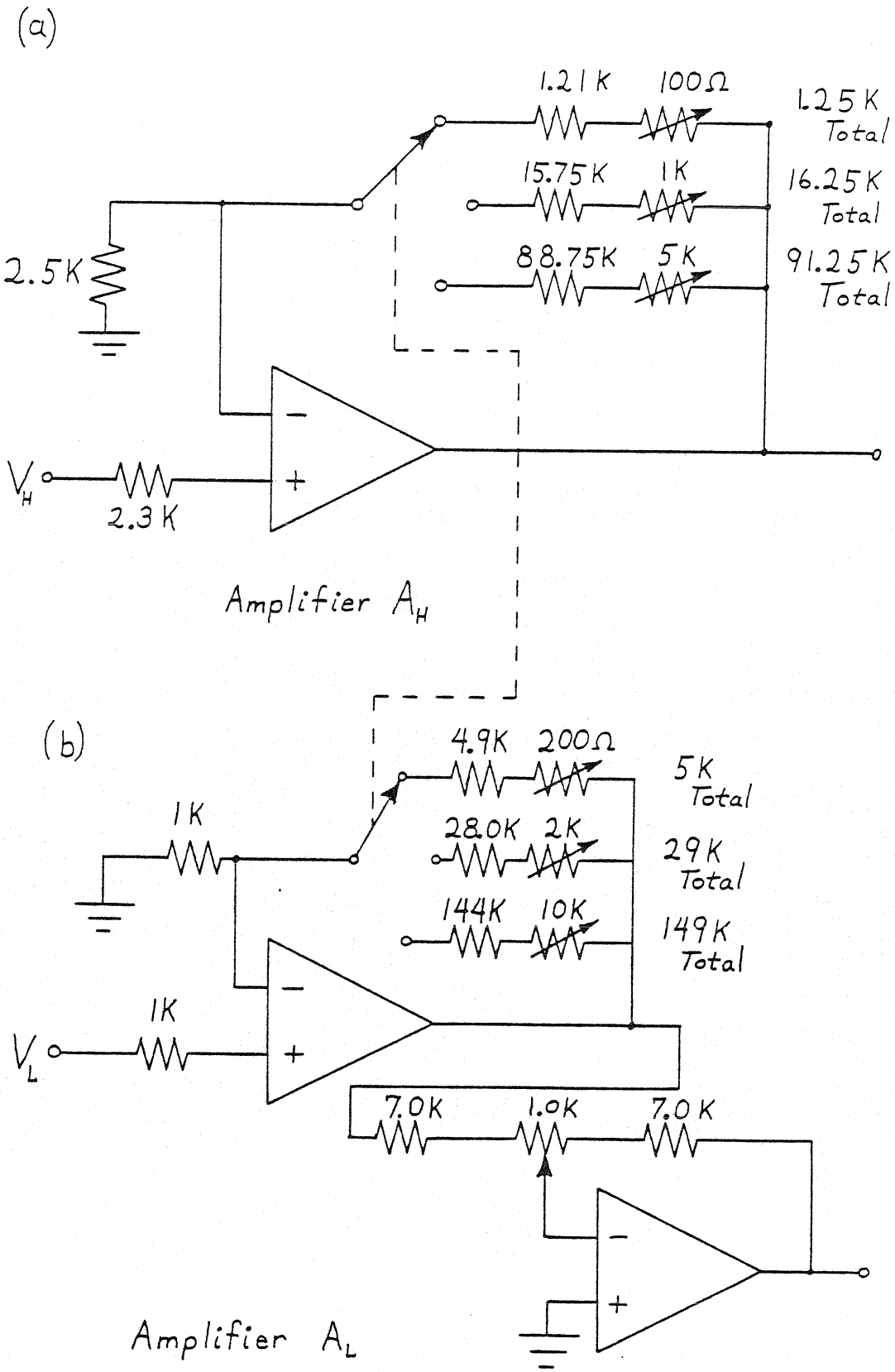
(a)
1.21K
100Ω
1.25K Total
15.75K
1K
16.25K Total
88.75K
5K
91.25K Total
2.5K
V_H
2.3K
Amplifier A_H
(b)
4.9K
200Ω
5K Total
1K
28.0K
2K
29K Total
144K
10K
149K Total
1K
V_L
7.0K
1.0K
7.0K
Amplifier A_L

Fig A8

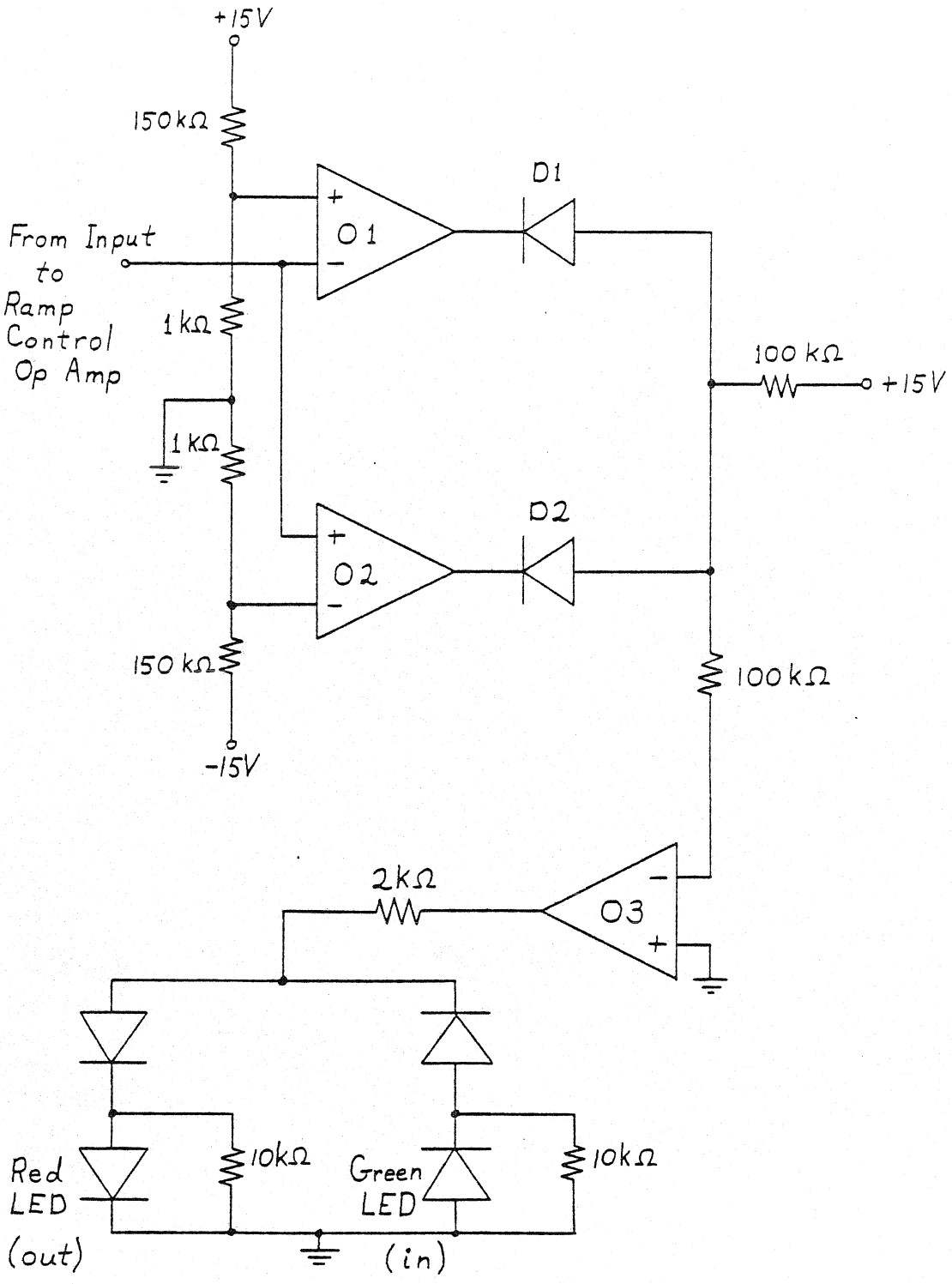
+15V
150kΩ
D1
O1
From Input to Ramp Control Op Amp
1kΩ
100 kΩ
+15V
1kΩ
D2
O2
150 kΩ
100kΩ
-15V
2kΩ
O3
10kΩ
Red LED
(out)
Green LED
(in)
10kΩ

Fig A9

output diodes (D1 and D2), causing a large positive voltage to appear at the inverting input of op amp 03. The output of 03 is then a large negative voltage which forward biases the green LED causing it to light. If, however, the input voltage exceeds + (-) 100 mV, the output of 01 (02) will then switch to a large negative voltage. This strongly forward biases D1 (D2), drawing the voltage at its anode negative, resulting in a negative voltage at the input to 03. The output of 03 then switches from a positive to a negative voltage, switching off the green LED and turning on the red LED, which signals the operator that something is wrong.

Thus, with the digitally controlled amp circuit, a precise voltage of known size may be applied across the tunnel junction by entering two twelve bit binary numbers to two DACs, setting a relay which selects R_N, setting a switch which selects A_H and A_L, and properly selecting R_S.

(b) Modulation Supply

The modulation supply circuitry is quite simple, it consists of a commercial sine wave generator (Heathkit model IG-18), a set of two tuned L-C filters, and a frequency doubler. The schematic is shown in Fig. A10.

The sine wave generator is set to supply modulation at 47.23 KHz. The reasons for choosing this frequency are determined by the detection circuitry (and so will be discussed in that section). A 1 KΩ ten-turn pot is placed across the output of the oscillator (labelled MOD AMPL). This pot allows a large enough signal to drive the frequency doubler and lock-in amplifier reference even when a very small modulation voltage is to be applied to the sample.

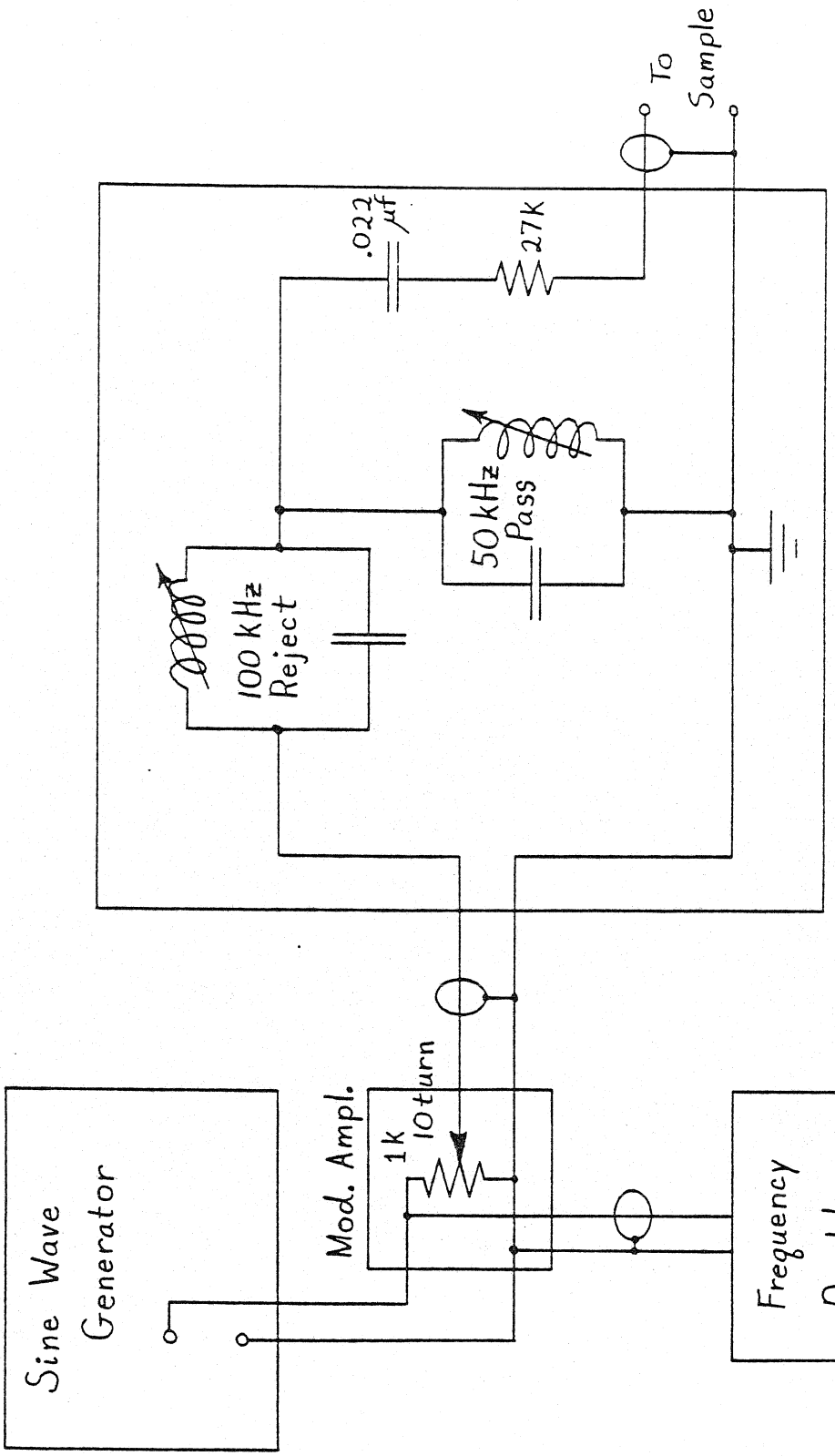

Fig A 10 Modulation Supply

The filter circuit simply consists of two tuned L.-C. notch filters. The first preferentially blocks any 94.46 kHz component that may be present in the signal, while the second preferentially passes the 47.23 kHz fundamental. This results in a very pure sine wave with extremely low second harmonic content.

The sine wave passes through a capacitor and resistor which isolate the modulation supply from the DC voltage of the ramp. The signal is then joined with the ramp voltage and the sum is applied across the junction.

When the first derivative is to be measured, some changes are made in the modulation supply. As mentioned in Appendix B, at 47 kHz the capacitive impedence (Z_c) of the junction overwhelms the resistive impedence which we want to detect. Since Z_c is proportional to frequency, it can be reduced to a manageable level by reducing the frequency by a factor of fifty, to 1.1 kHz. This frequency no longer coincides with the tuned filters, so the filters are simply bypassed. This does not cause problems since the fundamental to be detected is up to two orders of magnitude larger than the second harmonic, so the purity of the sine wave is not so critical.

The other branch from the oscillator proceeds through a Frequency Doubler to the lock-in reference. The lock-in amplifier used in our measurements (PAR HR-8) requires a reference at the frequency at which one wishes to measure. Thus, since we wish to measure the second harmonic, the frequency of the reference input must be exactly twice the frequency of the modulation supplied to the junction.

The frequency doubler makes use of an optical isolator to isolate the lock-in electronically from the rest of the modulation supply. This guards against ground loops and isolates the detection circuitry from the supply circuit.

The frequency doubler is shown in Fig. A11. The input from the sine wave generator is fed to the LED of the optical isolator. The phototransistor of the isolator is wired in a common emitter amplifier configuration with the input to the amplifier being the light emitted from the LED. The output from this amplifier stage is further amplified by a noninverting op amp circuit. The output of this stage then takes one of two routes, depending on whether the fundamental or harmonic is desired. For the fundamental, the signal just passes through a voltage divider to ground and the output is taken across one of the resistors. If the harmonic is opted for, the signal is fed through a half wave rectifier circuit to the output. This does not produce a sine wave at twice the input frequency but simply produces a signal with a second harmonic component large enough for the lock-in amplifier to use as a reference.

(c) Sample Holder

The sample holder block consists of three parts: first is the switch box, second is the sample holder itself, and third is the calibration unit.

The switch box provides the electrical connection between the measurement electronics and the sample holder (and so the samples), and also selects the particular junction to be measured. To the box is attached a ¼" phenolic rod approximately one meter long. With the sample holders bolted to the far end of this rod, the samples may be inserted down the neck of a standard 25 liter liquid helium dewar for measurement at 4.2 K.

The switch box [Fig. A12(a)] consists of a twelve-position switch. Nine of the positions connect the nine samples to the electronics, one

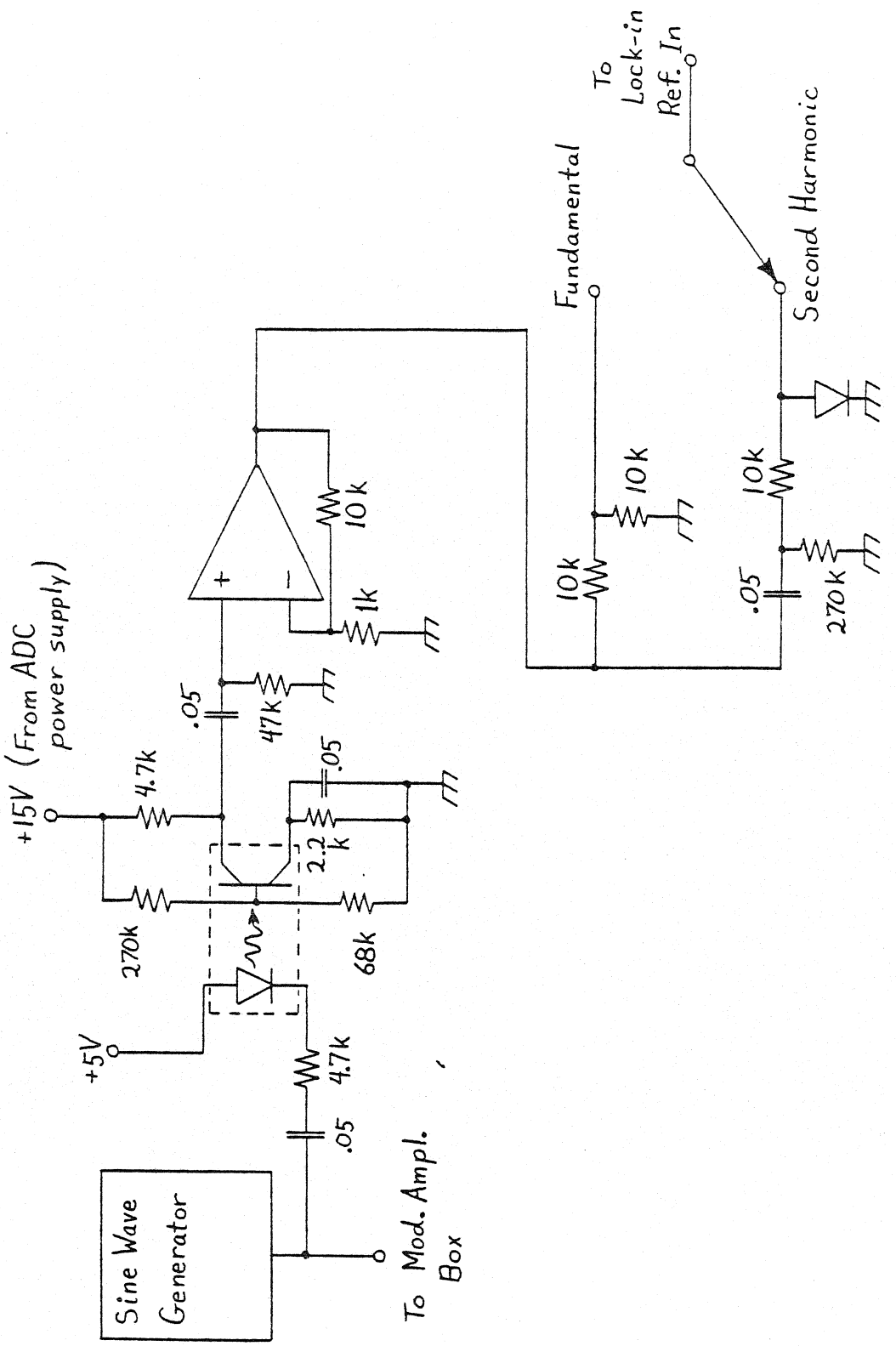
+15V (From ADC power supply)
4.7k
270k
68k
2.2 k
.05
47k
10 k
1k
+5V
4.7k
.05
Sine Wave Generator
To Mod. Ampl. Box
Fundamental
10k
10k
To Lock-in Ref. In
Second Harmonic
10k
.05
270k

Fig A11

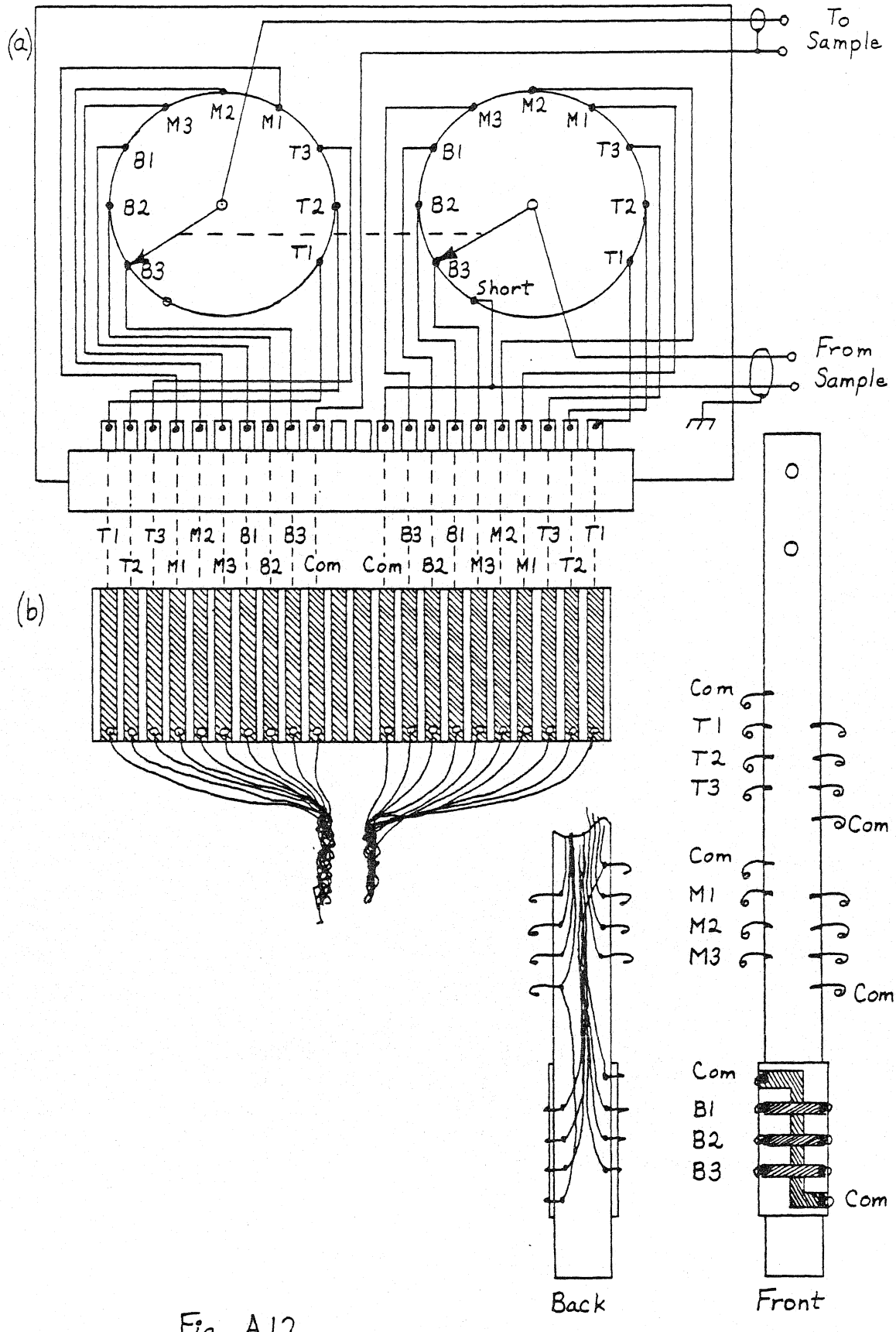
(a)
To Sample
From Sample
M3
M2
M1
B1
T3
B2
T2
T1
B3
Short
T1 T3 M2 B1 B3 B3 B1 M2 T3 T1
T2 M1 M3 B2 Com Com B2 M3 M1 T2
(b)
Com
T1
T2
T3
Com
Com
M1
M2
M3
Com
Com
B1
B2
B3
Com
Back
Front

Fig A12

position shorts the output, and the last two are open. Terminals are provided for the "To Sample" and "From Sample" connections to the electronics, and a 44-terminal card connector is mounted for the connection to the sample holder. Only 20 contacts are needed to the samples, so terminals on the opposite sides of the card connector are tied together in pairs to improve contact with the sample holder card.

The sample holder itself [Fig. A12(b)] consists of three parts: the support for the samples which provides the electrical contact to the junctions, two sets of ten-wire braids which connect the support to the contact card, and the contact card which plugs into the switch box.

The support consists of a thin strip of perforated vector board to which are attached leads of #26 tinned wire, spaced at proper intervals to make contact easily with the aluminum and lead strips of the samples. The connection between the leads and metal films is made with an indium tin alloy (Indalloy No. 1). On the back of the support, to each of the leads is soldered one wire from one of the two braids. Each braid consists of ten strands of teflon insulated #30 wire, nine wires are for the nine lead strips and the tenth makes contact with all three aluminum strips simultaneously. One braid brings the ramp plus modulation to the junctions and the other braid connects the junctions to the detection circuit. The wires are in separate braids to help isolate the output from the input and also to guard better against pick up of unwanted signals from the environment. The wires from the braids are then soldered to the connector card. This card consists of a double-sided copper clad p.c. board, which is etched to form copper strips on both sides of the board spaced so as to make contact with the contacts of the card connector

of the switch box. The two braids are connected to the card symmetrically, each wire being soldered to a pair of opposing copper stripes. This card is simply plugged into the switch box to connect all samples to the electronics.

The calibration boxes, mentioned above, are a set of calibrated variable resistors and capacitors used to calibrate the first derivative data. Electronically, a tunnel junction appears to be a resistance in parallel with a capacitance, so the calibration box consists of a set of switch selectable capacitors in parallel with a variable resistance, as shown in Figure A13. The resistance and capacitance may be varied to match the characteristics of the junction, the first derivative of which has been measured (as is described in the measurement procedure section). A switch is provided to connect the resistance to the four-wire ohms terminal of a precision digital volt meter so that the exact resistance may be recorded for calibration purposes.

(d) Detection Circuitry

The detection circuitry consists of three parts, as shown in Fig. A14: the tuned filter section (included only when measuring the second derivative), the lock-in amplifier, and the recording device.

As noted in the Modulation Source section, the characteristics of the detection circuitry determined the fundamental frequency used in the second derivative measurement. The lock-in amplifier used is a PAR HR-8 with a Type A preamplifier. From the noise contours of the preamp, it was determined that the best frequency for the harmonic would be near 100 KHz. At this frequency the source impedence required for the preamp is quite

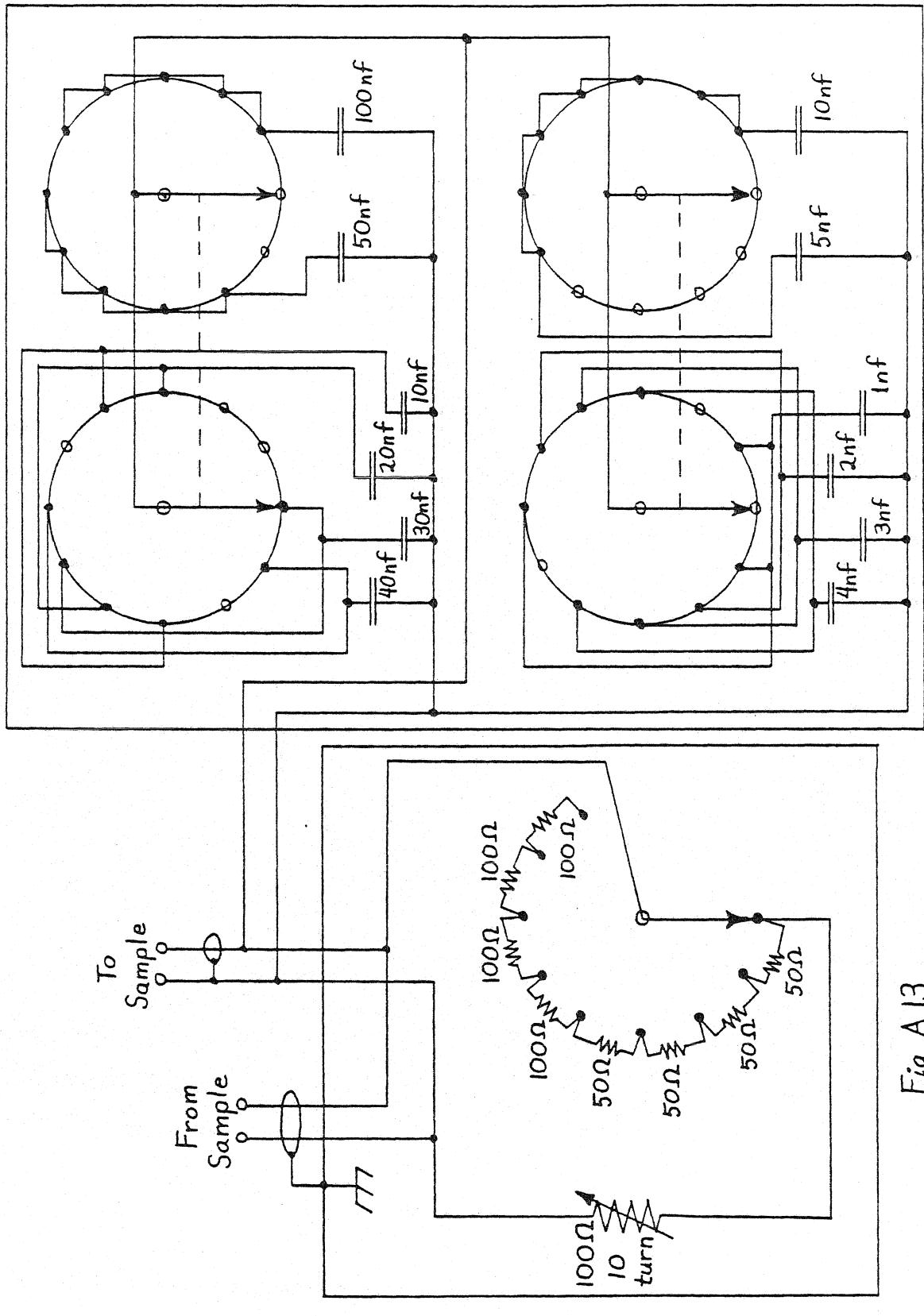
100nf
50nf
10nf
20nf
30nf
40nf
10nf
5nf
1nf
2nf
3nf
4nf
To Sample
From Sample
100Ω
100Ω
100Ω
100Ω
50Ω
50Ω
50Ω
50Ω
100Ω 10 turn

Fig A 13

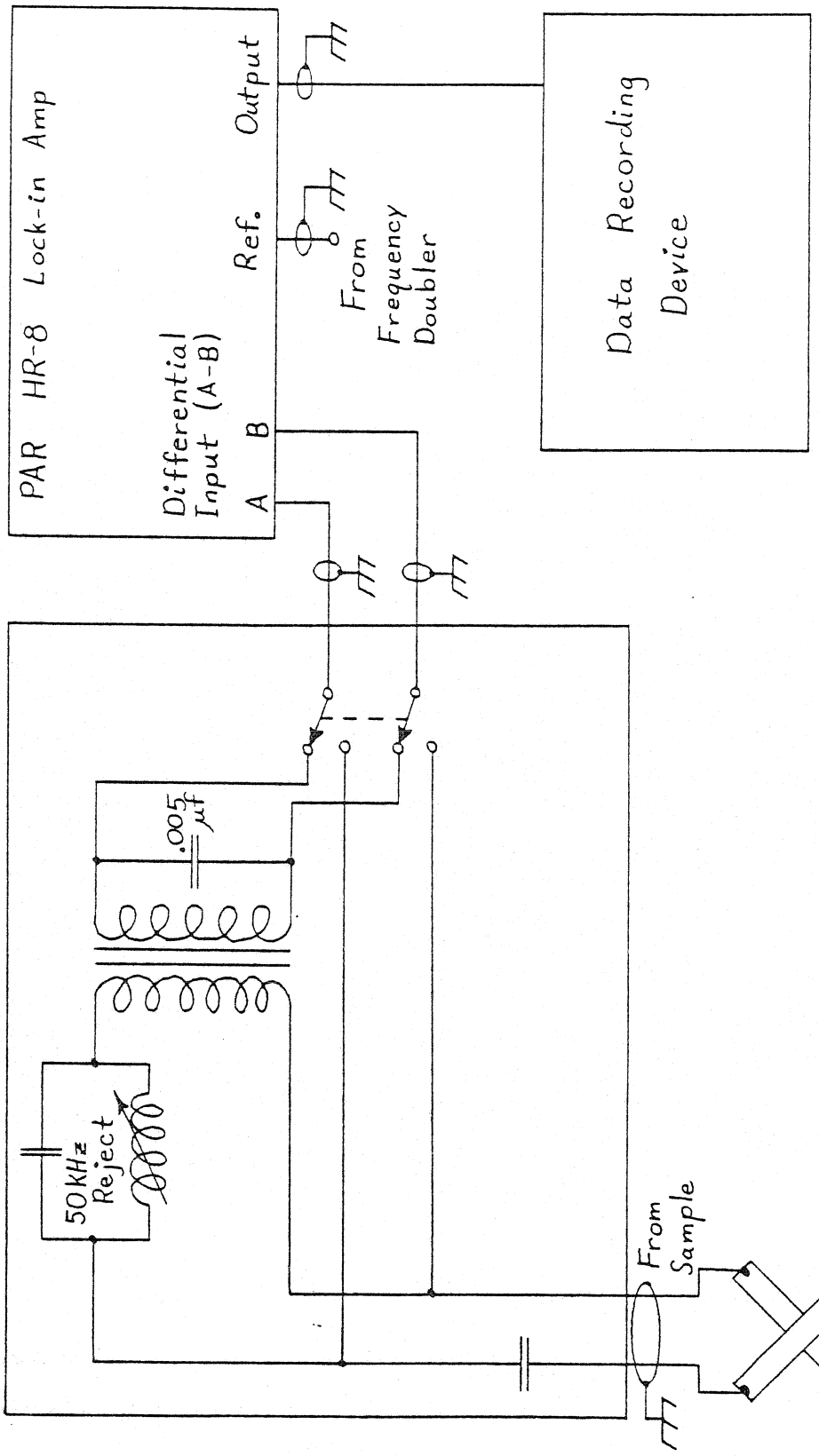
PAR HR-8 Lock-in Amp
Differential Input (A-B)
A
B
Ref.
Output
From Frequency Doubler
Data Recording Device
.005 μf
50 kHz Reject
From Sample
Ramp + Modulation To Sample

Fig A 14

high. Since the junction impedence itself is quite low, a torroid transformer was hand wound to match the frequency and impedence requirements of the preamp. With the torroid included in the filter circuitry, the circuit has an optimum frequency of 94.46 kHz. Thus the optimum fundamental is 47.23 KHz.

The filter section of the detection circuit consists of the torroid mentioned above, which, when a 0.005 μf capacitor is wired in parallel with the secondary windings. acts as a 94.46 kHz band pass filter. The transformer, along with the input capacitor, serve to isolate the lock-in amplifier from the DC component of the signal from the sample. A tunable LC filter is added to block selectively the, still large, fundamental component of the input.

As mentioned in the modulation section, the modulation frequency used in the first derivative measurements is 1.12 kHz. Since this is also the frequency of the signal to be detected, the filter and transformer must be bypassed. A switch, labelled $\frac{dI}{dV}$ / $\frac{d^2I}{dV^2}$, selects whether the filters are to be bypassed or included. The input capacitor must also be bypassed and a larger capacitance substituted, for the reason discussed in Appendix B. At the present time this must be done externally as described later in the measurement section of this appendix.

The output of this section is applied to the differential inputs of the lock-in preamp. The lock-in will detect that component of the input with the same frequency as the reference input (either the fundamental or second harmonic in this case), amplify it and present the desired result at the output terminal as a DC voltage. This output will be in the range -10 to +10 volts.

These results are then recorded as a function of the DC voltage across the junction. The spectrum is recorded in one of two ways. If the

record is to be made in analog form, the output of the lock-in is used as the Y-input of an X-Y recorder. The X-input is taken directly from the DC voltage which is present across the sample.

If the spectrum is to be recorded in digital form, as is done with the present detection system, the output of the lock-in is fed to an analog-to-digital converter (ADC), shown in Fig. A15. The ADC is an Analog Devices 12QZ 12-bit unit wired to accept and convert voltages in the range -10 volts to +10 volts. The ADC converts the DC voltage to a 12-bit binary number. Each bit is connected through a buffer to an optical isolator (as described in the Ramp Control section) and then on to the input interface of the PDP 11 computer. The ADC does not continuously convert analog input to digital output but only converts when it receives a command from the computer. Thus, an additional line from the computer to the ADC (also optically isolated) is included for this purpose.

The computer, thus, signals the ADC to make a conversion and then records the resulting number in memory. In general, the computer will take many ADC readings at each ramp voltage setting and then average the numbers together to get one datum point. To obtain the energy scale for the spectrum, the computer does not actually measure and record the DC voltage at the junction, but simply assumes that the ramp control circuitry is functioning correctly and records the starting voltage and voltage increment which were specified by the operator. The spectrum is then stored in a data file as an initial voltage, a voltage increment and a series of numbers, one for each spectrum datum. These datum points are recorded as numbers from 0.0 to 100.0, representing the % of full scale of the lock-in output, 0% being an output of +10 volts and 100% being an

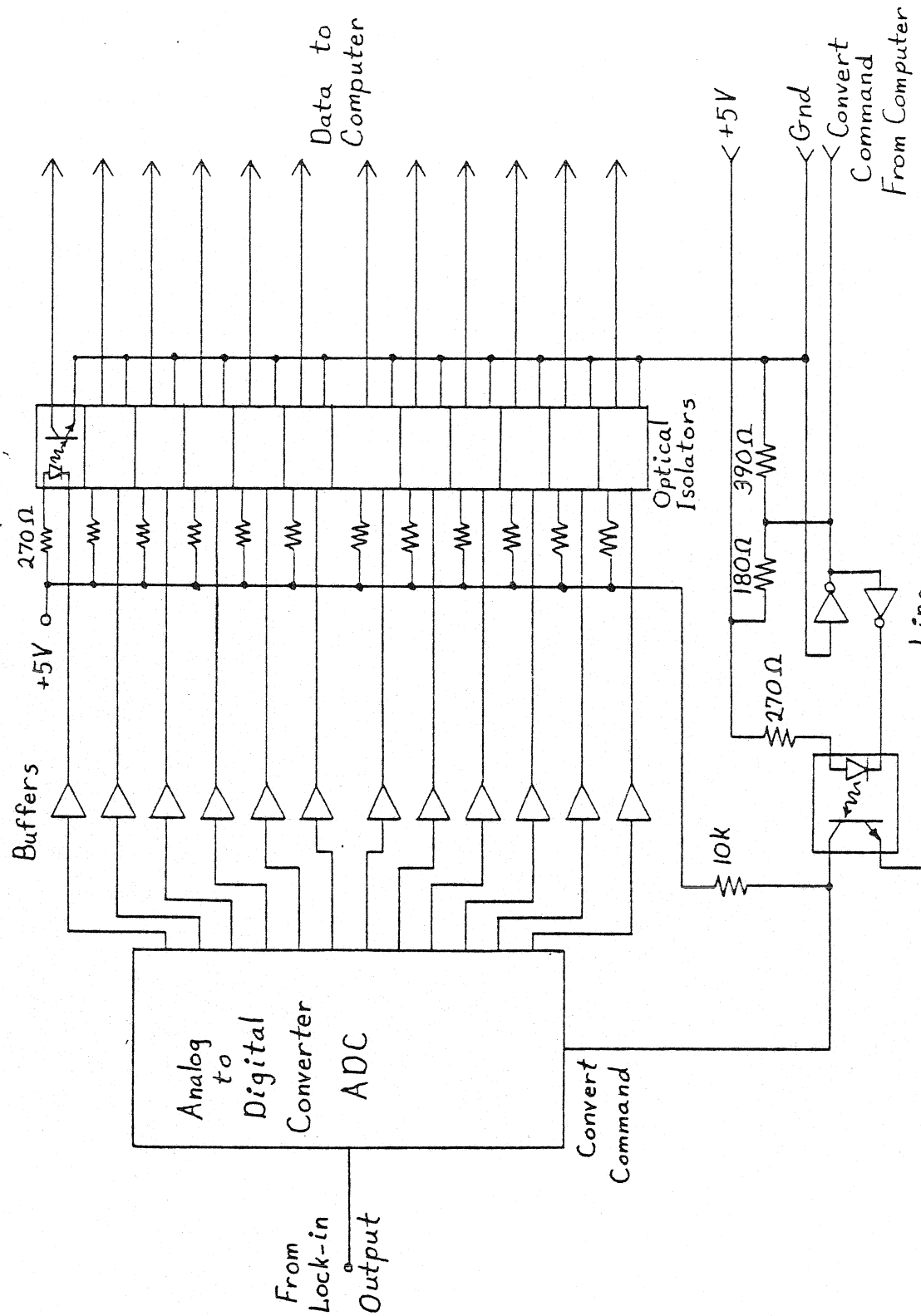
Data to Computer
+5V
Gnd
Convert Command From Computer
Optical Isolators
270Ω
390Ω
180Ω
270Ω
10k
Buffers
+5V
Line Driver
Analog to Digital Converter ADC
From Lock-in Output
Convert Command

Fig A 15

output of -10 volts. A plot of the spectrum may be obtained by means of a computer-controlled point plotter, as described in the measurement procedure section. Permanent storage of data files, as well as the operator programs, is on floppy disk.

A. II. Tuning the Measurement Electronics

There are basically four parts of the measurement electronics which require tuning and testing to obtain optimum performance. First is the PAR lock-in amplifier. The tuning procedure for the lock-in is needed both for the actual IETS measurements and for adjusting the tuned filters in the electronics. These tuned filters are the second segment of the electronics to be adjusted. The third set of procedures is concerned with testing and tuning the various components of the ramp control circuitry. This is the longest and most important section to be covered. Finally, the operation of the ADC circuit is adjusted.

Once these procedures are carried out, the electronics will be ready to use in IETS data acquisition.

(a) PAR Model HR-8 Lock-In Amplifier

Lock-in amplifiers are used to detect preferentially and to amplify periodic signals occurring at a fixed frequency ω, and phase, ϕ. At the same time, the lock-in time averages those components of the input occurring at all other frequencies, much reducing their contribution to the signal. In this way, a lock-in may extract a signal from an input in which the noise is of a greater magnitude than the signal itself. If, however, the lock-in is not tuned to the proper frequency and phase, it cannot distinguish the signal from the noise.

Tuning this lock-in is quite straightforward. The following is a set of instructions for setting up the lock-in to measure an arbitrary frequency, ω, assuming the operator is starting from scratch.

(1) First, one must set the front panel to the following initial settings, starting from the left of the panel.

The preamp switch is set to the central, A-B, position for measuring a differential input (as in the present measurement system) or it can be set to A (or B) to measure a single ended input.

The Sensitivity switch is set to a value lower (larger voltage) than one expects to be measuring, so as not to overload the lock-in when the input appears.

The large Frequency knob in combination with the multiplier switch below it are set to the frequency to be measured.

The Frequency Trim knob is set to 2.5.

The Signal Q is set to 9.

The Phase is set at 180 (an arbitrary starting point).

The Mode Switch is set to SEL. EXT.

The Ref. Atten. control is set at 1.0 with vernier fully clockwise.

The Time Const. is set at 300 msec with the inner, red knob set at 6 db/OCT.

The Meter/Monitor is set to Out.

The Zero Offset is set at zero with the toggle switch in its central position.

The Calibrate switch is set to OFF.

A reference signal of frequency ω must be fed into the Ref. In BNC input.

(2) At this point, enter the signal to be measured.

(3) Increase the sensitivity until a deflection away from zero (center)is seen on the meter.

(4) Adjust the phase setting to maximize this deflection. (The deflection may be in either the positive or negative direction.) Use the Zero Offset control to keep the meter needle on scale, if possible (if it cannot be kept on scale, switch to a lower sensitivity).

(5) Adjust the large Frequency knob to maximize the deflection further.

(6) Repeat steps (4) and (5) until maximum deflection is obtained. The frequency is now set.

(7) Adjust the Frequency Trim to maximize the meter reading. This will, in general, affect the phase so steps (4) and (7) should be carried out alternately until maximum deflection is found.

The lock-in is now tuned.

Note that the higher the Sensitivity setting used, (within reason), the more accuracy one can attain in the tuning.

(b) Filters

The tuned LC filters used in the electronics will, in general, very seldom require tuning once the circuits have been optimized. Very little extra equipment is needed to tune the filters, only a frequency counter and a tuning tool (plastic screwdriver). A small metal screwdriver may be used in place of the tuning tool.

(1) The first step is to hook up the electronics as if one were making a measurement, with two exceptions:

(i) Set up the DVM to monitor the modulation voltage at the input to the Modulation Filter; and (ii) In place of the samples, attach the Calibration Box set to 100 Ω with the capacitance section unplugged.

(2) Use the frequency counter to set the oscillator frequency to 47.231 ± 0.003 kHz.

(3) Set the Frequency Doubler switch to Fundamental, and set the derivative selector switch on the Measurement Electronics panel to dI/dV.

(4) Increase the output of the oscillator and Mod. Ampl. until 0.25 volts AC is read on the DVM (input to the modulation filters). This will correspond to approximately 2 mV AC across the dummy sample.

(5) Tune the lock-in to detect this 47.23 kHz signal, as per the procedure given in the previous section (no need to check the Freq. Trim for this procedure).

(6) Adjust the 50 kHz Pass variable inductance to maximize the signal on the lock-in while, simultaneously, adjusting the Mod. Ampl. pot to keep the modulation measured by the DVM constant. Also, check the lock-in phase setting to make sure it is kept optimized.

(7) Switch the derivative selector to d^2I/dV^2. This will drastically reduce the signal reaching the lock-in.

(8) Adjust the lock-in sensitivity and phase to measure this signal.

(9) Adjust the 50 kHz Reject filter on the Measurement Electronics panel to minimize the signal. This adjusting screw is set in about 1 inch from the front panel. Again, make sure that the lock-in phase is always set correctly

(10) Now set the oscillator frequency to 94.462 ± 0.003 kHz, with an output of approximately 1.5 volts, as measured by the DVM.

(11) Tune the lock-in to this 94.46 kHz signal.

(12) Adjust the 100 kHz Reject to minimize the signal reaching the PAR, again keeping the DVM reading constant and the lock-in phase set correctly.

(13) Since tuning one filter may affect the adjustment of the others, the procedure must be repeated until all three filters are optimized simultaneously.

(c) Ramp Control Circuitry

The ramp control circuitry is the most involved block of the electronics to check out and tune up. First, one must make sure that the digital signals are able to reach the DAC's from the computer. This primarily means checking the optical isolators, since they are the components most likely to fail. In the second step, one must switch each DAC back and forth from -10 volts to +10 volts output to set the "zero" and "range" of each. The next four steps serve to fine tune the operation of the two feedback amplifiers, A_H and A_L. The final step is to adjust the resistances, R_N, in order to calibrate the ranges of the Narrow DAC. The entire procedure is carried out with the Measurement electronics set up as if one were making a measurement. The modulation is set to zero, and the calibration box takes the place of the sample. All calibration measurements are made using the DVM, included in the electronics, equipped with small clip leads.

The ramp control circuitry is contained in the right half of the box labeled Measurement Electronics. Except for the panel switches, the

LED's and the power supply, all the ramp electronics are contained on one board, the layout of which is shown in Fig. A16. Almost all the connections are wire wrap, as opposed to solder or printed circuit. The power supply for the ramp is located in a separate box located immediately beneath the electronics mounted on the same panel as the Modulation Filters.

Tuning the ramp electronics should be carried out with the unit still mounted in the rack. Simply move the DVM, lift out the DVM shelf and remove the perforated top (and fan) from the Electronics box.

The first procedure to be described is the checking out of the optical isolators which connect the computer to the digital-to-analog converters. This is important since, if even a single isolator is not functioning, the DAC cannot receive all the information it needs to set the voltage to the correct value. This check is most directly accomplished by using the switches on the front panel of the computer to feed binary numbers directly to the DAC's, and thus the optical isolators. The problem with this procedure is that the computer needs to be halted ("ENABLE/HALT" switch down). This requires that no one else be using the computer at the time. A second procedure will be given later which is to be used if POL is running.

(1) Turn on computer, and set ENABLE/HALT switch to halt (down).

(2) Set the ADDRESS/DATA toggles to 764072 (base 8) or, in binary, 1,110,100,000,111,010 (1 is up, 0 is down). Then press LOAD ADRS button.

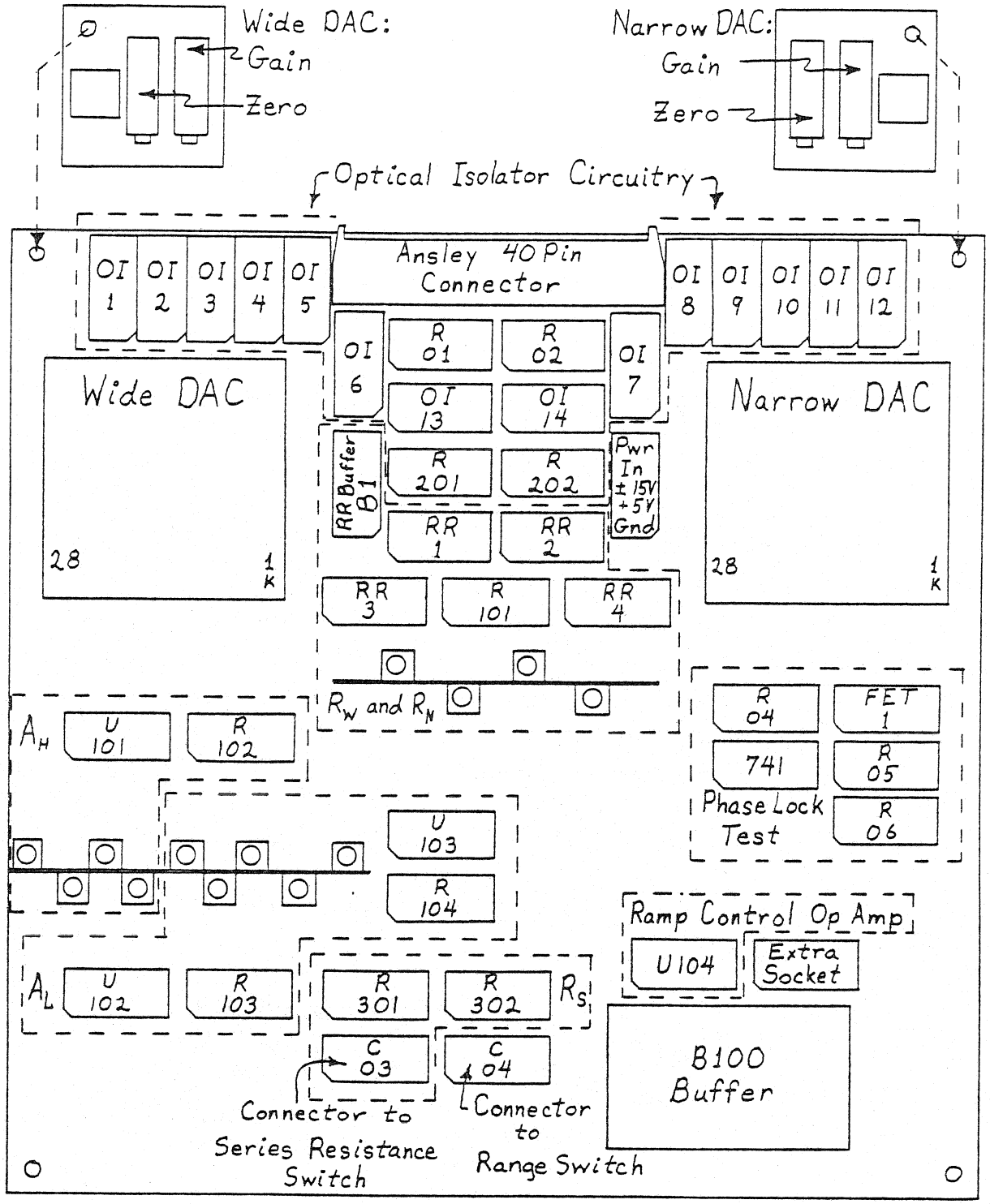
Wide DAC:
Gain
Zero
Narrow DAC:
Gain
Zero
Optical Isolator Circuitry
OI 1
OI 2
OI 3
OI 4
OI 5
Ansley 40 Pin Connector
OI 8
OI 9
OI 10
OI 11
OI 12
OI 6
OI 7
R 01
R 02
OI 13
OI 14
RR Buffer B1
R 201
R 202
Pwr In ± 15V +5V Gnd
RR 1
RR 2
RR 3
R 101
RR 4
Wide DAC
28
1 K
Narrow DAC
28
1 K
R_W and R_N
A_H
U 101
R 102
R 04
FET 1
741
R 05
Phase Lock Test
R 06
U 103
R 104
Ramp Control Op Amp
U104
Extra Socket
A_L
U 102
R 103
R 301
R 302
R_S
C 03
C 04
B100 Buffer
Connector to Series Resistance Switch
Connector to Range Switch

Fig. A16

(3) Set toggles to XXXX00 (base 8, X means any number will do, only the last 2 are important), and lift DEP three times. This enables the operator to feed numbers to the DAC's and the reed relays.

(4) Set toggles to 765072 (base 8), and press LOAD ADRS. (This is the address of the Wide DAC.)

(5) Set all toggles up to 1, and lift DEP three times. This sends a signal of all ones to all the optical isolators. (The computer automatically steps the address each time the DEP switch is toggled.)

(6) Check the voltage (with respect to chassis ground) at pins 2 through 15 of resistor networks R201 and R202 (see Figs. A16 and A17). All voltages should be between 2 and 6 volts.

(7) Reset toggles to 765072, and press LOAD ADRS.

(8) Set all toggles to zero (down), and lift DEP three times to set all optical isolators to zero.

(9) Remeasure the voltages, as in step 6. All should be less than 0.8 volts. This is where the optical isolators are most likely to be off if they have failed.

(10) If any voltages do not satisfy the above requirements, refer to Table AI to find which optical isolators are implicated, and replace them with new isolators. Make sure that the new isolator is functioning correctly.

If POL is being used on the computer, the following procedure may be used.

Standard numbering scheme for a 16 pin socket, top view.

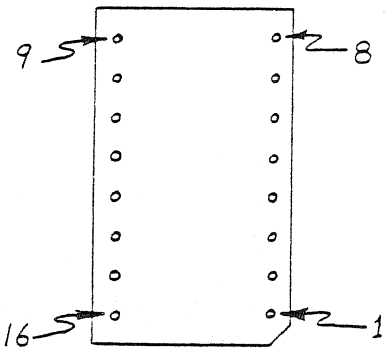

Layout for Optical Isolator sockets, two isolators per socket.

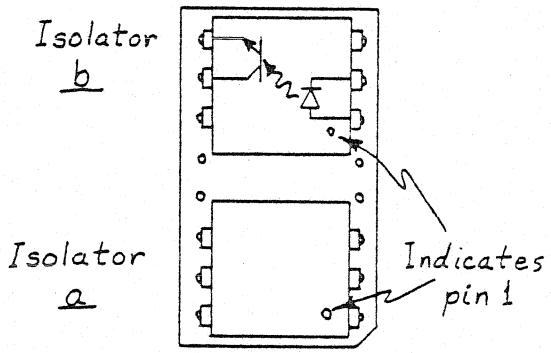

15-Resistor Component Carrier Layout, R201, R202.

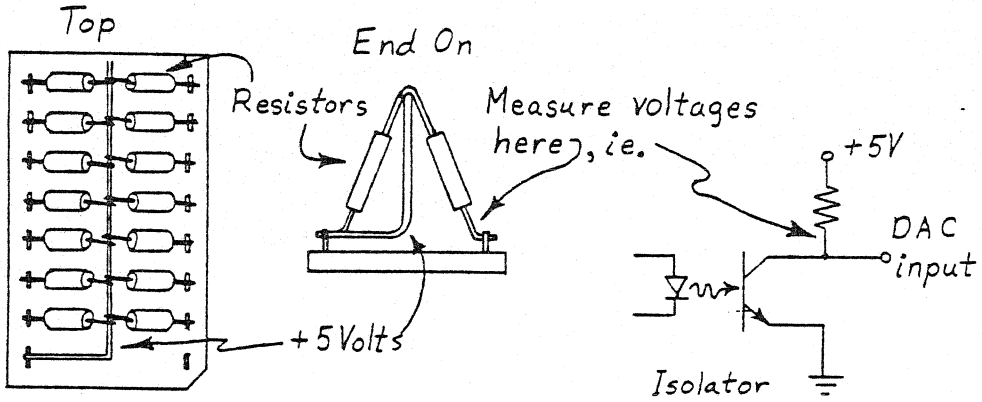

Fig A 17

Table AI

Resistor	Optical Isolator	As Input to:	Function
R201 pin 2	1a	Wide DAC pin 7	Wide DAC bit 11, MSB
3	1b	8	bit 10
4	2a	9	9
5	2b	10	8
6	3a	11	7
7	3b	12	6
8	4a	13	5
9	4b	14	4
10	5a	15	3
11	5b	16	2
12	6a	17	1
13	6b	18	0 LSB
14	13a	B1, pins 1, 2	Sets R_N to 10 K
15	13b	B1, pins 4, 5	Sets R_N to 20 K
R202 pin 2	7a	Narrow DAC pin 7	Narrow DAC bit 11, MSB
3	7b	8	10
4	8a	9	9
5	8b	10	8
6	9a	11	7
7	9b	12	6
8	10a	13	5
9	10b	14	4
10	11a	15	3
11	11b	16	2
12	12a	17	1
13	12b	18	0, LSB
14	14a	B1, pins 11, 12	Sets R_N to 50 K
15	14b	B1, pins 14, 15	Sets R_N to 100 K

(1) Type in the following using the Decwriter:

```
S:R   1;2
F:O   4;74
F:A   1;1
P:A   4;4
STA   4
S:F  74
S:D  19;0
END
EXE   4
```

This feeds 3777 (base 8) to the 2 DAC's.

(2) Measure the voltage at pins 2 through 13 of resistor networks R201 and R202 (Figs. A16 and A17). Pin 2 of both networks should be less than 0.8 volts, the rest should read between 2 and 6 volts.

(3) Next, type:

```
REE   4
IGN   1
S:D  19;.001
I:D  19;1
END
EXE   4
```

This sends 4001 to both DAC's.

(4) Remeasure pins 2 through 13 of R201 and R202. Now pin 2 should be high (2 to 6 volts), pins 3 through 12 should be less than 0.8 volt, and pin 13 will still be high.

(5) In order to set bit 0 (pin 13) low, type in:

```
REE   4
IGN   2
S:D  19;.011
I:D  19;11
END
EXE   4
```

This feeds 5000 (base 8) to the DAC's.

(6) Now pin 13 alone is measured on both sockets. It must be less than 0.8 volt.

(7) Next, type:

```
C:R   1;
C:R   2;
C:R   3;
C:R   4;
```

This feeds ones to the relay buffer which, in turn, feeds zeroes to the relays.

(8) Measure pins 14 and 15 of R201 and R202. They should all be high (more than 2 volts).

(9) Type:

```
S:R   1;
S:R   2;
S:R   3;
S:R   4;
```

This feeds zeroes to the relay buffer.

(10) Measure pins 14 and 15 again; they should all be less than 0.8 volt.

(11) If any voltages do not fall within the limits, use Table AI to locate the appropriate optical isolators and replace them with new ones. Make sure that the new isolators function correctly.

At this point, all optical isolators should be working correctly, and the tester may proceed to calibrating the DAC outputs. For this procedure, one must enter the DAC settings via the front panel switches of the PDP 11, since the full range of both DAC's cannot be reached using POL commands. As mentioned in the optical isolator test section, this requires that no one be using the computer to run experiments. The computer operations are very similar to those used to check the isolators.

(1) Turn on computer, and set ENABLE/HALT switch to halt.

(2) Enter 764072 (base 8) in the ADDRESS/DATA switches, and press LOAD ADRS.

(3) Set toggles to XXX00 and lift DEP three times, as before, enabling the operator to set the DAC's and relays.

(4) Set toggles to 765072 (base 8), and press LOAD ADRS.

(5) Enter XX7777 (all up), and lift DEP <u>once</u>.
This sets the Wide DAC to -10 volts.

(6) Enter XX3777 (base 8), and lift DEP <u>twice</u>.
This sets the Narrow DAC to zero and opens all the reed relays.

(7) Attach the + clip lead of the DVM to pin 16 of R101, the - lead to chassis ground, and leave them in position until the Wide DAC is set. The DVM should read exactly -10 volts; if it does not, adjust the Wide DAC "Zero" trim pot until it does.

(8) Enter 765072 and depress LOAD ADRS.

(9) Enter XX0000 (lowest 12 bits all 1's), and lift DEP once. This sets the Wide DAC to plus full scale.

(10) Read DVM; if voltage is not exactly +10 volts, adjust Wide DAC "Gain" trim pot.

(11) Repeat steps (4), (5), (7), (8), (9) and (10) until both -10 and +10 volt settings read correctly.

(12) Enter 765072, and press LOAD ADRS.

(13) Enter XX3777, and lift DEP switch once to zero Wide DAC.

(14) Enter XX7777, and lift DEP once to set Narrow DAC to -10 volts.

(15) Now attach the DVM + clip lead to pin 1 or 16 of any of the reed relays (RR1, RR2, RR3 or RR4); they will all read the output of the Narrow DAC. If the voltage is not exactly -10 volts, adjust the Narrow DAC "Zero" trim pot.

(16) Enter 765074 and press LOAD ADRS to address the Narrow DAC register.

(17) Enter XX0000, and lift DEP once.

(18) Read the voltage; if it is not exactly +10 volts, adjust the Narrow DAC "Gain" pot.

(19) Repeat steps (14) through (18) until both voltages are correct. (Remember, 765072 addresses the Wide DAC and 765074 addresses the Narrow DAC.)

Both digital-to-analog converters are now set. In general, when the DAC's are set to zero their outputs will not be exactly zero volts, but should be within a few tens of millivolts. This offset is simply due to normal nonlinearity in the DAC's and should not cause concern.

Now that one is sure that the DAC's can be set properly through the computer, one may proceed to calibrate the actual control circuitry. This involves tuning the two amplifiers A_H and A_L. These procedures are most easily carried out using POL. The first step is to calibrate the ramp ranges by adjusting the amplification of A_H. The second step is to check the unity gain inverter in A_L and then adjust the gain of A_L to compensate for differing lead impedences.

To adjust A_H, refer to that section of Fig. A16 labeled A_H, and the detailed drawing of that section in Fig. A18. Set the calibration box for 100 Ω, and set R_S to 700 Ω.

(1) Enter the following string of POL commands:

```
F:O   4;74
F:A   1;1
S:R   1;2
P:N   4
P:A   4;15
STA   4
S:F  74
S:D  19;0
LOO   0;10
W:S   6
S:D  19;1.0
W:S   7
S:D  19;0
CON   0
END   4
EXE   4
```

Amplifier A_H

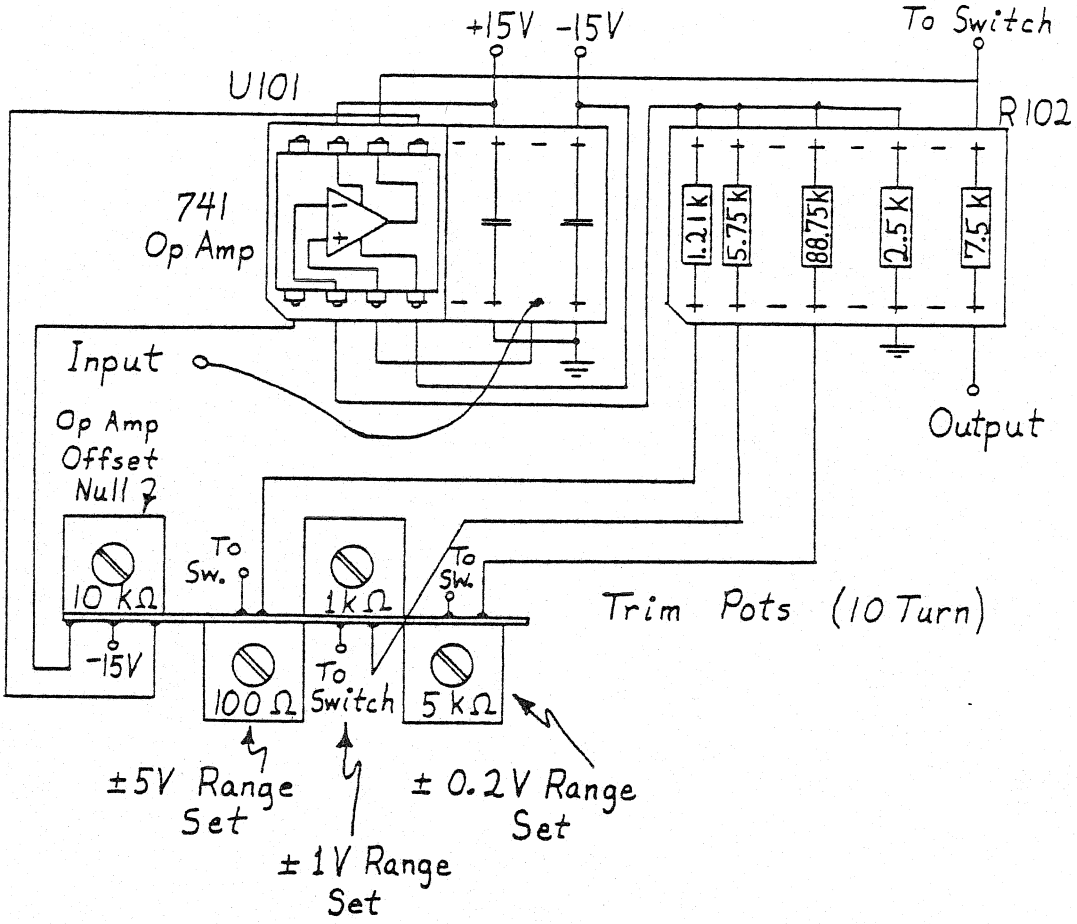

Fig. A18

This program will allow the operator to switch the Wide DAC back and forth between 0 and full scale (10V) using the switch box at the measurement station. The switch box is a small (2¼" x 2¼" x 4"), blue and red box with two momentary push buttons labeled 6 and 7.

(2) Using the DVM, measure the voltages (with respect to chassis ground) at U101 pin 7 and R102 pin 16. These are the voltages at the two inputs of the op amp.

(3) If the two voltages are not the same, adjust the 10 kΩ Op Amp Offset Null trim pot until they are.

(4) Plug the DVM input into the socket labeled DVM MOD, and set it to read DC volts (make sure the grounds of the DVM and Measurement Electronics are connected and the DVM GUARD switch is in).

(5) Set the Range switch to 0.2. The DVM should read within a few millivolts of zero; note this reading, v_{Low} .

(6) Press button 6; the voltage should now read near 0.2 volts; call this v_{High}.

(7) The difference $v_{High} - v_{Low}$ should be exactly 0.2 volts; if it is not, adjust the pot labeled 0.2 V Range Set (Fig. A18). Adjusting this will change v_{Low} slightly.

(8) Press button 7 to reset the DAC to zero and remeasure v_{Low}.

(9) Repeat steps (5) through (8) until $v_{High} - v_{Low}$ is <u>exactly</u> 0.2 volts. The program entered allows the operator to switch back and forth between zero and full scale ten times.

(10) Now set the Range switch to 1.0.

(11) Repeat steps (5) through (9), this time to adjust $V_{High} - V_{Low}$ to exactly 1.0 volt using the ±1 V Range Set pot. If the program stops, simply enter EXE 4 to restart.

(12) In theory, the same procedure can be followed to set the 5.0 volt range; however, in practice, the electronics, as they are presently set up, cannot drive the voltage across the sample to 5 volts and still have $R_S >> R_J$ as required for a current source (see the section on the description of the ramp circuit). Thus, one does not, in general, bother tuning this range.

The next series of steps involve tuning the A_L amplifier; see Fig. A16 to locate that section on the board, and Fig. A19 for details. The same program can be used for this section.

(1) Type EXE 4 to start the program, and set the DAC's to zero output.

(2) Using the DVM with clip leads, measure the voltages at U101 pin 7 and R103 pin 1. If the voltages are not the same, adjust the appropriate Op. Amp Offset Null pot until they are the same.

(3) Press button 6.

(4) Measure the voltages at R104 pin 1 and pin 3. These voltages should be exactly the same magnitude and opposite polarity. If they are not equal in magnitude, adjust the Inverter Balance pot until they are. This sets the gain of the inverter to minus one.

(5) For the next series of steps, the connections to the calibration box need to be modified. Take the cover off the Calibration Resistance box. Remove the "From Sample" cable and attach the cable that normally connects the DVM to the electronics. Plug the phono connector end into the Measurement Electronics "From

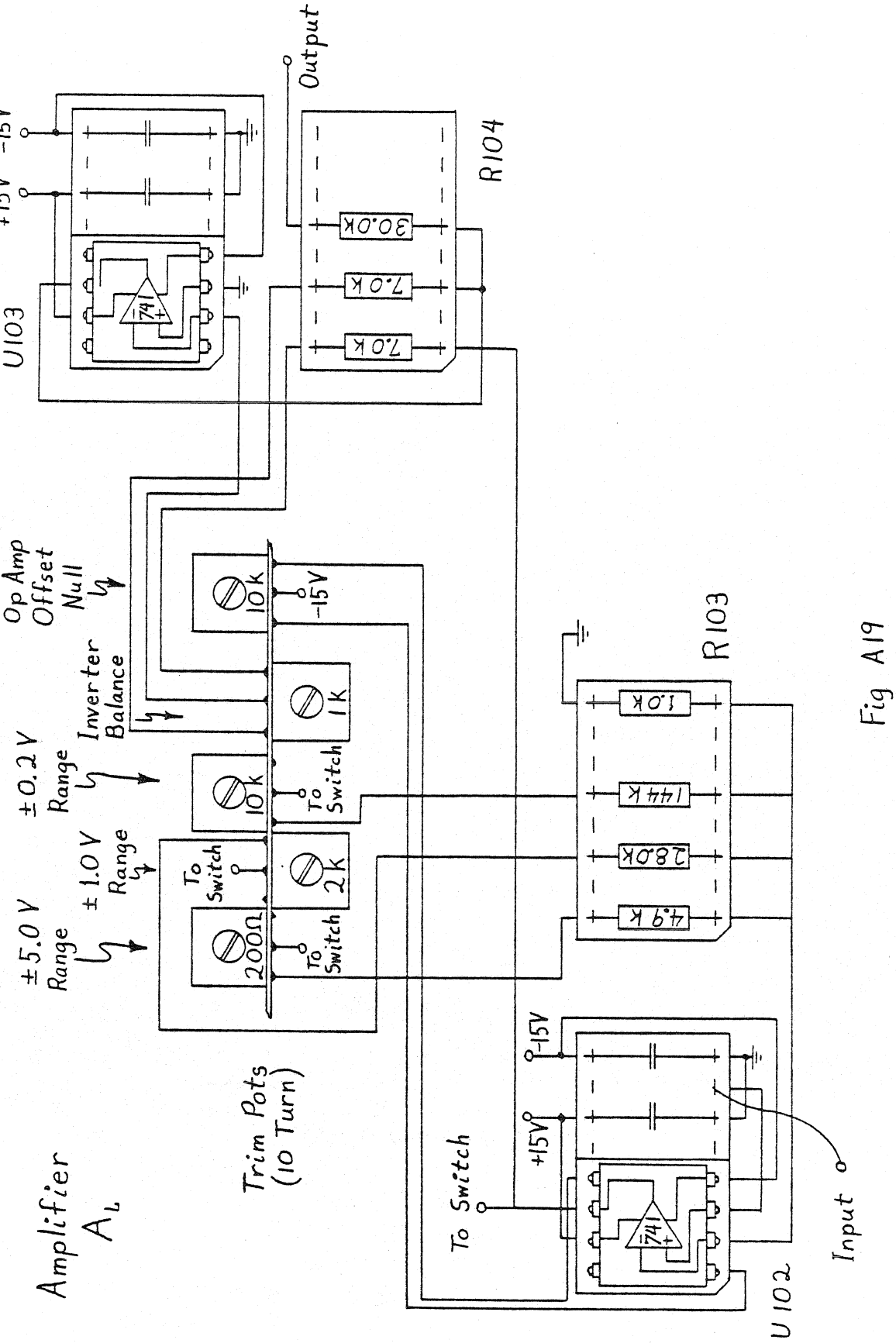
Amplifier
A_L
Trim Pots
(10 Turn)
To Switch
Input
U102
R103
R104
U103
Output
+15V
-15V
Op Amp
Offset
Null
Inverter
Balance
±0.2 V
Range
±1.0 V
Range
±5.0 V
Range
200Ω
2K
1K
10K
1.0K
144K
28.0K
4.9K
7.0K
30.0K
741

Fig A19

Sample" socket and attach clip leads to the banana plug end. Attach these clips to either side of the first 50 Ω precision resistor on the rotary switch, as shown in Fig. A20. Set the Calibration Box switch to 50 Ω. Attach the DVM clip leads to the same points, and press the GUARD button near the DVM inputs (it should now be out). Make sure there are no shorts between any cables and the box (ground).

(6) Set the Range switch to 0.2; the DVM should read near 0.2 volt.

(7) Change the potentiometer on the calibration box. The indicated voltage should not change when the pot is varied. If it does change, adjust the trim pot labeled ± 0.2 V Range (Fig. A19) until there is no change in voltage as the Calibration Box pot is varied over 10 Ω.

(8) Set the Range switch to 1.0 and repeat step seven, adjusting the ± 1.0 V Range trim pot.

(9) Again, the 5.0 volt range is not used so it need not be calibrated.

(10) To be safe, one should go back to the previous segment and check the calibration of A_H even though calibrating A_L should not have affected A_H.

(11) One may now put the Calibration Box back together; plug the From Sample cable back in and depress the DVM GUARD button so it is again in.

The only segment remaining deals with the setting of the Narrow DAC Range trim pots. For this, a new program is needed to switch the Narrow DAC, but the overall procedure is basically the same.

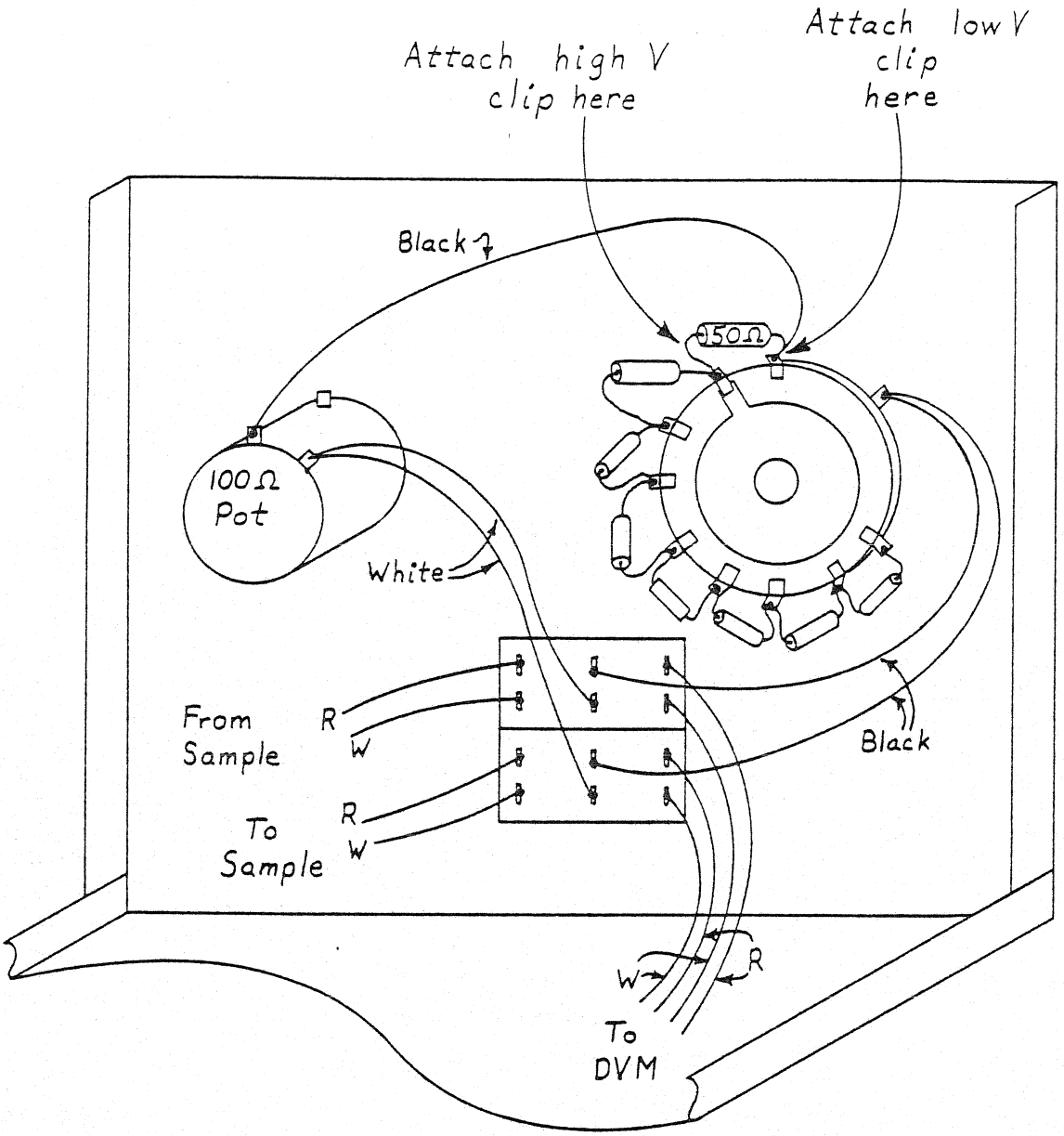

This corresponds to:

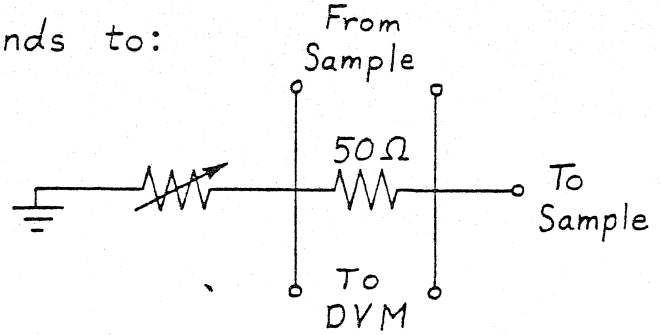

Fig A20

(1) Type in the following:

```
S:R   1;2
P:N   4
P:A   4;15
STA   4
S:F  74
S:D  19;0
LOO   0;10
W:S   6
I:D  19;1000
W:S   7
I:D  19;-1000
CON   0
END
EXE   4
```

(2) Plug the DVM into the DVM MOD socket.

(3) Set the Range switch to ± 1; the DVM should read near zero volts DC. Record this voltage, v_{Low}.

(4) Press button 6. The new voltage should be near 1 volt; call this v_{High}. For this relay setting, $v_{High} - v_{Low}$ should be <u>exactly</u> 1 volt; if not, adjust the pot labeled 100% (Fig. A21).

(5) Press button 7 to reset the Narrow DAC to zero, and recheck v_{Low}.

(6) Repeat steps (4) and (5) until $v_{High} - v_{Low}$ is <u>exactly</u> 1 volt.

(7) Next, type:

```
C:R   1;2
S:R   2;2
```

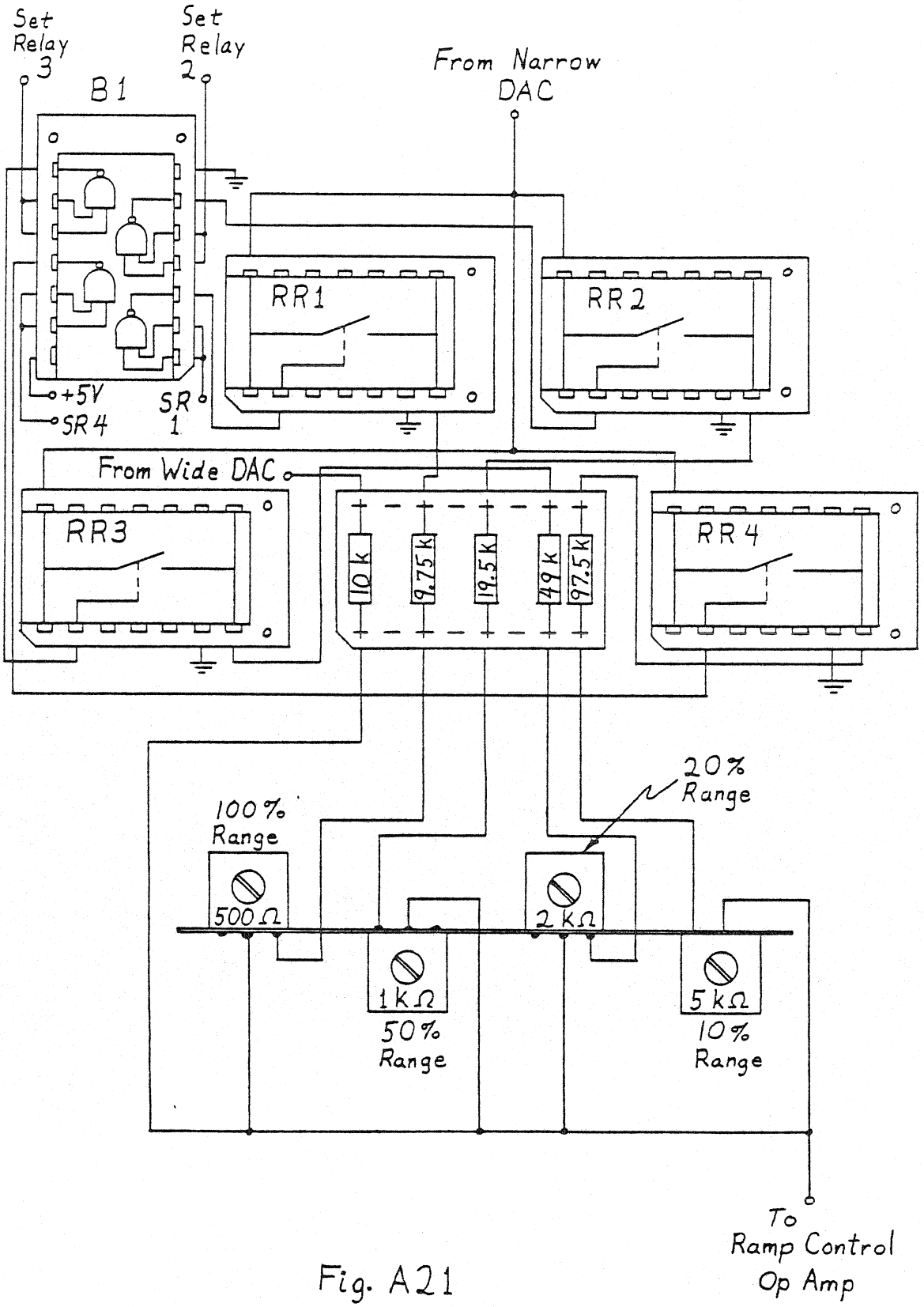
Set Relay 3
Set Relay 2
B1
From Narrow DAC
RR1
RR2
+5V
SR 4
SR 1
From Wide DAC
RR3
10 k
9.75 k
19.5 k
49 k
97.5 k
RR 4
20% Range
100% Range
500 Ω
2 kΩ
1 kΩ
50% Range
5 kΩ
10% Range
To Ramp Control Op Amp

Fig. A21

(8) With this relay setting, again using buttons 6 and 7 to switch between V_{High} and V_{Low}; the difference $V_{High} - V_{Low}$ should be set to <u>exactly</u> 0.5 volt by adjusting the trim pot labeled 50%.

(9) Type:

C:R 2;2

S:R 3;2

(10) Repeat step (8), setting $V_{High} - V_{Low}$ to 0.2 volt by adjusting the 20% pot.

(11) Type:

C:R 3;2

S:R 4;2

(12) Repeat step (8) again, setting $V_{High} - V_{Low}$ to 0.1 volt by adjusting the pot labeled 10%.

Remember, if the program stops before the calibration has been completed, simply type EXE 4 to re-execute.

This completes the standard testing and calibration procedures for the Ramp Control Circuitry.

(d) <u>ADC Circuit</u>

The Analog-to-Digital Converter circuit is quite straightforward to tune. This procedure consists of presenting two precise voltages to the input to the ADC and adjusting the trim pots to set the binary output to the correct values. One may, at the same time, check the operation of the optical isolators; however, their limits of operation are not so demanding as in the Ramp circuit.

To set the ADC properly, one needs a very stable DC voltage source

that can be set to a given voltage between -10 and +10 volts, with better than 1 mV accuracy. The ADC used (Analog Devices ADC-12QZ) is wired to convert any voltage between -10 and +10 volts to a binary number. There is an input voltage that corresponds to a change of the least significant bit (LSB) of the output, i.e., $20/2^{12}$ = 4.8 mV = LSB. One wants to adjust the "Zero" pot so that the ADC is just switching from 000000000000 to 000000000001 when $-10 + \frac{1}{2}$ LSB = -9.9976 V is presented at the input. One then wants to adjust the "Gain" pot so the output is just switching from 111111111110 to 111111111111 when $+10 - \frac{3}{2}$ LSB = +9.9927 V is fed to the input.

To proceed with the calibration, one must remove the ADC unit from the rack and remove the cover. The power and computer cables must be left connected. Figure A22 presents the layout of the ADC board.

(1) Enter the following short program on the computer:

```
S:R   1;2
F:O   4;74
F:A   1;1
P:A   4;10
STA   4
S:F  74
S:D  19;0
W:S   6
W:S   7
LOO   0;200
R:A  16;10
CON   0
END
EXE   4
```

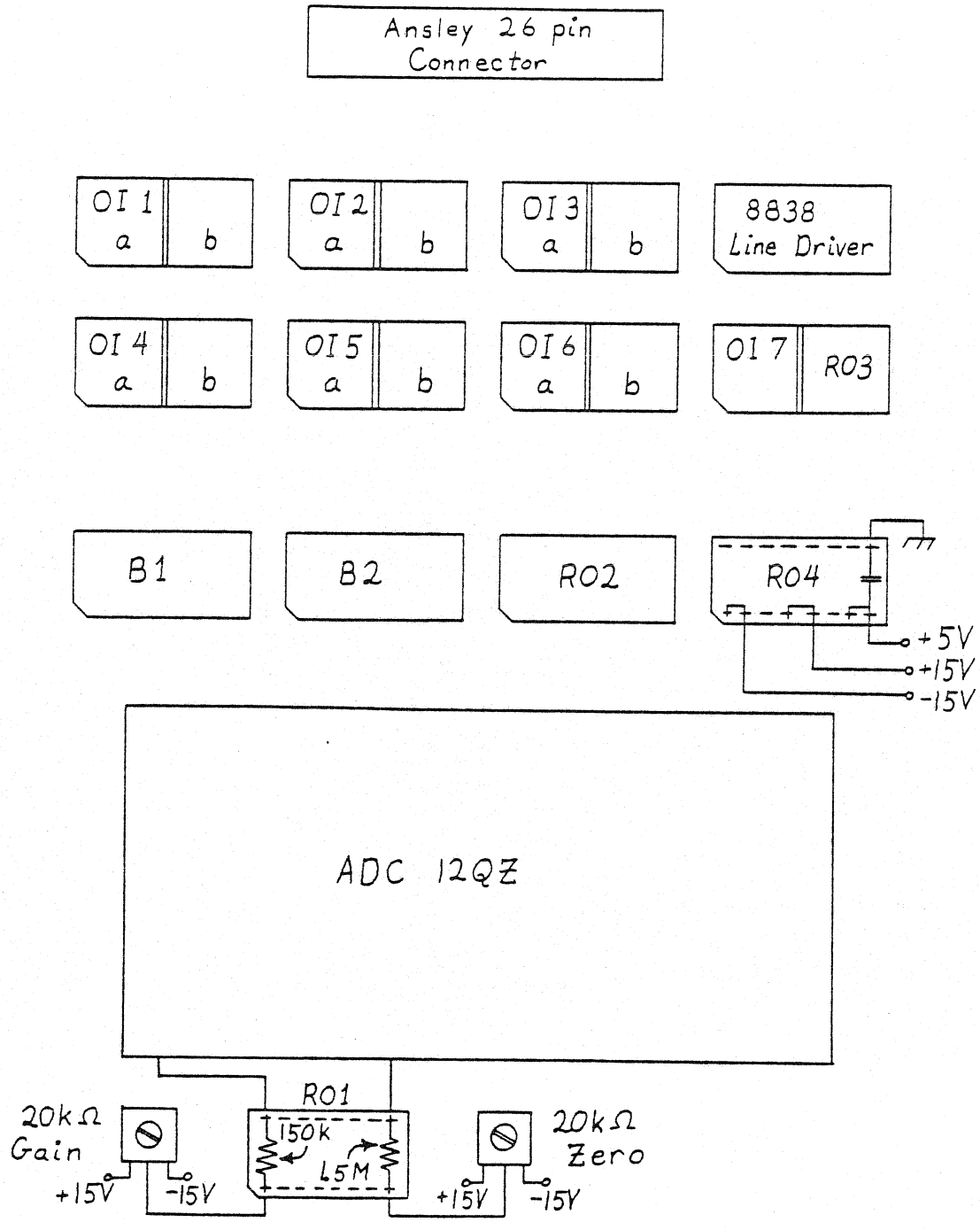
Ansley 26 pin Connector
OI 1 a b
OI 2 a b
OI 3 a b
8838 Line Driver
OI 4 a b
OI 5 a b
OI 6 a b
OI 7
RO3
B1
B2
RO2
RO4
+5V
+15V
-15V
ADC 12QZ
RO1
150k
1.5M
20kΩ Gain
+15V
-15V
20kΩ Zero
+15V
-15V

Fig. A22

This program simply has the computer continually send convert commands to the ADC for about ½ hour after buttons 6 and 7 are pressed sequentially.

(2) Set the voltage source to -9.9976 V using the 5½ digit DVM to check. Connect this voltage to the input to the ADC unit.

(3) Press buttons 6 and 7.

(4) Use the DVM with small clip leads to check the voltages at pins 2, 3, 5, 11, 13 and 15 of both B1 and B2. All voltages should be less than 0.8 volt (zero) except pin 15 of B2 (LSB). Leave the DVM connected to this pin and adjust the "Zero" trim pot until the indicated voltage is just switching from a zero (less than 1 V) to a one (more than 2 V).

(5) Reset the voltage source to -10.000 V so that all ADC output bits are zero.

(6) Measure the voltages at pins 10 and 15 of Optical Isolator sockets 1 through 6. If any voltage is greater than 0.8 volt, replace the corresponding isolator.

(7) Reset the voltage source to +9.9927 V.

(8) Again measure the voltages at pins 1, 3, 5, 11, 13 and 15 of B1 and B2, or at pins 2 through 7 and 10 through 15 of RO2. All voltages should be greater than 2 volts except, possibly, pin 15 of B2 (or pin 15 of RO2). Leaving the DVM attached to this pin, adjust the "Gain" pot until the voltage is just switching from a zero (less than 0.8 V) to a one (greater than 2V).

(9) Increase the output of the voltage source to 10.000 V so that all outputs of the ADC are logical ones.

(10) Remeasure the voltages at pins 10 and 15 of Optical Isolator sockets 1 through 6. If any voltages are less than 2 volts, replace the isolator. Then recheck its operation for a logical zero input [steps (5) and (6)].

(11) Type:

```
F:0   4;
ABO   4
```

to stop the program.

This completes the calibration and tuning operations for the IETS Measurement Electronics. The electronics should now be optimized and capable of accurately controlling the acquisition of inelastic electron tunneling spectra.

A. III. IETS Measurements Procedures

This section will discuss how the computer and electronics may best be used in obtaining inelastic electron tunneling spectra. It will be assumed that the operator has a working knowledge of POL; however, this is not necessary for the understanding of the basic principles. There are three topics that will be discussed here. The first concerns how the various measurement system parameters are chosen to suit best the spectra to be recorded. The second topic discusses how the measurement programs are structured. The last segment outlines the procedure for setting up the tunneling samples and electronics in preparation for measurement, as well as the actual recording of the spectra.

Many considerations must be taken into account when planning a tunneling measurement. These considerations will determine the various settings of the electronics and the details of the program to be used in obtaining the spectrum.

The first thing to be decided is whether the measurement is to be a first or a second derivative. A first derivative is only taken if one is planning to calibrate an already measured second derivative spectrum and will depend on the details of that second derivative measurement. For this reason, second derivative measurements will be discussed first and then the measurement of first derivatives will be addressed.

Deciding on a second derivative fixes four things:

(1) The frequency of the sine wave generator (47.23 kHz);

(2) The setting of the derivative selector switch d^2I/dV^2 ;

(3) The setting of the Frequency Doubler switch (Second Harmonic); and

(4) The details of the cabling of the electronics.

The next three items to be determined are concerned with that segment of the spectral range one wishes to record and the fineness of the scale between datum points within the spectrum. In other words, one wishes to decide on the starting voltage, the voltage range to be measured, and the increment between successive datum points.

In general, the voltage range of interest will lie between 30 meV and 500 meV. Below 30 meV, the phonon structure of the metal electrodes overwhelms any molecular vibrational features which may be present. At the high energy end, 500 meV lies above the highest fundamental vibrational levels generally seen (the OH stretching mode at 450 meV). It is possible to detect overtone and combination bands at higher energies, however. The exact range chosen for measurement will depend on the particular vibrational modes one wishes to investigate. An overall scan is usually made covering the entire 30 to 500 meV range. This "wide scan" serves both to check the overall quality of the particular junction and to aid in deciding upon which segments of the spectrum are worthy of more detailed study. For the more detailed spectra, the range is chosen to include some baseline in addition to the structures of interest. The baseline is necessary for determining peak shapes and accurate peak positions.

The step size is chosen in accord with the desired resolution. There is a lower limit to the resolution one may attain. Both thermal and modulation effects will broaden the tunneling peaks. The thermal effects are due to the smearing of the Fermi levels of both metal electrodes at

finite temperatures. If both metals are normal (as opposed to superconducting), this would correspond to 5.4kT, or 1.95 meV at 4.2K. The lead electrode is actually a superconductor at this temperature which reduces this broadening to some extent. Modulation broadening, as the name implies, is broadening of the tunneling structure due to the finite amplitude of the applied modulation voltage. This contributes $1.22v_w$ to the peak width. In general, at 4.2K with a 1 meV modulation a 1 meV wide peak will be broadened to 2.5 meV so that a step size of 0.5 meV will be small enough to take advantage of the available resolution. For very detailed scans over narrow ranges with lower modulation amplitudes smaller step sizes may be desirable. A step of 1 meV is adequate for the wide scan since less detail is necessary.

One uses this starting point, range and increment information to determine the settings for the Range switch and the narrow DAC relay. Since the voltage range of interest will lie between 30 and 500 meV. the most convenient Range setting is $\pm$ 1 volt, which allows the wide DAC to be set (with the S;D 19;x command, where x is in volts) anywhere between zero and + 1 volt (the S:D command signals an error if one tries to set the DAC to negative voltage). The step size and spectral range determine the necessary narrow DAC range which is determined by the S:R a;b setting. The S:R 1;2 setting provides a narrow DAC range of -1 to +1 volts with a minimum step of 1 meV. S:R 2;2 has a range of $\pm$ 500 meV with a minimum step of 0.5 meV; S:R 3;2 gives a range of $\pm$ 200 meV with a minimum step of 0.2 meV; and S:R 4;2 has a range of $\pm$ 100 meV with a minimum step size of 0.1 meV. Thus if one wishes to scan over 250 meV with increments of

0.1 meV one would need to record three scans using the relay setting 4;2, whereas, if a 0.5 step size is adequate, then one can measure the entire range in a single scan using the S:R 2;2 setting.

The next thing one must decide upon is the modulation amplitude to be used in the measurement. One must balance two competing considerations, signal-to-noise and resolution. Larger modulation amplitudes enhance the signal-to-noise but decrease the resolution (as described above). For the wide scans, where only qualitative information is desired, a 2 meV rms modulation is a good compromise; whereas for more detailed spectra where high resolution is desired, modulations of 1 meV rms and below are used. In general, the quality of the junction (signal-to-noise) and maximum sensitivity of the lock-in amplifier (100 neV) place a lower limit on the useful modulation voltage for any given junction.

The final three parameters to be decided upon before a measurement program may be written are the following: (1) Whether to measure the spectrum once or scan the spectrum several times and average the scans together; (2) The lock-in time constant to be used; and (3) The total measurement time. These three parameters are closely tied together and so must be considered simultaneously.

Rapidly scanning a spectrum many times and then averaging all the scans together to obtain a final spectrum has definite advantages in reducing certain types of noise [See the paper "Combined Use of a Lock-in Detector and a Multichannel Analyser for 1/f Noise Application to Tunneling Spectroscopy", A. Leger, B. Delmas, J. Klein and S. DeCheveigne, Revue de Physique Appliquee 11, 309 (1979)]. However, POL, as it

presently exists, is very cumbersome for scanning a spectrum more than approximately ten times. Theoretically, by measuring at 16 m sec per point, POL will automatically add scans into a single file; however, when this is attempted the computer "crashes", and all that had been stored in core is lost. As the system presently exists, 0.5 second per point is the minimum measurement rate. Rates faster than this interfere with the operation of the EEL spectrometer.

In order to measure a spectrum several times, each scan must be stored in a separate file until the program completes. The operator must then add these files together to obtain the final spectrum. Since there is space in core for only about 5000 data points at one time and three experimental stations use the computer simultaneously, there is a limit to the number of times a spectrum may be scanned in a single program. Five scans of 500 points each are, usually, a reasonable upper limit. This program may be rerun to obtain additional scans.

The lock-in time constant and the time that the computer measures each datum point are closely related. It is best to measure for a period just longer than the indicated time constant; for example, if the time constant is set for 1 second, one should measure each point for 1.2 seconds. One should also consider the number of scans to be made and the total time one wishes to spend measuring the complete spectrum. If several tunnel junctions are to be measured, it is best not to spend more than one hour on each spectrum. Wide scans shouldn't take more than 10 to 20 minutes. However, for the occasional very high resolution spectra, two to three hours measurement time may be necessary for

a single spectrum. For these long times, multiple scans are important in reducing the very low frequency components of the noise (commonly referred to as baseline drift).

The final items which need to be found are the energies of the most probable minima and maxima of the tunneling spectrum in the range to be measured. For a wide scan (30 to 500 meV) of a standard aluminum - aluminum oxide - lead tunnel junction, three important minima occur at the starting voltage (30 meV), 60 meV and 140 meV. The three highest points in the spectrum of a clean junction occur at 117 meV, 450 meV and the highest voltage (500 meV). If an adsorbate is present in the junction, additional maxima may need to be taken into account. For example if CH groups are present the (often very intense) C-H stretching mode at 360 meV may give the highest overall point in the spectrum. For the more detailed narrow range spectra the wide scans should be used to find the local minima and maxima. These parameters are necessary for finding the optimum sensitivity and zero offset of the lock-in amplifier when making the actual measurement, as will be discussed later in this section.

With the above information, one may now plan the spectra to be taken and write the necessary measurement programs. In addition, one has determined the amplitude of the modulation to be applied during the measurements, and the settings for the Range switch, lock-in time constant and relay.

The measurement programs are written in Peripheral Oriented Language (POL). There are, however, a few preliminary points regarding POL which need to be discussed which are not described in the POL manual. First is the set relay command, discussed above; S:R a;b, a = 1 to 4, determines

the range of the narrow DAC with respect to the range of the wide DAC and b = 1 to 3 specifies the position at which the Range switch has been set. When POL is started, all relays are cleared, so the operator may simply use the S:R command to set the desired relay. However, if a different relay setting is desired, the initial relay must be cleared before the second one is set. The C:R a;b (or C:R a;) command opens relay a. For example, if one initially has set S:R 1;2, one must type C:R 1;2 before typing S:R 2;2 to switch the relay setting from 1 to 2. The DAC commands, file heading information and graphics routines all require that the relay be set correctly.

The next points concern the IETS DAC commands. Number 19 references the tunneling DAC's. The S:D 19;v sets the wide DAC to the value v, where v is in volts. The I:D 19;i increments the narrow DAC by the amount i, where, in this case, i is in millivolts. Thus, S:D 19;0.5 will set the wide DAC to 500 meV while I:D 19;05 will increment the narrow DAC by 0.5 meV.

The tunneling ADC is referenced by number 16, so R:A 16;1.5 would read the ADC for 1.5 seconds.

The IETS system uses switches 6 and 7 in the W:S commands.

Finally, the commands DAOFF, DAEXP and OFFSET do not function correctly with tunneling data files. An error message is not flagged if they are used even though the resulting manipulation will not be what had been specified in the command.

The measurement program can be broken up into two sections. The first section enables the operator to adjust the electronics to the

particular junction to be measured, while the second section records the actual spectrum.

The first section of the program sets the ramp voltage to various values which allow the operator to optimize the electronics to the resulting signal levels. The details of how the electronics are adjusted will be discussed later. The program should first set the ramp to the maximum voltage to be reached in the measurement. This allows the operator to set R_s. After button 6 is pressed, the ramp is reset to a voltage near the center of the spectral range. At this point, the operator sets the modulation amplitude and tunes the lock-in to obtain a maximum response. When button 7 is now pressed, the program steps through all the primary minima and maxima which might be encountered in the spectrum, waiting three seconds at each point and ending at the maximum voltage. This helps the operator adjust the lock-in sensitivity and zero offset to obtain a maximum deflection. The entire process is then repeated three or four times so that final adjustments can be made.

The following is an example of the first section of a wide scan.

```
STA    4        Begins storing the program
S:F    74       References a dummy file
S:D    19;.5    Sets ramp to the maximum voltage
W:S    6        Waits until switch 6 is pressed
LOO    o;3      Cycles through the following sequence 3 times
S:D    19;.25   Sets ramp to mid voltage
W:S    7        Waits until switch 7 is pressed
```

```
S:D     19;.03
W:C     3
S:D     19;.06
W:C     3
S:D     19;.117
```

Sets the ramp to the various minima and maxima, waiting 3 seconds at each voltage step

```
W:C     3
S:D     19;.14
W:C     3
S:D     19;.36
W:C     3
S:D     19;.45
W:C     3
S:D     19;.5
```

Sets the ramp to the various minima and maxima, waiting 3seconds at each voltage step.

```
W:S     6       Waits at 0.5V until switch 6 is pressed
CON     0       Closes loop, after three cycles the program proceeds to
                the actual measurement.
```

In the measurement segment of the program, the ADC is read for the desired time period and the datum point recorded in the specified file. The ramp is then incremented by the desired amount and the ADC read again. This is repeated until the entire spectrum is recorded. This process is implemented by a simple loop as shown in the following example, again using the wide scan.

```
S:F     75      Specifies the file in which the data are to be stored
S:D     19;.03  Sets the ramp to the initial voltage
W:C     10      Waits 10 seconds for the electronics to settle
```

```
LOO    0;470
R:A    16;1.2
I:D    19;1
CON    0
```

Measures each of 470 data points for 1.2 seconds with 1 meV increments between points.

If multiple scans are desired, one simply includes an additional loop. The following illustrates this, assuming file 74 is referenced in the first segment of the program.

```
LOO    0;5
I:F    1
S:D    19;.03
W:C    10
LOO    1;470
R:A    16;1.2
I:D    19;1
CON    1
CON    0
```

This measures the same spectrum as in the previous example, but here the spectrum is recorded five times with the five scans being stored in files 75 through 79.

As a final step in the program, one should reset the DAC to 0.03 volts. This low voltage puts less of a load on the electronics between measurements as well as lessening the chance of voltage spikes affecting junctions when the Sample Holder box selector switch is used.

In practice, a first derivative spectrum is measured in order to calibrate a given second derivative spectrum; and so the modulation amplitude, spectral starting voltage, range and voltage increment used to measure the first derivative should match those used with the second derivative. For the first derivative, the fundamental frequency is being

measured which gives a much greater signal than the second derivative. Thus the time constant and measurement time per point can be shorter and only a single scan is necessary. In general, a time constant of 0.3 second and a measurement time of 0.5 second per point is adequate.

The first derivative program has three sections. In addition to the set-up and measurement sections, there is also a calibration section in which known resistance and capacitance values are measured, which can later be used to calibrate the first derivative.

In the first section of the program, the ramp is first set to a mid range voltage, where the operator sets the modulation amplitude and tunes the lock-in to the fundamental frequency signal. Since the first derivative is a smoothly decreasing function the program need only step between the minimum and maximum ramp voltage to be encountered in the spectrum. The program should wait for a switch at each of these voltages, since the operator will have to note meter readings at each. The following illustrates this.

```
STA    4
S:F    74          References dummy file
LOO    0;3         Performs the following three times
S;D    19;.25      Set ramp to mid range
W:S    6           Wait for switch 6 to be pressed
S:D    19;.03      Set ramp to initial voltage
W:S    7           Wait for switch 7
S:D    19;.5       Set ramp to final voltage
W:S    6  }        Wait for switches 6 and 7
W:S    7  }
```

```
CON    0
```

The measurement segment of the program is essentially the same as for the second derivative. First, the file in which the data are to be stored is referenced, the DAC is set to the initial voltage, and some settling time is allowed. Then the ADC is read and the ramp incremented until the spectrum is scanned. The following is a typical example.

```
S:F    77          Reference data file
S:D    19;.03      Set ramp to initial voltage
W:C    10          Wait ten seconds
LOO    0;470   )   Record 470 data points measuring each for 0.5
R:A    16;.5   )   second with 1 meV increments between points.
I:D    19;1    )
CON    0       )
```

Unlike the second derivative measurement programs, the first derivative programs need a calibration section. The idea is that since the first derivative is proportional to the dynamic impedance of the tunnel junction, one should be able to use a "calibration box" (described earlier) to match the known calibration impedances to the measured junction impendance at several points spanning the verticle range of the first derivative spectrum. The digital volumeter is used to measure directly the actual resistance of the calibration box at these points. The calibration points can later be used to calibrate the vertical scale of the measured first derivative. Ten calibration points are measured and can be conveniently stored in the last ten slots of the same file which holds the spectrum itself (500 slots are allocated for the file

but only 470 data points are recorded for the spectrum). The calibration section of the program is, in itself, quite simple, as shown in the following example.

S:D	19;.25	Sets ramp to 250 meV, at which voltage all calibration points are measured.
S:S	490	Start storing the calibration points in slot 490 of file 77.
LOO	0;10	Ten points are to be measured
W:S	6	Wait until both buttons 6 and 7 are pressed before measuring a point
W:S	7	
R:A	16;.5	Read ADC for 0.5 second
I:S	1	Next point to be stored in the next file slot
CON	0	Closes the loop
S:D	19;.03	Resets ramp to 30 meV

One should now be able to write measurement programs to obtain first and, more important, second derivative inelastic electron tunneling spectra.

The next step in the measurement procedure is setting up the electronics correctly for the particular measurement to be made.

In the set up procedure to be outlined here, it will be assumed that second derivative spectra are to be measured first.

The first thing the operator must do is to check that the measurement electronics are hooked up correctly, as this will vary depending on the type of data to be recorded. Figure A23(a) presents the layout of the electronic components in the measurement rack; while Figs A23(b), (c) and (d) show the external cabling appropriate for measuring second

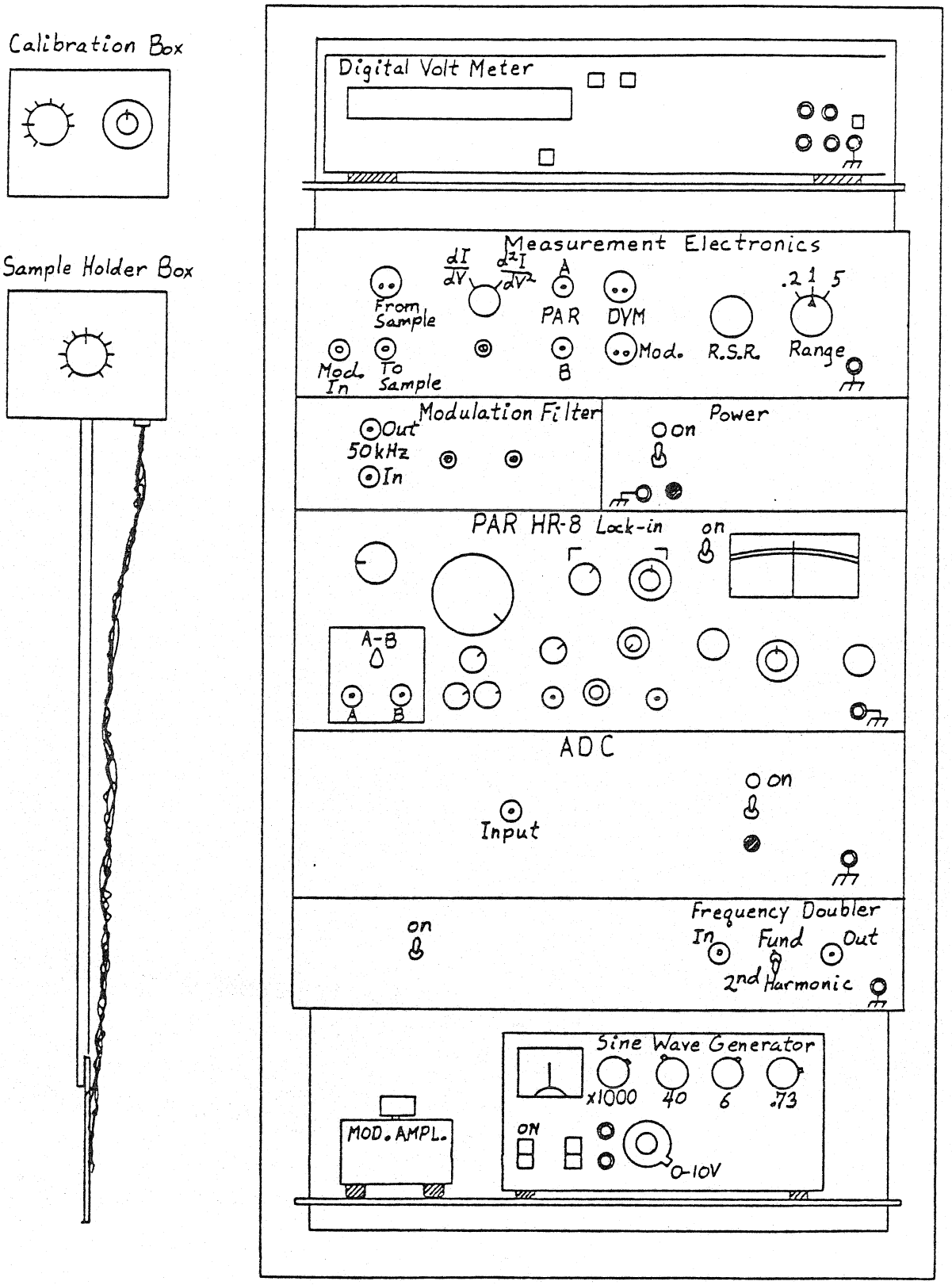
Calibration Box
Sample Holder Box
Digital Volt Meter
Measurement Electronics
dI/dV
d²I/dV²
A
PAR
DYM
.2 1 5
From Sample
Mod. In
To Sample
B
Mod.
R.S.R.
Range
Modulation Filter
Out
50kHz
In
Power
on
PAR HR-8 Lock-in
on
A-B
A
B
ADC
Input
on
Frequency Doubler
In
Fund
Out
2nd Harmonic
on
Sine Wave Generator
x1000
40
6
.73
MOD. AMPL.
ON
0-10V

Fig. A 23 (a)

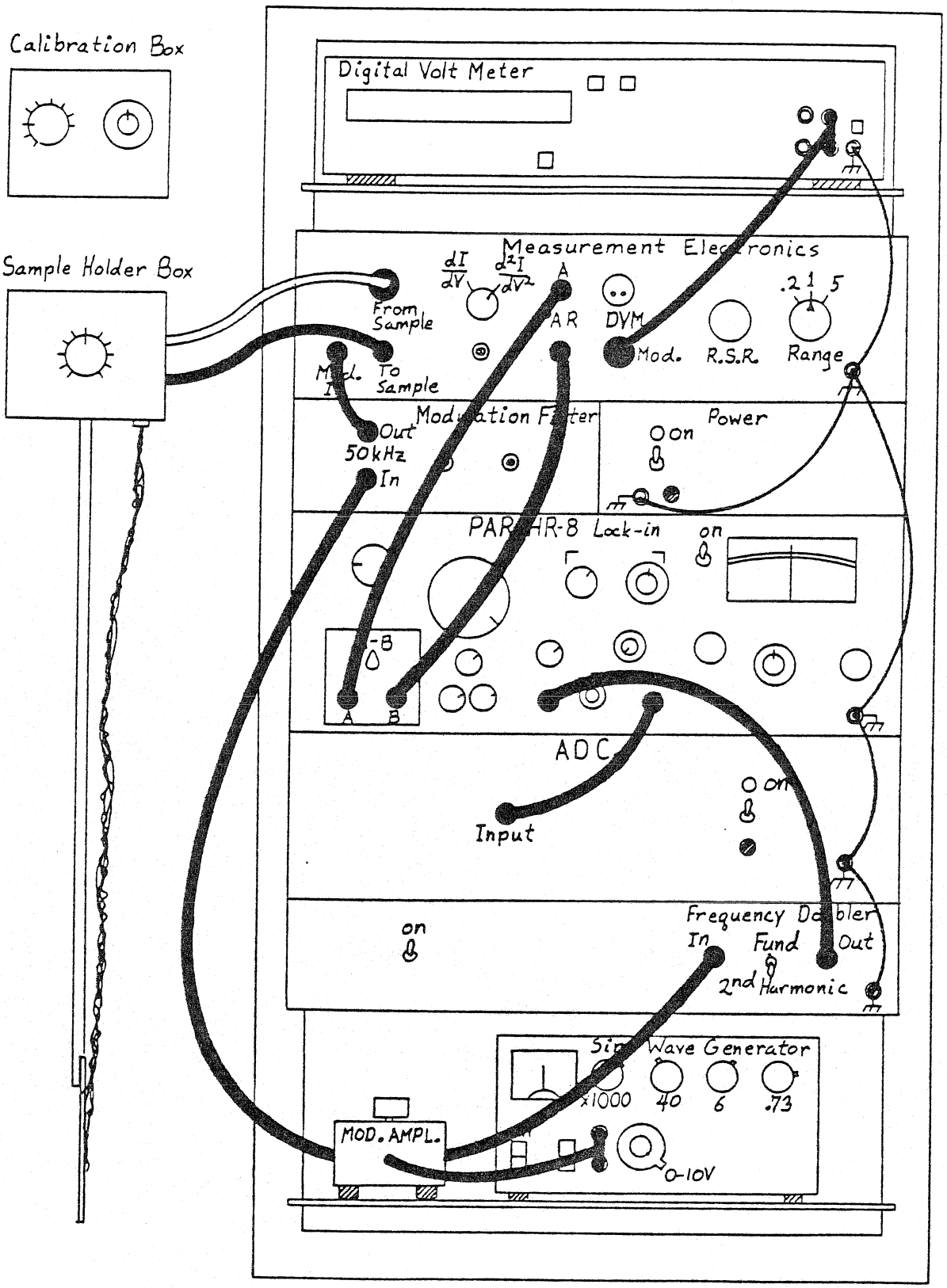
Calibration Box
Sample Holder Box
Digital Volt Meter
Measurement Electronics
dI/dV
d²I/dV²
A
R
DVM
Mod.
R.S.R.
Range
.2 1 5
From Sample
To Sample
Out
50kHz
In
Modulation Filter
Power
on
PAR HR-8 Lock-in
on
-B
A
B
ADC
Input
on
Frequency Doubler
In
Fund
Out
2nd Harmonic
on
Sine Wave Generator
x1000
40
6
.73
MOD. AMPL.
0-10V

Fig. A 23 (b)

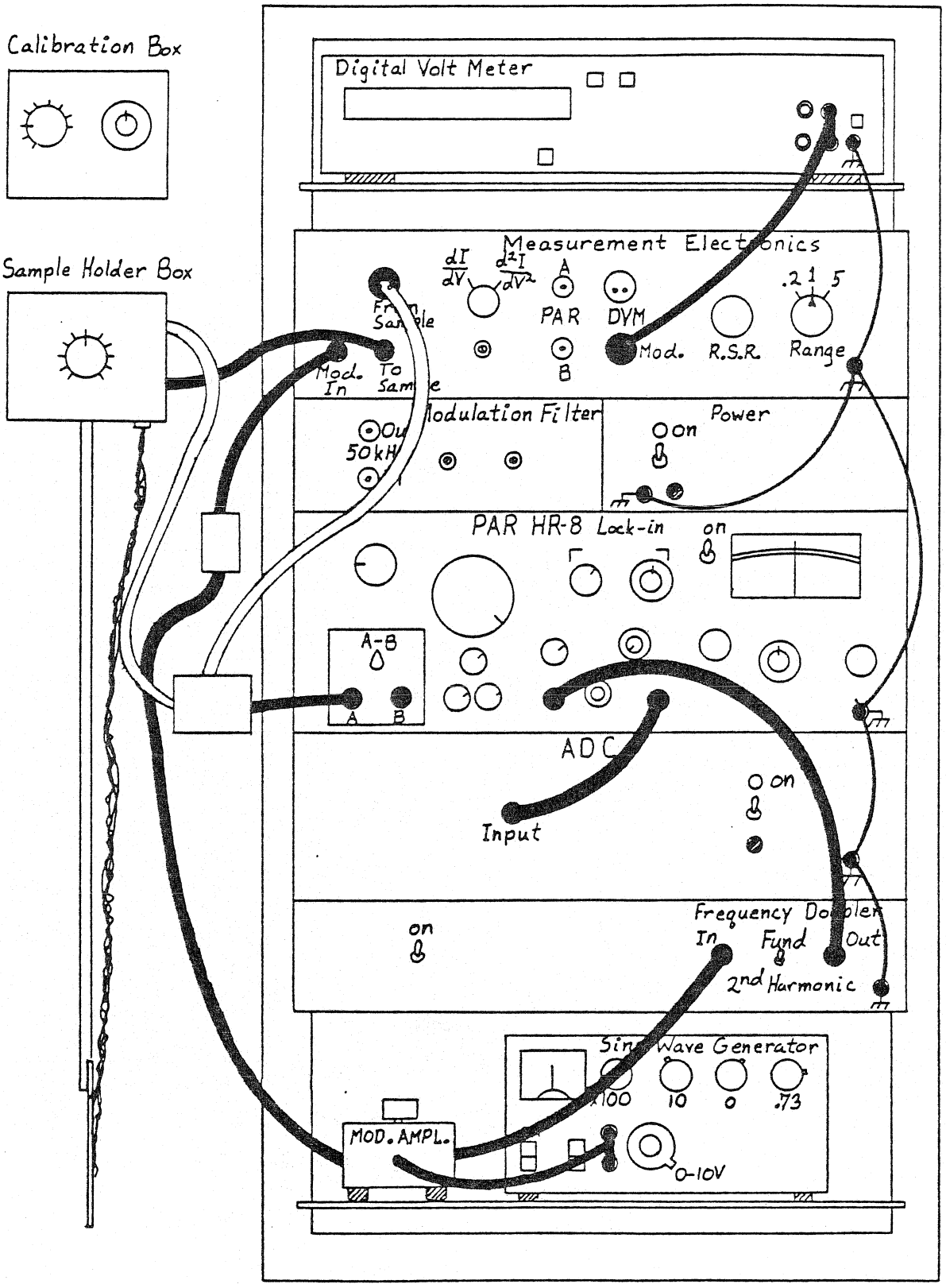
Calibration Box
Sample Holder Box
Digital Volt Meter
Measurement Electronics
dI/dV
d²I/dV²
A
B
PAR
DVM
Mod.
R.S.R.
Range
.2 1 5
Mod. In
To Sample
Modulation Filter
50kH
Power
on
PAR HR-8 Lock-in
on
A-B
A
B
ADC
Input
on
on
Frequency Doubler
In
Fund
Out
2nd Harmonic
Sine Wave Generator
100
10
0
.73
MOD. AMPL.
0-10V

Fig. A 23 (c)

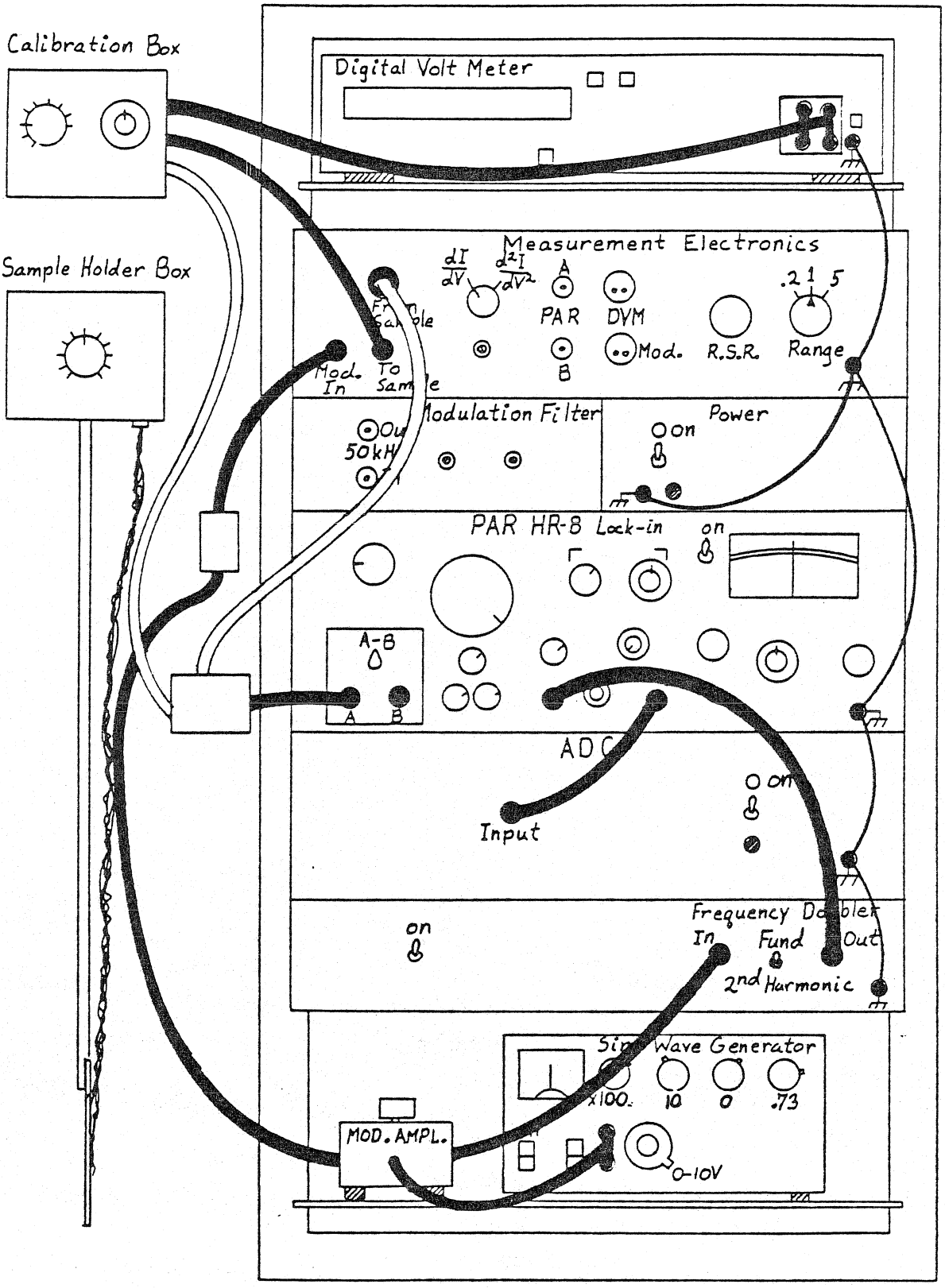
Calibration Box
Sample Holder Box
Digital Volt Meter
Measurement Electronics
dI/dV
d²I/dV²
A
B
PAR
DVM
Mod.
R.S.R.
Range
.21 5
Mod. In
To Sample
Modulation Filter
50kH
Power
on
PAR HR-8 Lock-in
A-B
A B
ADC
Input
Frequency Doubler
In
Fund
Out
2nd Harmonic
Sine Wave Generator
x100.
10
0
.73
MOD. AMPL.
0-10V

Fig. A 23 (d)

derivative, first derivative, and first derivative calibration data respectively. Since second derivatives are to be measured first, the external cabling should be arranged as illustrated in Fig A23(b).

All power switches should remain on to insure that the electronics will be warmed up and thermally stable.

In addition, one should check the following settings: On the Measurement Electronics panel, the derivative selector switch is on d^2I/dV^2, the Range switch is on the desired value (usually 1), the Ramp Series Resistor is set to its highest value (10kΩ). The switch on the Frequency Doubler panel should be set to Second Harmonic. The sine wave generator is set to 47.23kHz (since only the multiplier switch should ever be changed it is usually sufficient to check that this switch is set to x1000). The output of the oscillator is set to zero.

The computer should now be made ready. To start up the system, the following sequence is followed. The X-Y Plotter, Point plotter electronics, storage oscilloscope, Decwriter and PDP-11 computer are turned on. Next, the base 8 number 167700 is entered on the front panel address toggles of the computer, and the LOAD ADRS and START buttons are pressed. The Decwriter should then type RT-11SJ V02B-05 and a period.

On the same line as the period, the operator types R POL to enter POL. The relay can now be set and space assigned to the files to be used in the data acquisition and storage, for example.

```
S:R    1;2
F:O    4;74
F:A    1;1
```

```
F:O    4;75
F:A    5;500
```

This sequence sets relay 1, assigns one space to the dummy file, 74, and assigns 500 spaces to each of files 75 through 79. At this point, the ramp is still putting out too much voltage (due to how the DAC inputs are initialized when POL is started up). To remedy this, one enters and executes the following short program:

```
P:A    4;4
STA    4
S:F    74
S:D    19,.03
END
EXE    4
```

The computer will immediately type STOP 4. This simply resets the ramp to 30 meV.

Finally, one nulls this short program and assigns adequate space for the actual measurement program, which is then entered either through the Decwriter or through retrieval of the prewritten and stored program from the appropriate floppy disc.

The next step is the transfer of the desired samples from storage to the measurement system. The samples are stored in a liquid nitrogen storage dewar. For compactness, the sampleholder wires are folded into about a 10 cm loop which is tied with a short length of heavy wire; the sample holer is then stored in one of six numbered cylinders in the storage dewar. During the transfer and mounting, the samples themselves

must remain immersed in liquid nitrogen as much of the time as possible. To insure this, two dewars (about 7 x 30 cm) should first be filled with liquid nitrogen. The sample holder is then quickly transferred from the storage dewar to one of the small dewars. The samples (slides) must be below the nitrogen level but the wires should be untied and allowed to warm. One should not attempt to straighten the wires while the insulation is still at liquid nitrogen temperature or the insulation will crack. Both small dewars (with the samples) are now brought to the table beside the measurement electronics. The sample holder contact card is plugged into the socket in the sample holder box. The dewar containing the samples is now filled to within about 1 cm of the rim with liquid nitrogen from the second dewar. The sample holder box can now be positioned so that the far end of the phenolic rod just rests on the rim of the dewar containing the samples with the flat on the rod up, as shown in Fig A24. The samples themselves are attached to the rod by means of two 2-56 x 3/16" socket head screws; the slides (samples proper) must be positioned on the same side of the vector board as the phenolic rod, as shown. The sample holder wires should now be straightened out along the phenolic rod and the samples immersed in the small nitrogen dewar to precool as much of the rod and wires as possible before insertion into the liquid helium dewar. The cap on the helium dewar is removed and the samples quickly transferred from the nitrogen to the helium, being careful not to catch any wires on the narrow mouth of the liquid helium dewar. The samples are inserted into the helium dewar as far as they

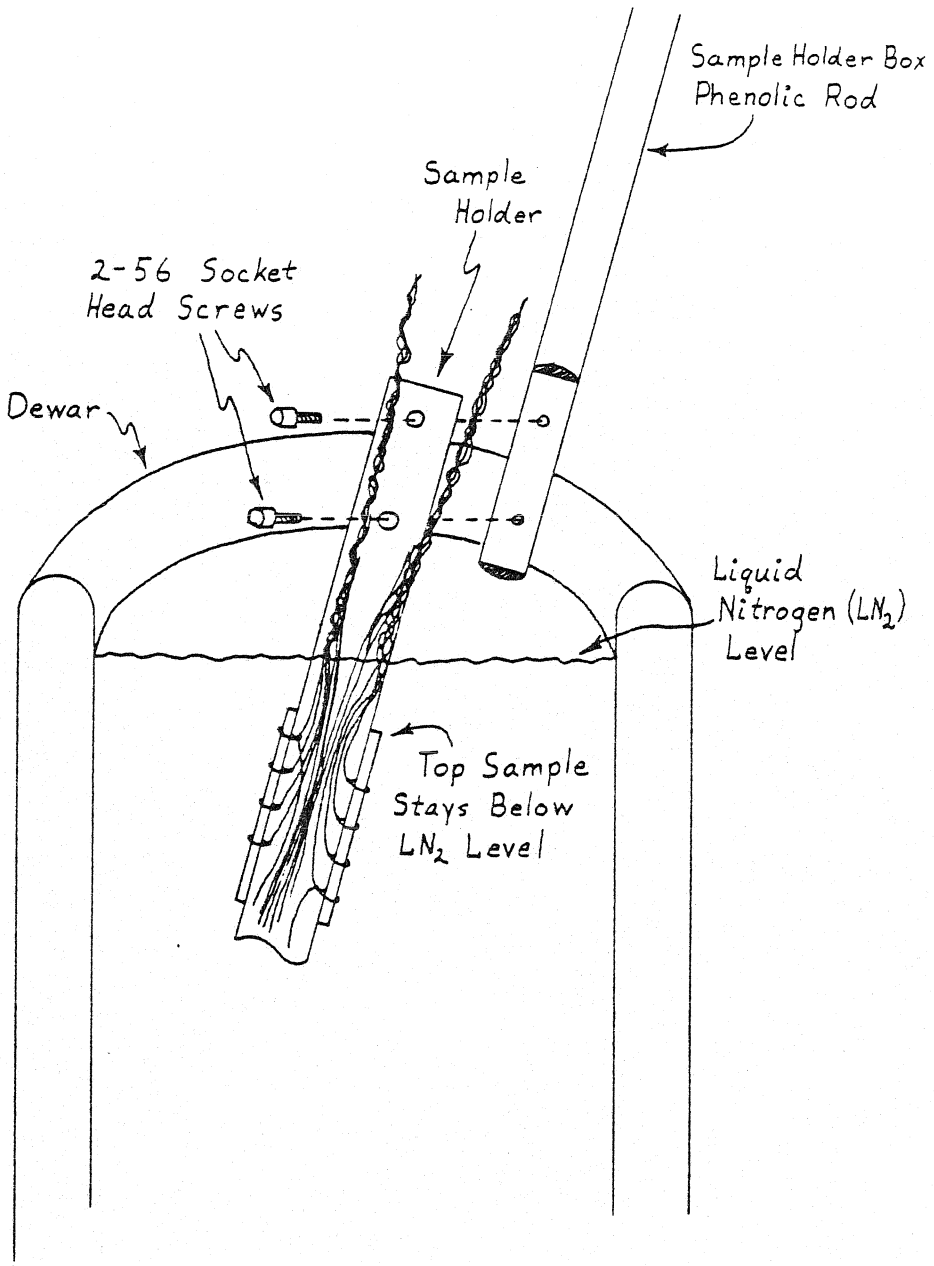
Sample Holder Box
Phenolic Rod
Sample
Holder
2-56 Socket
Head Screws
Dewar
Liquid
Nitrogen (LN_2)
Level
Top Sample
Stays Below
LN_2 Level

Fig. A24

will go and a cloth is wrapped around the mouth of the dewar and sample holder rod to provide some insulation.

The cables labeled "To Sample" and "From Sample" are now connected between the appropriate sockets in the sample holder box and the measurement electronics. The switch on the sample holder box is used to select the junction to be measured.

The DVM should be set to read DC volts on the AUTO range, and connected to the DVM MOD socket of the electronics. The DVM guard button should be in and the ground of the DVM connected to the ground of the electronics via a banana cord.

The system is now set to start the actual measurement procedure; the measurement program is executed.

The Ramp Series Resistor is switched to lower values until the DVM just reads the maximum voltage to be reached in the spectrum (switching the series resistor to lower values will not change this voltage reading, but the resistance should be as large as possible). When switch 6 is pressed, the ramp will change to a voltage near the middle of the spectrum range. The DVM is now switched to read AC volts. The meter will not read exactly zero; note this reading and call it v_o (v_o is usually around 0.15 veV). While watching the panel meter on the sine wave generator, increase the output of the generator until the meter reads just over half scale. The MOD AMPL pot is adjusted until the DVM reads the desired modulation voltage plus v_o. The lock-in amplifier is now tuned to the resulting second harmonic signal as described in the tuning section of this Appendix. In general, only the phase, sensitivity and zero offset

need to be adjusted between measurements. The complete lock-in tuning procedure only needs to be carried out about once a month unless first derivative spectra are also being measured. In this case the lock-in should be fully returned each time one switches between derivatives. Note that the lock-in meter deflection must be maximized to the left in the tuning. The lock-in time constant is left on 300 m sec, and button 7 is depressed. The program will now step through the minima and maxima of the spectrum. The deflection of the lock-in meter needle should span as much of the meter as possible without going off scale at any point. The lock-in sensitivity and zero offset should be adjusted to attain this and the program recycled through the minima and maxima to check the deflection.

Note that if the noise indicated by the meter needle (when the ramp voltage is fixed) is greater than 5 to 10% of full scale with the lock-in properly adjusted, then the resulting spectrum is likely to be too noisy to be usable.

When the program has cycled through the minima and maxima the prescribed number of times, the program is set to start measuring the spectrum. The time constant should be set to the desired value and the proper button pressed. The program will automatically enter the measurement phase.

One may monitor the progress of the spectrum as it is being recorded by "pushing" the appropriate data file onto the storage scope display stack, as described in the POL manual. As the file is pushed onto the scope, the x-axis runs from -1 to +1 volt. This must be modified by the

use of the X:M and X:E commands so that the range of the spectrum being measured covers most of the x-axis. The optimal values for these commands may easily be found. For the command X:M α, if X_o is the desired left hand edge of the x-axis, (in meV) then $\alpha = -\left[X_o + 1000\right]/20$, so if X_o = 20 meV $\alpha = -^{1020}/20 = -51$. For the X:E β, command, if the desired range is ΔX meV, then β = INT $\left[^{200}/\Delta x\right]$ (the parameter β must be an integer). Thus, for a wide scan (30 - 500 meV), X:M -51 and X:E 4 are used.

The range of the Y-axis covers the full scale deflection of the lock-in panel meter; 0% represents the right hand edge of the meter and 100% corresponds to the needle pointing to the left hand edge.

When the program has completed its run, the computer will type STOP 4.

If the spectrum is to be kept it should be immediately stored on floppy disc. If multiple scans were made, all the scans must be added into the appropriate file, and the sum stored on disc.

The spectrum may now be made ready for plotting. The point plotter will only plot what appears on the lower 3/4 of the storage scope display, so the spectrum must be moved and compressed or expanded until it utilizes that 75% most efficiently. The most useful commands are the Y:M and EXP commands, which are described in the POL manual. Since the Y:E command only takes integer values, it is of little use.

One may use the S:C and LIST commands to locate peak positions. However, due to drift and slight misadjustments of the electronics as well as effects due to the lead superconducting gap, the energy listed for a given datum point will not correspond to the exact voltage that was

applied to the junction when that point was measured. To obtain an accurate scale for the energy axis, one must measure the actual voltage which appears across the junction at several points along the x-axis. This can then be corrected for the energy gap of superconducting lead at 4.2K.

The following procedure will provide eleven check points. First the following program is entered;

```
STA    4
S:F    75
S:D    19;v_o          (where v_o is the appropriate initial voltage, e.g.,
                        0.03)
LOO    0;10
W:S    6
LOO    1;50
R:A    16;.2
I:D    19;v_i          (where v_i is the appropriate increment, e.g., 1)
CON    1
W:S    7
CON    0
S:D    19;.03
END
```

The DVM is set to read DC volts on the auto scale and is plugged into the MOD socket of the electronics. The modulation voltage is at zero, and the lock-in meter is centered. The zero offset is set to 2 (out of 100) with the toggle off (center position). The next several steps are then

followed:

(1) Execute the program.

(2) Record the DVM reading.

(3) Press button 6.

(4) Wait until the voltage stops, and record the DVM reading.

(5) Switch the zero offset toggle to the - (minus) side.

(6) Press buttons 7 and 6 in succession.

(7) Repeat step (4).

(8) Switch the zero offset toggle to its center (off) position.

(9) Repeat step (6).

(10) Repeat steps (4) through (9) until all 11 readings have been recorded.

This procedure will provide eleven voltages spaced by fifty increments each. Also if file 75 is plotted out, one will get a calibrated square wave pattern which can be directly compared to plotted spectra. To adjust for the lead superconducting gap, one simply subtracts 1.26 meV from all the measured voltages. The linearity of the energy axis should be quite good (less than ½% variation among the intervals measured above). With this information, one can determine quite accurately what energy corresponds to a given datum point in a file.

In order to measure first derivative spectra, the electronics must be modified somewhat. The derivative selector switch must be set to dI/dV, and the Frequency Doubler toggle set to Fundamental. On the sine wave generator the frequency multiplier switch is changed from X1000 to X100, the 0-100 dial is switched from 40 to 10, the 0-10 switch is changed from 6 to 0. The 0-1.2 setting is left untouched, since it

utilizes a continuous potentiometer which cannot be accurately reset without the aid of a frequency counter. To switch back to the modulation frequency used for second derivative measurements, the three switches are simply reset, respectively, to X1000, 40 and 6. The cabling must be altered to bypass the modulation filters. The input capacitor to the measurement electronics must also be bypassed while still completing the feedback loop required for the ramp control, as discussed in Appendix B. The overall cabling is shown in Fig. A23(c). The details of the wiring along with the two additional boxes are shown in Fig. A25. The box on the modulation cable consisting of a 100 kΩ resistor in series with a .001 μf capacitor simply serves to increase the output impedance of the modulation supply, better defining its constant current status. The second box couples the signal from the sample through a large (250 μf) capacitor directly to the lock-in preamp while also connecting the signal back to the Measurement Electronics to complete the ramp control feedback loop.

The desired junction is selected.

The first derivative measurement program is entered and executed.

With the ramp now set at mid voltage, the modulation voltage is set, as described for the second derivative. The lock-in must be tuned to the signal occurring at the fundamental frequency (now 1.1 kHz), as described earlier in this Appendix. The phase setting is locked in to prevent it from being accidentally altered, since the phase must remain the same through the calibration segment of the program.

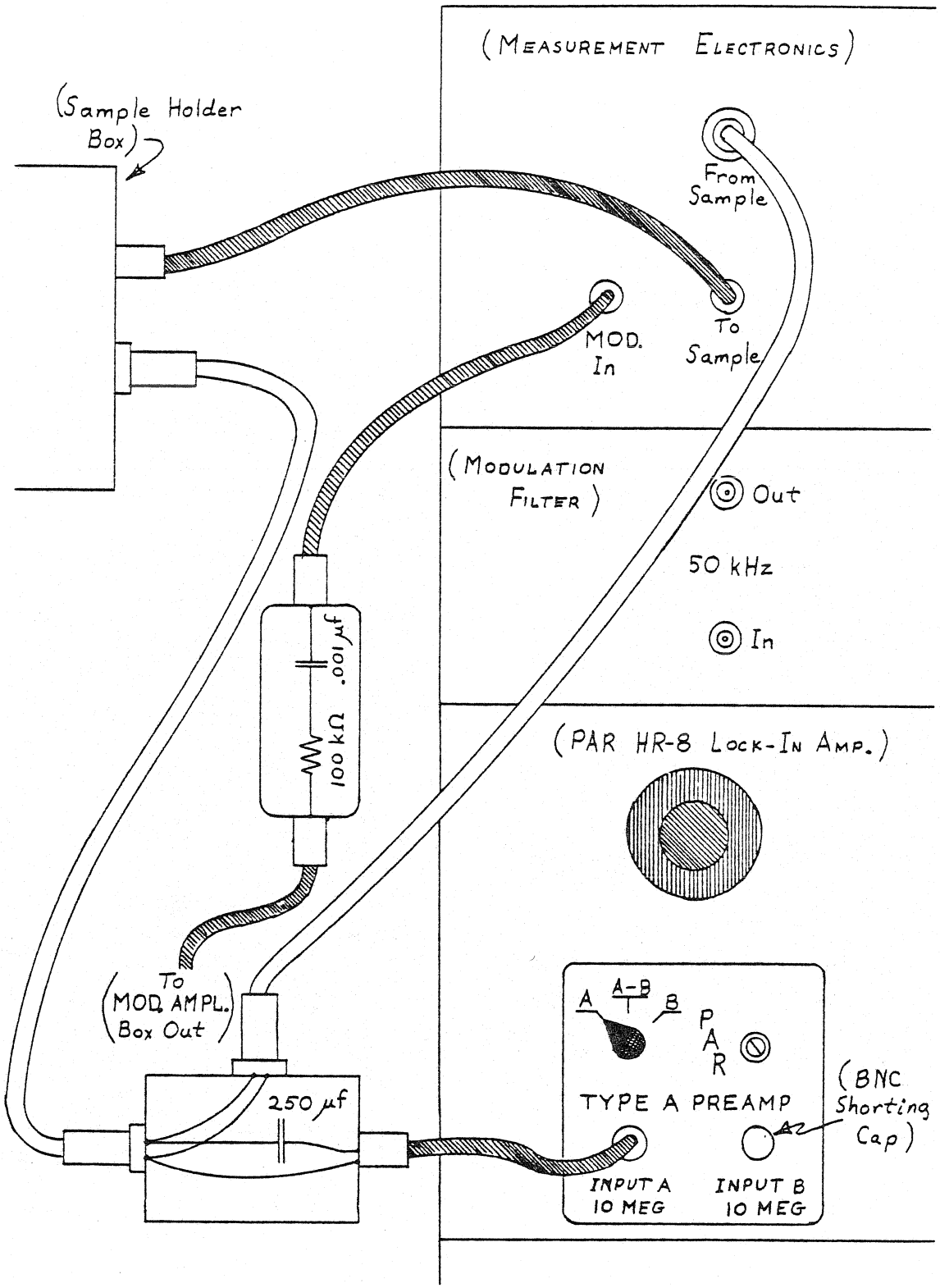
(Measurement Electronics)
(Sample Holder Box)
From Sample
To Sample
MOD. In
(Modulation Filter)
Out
50 kHz
In
.001 μf
100 kΩ
(PAR HR-8 Lock-In Amp.)
To (MOD. AMPL. Box Out)
250 μf
A
A-B
B
PAR
TYPE A PREAMP
(BNC Shorting Cap)
INPUT A 10 MEG
INPUT B 10 MEG

Fig. A25

When button 6 is pressed, the ramp is set to 30 meV. Button 7 then sets the ramp to 500 meV, and then when button 6 and 7 are pressed sequentially the ramp is reset to 250 meV (mid range). The sensitivity and zero offset are adjusted so that when the ramp is stepped between these voltages the lock-in meter deflection is a maximum without going off scale. When this is set, the zero offset knob is locked in position. The operator must carefully record the position of the lock-in meter needle when the ramp is at mid voltage, M_m, when the ramp is at the initial voltage, M_o, and when the ramp is at full scale, Mf. These will be needed in setting up the calibration box later.

After these voltages have been stepped through the appropriate number of times, the program automatically measures the first derivative spectrum, and then resets the ramp to mid voltage.

When the complete spectrum has been recorded, the calibration points must be taken. Detach the "To Sample" and "From Sample" cables from the same holder box and plug them into the appropriate sockets in the calibration box. Also, the four wire cable labeled "To DVM" on the calibration box must be plugged into the 4-wire ohms banana plugs of the DVM, as shown in Fig. A23(d). The DVM is set to read 4-wire ohms. The electronics are now set up to obtain the calibration points. The procedure used is outlined below.

(1) Set the calibration box toggle switch to "To Meas. Electronics".

(2) Set the calibration box resistance, R_c, to the junction resistance measured at the time of the sample fabrication; or, better, if the junction resistance was recorded for the samples cooled in liquid nitrogen, use that value.

(3) Adjust the calibration box capacitance, C_c, so that the lock-in meter reads a value near M_m.

(4) Adjust R_c so that the lock-in meter reads exactly M_m.

(5) Switch the lock-in 0^o - 90^o - 180^o - 270^o phase switch 90^o away from its present position and switch the zero offset toggle to its center (off) position.

(6) Adjust the capacitance so that the meter reads as close to zero center) as possible.

(7) Set the phase and zero offset switches back to their original positions.

(8) Repeat steps (4) through (7) until both in phase and quadrature readings are correct (i.e., M_m and 0 respectively). C_c is now set and need not be adjusted any further; record C_c.

(9) Adjust R_c so that the meter reads M_i.

(10) Switch the calibration box toggles to "To DVM" and switch the zero offset toggle to its center position.

(11) Record the resistance shown on the DVM, call it R_o.

(12) Switch the calibration box and zero offset toggles back to their original positions and wait for the electronics to settle (15-30 seconds).

(13) Adjust R_c to set the meter at M_f.

(14) Repeat step (10).

(15) Record this resistance, R_f.

(16) Find $(R_o - R_f)/9$; this is the resistance increment, R_i.

(17) Set R_c to R_f; note the actual resistance reading from the DVM.

(18) Repeat step (12).

(19) Press buttons 6 and 7 in succession to record the calibration point.

(20) Repeat step (10).

(21) Set R_c to $R_f + nR_i$ (where n = 1 through 9 for the remaining 9 points) and record the resistance shown on the DVM.

(22) Repeat steps (18) and (19).

(23) Repeat steps (10) through (22) until all calibration points are recorded.

If all ten calibration points have been taken correctly, the computer will immediately type STOP 4. The first derivative file may now be stored on disc. The spectrum itself is not worthy plotting out; however, one may find it useful to have the file displayed on the storage scope in order to follow the progress of the program.

This concludes the description of the inelastic electron tunneling spectroscopy measurement electronics. One should now understand: (1) The design and operation of the circuitry used; (2) How to tune the electronics to obtain optimum performance; and (3) How to use the electronics effectively to obtain IET spectra as well as first derivative and calibration data.

Appendix B

Inelastic Electron Tunneling Spectroscopic Calibration

APPENDIX B. Inelastic Electron Tunneling Spectral Calibration.

The measurement electronics used by this group (and by most other groups doing IETS) produces a spectrum which is proportional to d^2V/dI^2 as a function of the voltage drop across the junction. This can be easily understood by noting the fact that the ramp and modulation sources are constant current sources. Thus, the resulting voltage drop may be expanded in a Taylor series,

$$V(I_o + \delta I \cos\omega t) = V(I_o) + \left(\frac{dV}{dI}\right)_{I_o} \delta I \cos\omega t + \frac{1}{2}\left(\frac{d^2V}{dI^2}\right)_{I_o} (\delta I)^2 \cos^2\omega t + \ldots \quad (1)$$

where I_o is the DC component of the ramp current and δI is the amplitude of the modulation applied at frequency ω. The $\cos^2\omega t$ term may be re-written as $\frac{1}{2}(\cos 2\omega t + 1)$. Thus, the voltage measured at the frequency 2ω is

$$V(2\omega) = \frac{(\delta I)^2}{4}\left(\frac{d^2V}{dI^2}\right)_{I_o}, \quad (2)$$

and the voltage at the frequency ω is

$$V(\omega) = \delta I \left(\frac{dV}{dI}\right)_{I_o}. \quad (3)$$

While peak positions and qualitative relative peak intensities may be found from the, as measured, IET spectra, quantitative spectral analysis will require spectra calibrated in meaningful units. At present, IETS theory is still in an early stage of development, not practically usable in data analysis or as a predictive tool. However, in order to test the

accuracy of the theory as it develops, the availability of calibrated tunneling data will be invaluable. Also, once the theory has proven itself useful, tunneling spectra must be routinely calibrated to make use of this theory.

Theoretical calculations of inelastic electron tunneling are most easily carried out in terms of the current as a function of applied voltage. Thus, it would be most useful to have data in the form of d^2I/dV^2 $(= \frac{d\sigma}{dV})$ for the second derivative and $dI/dV (= \sigma$, the dynamic conductance) for the first derivative. These two derivatives are related to the measured derivatives by

$$\frac{d^2I}{dV^2} = -\sigma^3 \frac{d^2V}{dI^2} \tag{4a}$$

$$\frac{dI}{dV} = \left(\frac{dV}{dI}\right)^{-1} = \sigma. \tag{4b}$$

The calibration procedure is quite straightforward, requiring four steps: (1) Measure the second and first derivative spectra along with ten first derivative calibration points, as described in Appendix A; (2) Use equations (2), (3) and (4) to find the quantity $\frac{1}{\sigma(eV)} \frac{d\sigma}{deV}$ in units of $(meV)^{-1}$; (3) Use the calibration points to convert the measured first derivative spectrum to $\sigma(eV)$ in units of mho's; (4) Multiply the result of step (2) by the calibrated $\sigma(eV)$ to finally obtain $\frac{d\sigma}{deV}$ (eV) in $(ohms - meV)^{-1}$. Often the second derivative spectrum is normalized to the conductance at a certain reference voltage. Since our measurement electronics are optimized at a potential of 250 meV, we use the value of σ at that point $(\sigma(eV = 250) = \sigma_o)$. This gives us $\frac{1}{\sigma_o} \frac{d\sigma}{deV}$ (eV). It is

sometimes more desirable to have the quantity $\frac{1}{\sigma(eV)}\frac{d\sigma}{deV}(eV)$, as discussed by Klein et al. (1). This simply involves the point-by-point division of the calibrated second derivative spectrum by the calibrated first derivative.

There are some points concerning the measurement of the first derivative and first derivative calibration points which must be discussed. As mentioned in Appendix A, the junction appears to the measurement electronics to be a capacitor in parallel with a resistor, with typical values of 60-100 nf and 30-200 Ω, respectively. The capacitance of the sample will depend on the physical dimensions of the junction and the dielectric constant of the oxide barrier, all of which will remain essentially constant with applied voltage. The apparent resistance of the sample, on the other hand, is due to the electrons actually tunneling through the barrier region. Thus, it is the resistance which has the voltage dependence. However, the measurement electronics, when measuring the first derivative, actually detects the dynamic impedance of the sample, so the relevant quantity is $Z = \left[\left(\frac{1}{Z_c}\right)^2 + \left(\frac{1}{R}\right)^2\right]^{-\frac{1}{2}}$, where $Z_c = (2\pi fC)^{-1}$ is the capacitive impedance, f is the modulation frequency and C is the capacitance. Unless Z_c is large enough so that its contribution to Z is negligible, this capacitance will cause some problems. Luckily, Z_c may be easily increased simply by decreasing the modulation frequency.

To illustrate the effect of the capacitance on the measured Z, take two typical resistances R_o = 100 Ω and R_1 = 110 Ω, representing a junction resistance change of 10%, and $Z_c = \frac{2\times10^6}{f}$ (corresponding to a C of

approximately 80 nf). At a measurement frequency of 50 kHz, Z_c = 40 Ω which yields a Z(R = 110 Ω) = 37.6 Ω and Z(R = 100 Ω) = 37.1 Ω, or ΔZ/Z of about 1%. Thus the change in the measured first derivative is only 1/20 of the actual resistance change, and even the relative change $\left(\frac{\Delta Z}{Z}\right)$ is a factor of 10 low. Decreasing the frequency to 5 kHz yields a Z_c of 400 Ω, and Z(R = 110 Ω) = 106.1 and Z(R = 100 Ω) = 97.0, ΔZ = 9.1, $\frac{\Delta Z}{Z}$ = .094. This is quite a bit better, now ΔZ is 91% of ΔR and $\frac{\Delta Z}{Z}$ is 94% of the actual value. However, this is still not so good as we can do. Decreasing f by one more factor of ten to 500 Hz gives a Z_c of 4000 Ω, Z(R = 110 Ω) = 109.96 Ω and Z(R = 100 Ω) = 99.97 Ω, ΔZ = 9.99 Ω and $\frac{\Delta Z}{Z}$ of 9.99%. Here the measured Z is well less than one percent different from the resistance and the change in Z is within about one-tenth of one percent of change in R. Thus, by simply decreasing f from 50 kHz to 500 Hz, we have gone from a first derivative signal that is almost independent of changes in R, to a signal which closely matches the resistive contribution to the junction impedence.

Another effect which the capacitance may have is on the shape of the Z(R) curve. We would like Z(R) to be as close to linear as possible. Assuming $Z_c > R$, we may approximate Z by $R\left[1 - \frac{1}{2}\left(\frac{R}{Z_c}\right)^2\right]$. For uniform, small increments in resistance, δR, the corresponding changes in Z will be

$$\Delta Z = (R + \delta R)\left[1 - \frac{1}{2}\frac{(R + \delta R)^2}{Z_c^2}\right] - R\left[1 - \frac{1}{2}\frac{R}{Z_c}\right]^2$$

$$= \delta R - \frac{1}{2}\frac{1}{Z_c^2}\left[(R + \delta R)^3 - R^3\right]$$

Assuming that $\delta R/R << 1$, $(R + \delta R)^3 \simeq R^3 \left[1 + 3(\frac{\delta R}{R})\right]$

$$\Delta Z \simeq \delta R - \frac{3}{2} \left(\frac{R}{Z_c}\right)^2 \delta R$$

$$= \delta R \left[1 - \frac{3}{2} \left(\frac{R}{Z_c}\right)^2\right]$$

Thus, we see that for uniform increments in R, the size of the corresponding change in Z will depend on the resistance, meaning, for a junction with linearly decreasing R, the measured Z will take on a quadratic component. This is another reason to make Z_c large.

One cannot, however, continue to reduce the modulation frequency indefinitely since the signal-to-noise of the electronics decreases slightly with decreasing frequency due to the characteristics of the preamp of the lock-in detector and the lock-in detector itself. In practice, a good compromise is to modulate and measure at approximately 1000 Hz.

There is one additional problem encountered when using these low frequencies. In the Measurement Electronics circuitry, there is a small, series D.C. blocking capacitor between the From Sample input and the output to the PAR. Since the impedance of this capacitor is proportional to $1/f$, as the frequency is decreased, Z_c increases, decreasing, in turn, the signal reaching the lock-in. This blocking capacitor may easily by bypassed by inserting the divider box discussed in Appendix A (Fig. A25). This box couples the signal from the sample through a large (250μf) capacitor directly to the lock-in preamp while connecting the signal back to the Measurement Electronics to complete the feedback loop in the ramp control circuit.

With this arrangement, measuring at approximately 1.1 kHz the

tunnel junction resistance is accurately measured.

The mathematical description of the calibration procedure will be given next, followed by a description of the computer program which carries out the calibration. Finally, examples will be given.

From equations (2) and (4a) we obtain

$$\frac{d^2I}{dV^2} = \sigma^3 \frac{4}{(\delta I)^2} V(2\omega)$$

Dividing through by one power of σ and using equations (3) and (4b) we arrive at

$$\frac{1}{\sigma}\frac{d^2I}{dV^2} = \left(\frac{\delta I}{V(\omega)}\right)^2 \left(\frac{4}{\delta I^2} V(2\omega)\right)$$

$$\frac{1}{\sigma}\frac{d^2I}{dV^2} = 4\frac{V(2\omega)}{\left[V(\omega)\right]^2} \qquad (5)$$

The two voltages, $V(\omega)$ and $V(2\omega)$, are directly measurable , and, in fact, are the measured first and second derivative spectra, respectively.

In order to find the calibrated second derivative, d^2I/dV^2, alone, the first derivative, σ, must be calibrated. Since resistance is a directly measurable quantity, the first derivative may be calibrated by comparison with independently measured calibration points. First, the ten calibration values as stored by the computer, y_i, and the ten calibration resistances as recorded by the operator from the DVM, R_i, are fit to the equation

$$y_i = a_o + a_1 R_i + a_2 R_i^2. \qquad (6)$$

A least squares fit of the three parameters, a_0, a_1 and a_2, is obtained from all ten y_i's and R_i's. A quadratic, as opposed to a linear, equation is used to account for any slight nonlinearities which may exist in the measurement and recording apparatus.

Equation (6) may be inverted to find the resistance which corresponds to a given value as stored in the computer, $R = \left[-a_1 + \sqrt{a_1^2 - 4a_2(a_0 - y)}\right]/2a_2$. If we define $Y(eV)$ to be the first derivative as stored by the computer in the data file, the corresponding resistance, $R(eV)$, is given by

$$R(eV) = \left[-a_1 + \sqrt{a_1^2 - 4a_2(a_0 - Y(eV))}\right]/2a_2 \qquad (7)$$

The conductance may then be obtained simply by inverting Eq. (7)

$$\sigma(eV) = \left[R(eV)\right]^{-1} = 2a_2/\left[-a_1 + \sqrt{a_1^2 - 4a_2(a_0 - Y(ev))}\right]. \qquad (8)$$

Finally, to find the calibrated second derivative, we simply perform a point by point multiplication of the spectra obtained by using equations (5) and (8), resulting in the calibrated spectrum, $\frac{d^2I}{dV^2}(eV)$.

It must be kept in mind that this calibration procedure is not perfectly accurate. Small effects such as slight nonlinearities in the measurement set-up will contribute. Also, equations (2) and (3) are not perfect equalities. Higher order terms will enter these equations but they will be on the order of $(\delta I)^2$ (or more) smaller than the primary signal. A more self consistent calibration procedure has been developed by Adler and Straus (2) which takes into account these small effects.

The computer program to carry out this calibration is straightforward. However, since this program is designed to be run on the IBM 370, the data must be in a form which the IBM may use. This requires trans-

ferring the data from floppy disc to magnetic tape and then reordering the data on the tape into a logical arrangement, as described in Appendix B of Howard E. Evans' Ph.D. Thesis (3). Once this has been done, the desired data files may be retrieved from tape by means of the GETDTA subroutine.

In addition to the data which have been stored on disc, one must supply additional data which had been manually recorded at the time of the measurement. These consist of (1) the number of spectra to be calibrated; (2) the names of these files in RADIX 50 code (3); (3) the measured initial ramp voltage; (4) the measured spectral voltage increment; (5) the lock-in amplifier zero offset for both the first and second derivative spectra (these are numbers between 0 and 10 recorded from the 10 turn zero offset pot); (6) the lock-in sensitivities used in recording the first and second derivatives; and (7) the ten measured calibration resistances.

The actual calibration manipulations are relegated to a subroutine, CALIB. The calling sequence for this routine is CALL CALIB (RCAL, A, SSQ, Y, Y1OFF, Y2OFF, SENS1, SENS2).

RCAL is a 3 x 10 array containing the first derivative calibration data. Column 1 holds the ten calibration resistances measured by the operator. Column 2 contains the ten corresponding calibration values as stored by the computer and column 3 holds the uncertainties in the calibration points. Usually 1's are entered in the third column.

A is a linear array containing the three coefficients to equation (6)

determined by the subroutine from a least squares fit to the data in RCAL.

SSQ is the variance of the above-mentioned least squares fit.

Y is a 2 x 512 array containing the uncalibrated first and second derivative data in columns 1 and 2, respectively, as input and as output, contains the calibrated first and second derivative spectra in units of mho's and $(\text{ohm-meV})^{-1}$, respectively. Only the first 471 entries in each column are considered data points, to coincide with the standard wide scan described in Appendix A.

Y1OFF and Y2OFF are the zero offsets recorded by the operator for the first and second derivative spectra, respectively. These numbers are in the range 0 to 10 where 10 is when the lock-in zero-offset is turned a full 10 turns in the minus (-) direction; e.g., a Y2OFF of 1.4 corresponds to -1.40 turns of the zero-offset potentiometer.

SENS1 and SENS2 are the lock-in amplifier sensitivity settings used (and recorded by the operator) during the measurement of the first and second derivative spectra, respectively, in microvolts.

This subroutine is written specifically to calibrate the 471 point "wide scan" discussed in Appendix A. In order to calibrate other spectra the subroutine must be modified somewhat.

Subroutine CALIB is listed on the following pages.

```
      SUBROUTINE CALIB(RCAL,A,SSQ,Y,Y1OFF,Y2OFF,SENS1,SENS2)
C  ROUTINE TO CALIBRATE FIRST AND SECOND DERIVATIVE DATA
C
C  Y = 2X512 ARRAY CONTAINING SPECTRAL DATA
C     COLUMN 1 CONTAINS 1ST DERIVATIVE DATA
C      COLUMN 2 CONTAINS 2ND DERIVATIVE DATA
C      471 POINTS ARE USED
C  RCAL = 3X10 ARRAY OF 1ST DERIV. CALIBRATION POINTS
C      COLUMN 1 HOLDS THE RESISTANCES
C      COLUMN 2 HOLDS THE COMPUTER VALUES
C      COLUMN 3 HOLDS THE UNCERTAINTIES, OR ALL 1'S
C  Y1OFF = ZERO OFFSET FOR 1ST DERIV. (BETWEEN 0 AND 10)
C  Y2OFF = ZERO OFFSET FOR 2ND DERIV. (BETWEEN 0 AND 10)
C  SENS1 = LOCK-IN SENSITIVITY FOR 1ST DERIV. (IN MICROVOLTS)
C  SENS2 = LOCK-IN SENSITIVITY FOR 2ND DERIV. (IN MICROVOLTS)
C  START = STARTING POINT OF SPECTRUM IN MILLIVOLTS
C  STEP = INCREMENT IN MILLIVOLTS
      REAL RCAL(3,10),A(3),Y(2,500),B(5)
      DOUBLE PRECISION  STOR(3,9)
C  CONVERT SENSITIVITIES TO MEV
      SENS1 = SENS1/1000.
      SENS2 = SENS2/1000.
C  FIND (1/ SIGMA) D SIGMA/D V
      DO 5 I=1,471
      SIG=(Y(1,I)/50.+Y1OFF-1.)*SENS1
      SIGSQ = SIG*SIG
      Y2 = Y(2,I)
      Y(2,I)=4.*(Y2/50.+Y2OFF-1.)*SENS2/SIGSQ
    5 CONTINUE
C  CALIBRATE SIGMA
   22 FORMAT(2F8.3)
      WRITE(6,22)(RCAL(1,I),RCAL(2,I),I=1,10)
      CHISQ = 0.
      CALL LSQUAR(RCAL,10,3,A,CHISQ,STOR)
      SSQ = CHISQ
      WRITE(6,21) A,SSQ
```

```
   21 FORMAT(' A1=',E12.5,' A2=',E12.5,' A3=',E12.5,' CHISQ=',E12.5)
      ASQ = A(2)*A(2)
      DO 19 K=1,10
      RC = RCAL(2,K)
   19 RCAL(2,K) = (SQRT(ASQ-4.*(A(1)-RC)*A(3))-A(2))/(2.*A(3))
      WRITE(6,211)
  211 FORMAT(//'  REXP     RCALC')
      WRITE(6,22)(RCAL(1,I),RCAL(2,I),I=1,10)
      DO 20 J=1,471
      Y1 = Y(1,J)
      Y(1,J) = 2.*A(3)/(SQRT(ASQ-4.*(A(1)-Y1)*A(3))-A(2))
   20 CONTINUE
C  FIND D SIGMA/D V
      DO 25 J=1,471
      Y2 = Y(2,J)
      Y(2,J) = Y(1,J)*Y2
   25 CONTINUE
      RETURN
      END
```

The first segment of the subroutine accomplishes four things: (1) converts the sensitivities to meV and for each spectral voltage, (2) converts the measured first derivative datum point to the actual voltage (in meV) which it represents, $V(\omega)$, and squares this, $V^2(\omega)$, (3) converts the corresponding second derivative datum point to the true measured voltage (also in meV) which it represents, $V(2\omega)$, and finally (4) does a point by point division and multiplies the result by 4 to obtain $4V(2\omega)/[Y(\omega)]^2 = \frac{1}{\sigma}\frac{d\sigma}{dV}$ in meV.

The second segment of the subroutine conducts the first derivative calibration. First the library subroutine LSQAR (4) conducts a least squares fit of the ten calibration resistances R_c, and corresponding ten stored values, Y_c, to the quadratic

$$Y_c = A(1) + A(2)R_c + A(3)R_c^2.$$

As output LSQAR provides the array containing the three parameters, A(1), A(2) and A(3) as well as the chi squared value for the fit. The values for the A's and chi squared are then written. As a test, the quadratic is inverted and the Y_c and A values are inserted to calculate the resistances which the equation predicts. These calculated resistances should correspond closely to the calibration resistances which were entered. Both the measured (REXP) and calculated (RCALC) resistances are printed out. The equation is then modified slightly to determine conductance rather than resistance

$$Y1_i = 2A(3)\Big/\left\{\sqrt{\left[(A(2))^2 - 4A(3)(A(1) - Y1_i)\right]} - A(2)\right\}.$$

The uncalibrated first derivative datum point is entered in the right

hand side of the equation and the calibrated conductance value is calculated. This conductance is stored back in the data array. At the conclusion of this segment, column 1 of array Y contains the calibrated first derivative and column 2 holds the spectrum corresponding to $\frac{1}{\sigma}\frac{d\sigma}{dV}$.

The final section of the routine conducts a point-by-point multiplication of the second column by the first column to obtain $\frac{d\sigma}{dV}$. This spectrum is then stored in column 2 of Y.

Control is then returned to the program which called CALIB.

As an example of the use of CALIB, a short program was written to retrieve uncalibrated first and second derivative data from magnetic tape. The uncalibrated second derivative is plotted. Subroutine CALIB is then called to calibrate the IET spectra. The second derivative is then divided by the conductance measured at a ramp voltage of 250meV and the result, $\frac{1}{\sigma_o}\frac{d\sigma}{dV}$, is plotted. Finally, a point-by-point division of σ into $\frac{d\sigma}{dV}$ is conducted and that result, $\frac{1}{\sigma}\frac{d\sigma}{dV}$, is plotted. That program and the three corresponding plots follow.

```
//TSTPLT  JOB (56706,WAB,CHE),'WM BOWSER',TIME=(0C,30),TYPRUN=COPY
/*JOBPARM TAPES=(0,0,1)
/*JOBPARM REGION=256K
/*REQUEST IET004,9M,R
//  EXEC  FORTG
//SYSLIB  DD
//        DD
//        DD  DSN=SSS.EXTRA.CITLIB,UNIT=SYSDA,DISP=SHR,VOL=SER=CITSL1
//SYSPLTON  DD   SYSOUT=A
//FORT    DD  *
C  PROGRAM TO RETRIEVE DATA FROM MAGNETIC TAPE
C     PLOT UNCALIBRATED 2ND DERIVATIVE SPECTRUM
C     CALIBRATE 1ST AND 2ND DERIVATIVE DATA
C     PLOT CALIBRATED 2ND DERIVATIVE SPECTRUM
      REAL Y(2,512),RCAL(3,10),A(3),B(5),XP(473),YP(473),CCC(3)
      REAL DATA(20,512)
      INTEGER  NAME(20,6)
C     READ IN DATA FILES
      READ(5,4) (NAME(1,J),J=1,6),(NAME(2,K),K=1,6)
    4 FORMAT(12I3)
      WRITE(6,4) (NAME(1,J),J=1,6),(NAME(2,K),K=1,6)
      NF = 2
      CALL GETDTA(NF,NAME,DATA)
      DO 5 I=1,512
      Y(1,I) = DATA(1,I)
      Y(2,I) = DATA(2,I)
    5 CONTINUE
      READ(5,8) START,STEP,Y1OFF,Y2OFF,SENS1,SENS2
    8 FORMAT(6F8.3)
      READ(5,10) (RCAL(1,I),I=1,10)
   10 FORMAT(10F7.2)
      DO 15 I=1,10
      II=490+I
```

```
      RCAL(2,I) = Y(1,II)
      RCAL(3,I)=1.
   15 CONTINUE
      XP(1)=0.
      XP(473)=500.
      DOC(1)=0.
      DOC(2)=0.
      DOC(3)=1.
      YP(1) = Y(2,2)
      YP(473) = Y(2,471)
      YMN=YP(1)
      YMX=YP(1)
      YP(2)=YP(1)
      XP(2)=START
      DO 185 J=2,471
      IP=J+1
      YP(IP) = Y(2,J)
      XPI = J-1.
      XP(IP) = START+XPI*STEP
      IF(YP(IP).LT.YMN) YMN=YP(IP)
      IF(YP(IP).GT.YMX) YMX=YP(IP)
  185 CONTINUE
      CALL LABEL(0.,0.,0.,500.,15.,10,'V IN MEV',E,0)
      CALL LABEL(0.,0.,YMN,YMX,10.,5,'ARBITRARY UNITS',15,1)
      CALL XYPLOT(473,XP,YP,0.,500.,YMN,YMX,DCC,-1)
      CALL CALIB(RCAL,A,SSQ,Y,Y1OFF,Y2OFF,SENS1,SENS2)
C     PLOT CALIBRATED SECOND DERIVATIVE DATA
      XP(1)=0.
      XP(473)=500.
      DOC(1)=0.
```

```
      DOC(2)=0.
      DOC(3)=1.
      YP(1) = Y(2,2)/Y(1,225)
      YP(473) = Y(2,471)/Y(1,225)
      YMN=YP(1)
      YMX=YP(1)
      YP(2)=YP(1)
      XP(2)=START
      DO 85 J=2,471
      IP=J+1
      YP(IP) = Y(2,J)/Y(1,225)
      XPI = J-1.
      XP(IP) = START+XPI*STEP
      IF(YP(IP).LT.YMN) YMN=YP(IP)
      IF(YP(IP).GT.YMX) YMX=YP(IP)
   85 CONTINUE
      CALL LABEL(0.,0.,0.,500.,15.,10,'V IN MEV',E,0)
      CALL LABEL(0.,0.,YMN,YMX,10.,5,'(1/S(V=250))DS/DV IN 1/MEV',26,1)
      CALL XYPLOT(473,XP,YP,0.,500.,YMN,YMX,DOC,-1)
      YP(1)=Y(2,2)/Y(1,2)
      YP(473)=Y(2,471)/Y(1,471)
      YMN=YP(1)
      YMX=YP(1)
      YP(2)=YP(1)
      DO 285 J=2,471
      IP=J+1
      YP(IP)=Y(2,J)/Y(1,J)
      IF(YP(IP).LT.YMN) YMN=YP(IP)
      IF(YP(IP).GT.YMX) YMX=YP(IP)
  285 CONTINUE
```

```
      CALL LABEL(0.,0.,0.,500.,15.,10,'V IN MEV',E,0)
      CALL LABEL(0.,0.,YMN,YMX,10.,5,'(1/S )DS/DV IN 1/MEV',20,1)
      CALL XYPLOT(473,XP,YP,0.,500.,YMN,YMX,DCC,-1)
      STOP
      END
```

```
//DATA    DD     *
 20 19 20 30 37 36 20 19 20 30 37 37
30.09    0.977    4.17     1.40     500.0    2.0
52.70  53.96  55.07  56.27  57.52  58.72  59.91  61.10  62.28  63.49
//READRC01  DD UNIT=TAPE16,LABEL=(1,BLP,,IN),DISP=CLD,
//             VOL=SER=IET004,
//             DCB=(RECFM=U,BLKSIZE=2304)
//
```

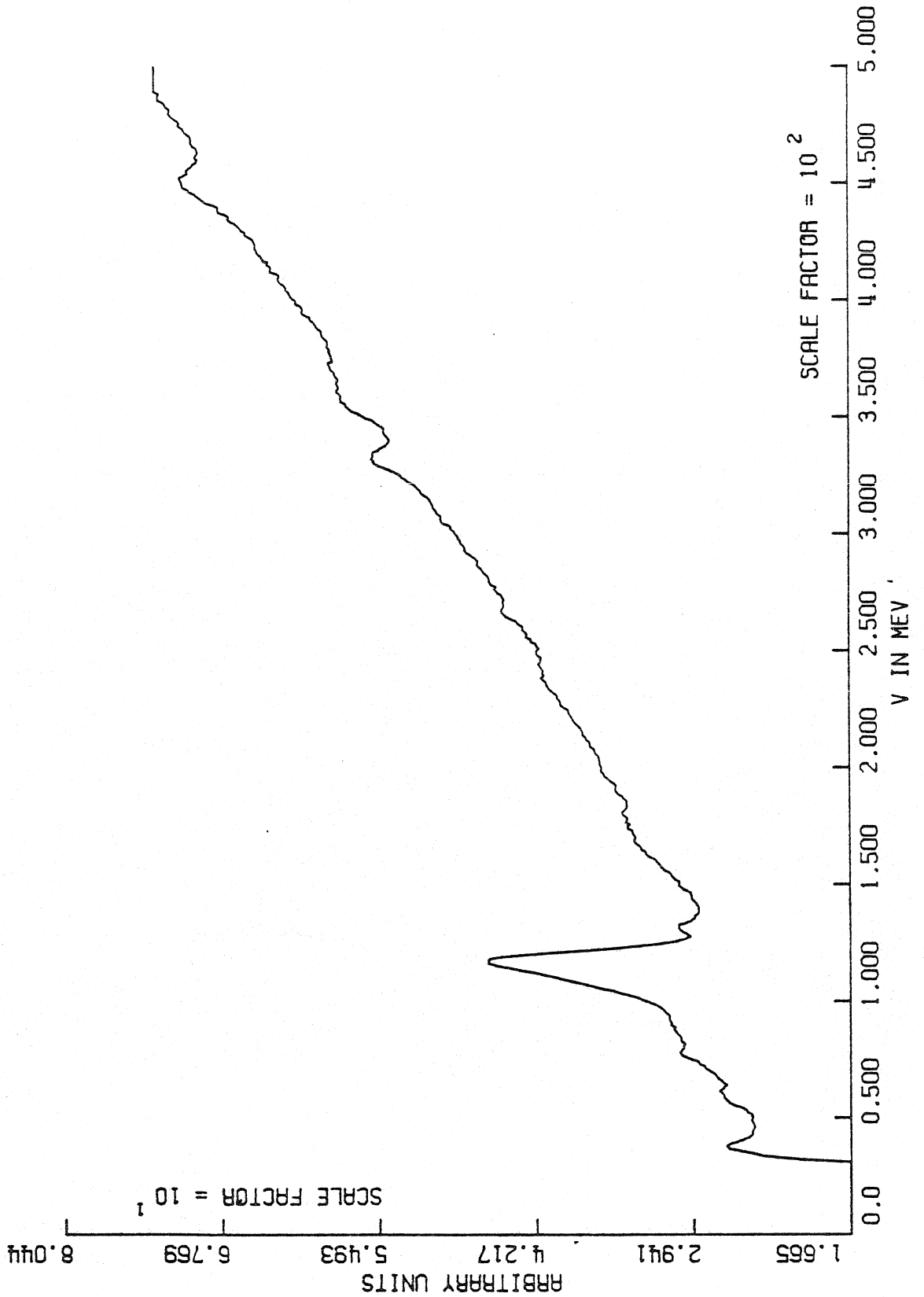
ARBITRARY UNITS
1.665
2.941
4.217
5.493
6.769
8.044
SCALE FACTOR = 10 1
0.0
0.500
1.000
1.500
2.000
2.500
3.000
3.500
4.000
4.500
5.000
V IN MEV
SCALE FACTOR = 10 2

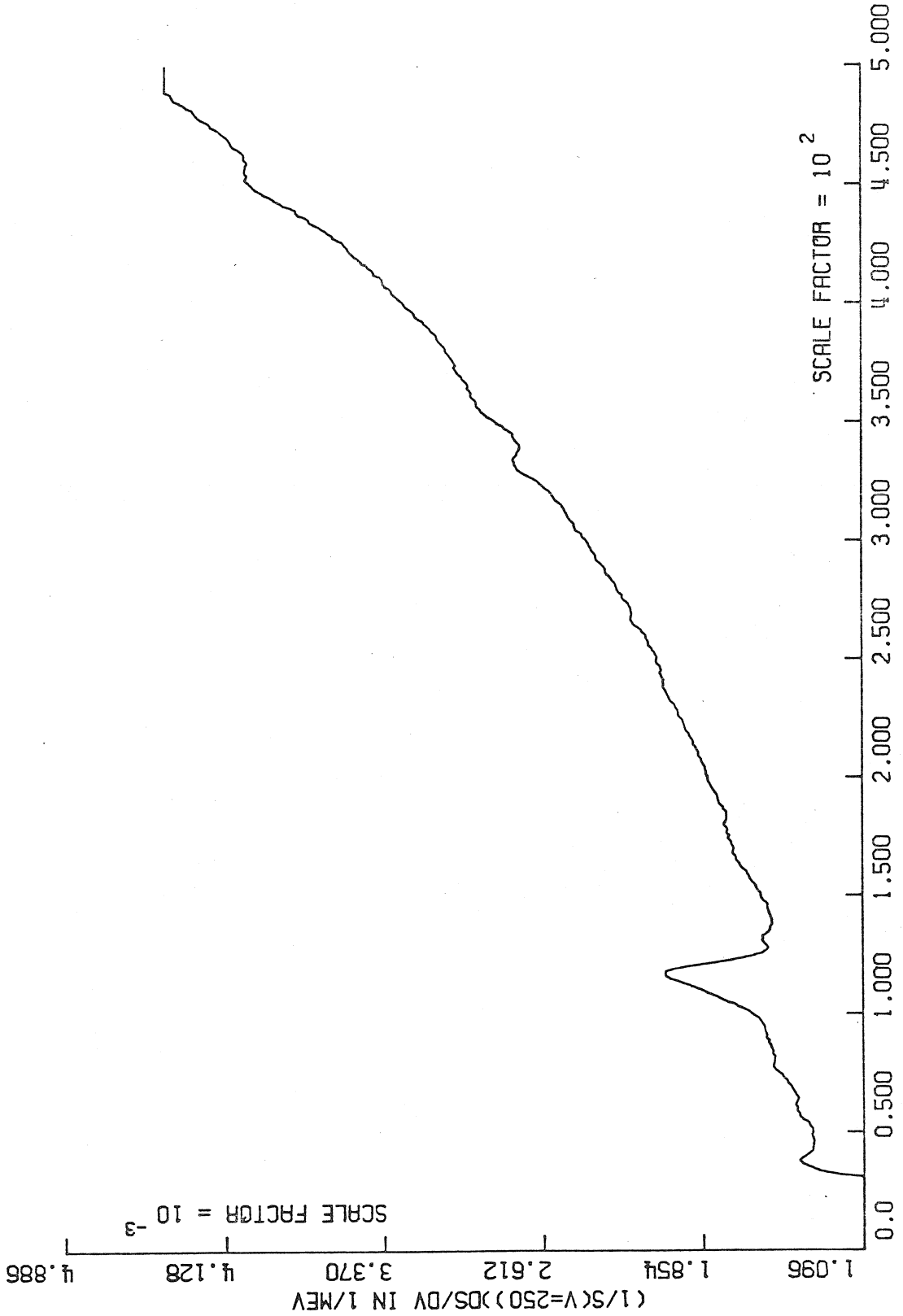
(1/S(V=250))DS/DV IN 1/MEV
1.096
1.854
2.612
3.370
4.128
4.886
SCALE FACTOR = 10 -3
0.0
0.500
1.000
1.500
2.000
2.500
3.000
3.500
4.000
4.500
5.000
V IN MEV
SCALE FACTOR = 10 2

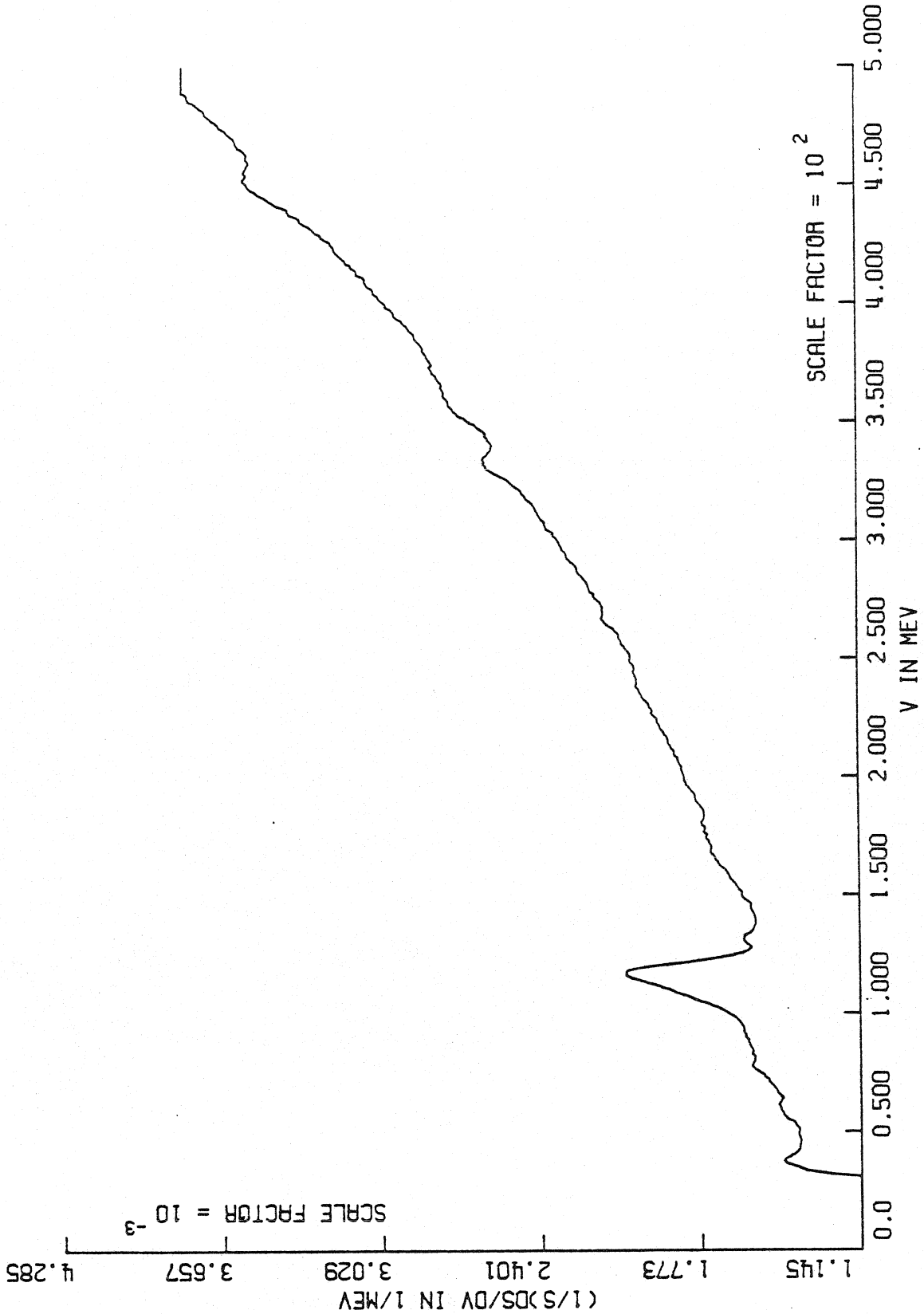
SCALE FACTOR = 10 -3
(1/S)DS/DV IN 1/MEV
1.145
1.773
2.401
3.029
3.657
4.285
0.0
0.500
1.000
1.500
2.000
2.500
3.000
3.500
4.000
4.500
5.000
V IN MEV
SCALE FACTOR = 10 2

References

1. J. Klein, A. Léger, B. Delmas and S. DeCheveigne, Revue Phys. Appl. 11, 309 (1976).

2. J. G. Adler and J. Straus, Rev. Sci. Instrum. 46, 158 (1975).

3. H. E. Evans, Ph.D. Thesis, Califrnia Institute of Technology, 1980.

4. LSQUAR subroutine information sheet, Jorgenson Computer Center, Caltech.

Appendix C

Considerations for the Design of a System for Inelastic Electron Tunneling Junction Fabrication

APPENDIX C: Considerations for the Design of a System for Inelastic Electron Tunneling Junction Fabrication.

An inelastic electron tunneling spectroscopy (IETS) junction fabrication system is quite straightforward to design and may be assembled at reasonable cost. This appendix will discuss the basic features necessary for a fabrication system followed by the optional features which increase the versatility of this technique. The second half of the appendix will describe the three systems used and/or designed by the author for IETS.

The first piece of equipment needed is a vacuum chamber. Since IETS junction fabrication involves the evaporation of metals, high vacuum (less than 10^{-4} torr) is necessary to obtain good quality metal films. Better vacuum is very desirable since IETS is very sensitive to contamination, especially from hydrocarbons. A liquid nitrogen trapped diffusion pumped glass bell jar system works well. The system should have several feed-through ports available for the apparatus to be described below. The system should also pump down to working vacuum in a reasonable amount of time (1 to 2 hours).

The first thing to be considered is the metal deposition. Evaporation of two metals, usually aluminum and lead, is required. We have found that the source which works best for the Al is a coiled tungsten filament upon which small U's of 1 mm Al wire are hung. For the Pb, a 0.005" x ½" W or Mo dimple boat works well. Some kind of shield must be placed between the evaporation sources to prevent intercontamination of the metals. The conductors to these sources inside the vacuum system are generally constructed of copper stock (OFHC copper is best), as this will easily handle the required currents without overheating. Three medium to high current (at

least 100 amps) vacuum electrical feedthroughs are needed to get the power into the system. The current supply for the sources may be as simple as a Variac controlling the input to a high output current a.c. transformer (100 A at 5 volts is adequate). A high current a.c. ammeter is very helpful in reproducing evaporation parameters. The amount of metal being deposited on the sample must be determined. A quartz crystal microbalance positioned next to the sample equally distant from the sources is the most convenient method to do this. A quartz crystal microbalance of very reasonable accuracy may be relatively inexpensively assembled. A quartz crystal oscillator (e.g., a Sloan #900010 oscillator head) is driven by a regulated 5 volt power supply. The quartz crystal will then oscillate at a frequency near 5 MHz, this frequency can easily be measured with an inexpensive frequency counter (e.g., Data Precision model 5740). As a metal is deposited on the quartz crystal, the frequency drops linearly with the mass of metal deposited. This microbalance may be easily calibrated for thickness determination as described elsewhere (1).

To define the lateral size and shape of the metal films deposited on the sample substrate, a changeable set of masks is needed. The mask assembly should have three positions. The first accurately locates the mask for the Al strip over the substrate. The second accurately positions the mask for the Pb strips. The final position completely exposes the samples and is used during the oxidation and adsorbate exposure stages. A fourth position completely shielding the sample is optional. The masks are usually moved via a mechanical feedthrough and positioned over the sample either visually or using physical stops.

A shutter is also needed to control the metal depositions and sample exposures. A mechanical (rotary) feedthrough is also used to move the shutter.

The sample substrate should be mounted sturdily far enough from the metal sources so that the resulting films will be uniform and smooth. The substrate should also be close enough to the masks (about 2 mm) that the patterns of deposited metal will be sharp, it should not, however, be so close that the masks will interfere with the samples when the masks are changed. The shutter is positioned close to the front of the mask.

The oxidation of the Al film to form the tunneling barrier may be accomplished in several ways, for example, by thermally oxidizing in air or by dipping in liquid water. However, the preferred method in this group is to oxidize the Al in a glow discharge initiated in high purity oxygen within the vacuum system. With this approach, the sample need not be exposed to the atmosphere before the junction is completed. Plasma oxidation requires a regulated high voltage power supply rated to at least 1500 V at 30 mA (e.g., Fluke model 412B) and a high voltage vacuum feedthrough. Inside the vacuum system, the high voltage proceeds to an electrode, usually Al wire, positioned about 7 to 10 cm from the samples. Near this electrode, blocking line-of-sight between the samples and the electrode is an aluminum shield. The discharge itself is predominantly between the electrode and this shield. Outside the vacuum system, in the high voltage line are usually placed some series resistors (e.g., three 2.5 KΩ, 2 W resistors). By measuring the voltage drop across one of these resistors, the discharge current may be monitored. The exact placment of the electrode and shield must be finally determined by trial-and-error.

One must also have some provision for adding the oxygen to the vacuum system. A metering valve controlling the flow from a regulated oxygen cylinder works well. It is often desirable to ground or even apply a small positive voltage to the Al strip during the discharge to enhance the oxidation rate.

One also needs a means of introducing adsorbates into the vacuum system. The feedthrough used for this could be the same one used to introduce the oxygen. For high vapor pressure solids or liquids, a separate inlet may be desirable. Low vapor pressure solids may be introduced via a breakable ampule physically located inside the vacuum system.

An instrumentation (electrical) feedthrough is also needed for the deposition monitor and any electrical connections which are to be made to the sample.

Finally, it is useful to vent the vacuum system back to atmospheric pressure using high purity N_2 gas. This reduces the amount of water vapor reaching the system and reduces the subsequent pumpdown time.

This basic vacuum system is illustrated in Fig. C1. With this system one may study a wide range of adsorbates on aluminum oxide at room temperature. There are several things, however, that may be added to this basic system to enhance its versatility significantly.

Control of the sample temperature during fabrication can be very useful. Cooling capability may be used, for example, to stabilize weakly bound adsorbates on the oxide surface or to prevent the formation of large metal islands when doing low coverage supported metal evaporations. The ability to heat the sample is useful, for example, in investigating activated or temperature dependent reactions.

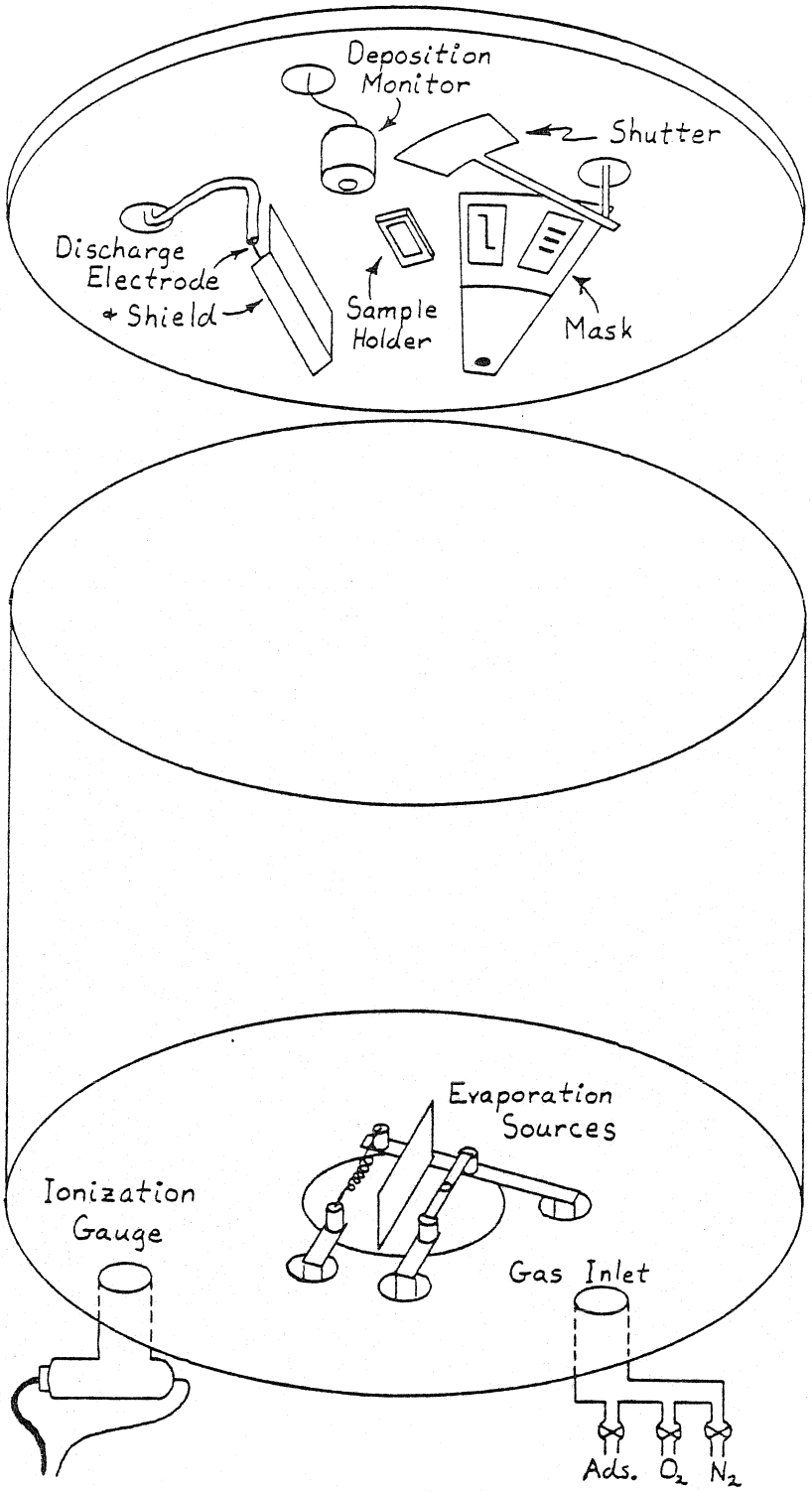
Deposition
Monitor
Shutter
Discharge
Electrode
+ Shield
Sample
Holder
Mask
Evaporation
Sources
Ionization
Gauge
Gas Inlet
Ads.
O_2
N_2

Fig. C1

Cooling of the sample is achieved by having the sample holder in good thermal contact with something which may be cooled from outside the vacuum system. Two ways of doing this are to mount the sample holder on a cold finger into which a coolant (liquid nitrogen) may be added or else have the sample holder mounted to a closed cooling line through which liquid nitrogen or some other refrigerant may be flowed.

There are basically two ways to heat the sample. The first is to heat the entire sample holder with some form of heating element. This is quite straightforward and requires no explanation. The second method is to heat resistively only the Al strip. This method is described in detail in chapter 2 of this thesis.

In order to monitor the temperature of the sample when cooling or when using a heater, a thermocouple must be attached to the sample substrate.

One must take into account that the thermocouple, internal heater leads, and the leads for the resistive heating scheme will increase the number of leads which must be accommodated by the instrumentation (electrical) feedthrough.

Another improvement, which may be incorporated when designing a new fabrication system, is the ability to make more than one set of junctions at one time. The sample holders should be independent so that the samples may be heated or cooled independently. Also, the shutter should be designed to provide for exposing a single sample at a time, for example, if the Pb is to be deposited on the samples individually. This independence will allow one to vary certain parameters (e.g., temperature) on the separate samples while assuring that the other conditions are identical

between samples. The ability to make more than one sample at a time can also save a signficant amount of time. For example, for a system which takes 2 hours to pump down, if the actual fabrication takes one hour, for a system so equipped, three samples may be made in three hours; whereas if only one sample could be made at a time, 9 hours would be required for the same three.

Having multiple samples will, however, add complications. The samples will, in general, have to be farther from the evaporation sources so that the metal films deposited on all samples from any source will be approximately the same thickness. Also, the placement and detailed design of the plasma discharge electrode and shield become critical since all samples must oxidize at very close to the same rate. Multiple samples will also increase the number of pins required on the electrical feedthrough.

Finally, additional evaporation sources can be useful, and are necessary in doing any evaporated supported metal work with IETS.

The three IETS junction fabrication systems used and/or designed by the author span the range from quite basic to versatile.

The first system used by the author was basic. It was based on a liquid nitrogen trapped oil diffusion pumped vacuum system with base pressure 1×10^{-6} torr. Vacuum feedthrough ports were provided in the baseplate and the top plate. The sides of the system were formed by a 18" x 18" glass cylinder. Two metal evaporation sources were provided at the baseplate, along with an electrical feedthrough for the quartz crystal thickness monitor. The top plate accommodated most of the apparatus. The single sample holder was mounted on a shallow cold finger which had provision for a cartridge heater for sample heating. The mask assembly was

operated by a high vacuum rotary/linear feedthrough with an external slot-and-key arrangement for accurately aligning the masks since the operator could not see into the system for visual alignment. The shutter was a simple blade shutter attached to a second rotary feedthrough with an external indicator to show the position of the shutter inside the bell jar. The discharge electrode and shield were also mounted to the top plate along with the high voltage feedthrough. A simple multiwire electrical feedthrough was located near the sample holder providing electrical connections to the sample and allowing for resistive heating of the Al. The top plate also held separate valved inlets for the introduction of oxygen and adsorbates.

With this system one could study adsorption on aluminum oxide at room temperature and above. The ultimate pressure, however, was not considered good enough to study supported metals or adsorptions below room temperature.

The experience gained working on the above system aided the author (with the assistance of Howard E. Evans) in designing and building the MkI fabrication system, which is to be discussed next. The layout of this system along with a detailed discussion of the procedures followed when using the MkI system in junction fabrication are discussed elsewhere (1). Thus, this section will only discuss the considerations in the design of some of the major components of the system.

The MkI system is based on an 18" glass bell jar vacuum system. It is pumped by a 4" CVC oil diffusion pump with a liquid nitrogen cooled baffle. Base pressure with the diffusion pump is below 5×10^{-7} torr. To improve the base pressure of this system, a "homemade" glass, liquid nitrogen jacketed titanium sublimation pump may be attached directly to

the bell jar by way of a 4" glass O-ring sealed flange. With the sublimation pump operating, the base pressure is improved by a factor of about 20 (to approximately 1 x 10^{-8} torr). A limited number of feedthrough ports are available, all of which are located in the baseplate. This limitation, along with monetary constraints, had to be taken into account in the design of the system.

The attainable vacuum of this system is low enough that supported metal work is feasible. To allow for this, provision for four metal evaporation sources was included. This will allow not only for the study of single metal catalysts but also for coevaporated binary systems. To prevent intercontamination of the metal sources and also to cut down on the amount of unnecessary coating of the inside of the vacuum system, the evaporation sources are enclosed in a stainless steel box, each source with its own chamber with a slot in the top to allow for a line-of-sight path to the samples. The power to the sources is supplied by 7.5 volt 3KVA transformer, the input of which is controlled by a Variac. The output AC current is monitored by a 150 ampere Westinghouse panel meter.

To augment the versatility of the system, provision for making three samples per run was added. The three sample holders are mounted approximately 3.5 cm apart, 40 cm from the evaporation sources. These dimensions were estimated (2) to be adequate to insure that the amount of metal deposited from any one of the four sources on all three samples would be approximately the same. The sample holder bases are 5/8" x 1 ½" x ¼" copper blocks permanently mounted to the support table with minimal thermal contact between the bases and the table. To each base is silver soldered a separate ¼" stainless steel cooling line through which liquid nitrogen

may be flowed to cool the sample. The sample holder itself should be easy to dismount since it must be removed from the system to change samples. Since provision for several electrical contacts to the sample is desired, the associated wires need to be disconnected easily also. The resulting design is shown in Fig. C2. The main body of the sample holder is a 5/8" x 1 ½" x ¼" copper block with a shallow (1/32") area milled out in its face to accommodate the ½" x 1" glass slides which are used as the sample substrates. Two Macor ceramic blocks are bolted to either side of the copper block. Each ceramic block has three vertical holes through which the 18 gauge wire leads pass. These wires are held in place by set screws which screw into the tapped side holes. In this way, the leads are held firmly in place while being electrically isolated from ground and from each other. For easy dismounting, the far ends of the lead wires are soldered to gold plated mini banana jacks which, when the sample holder is mounted in the system, are plugged into mini banana plugs permanently mounted to the support table. The glass slide substrate is held in place on the sample holder by these leads which are soldered to the slide, with In-Sn solder (1). The sample holder blocks are bolted, face down, to the sample holder bases with two #4-40 screws. With this arrangement, the three sample holders may be easily removed from the system and the samples changed conveniently.

A special set of sample holder blocks were made in which custom heaters were installed. With these heaters, the sample holders and samples can be heated to several hundred degrees centrigrade. Provision for the heater leads and sample thermocouple in the banana connections were made also.

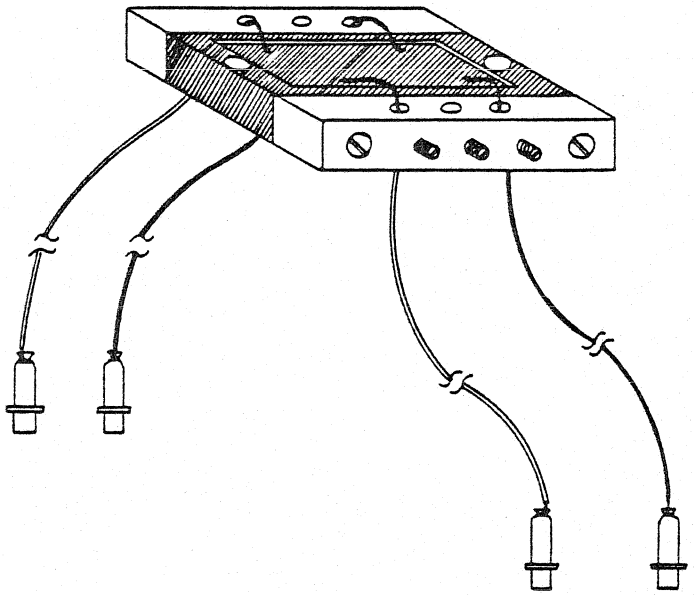

Fig. C2

With all these electrical connections, the electrical feedthrough became a problem. All together, 38 leads had to be accommodated, but standard O-ring sealed high vacuum feedthroughs generally have at most only twelve pins. Since the number of ports available was not large, a special feedthrough was designed. The body is a 4" x 4" x 3 ½" Al block machined so that the top seals to a 2" port on the bell jar base plate with an O-ring seal. Each side face of this block is machined to form a separate port to accommodate a Cooke Vacuum Products 11 pin electrical feedthrough (model V96-78-13). The center of this block is bored out to provide access between these feedthroughs and the inside of the vacuum system. In this way, 44 connections are inexpensively accommodated at a single 2" port.

The plasma discharge electrode and shield are fairly standard.

The mask and shutter arrangement was more difficult to design. The operator needs to be able to rotate the shutter to cover and uncover the samples. He also must move the masks away from the samples when a different set of masks are to be rotated into place. Due to a shortage of feedthrough ports (and funds) all of this has to be accomplished with a single rotary and linear high vacuum feedthrough. The feedthrough is an O-ring and grease sealed unit which has been modified to be pumped differentially. The design for the mask and shutter drive assembly is illustrated in Fig. C3. The mask and shutter are mounted on concentric shafts each with its own driven gear. One of these gears at a time is engaged by the drive gear which is connected back to the shaft of the rotary/linear feedthrough via two universal couplers and an expandable shaft (two concentric shafts which may slide lengthways with respect to each other but cannot rotate

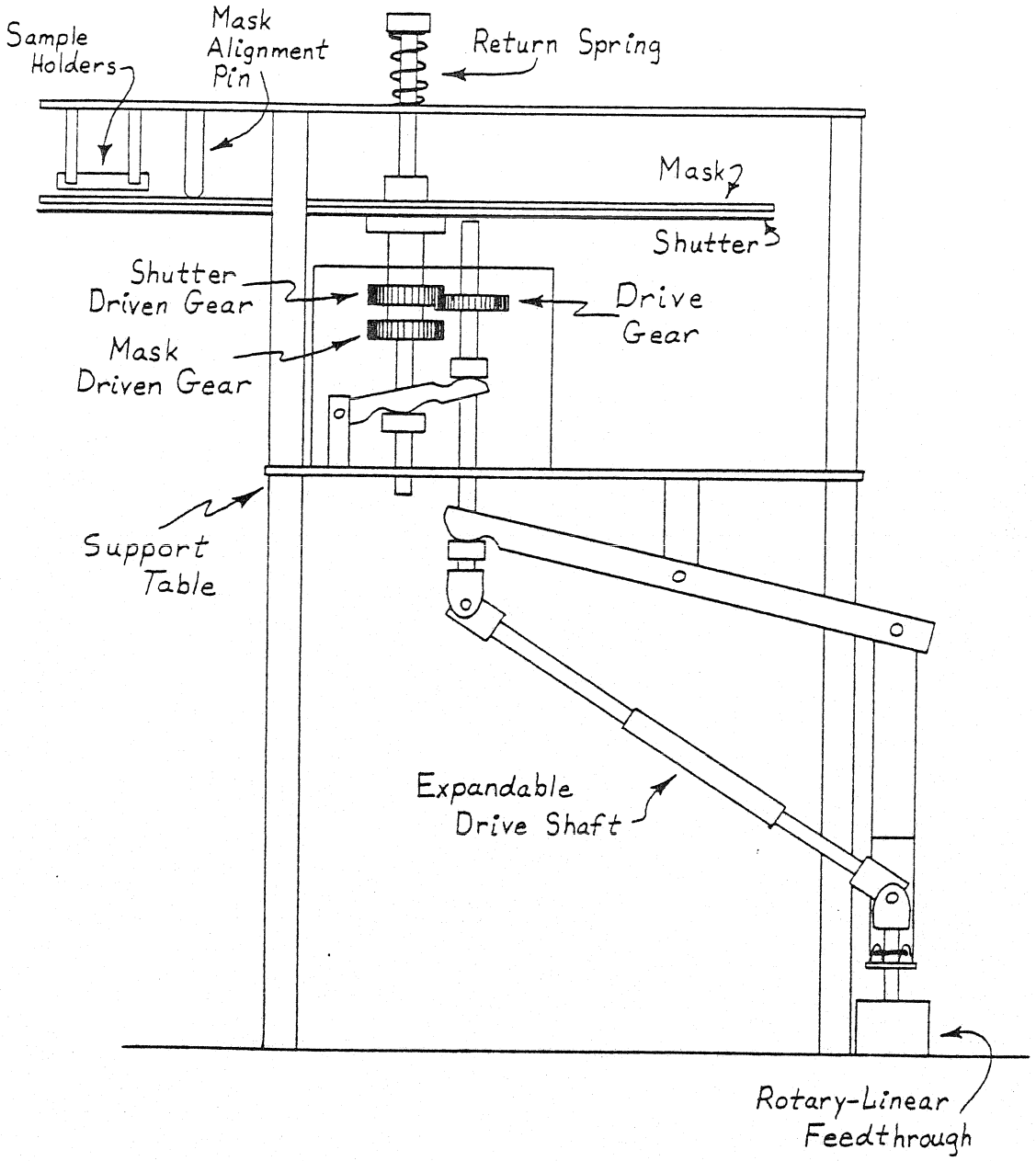
Sample Holders
Mask Alignment Pin
Return Spring
Mask
Shutter
Shutter Driven Gear
Drive Gear
Mask Driven Gear
Support Table
Expandable Drive Shaft
Rotary-Linear Feedthrough

Fig C3 (a)

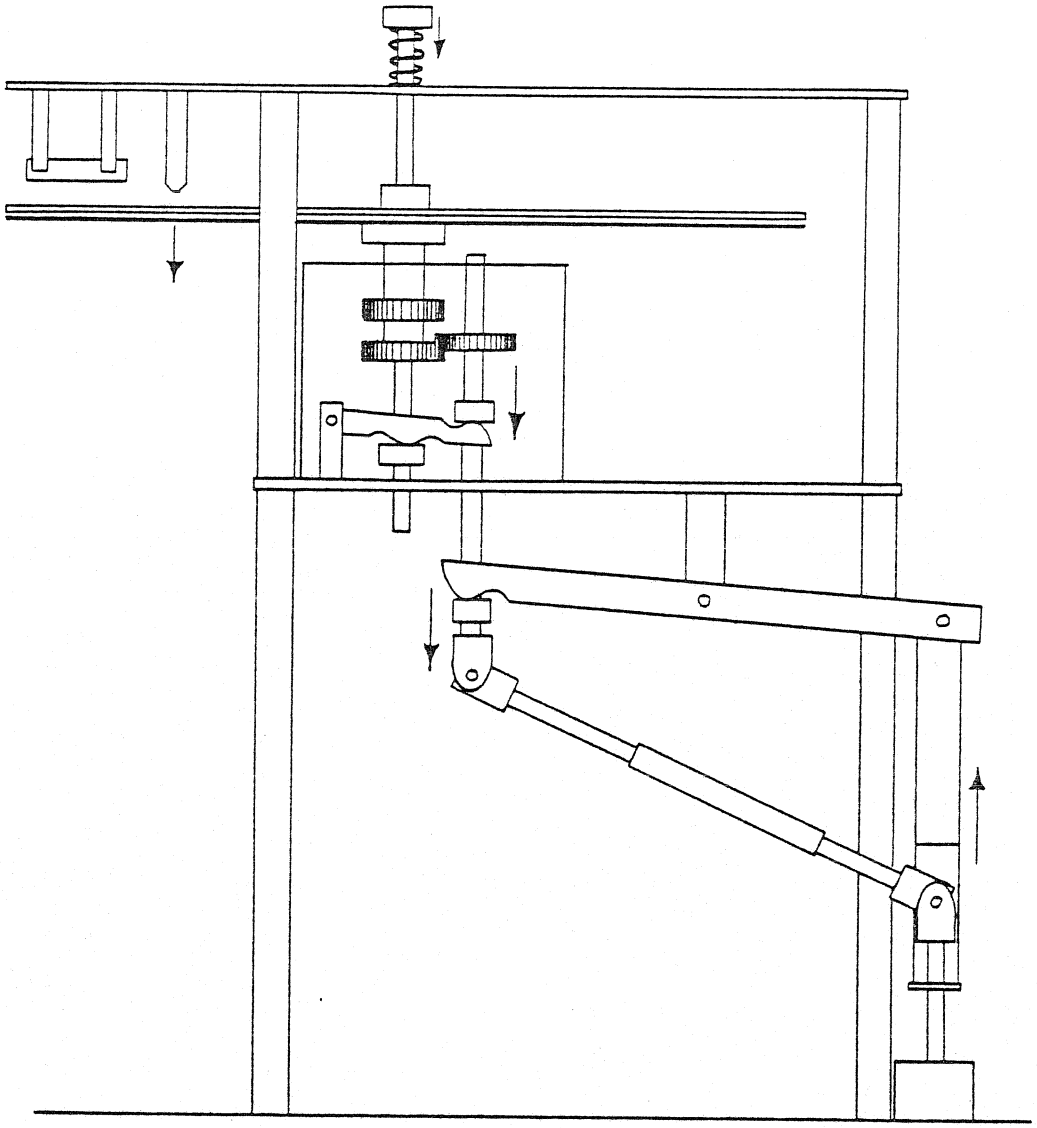

Fig. C3 (b)

independently). With the assembly in the normal, up, position shown in Fig. C3(a), the drive gear engages the shutter driven gear and the masks are locked in position by an alignment pin. The shutter may now be rotated by turning the shaft of the feedthrough. The shutter is positioned visually by the operator, a portion of the bell jar being kept free of evaporated metal by a shield to provide a window for this. To change masks, the following things occur (illustrated in Fig. C3(b)): Pushing in on the rotary/linear feedthrough shaft forces the back of a lever arm up, the front of which, in turn, pushes the drive shaft down. The drive shaft is coupled to the driven shafts through a second lever, so when the drive shaft is pushed down, the shutter and mask assembly is also forced down. Since the drive shaft moves down approximately twice as far as the driven shaft, the drive gear moves from being engaged with the shutter gear down to being now engaged to the mask gear. At this point the masks have moved an additional 1 to 1 ½ cm away from the samples. By turning the feedthrough shaft, a new set of masks may be rotated into position. The masks are approximately aligned visually. When inward pressure is released from the feedthrough shaft, a coil return spring on the driven shaft forces the mask and shutter assembly back up. A tapered alignment pin rigidly mounted to the support table is fit into one of a set of holes in the mask assembly to align the masks over the samples accurately. The assembly is now back in its up position with the shutter engaged.

The shutter itself is simply a stainless steel disk with a 90^{o} arced slot approximately 5 cm wide cut in one edge. This slot allows all three samples to be exposed simultaneously. On the opposite side of the disk is cut another slot, this one only large enough to expose one sample at a time.

This disk is bolted to a collar which in turn is bolted to a short section of ½" stainless steel tubing which serves as the shutter driven shaft. This shaft fits outside a section of 3/8" stainless rod which serves as the mask driven shaft.

The mask assembly consists of several sections. Four radial arms 90^{o} apart are mounted to the 3/8" driven shaft. Three mask support plates are mounted to these radial arms, completing 3/4 of a disk. Each mask support plate holds one set of masks: one has the masks for the Al strip, the second has the mask for the Pb strips, and the third holds blank masks. The masks themselves are 1" x 1 3/4" x 0.05" Al plates into which the appropriate patterns are milled. The fourth segment of the mask assembly is left open to expose all three samples completely, as is necessary during the oxidation and adsorbate exposure stages of the fabrication.

The vacuum chamber is connected to a gas handling manifold which is discussed in detail elsewhere (1).

This vacuum system has proved to be a very versatile tool.

The MkII fabrication system is a third generation unit that has been designed and is presently being assembled. This system is based on a Varian ion and titanium sublimation pumped ultra high vacuum system with a base pressure below 5×10^{-10} torr. The system was supplied with a 12" x 14" glass bell jar mounted on an 11" x 36" cylindrical stainless steel chamber upon which are mounted ten conflat flanged feedthrough ports and a roughing line port. The system is roughed out by two sorption pumps. To minimize chamber volume and to do away with the large glass surface area, the glass bell jar has been replaced by a flat stainless steel plate. A good vacuum seal between the top plate and the chamber was obtained by

two concentric viton O-rings mounted in the top plate, the region between the O-rings being differentially pumped.

The system was designed so that all components related directly to the sample holders and samples are mounted on the top plate; while the evaporation sources, discharge electrode and shield, and any miscellaneous components reside in the lower chamber.

The top plate consists of a 14" x ½" stainless steel disk with three grooves near the outer edge of (inner) diameter 12", 12 ½" and 13". The inside and outside grooves are for O-rings while the 12 ½" groove is evacuated by a mechanical pump, providing a differentially pumped seal. Six feedthrough ports are welded into the top plate. Two ports are for the cold fingers upon which the sample holders are mounted, two ports are for 8-pin UHV electrical feedthroughs and two (mini-conflat) ports are for UHV bellows sealed rotary feedthroughs: one of these drives the mask assembly, and the second holds the shutter. Fig. C4(a) shows the layout of the inside face of the top plate with only the sample holders in place; and Fig. C4(b) shows the plate with shutter, mask assembly, deposition monitor head and electrical feedthroughs in position. A shield will be present over the electrical feedthroughs to prevent evaporated metal from shorting the leads.

The sample holder assembly is based on previous designs. Due to lack of space, provision for only two sample holders was included. This had the benefit of simplifying the design of several other components of the system, as compared to the MkI system. The sample holder itself is very similar to the MkI design except that the Macor blocks are replaced by four individual Macor clamps which hold the wire leads to the sample holder. These ceramic

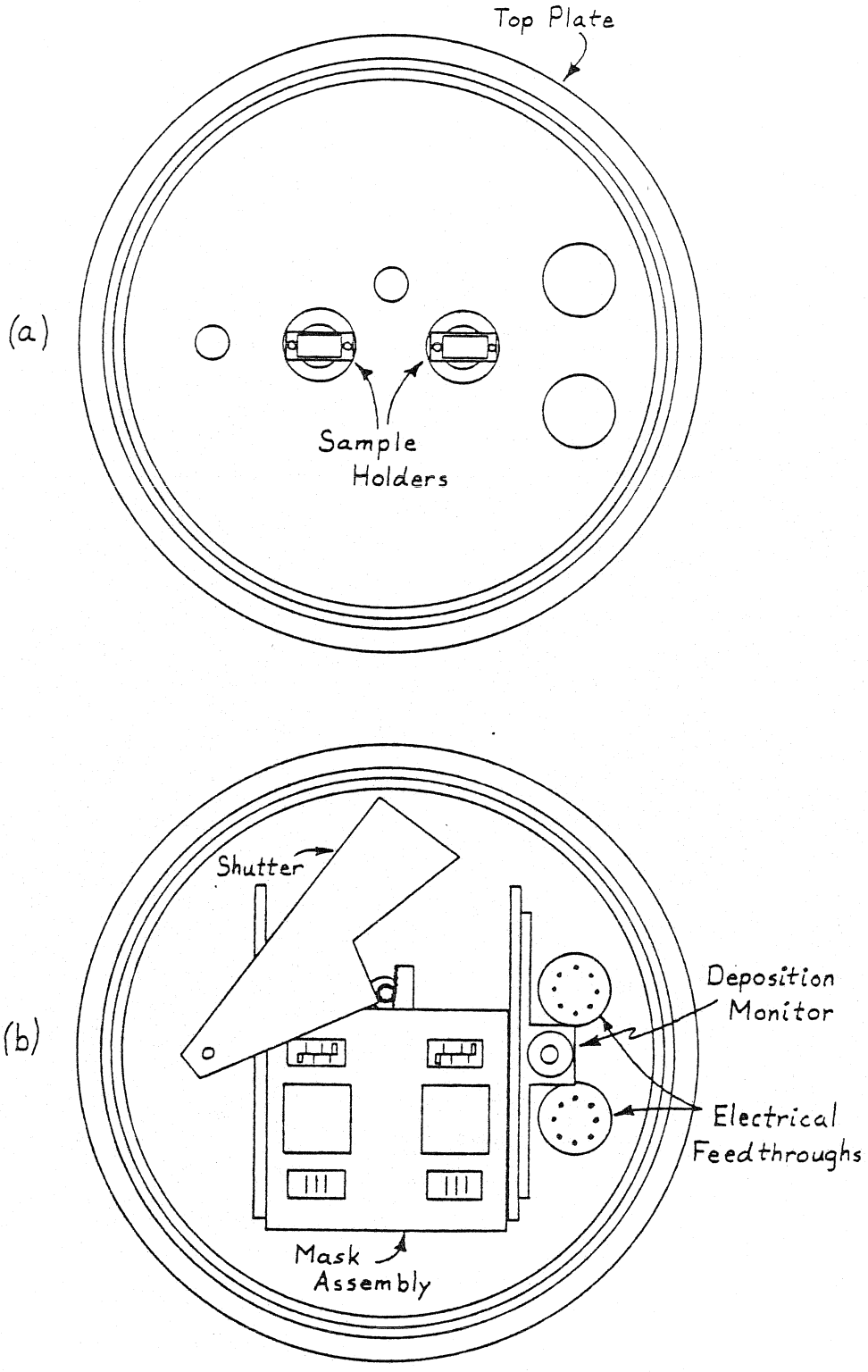
Top Plate
(a)
Sample
Holders
(b)
Shutter
Deposition
Monitor
Electrical
Feedthroughs
Mask
Assembly

Fig. C4

clamps are much simpler to make and are more durable than the tapped ceramic blocks. The sample holders are clamped to 1" stainless steel cold fingers by means of split ring assemblies as shown in Fig. C5. The two split rings are not identical. Liquid nitrogen may be poured into the cold fingers to cool the samples. The samples may also be heated from outside the vacuum system. The heaters consist of copper plugs into which fit 3/8" x 1 3/8" Hotwatt cartridge heaters. The plugs then fit snugly in the bottom of the cold finger. Since these cold fingers are subject to severe temperature cycling, they are more likely to develop leaks than if there were no cycling. So as not to disable the entire system if one cold finger develops a leak, these cold fingers are mounted on 2 3/4" conflat flanges and may be removed from the top plate after removing the sample holders and split ring assemblies. This makes repairs much more convenient than if the cold fingers were welded directly to the top plate.

The mask assembly is positioned in front of the sample holders. This assembly, illustrated in Fig. C6, consists of a support table, a slide which holds the masks, the masks themselves, and an UHV rotary feedthrough upon which is mounted a pinion gear. The masks themselves are identical to those used in the MkI system. The slide has four guide pins which fit into slots milled into the sides of the support table. A rack gear is mounted to the slide and meshes with the pinion gear of the rotary feedthrough. Thus, by rotating the feedthrough, the slide may be moved back and forth with respect to the table. The slots in the table are positioned so that when the slide is positioned as far as it will go in either direction, the appropriate masks will be correctly positioned in front of the samples. These positive stops remove the necessity of any visual alignment

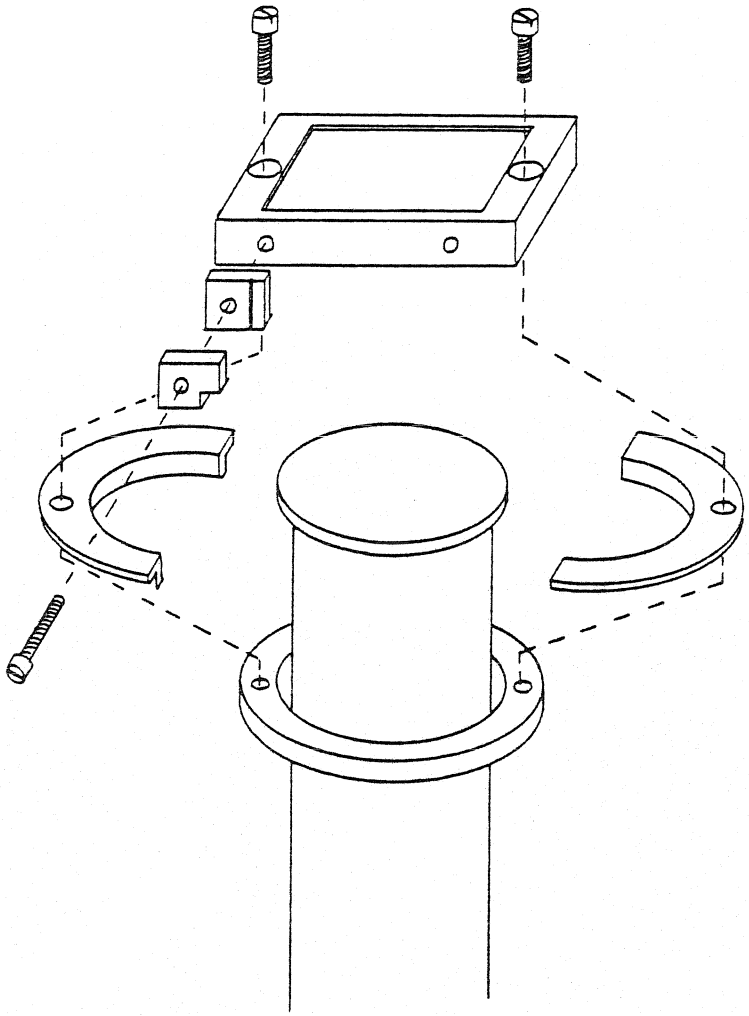

Fig. C5

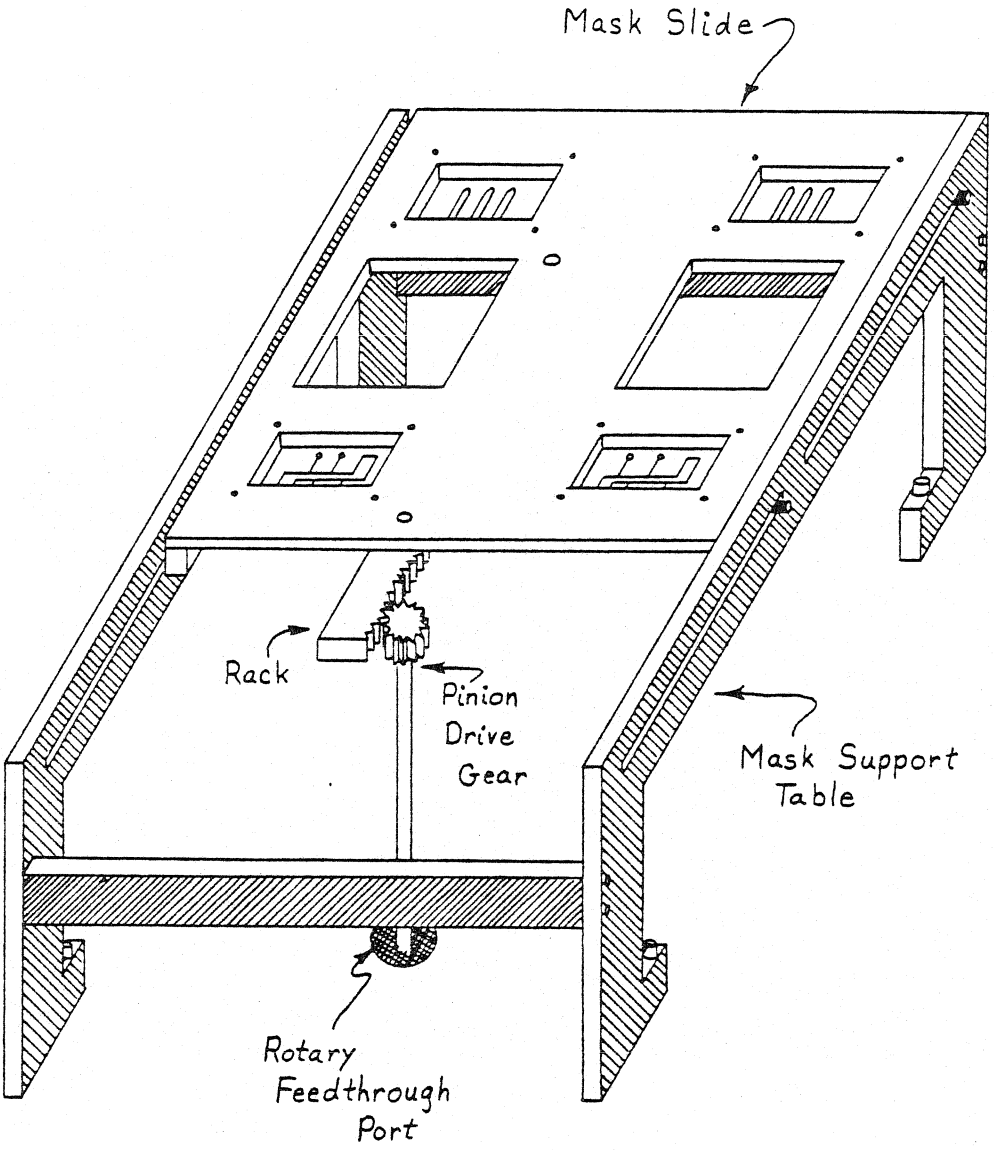
Mask Slide
Rack
Pinion
Drive
Gear
Mask Support
Table
Rotary
Feedthrough
Port

Fig. C6

of the masks. The center, open, position of the slide may be positioned easily by turning the rotary feedthrough 1.5 turns away from either stop. The support table is firmly bolted to the top plate. To gain access to the sample holders, the two guide pins on the rack end of the slide are unscrewed and the slide flipped out of the way, as shown in Fig. C7.

The shutter, seen in Fig. C4(b), is a thin stainless blade designed so that none, one, or both of the samples may be exposed, depending on how the shutter is positioned. The position of the shutter is determined by an indicator flag attached to the outside of the rotary feedthrough to which the shutter is mounted.

The deposition monitor oscillator head is mounted to a support beside the mask support table at the same level as the samples, as seen in Fig. 4(b).

Electrical connections to the outside are provided by two 8-pin feedthroyghs. All insulation on the wire leads is UHV compatible, and for the most part, ceramic.

The lower section of the vacuum chamber holds the rest of the vacuum components. These include : (1) The evaporation sources for metal deposition (three are provided); (2) The plasma discharge electrode and shield; (3) Both a Millitorr gauge and a nude ionization guage so that pressures between 10^{-1} and 10^{-11} torr may be monitored; (4) A port connecting the chamber to the gas handling manifold, described elsewhere (1); (5) A small EAI quadrupole mass spectrometer to monitor background gasses, adsorbates and, possibly, reaction products; and (6) A liquid nitrogen trapped 2" Varian oil diffusion pump.

The evaporation sources are basically the same as before. The

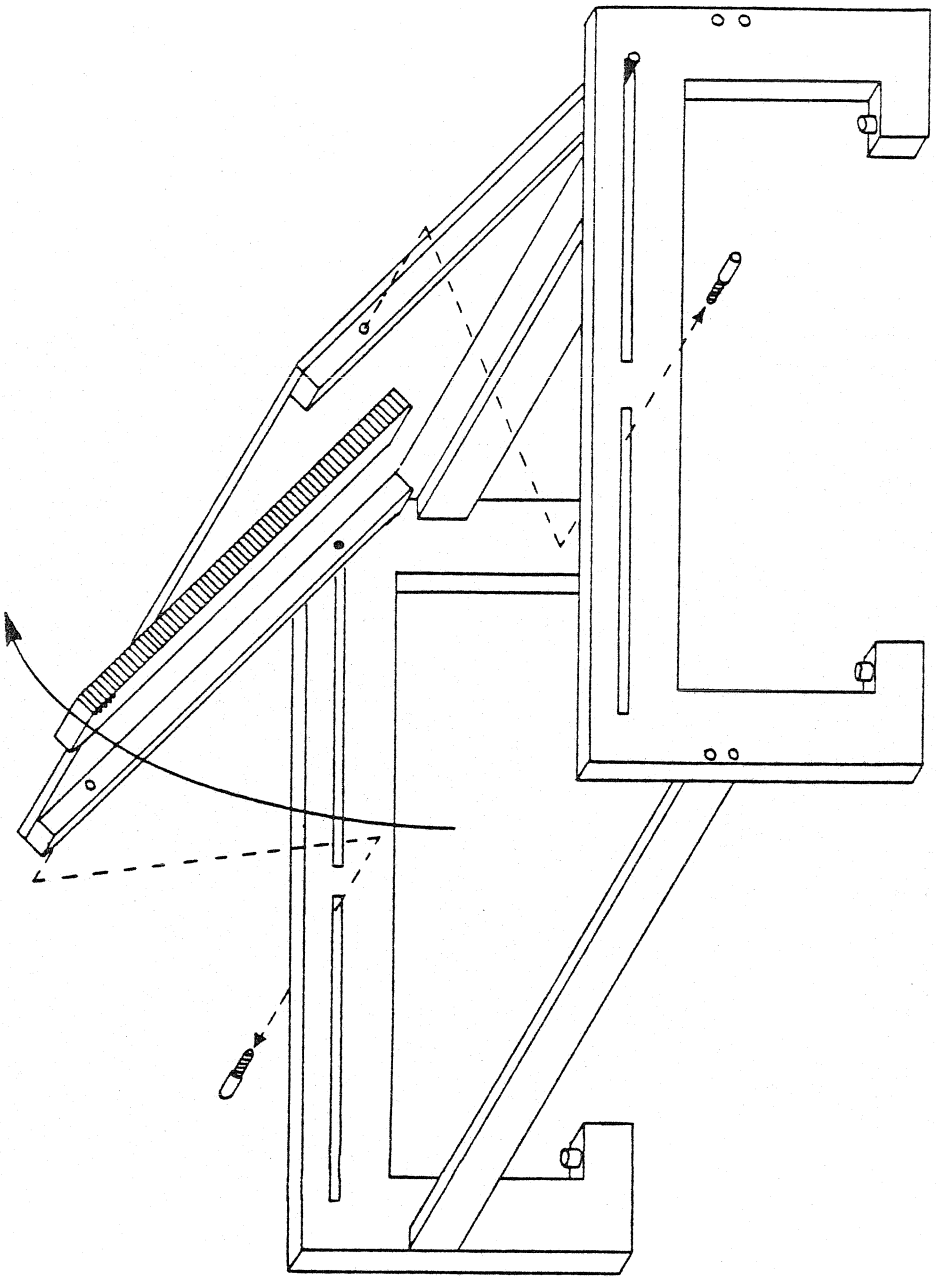

Fig. C7

connections are made from OFHC copper stock and extend down into the chamber approximately 32 cm, approximately 25 cm away from the samples. The sources are positioned so that both samples are the same distance from each source. Again, stainless steel shielding is placed around the sources. However, in this system, the shield between sources is a thin double wall. Thus, evaporating metal from one source will not directly heat (and possibly evaporate) metal which had been deposited on the shield in an adjacent source chamber. Electrical connections to the outside are through individual medium and high current UHV feedthroughs. Power is supplied by a Varian 2 KVA filament power supply.

The plasma discharge arrangement is basically the same as in the previous two systems. The power supply for this is a Varian glow discharge unit.

The diffusion pump was added to the system to aid in pumping down the system. The sorption pumps quickly evacuate the chamber to about 10^{-3} torr. However, the (old) Varian ion pump is very ineffective above 1×10^{-5} torr. The sublimation pumps help somewhat in this range, but it is still time consuming in going between 10^{-3} and 10^{-5} torr. This is the range in which a diffusion pump is very effective. Thus, using sorption pumps to 10^{-3} torr, diffusion pump between 10^{-3} and 10^{-6} torr, and an ion pump and a Ti sublimation pump below 10^{-6} torr, the system can be rapidly evacuated to low pressure. Since the diffusion pump is only open to the system a short time contamination from backstreaming is negligible.

The mass spectrometer should be very useful in determining exactly what the sample is being exposed to. It may also be useful in determining reactions by detecting products which may appear during exposures.

This system should prove to be the most versatile fabrication system of the three.

To conclude, basic design considerations for IETS junction fabrication systems have been discussed, and three examples of actual systems have been described.

References

1. H. E. Evans, PhD Thesis, California Institute of Technology, 1980.

2. L. Holland, Vacuum Deposition of Thin Films, Wiley, N.Y., 1956, p. 141.

Appendix D

An XPS Investigation of Alumina Thin Films Utilized in IETS

Abstract

X-ray photoelectron spectroscopy (XPS) has been applied to characterize a number of different aluminum oxide (alumina) thin films utilized in inelastic electron tunneling spectroscopy (IETS). Since IETS has been found to be an effective means for obtaining vibrational information on catalytic systems, reliable means of clarifying the exact relationship between the IET thin film "model" catalysts and high surface area commercial aluminas are of considerable importance. XPS data might profitably provide such a means of comparison, although sufficiently reliable XPS data for commercial samples are not currently available. The various thin film aluminas are characterized as to their chemical nature, chemical state distributions, and relative oxygen-to-alumina concentration ratios by analysis of peak positions, peak widths and peak intensities, respectively. Moreover, effects due to heating and halogenating the surface have been investigated independently, since these are commonly utilized to enhance the catalytic behavior of commercial aluminas.

1. Introduction

Inelastic electron tunneling spectroscopy (IETS) is a valuable experimental technique for probing the vibrational structure of molecules near insulating (metal oxide) surfaces (1). In particular, IETS has shown significant promise as a means of monitoring structural changes characteristic of catalytic reactions. This has been demonstrated for systems involving both alumina and alumina-supported metal catalyst surfaces. Specific examples of work in this area include studies of CO chemisorption on alumina-supported Rh particles (2), the adsorption of ethanol on Ag particles supported on alumina (3), and the formation of surface ethoxide and acetate structures during ethanol adsorption on alumina (4), with comparisons to corresponding acetate structures observed for adsorbed acetaldehyde and acetic acid (5). Important results have also been obtained recently for metal cluster compounds adsorbed on alumina. The structure of adsorbed chlorodicarbonylrhodium dimer, $[RhCl(CO)_2]_2$, has been observed and compared with the previous results of CO adsorption on supported Rh particles (6); and the polymerization reactions of ethylene, propylene and acetylene have been studied over $Zr(BH_4)_4$ complexes supported on alumina surfaces (7).

Widely used industrially as catalysts and catalyst support materials, there are a number of different forms of alumina. Some of the known, distinct types of alumina are listed in Table 1, and additional forms are continuing to be discovered or synthesized. These various forms can differ slightly from one another in crystal structure. Variations exist also in the relative amounts of bulk hydration, ranging from extremely "dry" α-alumina (Al_2O_3) to forms such as tucanite ($Al_2O_3 \cdot 3.5\ H_2O$) which can

contain significant amounts of interlamellar water. Most of the more catalytically active aluminas have been found to contain from a few tenths to several percent H_2O, being characterized by the formula $Al_2O_3 \cdot nH_2O$, where $0 < n \lesssim 0.6$. A number of excellent references are available detailing the physical as well as the catalytic properties of aluminas (8, 9). An important point is that the catalytic properties are determined by the exact form of alumina being utilized, which, in turn, depends markedly on the origin and preparation of the alumina. This dependence of catalytic properties on preparation technique has often led to disagreements between catalytic results obtained in different laboratories. Indeed, it has been noticed that results obtained with the same catalyst can vary with time as subtle changes occur in the nature of the catalyst, particularly when even a small amount of hydration or dehydration takes place (10).

The alumina surfaces utilized in IETS studies to model commercial aluminas are formed by oxidizing the top 20 - 30 Å of an aluminum electrode which has been evaporated in the form of a thin strip onto a clean ceramic substrate. After the desired reactants are allowed to adsorb and interact on the surface of this thin oxide layer, IET samples are completed by the evaporation of top metal electrodes. Electrons tunnel through the oxide barrier when a voltage is applied across the sample, and they can lose energy during the tunneling process by exciting vibrational modes of molecules in, or near, the barrier region. Such excitations can occur only when the applied bias voltage is greater than, or equal to, an energy equivalent to a vibrational excitation. These excitations lead to small increases in the tunneling current which become peaks when d^2V/dI^2

(proportional to the second derivative of tunneling current with respect to voltage, d^2I/dV^2) is plotted against the applied voltage, V. Peak positions in this representation are indicative of vibrational excitation energies and have been shown to yield analogous information to that obtained by optical techniques such as infrared and Raman spectroscopies. Complete experimental and theoretical details of IETS are available in the literature (11).

Formation of the thin oxide films on the aluminum underlayer in IETS studies has been accomplished in a number of ways, including (1) exposure to a plasma discharge of pure O_2, H_2O or a mixture of the two (12), (2) immersing briefly in liquid H_2O external to the vacuum system (13), and (3) heating in air (14). In view of the complexities associated with the commercial aluminas outlined above, we can expect that each of these oxidation procedures might possibly produce an alumina film with unique structure, degree of hydration and catalytic activity. The limited experimental evidence available on thin alumina films indicates that this is indeed the case. These results will be discussed together with those of the current study in Sec. 3. It is important, therefore, to characterize IET aluminas prepared by different methods in order to make valid comparisons between results obtained on the various surfaces. Also, it is clear that IETS studies of these model alumina catalysts will be of maximum value if correlations can be made with commercial aluminas. Only one study has been attempted in this area heretofore (50).

The current study was performed in order to characterize alumina films prepared by the various oxidation procedures utilized in IETS experiments to facilitate comparisons among them, as well as to provide

characteristic information which might be related also to commercial aluminas. X-ray photoelectron spectroscopy (XPS) was utilized in this investigation. It is capable of providing information concerning the environment of separate chemical elements near the surface. Various amounts of bulk hydration, or even different crystal structures, produce shifts in the binding energies of core level electrons which are revealed in XPS. Details of XPS experiments are available elsewhere (15). This technique has been applied here to characterize the thin oxide layers formed on clean, evaporated Al films by some of the oxidation techniques employed in IETS studies reported in the literature. Also, since halogen atoms are often added to aluminas as "promoters" of greater catalytic activity, we have studied the effects of fluorination of some of the separate oxide surfaces, and on one particular surface have examined perturbations due to varying degrees of fluorination. The adsorption of chlorine on one surface was studied also. Details of experimental procedures and results are presented and discussed in the following two sections. Our conclusions are presented in Sec. 4.

2. Experimental Details

Samples were prepared in an oil diffusion pumped bell jar with a base pressure of 10^{-7} torr. Aluminum (Balzers 99.99%) was evaporated to a thickness of 1000 Å onto clean 10 mm x 12 mm glass substrates cut from #2 thickness (0.2 mm) glass cover slips. The top few atomic layers of the aluminum were then oxidized by one of the methods reportedly used to form alumina surfaces in IETS studies of model catalyst systems. The

various oxidation procedures are listed in Table 2. After oxidation, the samples were transported in a desiccator under nitrogen to the XPS spectrometer.

XPS measurements were accomplished in a modified HP-5950A ESCA spectrometer with a base pressure below 10^{-9} torr. A more complete description of the particular instrument utilized in this study is presented elsewhere (16). A sample preparation chamber is connected directly to the spectrometer and consists of a stainless steel dry box with an introduction lock. A positive pressure of five psi of nitrogen dried over LN_2 is maintained at all times inside the sample preparation box. Inside this chamber, samples were removed from the desiccator and mounted between a gold backing platen and a gold window placed on the top surface of the sample, then attached to a probe and inserted through an interlock into the spectrometer. The gold platen and window are utilized routinely in these procedures to minimize undesirable charging of insulator and semiconductor surfaces, although this is not expected to be relevant in the current study. Further comments and a discussion of charging effects are presented below.

Some samples prepared by the same oxidation techniques listed in Table 2 were exposed to vapors of HF and HCl. This was accomplished by opening a container of one of the acids inside the sample preparation chamber. For heavy (saturation) exposures, samples were placed alongside the open container for up to one minute. Lower exposures could be obtained by first removing the acid container before placing samples inside the chamber. Both high and low exposures of HF were studied on O_2 discharge (type 1) samples. A high exposure of HCl to this type of

surface was also studied. Low exposures of HF on types 3 and 5 of oxidized aluminum, as well as on O_2 discharge samples subsequently exposed to HCl, were similarly investigated.

XPS measurements were made at room temperature utilizing a monochromatized beam of X-radiation from an aluminum ($K\alpha$ = 1486.6 eV) source. Channel sampling densities ranged from 0.03 to 0.04 eV/channel. Typical signal-to-noise characteristics are illustrated in Fig. 1, which shows representative spectra of an O1s line and an Al2p line, these being two of the most important spectral features monitored in this study. A number of samples prepared according to one specific set of conditions were measured to check reproducibility and establish error limits. Each sample was first observed with a wide scan from a binding energy of zero to 1280 eV to determine basic elemental composition. A typical wide scan is shown in Fig. 2a, which is a spectrum for a low exposure of HF on alumina prepared in an O_2 discharge. This was followed by a closer examination of particular peaks of interest, such as the Al2p, Al2s, O1s, O2s, C1s, F1s, Cl2p and/or Cl2s lines. On some samples the oxygen KLL Auger transition near 980 eV was studied also.

3. Results and Discussion

The XPS technique has been utilized previously to distinguish various oxidation states of metals such as Ni (17), Mg (10), Pb (18), Cu (19) and Pt (20). In another recent detailed study, Grunthaner et al. (21) have observed a number of Si oxidation states within a thin oxide film grown on Si. Thus, the XPS spectra can be expected to reveal differences in structure and stoichiometry among the variously oxidized alumina films if such

differences actually exist. There is significant experimental evidence which indicates that such differences will indeed be present. Fundamental studies of the initial oxidation of Al single crystals (22.23), as well as of polycrystalline (evaporated) Al films (24), have demonstrated that aluminum can exist over a range of oxidation states within thin oxide layers. Using XPS, oxide formation on evaporated films was noted, the exact nature of which depended entirely on the extent of oxygen exposure. This variation in the nature of the oxide was determined by observing a continuous shift in the oxide Al2p peak position from a binding energy of 75.4 eV to 75.7 eV as a function of oxygen exposure. On the (111), (110) and (100) surfaces of Al single crystals, three separate initial interaction mechanisms between oxygen and aluminum were reported. On the (110) surface, it was found that oxygen adsorption causes a surface reconstruction, and that oxygen atoms are bound to more than the first layer of Al atoms. For the (111) plane, no reconstruction or bonding to lower substrate levels of Al atoms was observed. Initial stages of oxygen adsorption on Al(100) left a surface layer of clean Al, all the oxygen atoms being incorporated into the bulk below the surface. These results illustrate that a variety of Al-O compounds and interactions can occur in surface oxide layers.

Structural variations might cause, or result from, different aluminum-oxygen coordinations. Although oxide films such as those used in IETS experiments are generally considered to be amorphous, this is not necessarily the case. Herfert (25) has observed structural variations in anodic films on Al depending on preparation conditions. Both crystal-

line and amorphous films, as well as mixtures of the two, were observed. Other results have confirmed this observation (26 - 28). Even though XPS is not necessarily capable of determining structural parameters, it does reflect the distinct chemical environments created by different structures. Herfert (25) found also that anodic films could be hydrated to a greater or lesser extent as a function of the precise conditions during formation. This parallels the work of Bowser and Weinberg (12), who, in an extensive IETS study, have shown that it is possible to vary the degree of bulk hydration in alumina films by varying the substrate temperature while oxidizing in a plasma discharge of H_2O vapor. Hydration would not only result in peak position shifts in the XPS spectra, but also in changes in the ratio of aluminum to oxygen concentrations. Relative concentrations can be determined approximately by monitoring XPS peak intensities. Finally, observed variations in catalytic activity indicate also differing types of aluminas among the alumina films utilized in IETS. For example, significant differences in the number of active sites for acetaldehyde adsorption at room temperature can be seen when comparing IETS results of Evans and Weinberg (5) with those of Brown et al. (29), even though oxide films in the two studies were formed in relatively similar manners.

In agreement with our anticipations, oxide layers grown on evaporated Al films via procedures outlined in Table 2 are each characterized by unique XP spectra. Peak positions for the various alumina films are presented in Table 3 (numerical form) and in Fig. 3a (graphical representation). In both cases, peak positions are tabulated relative to the Al 2p line from bulk aluminum underlying the thin oxide layer, which is detectable since the oxide thickness is less than the escape depth for these photoelectrons of high kinetic energy. This difference could be determined

much more precisely (deviations less than ± 0.05 eV) than could absolute peak positions due to the difficulty of determining accurately the exact onset of the Fermi level. Absolute peak positions can be determined by adding the binding energy of Al 2p electrons for bulk aluminum to the values of Table 3. Various studies report this value as lying between 72.6 (30,31) and 75.0 eV (32), although the most reliable value for this binding energy is perhaps 73.0 eV (24). The first five samples listed in Table 3 and Fig. 3 correspond to alumina layers formed by the various oxidation procedures listed in Table 2. In much of the following, other samples will be related to the O_2 discharge-oxidized alumina since that is the procedure utilized in our IETS experiments. Aluminum and oxygen electronic levels for the thermally oxidized alumina appear at energies 0.15 to 0.3 eV lower than corresponding levels for O_2 discharge samples. In the case of H_2O discharge-formed alumina, aluminum levels are approximately 0.15 eV higher and oxygen levels approximately 0.15 eV lower than for the O_2 discharge. Aluminas formed by direct contact with liquid water show larger shifts to higher binding energies relative to the positions of O_2 discharge peaks, being on the order of 0.25 eV for Al 2p and 2s levels, and approximately 0.3 and 0.6 eV for the O1s and 2s levels, respectively. Heating oxide layers formed in an O_2 discharge above 850 K causes a rather uniform shift of from 0.3 eV to 0.6 eV to higher binding energies for both the aluminum and oxygen peaks. Shifts to higher energies for both aluminum and oxygen levels with heating has been noted earlier in studies of thin aluminum oxide films (33).

Few, if any, general trends are evident in examining the data. Thermally oxidized alumina appears to be more similar to O_2 discharge

samples than to samples heated after plasma oxidation. Likewise, alumina formed in a discharge of H_2O is more similar to O_2 discharge-formed alumina than to that formed in liquid H_2O. Since immersion of aluminum in water is known to yield a product similar to boehmite, containing 18 to 45% by weight of H_2O (34,35), this seems to indicate that the range of aluminas that can be prepared with an H_2O discharge (as discussed above) is more closely related to catalytically "active" aluminas (containing significantly less H_2O) than to less active alumina mono- or trihydrates. Relative peak intensity data, presented in Table 4, indicate H_2O or OH concentrations for the various aluminas in the order liquid H_2O > H_2O discharge > O_2 discharge > thermal O_2 > heated in argon. There is no obvious correlation between peak positions and O/Al concentration ratios. Although Pitton, et al. (36) proposed that oxide peak positions decrease with progressive loss of water, more thorough studies have shown that this is actually opposite to the behavior exhibited by magnesium oxide and hydroxide (10), and by commercial γ- and α-aluminas (37). It appears, therefore, that no generally applicable correlation can be made between water content of these oxides and XPS peak positions at this time. In connection with discussions concerning extents of hydration, it should be noted that several difficulties are encountered when attempting to extract valid concentration information from peak intensity data. For example, pumping in vacuum can affect chemical structures, especially by dehydration reactions, an effect which has been observed previously (38). The possibility exists also that this is not necessarily a uniform effect, i.e., dehydration and/or structural rearrangements in vacuum may occur more readily with some types of samples than with others. Even beyond these possible changes in oxygen and aluminum concentrations during measurements in vacuum, a determination of absolute concentrations from XPS peak intensity measurements is approximate at best.

XPS peak intensities can be affected by a number of factors, such as contamination, analyzer and detector efficiencies, X-ray source photon flux, etc. (39). These can vary signficantly from instrument to instrument, sample to sample, or even as a function of time. Based on previous studies in the literature, it appears that even the most precise absolute intensity measurements can only be repeated within approximately 30% (40). Madey et al. (38) have reported that although absolute intensity measurements are unreliable, consistent trends can be reproduced by measuring relative peak areas. Using this approach to present the intensity data in this study (see Table 4) has indicated that repeated measurements of relative intensities are consistent to within approximately ± 3%. Finally, a determination of even concentration ratios is complicated by an incomplete understanding of exact photo-ionization cross-sections for the various elements and electronic levels (as indicated in Table 4). Therefore, we believe that the information presented in Table 4 for relative oxygen and aluminum concentrations accurately represents general trends among the various aluminas, although it may not be an accurate indication of absolute concentrations of the individual chemical elements.

Data for aluminas exposed to HF and HCl are presented also in Fig. 3 and Table 3. Lower exposures of HF on O_2 discharge, H_2O discharge, or the heated (in Ar) samples had little effect on the oxygen or aluminum peaks. Absolute determination of the fluorine concentrations is uncertain, as discussed above. Our best estimates indicate a coverage of from 0.1 to 0.33 monolayer. Relative intensity measurements indicate the same fluorine coverage in each case. Preheating the alumina can be seen to have a definite effect on the F1s binding energy, shifting it to approximately

0.75 eV higher binding energy than for the unheated O_2 discharge alumina. Samples listed as "Exposed to HF" and "Exposed to HCl" represent, respectively, samples oxidized in an O_2 discharge and exposed subsequently to more extensive amounts of HF, or to lower amounts of HF followed by HCl. Extensive exposure of samples oxidized in an O_2 discharge to HF more than doubles the surface fluorine concentration. O_2 discharge oxidized samples first exposed to the lower amounts of HF and then to more extensive amounts of HCl have approximately equivalent F and Cl concentrations on the surface. Higher halogen concentrations also shift peaks to higher binding energies, but this has less effect on the F1s peak than does preheating. Also, increasing halogen concentration has the same effect on the nature of the F1s level regardless of whether fluorine or chlorine is being added to the surface.

One unexpected feature of this study resulted in an increased awareness of the possible introduction of impurities into samples with few obvious means of detecting them. Even low levels of impurities can greatly affect catalytic properties. For example, Rubinshtein, et al. (41) found that previously reported observations of apparent H_2 adsorption on Al_2O_3 were actually due to reduction of Fe_2O_3 impurities. The XPS samples used in this study were prepared over the course of a number of months. At one particular time, XPS samples were prepared within a few days after the vacuum system had been utilized to prepare IETS samples with ferrocene adsorbed on the alumina. While the base pressure of the vacuum system remained at a constant level over the time elapsed in making these junctions, the XPS samples made later showed a great deal of Fe contamination, as shown in Fig. 2b. Although the incorporation of Fe impurities into the IETS alumina films could significantly alter their catalytic properties, the possibility exists that such impurity-induced

perturbations might mistakenly be attributed only to alumina-adsorbate interactions. Additional pumping with intermittant oxygen discharges removed the source of Fe impurities from our sample fabrication system. Based on our experience in this case, we feel that care needs to be taken to insure against unwanted (and, worse yet, unknown) impurities which might alter the nature of an experiment and lead to misinterpretations of the data.

Widths of XPS peaks, although functions of several variables, are indicative of the distribution of chemical states for a particular element. Data for the full-width at half-maximum (FWHM) of the Al 2p, Al 2s and O 1s levels of the various alumina samples are shown in Table 5. With the exception of the sample containing the Fe impurity, little variation is seen in widths of the Al 2p and 2s levels. The width of the O 1s level appears to be more sensitive to variations among the oxide samples. In particular, it is interesting to note that the presence of halogens broadens the peak by approximately 0.4 eV. Heating tends to cause a significant sharpening of the O 1s chemical state distributions, since the peak widths for samples heated in argon after oxidation and samples oxidized thermally are at least 0.3 to 0.4 eV less than corresponding peak widths for any of the other samples. Also, the O 1s peak widths for the heated and thermally oxidized samples are extremely similar, even though peak positions indicated very little similarity between these two types of samples. Again, although Pitton, et al. (36) claim a correlation between peak position and peak width (the peak width having an inverse relationship to shifts in the binding energy), no general correlation is apparent in our data.

In principle, the XPS data offer an excellent means of comparison

between thin films of oxidized aluminum and samples of commercial aluminas since the results include information on chemical composition, chemical environments of each of the separate elements, relative elemental concentrations, and distributions of distinct chemical states. At the present time, however, attempts to relate the alumina films to commercial bulk aluminas are complicated by the absence of sufficient, reliable data on the bulk samples. Difficulties arise in attempting to obtain data on bulk aluminas due to charging effects, a common problem for photoemission from semiconducting and insulating surfaces. The presence of positive or negative charge trapped at the surface or in the bulk of an insulator such as alumina causes variations in potential within the substrate, which in turn lead to apparent shifts in binding energies and some line broadening. Charging is not a problem for our oxidized films due to their thickness (on the order of 20 Å) and their intimate contact with the underlying bulk aluminum (conducting) layer. As static charging may easily vary with measurement time, measurements should be accomplished by multiple rapid sweeps through the entire energy range so that any charging will affect all spectral features uniformly. Various methods of compensating for charging of bulk oxide samples have been attempted. These include gold decoration (42,43), simultaneous flooding of the surface with low-energy electrons (44), and referencing to contaminant carbon (36,45), the Al 2p (oxide) line (37), or a convenient Auger feature such as the oxygen KLL transition (31).

Gold decoration, which involves gold vapor deposition on top of all but a small window area of the sample, has in certain cases been found to alter the chemical nature of the surface of the sample (39). Grunthaner

et al. (21) have found the use of electron "flood guns" to be inferior to operating under normal conditions with only the low background of secondary electrons present. An extensive survey of some referencing techniques by Madey et al. (38) agrees with these conclusions, indicating that both gold vapor deposition and electron flooding are inferior as means of compensating for static charging to the method of referencing to the C 1s level, which itself was found to be reliable only to within a standard deviation of 0.41 eV.

Siegbahn et al. (46) were the first to suggest that residual carbon could be used as an internal standard for binding energy measurements. This practice has been rather widespread, although the method is being met with increasing dissatisfaction (47). The most precise and extensive data available on aluminas indicate that the major problem encountered in referencing to the C 1s level of contaminant carbon is the lack of knowledge of its chemical state (37,38). Such contamination might, for example, come from the atmosphere, from pump oil or grease on vacuum seals, or from the support used for mounting since many alumina powders are examined by dusting onto two-sided adhesive tape and mounted in this manner in the spectrometer (10). The intensity, lineshape and even the number of observed C 1s peaks vary considerably from sample to sample. Madey et al. (38) illustrate this point in their work. Jørgensen and Berthou (48) have utilized C 1s referencing in a number of studies. Examining a range of aluminas along with Pitton (36), they reported unsystematic C 1s peak variations over a range of 3 eV. On some samples, two peaks were visible, while on others, only one was present. Variations in Al 2p and O 1s peak positions among the different aluminas, determined by referencing to the

C 1s peak, were in general less than the standard deviation of approximately 0.4 eV that can be expected for C 1s referenced data. When this level of uncertainty is taken into account, most of the variations and differences they report become totally obscured. Comparisons of our data with their results for commercial samples indicate only that films oxidized in liquid H_2O are more like AlO(OH) or aluminum trihydrate than are films oxidized in O_2 or H_2O discharges, or thermally. Their results for O/Al atomic ratios offer little means of comparison since these were obtained by a semi-quantitative analysis of signal amplitudes, a method which appears to be unreliable for even indicating general trends (38).

Ogilvie and Wolberg (37) have proposed using the Al 2p line as an internal standard when working with bulk aluminum oxides, and similar methods of referencing have proven effective with other oxide studies (21). They showed that while standard deviations for absolute positions of the Al 2p, C 1s and O 1s lines are as much as 1.2 eV for measurements on a number of γ-alumina samples, the Al 2p-O 1s difference had a standard deviation of only 0.12 eV for the same measurements. Similar precision was obtained for Zn/Al_2O_3 catalysts. Unfortunately, this type of data is not available for a range of different commercial aluminas which might be compared profitably with our results on alumina films. Fig. 3b illustrates our data using the Al 2p (oxide) peak as the internal reference. This is in a form which may be compared directly to similar data on commercial aluminas as it becomes available. One possible problem of using data in this form to distinguish among various types of aluminas is the lack of uniqueness exhibited from sample to sample. Referencing to the Al 2p (oxide) line tends to obscure peak position variations, as can be seen by comparison with Fig. 3a which represents absolute peak positions. Thus, although

referencing to the Al 2p level for commercial (bulk) aluminas yields precise results, it may reduce peak position variations between samples to the point where closely related aluminas cannot be identified uniquely. Pitton, et al. (36) believe that changes in the chemical nature of aluminum oxides shift the Al and O peaks in the same direction, often by approximately equivalent amounts. This indicates also that absolute differences may be hidden by this type of referencing. More extensive results are necessary to determine the value of this technique with regard to aluminas.

Wagner (31) has suggested a different type of internal reference when working with oxides that would not result in obscuring important peak position differences. He proposes the use of an "Auger parameter", this being the difference in positions between an XPS peak of interest and a convenient Auger transition. Auger lines frequently exhibit far larger chemical shifts than photoelectron lines, mainly because they are more strongly affected by extra-atomic relaxation energies. Chemical shifts over a range of 6.8 eV have been observed for the Al(KLL) Auger peak as the aluminum oxidation state varies from zero to +3 (49). Fig. 4 shows data for the Al 2p, O 1s and O 2s levels referenced to the O(KLL) Auger transition for films oxidized in an O_2 discharge, thermally in O_2-enriched air, and in liquid H_2O. In order that data for the various electronic levels can be presented using a common energy axis, the relevant peak position difference for the O_2 discharge sample is placed at zero and differences for the other samples related to it. This figure indicates that referencing to an Auger transition would be an effective means of interpreting XPS results of metal oxides (such as aluminas). Again, however, such data are not yet available to allow comparisons.

4. Conclusions

In summary, we have presented results for XPS investigations of thin alumina layers made by oxidizing the top few atomic layers of evaporated aluminum films. Oxidation was carried out via a number of methods which have been utilized previously in IETS studies, and these variously oxidized samples compared by means of analyzing peak positions, peak widths, and relative O/Al concentration ratios. As anticipated, distinct spectral differences were apparent between the various types of alumina films. The effects of adding halogens to the surface were observed also. Heating was shown to cause similar, significant sharpening of chemical state distributions for oxygen in both thermally oxidized samples and samples heated in an inert atmosphere after oxidation in an O_2 discharge. No generalized correlations could be made, however, between peak positions and either chemical state distributions (peak widths) or extents of hydration (O/Al ratios). No comparisons can be made with XPS results for commercial aluminas as yet due to the lack of reliable data on bulk samples. Internal referencing to an Auger transition or between Al and O XPS lines appear to be the most promising means of producing precise, accurate results for bulk aluminas, but more results are required before definitive evaluations of these methods applied to aluminas can be accomplished. As reliable XPS results on commercial samples become available, comparisons may then be readily made with the data for thin alumina films presented here. One important comparison can be made immediately, however. Our results indicate that the chemical nature of thermally oxidized films is similar to that of alumina films prepared in an O_2 or H_2O discharge. Thus, IETS studies utilizing discharge-grown oxides might be

compared directly to studies with thermally grown oxides. This is important since thermal oxide films have been related to commercial γ-alumina by catalytic studies (50).

The current study reveals important information on the chemical nature of various thin alumina films, which can be added to information already available on many of the physical properties of similar films. Similarities and differences resulting from different oxidation procedures are now apparent, allowing more accurate comparisons among IETS studies done on various alumina surfaces. Finally, although further studies are certainly necessary, the current study provides significant information which should allow comparisons among IETS studies done on alumina films and studies on commercial bulk aluminas when additional reliable XPS data are available for commercial samples.

Acknowledgment

We appreciate the very valuable advice and assistance of Dr. B. F. Lewis. Financial support by the National Science Foundation under Grant Number ENG78-16927 is gratefully acknowledged.

References

1. E.g., J. Lambe and R. C. Jaklevic, Phys. Rev. 165, 821 (1968). Inelastic Electron Tunneling Spectroscopy, T. Wolfram, ed., Springer-Verlag, N.Y., 1978.
2. P. K. Hansma, W. C. Kaska and R. M. Laine, J. Am. Chem. Soc. 98, 6064 (1976).
3. H. E. Evans, W. M. Bowser and W. H. Weinberg, Surface Sci. 85, L497 (1979).
4. H. E. Evans and W. H. Weinberg, J. Chem. Phys. 71, 1537 (1979).
5. H. E. Evans and W. H. Weinberg, J. Chem. Phys. 71, 0000 (1979).
6. W. M. Bowser and W. H. Weinberg, in preparation.
7. H. E. Evans and W. H. Weinberg, J. Am. Chem. Soc. (in press).
8. B. C. Lippens and J. J. Steggerda, Physical and Chemical Aspects of Adsorbents and Catalysts, B. G. Linsen, ed., p. 171, Academic Press, N.Y., 1970.
9. K. Wefers and G. M. Bell, Technical Paper # 19, Alcoa Research Laboratories, 1972.
10. H. Vinek, J. Latzel, H. Noller and M. Ebel, J. Chem. Soc. Faraday Trans. I 74, 2092 (1978).
11. W. H. Weinberg, Ann. Rev. Phys. Chem. 29, 115 (1978).
12. W. M. Bowser and W. H. Weinberg, Surface Sci. 64, 377 (1977).
13. Y. Scarlatos, R. C. Barker and G. L. Haller, Surface Sci. 43, 353 (1974).
14. J. T. Hall and P. K. Hansma, Surface Sci. 77, 61 (1978).
15. E.g., M. Cardona and L. Ley, Topics in Applied Phys. 26, (1978).
16. F. J. Grunthaner, NBS Special Publication 400-23, p. 151, March, 1979.
17. K. S. Kim and N. Winograd, Surface Sci. 43, 625 (1974).
18. K. S. Kim, J. J. O'Leary and N. Winograd, Anal. Chem. 45, 2214 (1973).

19. S. Evans, J. Chem. Soc. Faraday Trans. II 71, 1044 (1975).

20. K. S. Kim, N. Winograd and R. E. Davis, J. Am. Chem. Soc. 93, 6296 (1971).

21. F. J. Grunthaner, P. J. Grunthaner, R. P. Vasquez, B. F. Lewis, J. Maserjian and A. Madhukar, J. Vac. Sci. Technol. (submitted).

22. C. W. B. Martinson, L. G. Petersson, S. A. Flodström and S. B. M. Hagström, Proceedings of the 7th International Vacuum Congress and Proceedings of the 3rd International Conference on Solid Surfaces, Vienna, 1977, p. 869, F. Berger and Söhne, Vienna, 1977.

23. S. A. Flodström, C. W. B. Martinsson, R. Z. Bachrach, S. B. M. Hagström and R. S. Bauer, Phys. Rev. Letters 40, 907 (1978).

24. S. A. Flodström, R. Z. Bachrach, R. S. Bauer and S. B. M. Hagström, Phys. Rev. Letters 37, 1282 (1976).

25. R. E. Herfert, Technical Report AFML-TR-76-142, Northrup Corporation, August, 1976.

26. D. J. Stirland and R. W. Bicknell, J. Electrochem. Soc. 106, 481 (1959).

27. P. Bodson, F. Bouillon and M. Jardinier-Offergeld, Metallurgie 6, 47 (1966).

28. L. Harris, J. Opt. Soc. Am. 45, 27 (1955).

29. N. M. D. Brown, R. B. Floyd and D. G. Walmsley, J. Chem. Soc. Faraday Trans. II 75, 17 (1979).

30. A. Barrie, Chem. Phys. Letters 19, 109 (1973).

31. C. D. Wagner, J. Chem. Soc. Faraday Discussions 60, 291 (1976).

32. P. Lorenz, J. Finster, G. Wendt, J. V. Salyn, E. K. Zumadilov and V. I. Nefedov, J. Elec. Spec. 16, 267 (1979).

33. K. Hirokawa, F. Honda and M. Oku, J. Elec. Spec. 6, 333 (1975).

34. W. J. Bernard and J. J. Randall, J. Electrochem. Soc. 107, 483 (1960).

35. W. Vedder and D. A. Vermilyea, Trans. Faraday Soc. 65, 561 (1969).

36. O. Pitton, C. K. Jørgensen and H. Berthou, Chimia 30, 540 (1976).

37. J. L. Ogilvie and A. Wolberg, Appl. Spec. 26, 401 (1972).

38. T. E. Madey, C. D. Wagner and A. Joshi, J. Elec. Spec. 10, 359 (1977).

39. C. Defossé, P. Canesson, P. G. Rouxhet and B. Delmon, J. Catal. 51, 269 (1978).

40. C. K. Jørgensen and H. Berthou, J. Chem. Soc. Faraday Discussions 54, 269 (1972).

41. A. M. Rubinshtein, K. I. Slovetskaya, T. R. Brueva and E. A. Federovskaya, Dokl. Akad. Nauk. SSSR. 167, 1308 (1966).

42. C. R. Ginnard and W. M. Riggs, Anal. Chem. 46, 1306 (1974).

43. D. S. Urch and M. Webber, J. Elec. Spec. 5, 791 (1974).

44. D. A. Stephenson and N. J. Binkowski, J. Non-Cryst. Solids 22, 399 (1976).

45. W. P. Dianis and J. E. Lester, Anal. Chem. 45, 1416 (1973).

46. K. Siegbahn, C. Nordling, A. Fahlman, R. Nordberg, K. Hedman, G. Johansson, T. Borgmark, S. Karlsson and B. Lindberg, ESCA, Almquist and Wiksells, Uppsala, 1967.

47. C. R. Brundle, Appl. Spec. 25, 8 (1971).

48. C. K. Jørgensen and H. Berthou, Chem. Phys. Letters 31, 416 (1975).

49. J. E. Castle, L. B. Hazell and R. Whitehead, J. Elec. Spec. 9, 247 (1976).

50. P. K. Hansma, D. A. Hickson and J. A. Schwarz, J. Catal. 48, 237 (1977).

51. J. H. Scofield, J. Elec. Spec. 8, 129 (1976).

52. V. I. Nefedov, N. P. Sergushin, I. M. Bond and M. B. Trzhaskovskaya, J. Elec. Spec. 2, 383 (1973).

53. C. D. Wagner, Anal. Chem. 44, 1050 (1972).

Table 1

Some Aluminum Oxides and Hydroxides

Preferred Names	Form
Gibbsite or α-alumina trihydrate	$Al(OH)_3$
Bayerite or β-alumina trihydrate	$Al(OH)_3$
Nordstrandite	$Al(OH)_3$
Boehmite or α-alumina monohydrate	AlO(OH)
Diaspore or β-alumina monohydrate	AlO(OH)
ρ-alumina, χ-alumina, η-alumina, γ-alumina	$Al_2O_3 \cdot nH_2O$, $0 < n < 0.6$ (dehydrated below 600 C)
κ-alumina, θ-alumina, δ-alumina	"nearly" anhydrous Al_2O_3 (dehydrated between 900 - 1000 C)
Corundum or α-alumina	Al_2O_3

Table 2

Alumina Film Preparation

Sample Type	Oxidation Procedure	Reference to Use in IETS
1. O_2 Discharge	Exposed to plasma discharge of O_2 (Matheson Research Grade, 99.99%) for 15 minutes.	Ref. (12)
2. Thermal O_2	Heated in O_2 enriched air at 600 K for 10 minutes.	Ref. (14)
3. H_2O Discharge	Exposed to plasma discharge of tripley distilled H_2O for 20 minutes.	Ref. (12)
4. Liquid H_2O	Immersed in liquid H_2O for a few seconds, then dried immediately in a stream of N_2.	Ref. (13)
5. Heated	Oxidized as type 1, then heated in Ar (Matheson Prepurified Grade, 99.998%) at 850 K for 10 minutes.	

Table 3

Binding Energy Differences Compared to Bulk Al 2p in eV

Sample	Al 2p (oxide)	Al 2s	O 1s	O 2s	O (Auger)	C 1s	F 1s
O_2 Discharge	2.54	47.36	459.87	-48.40	906.72	213.10	613.83
Thermal O_2	2.42	47.21	459.56	-48.57	906.87	-	-
H_2O Discharge	2.66	-	459.87	-48.53	-	213.4-	613.94
Liquid H_2O	2.77	47.62	460.49	-47.42	907.08	-	-
Heated in Ar	3.10	-	460.13	-47.81	-	213.88	614.57
Exposed to HF	2.67	-	-	-	-	-	614.16
Exposed to HCl	2.89	47.70	460.39	-47.99	-	213.46	614.16
Fe Impurity	2.06	47.01	459.45	-48.00	904.13	-	-

Table 4

Oxygen-to-Aluminum Concentration Ratios

Sample	(Intensity O 1s/Intensity Al 2p)* $\frac{1}{5.4^a}$
O_2 Discharge	1.56 ± 0.04
Thermal O_2	1.52
H_2O Discharge	1.60
Liquid H_2O	1.85
Heated in Ar	1.41

[a]This factor takes into account photo-ionization cross-section differences between the O 1s and Al 2p levels. This value was taken from Ref. (51). Other authors have reported values of 5.6 (39), 4.6 (52), 3.7 (53) and 3.3 (40).

Table 5

Peak Widths (FWHM), eV

Sample	Al 2p	Al 2s	O 1s
O_2 Discharge	1.65	2.2	2.6
Thermal O_2	1.7	2.3	2.25
H_2O discharge	1.7	-	2.5
Liquid H_2O	1.65	2.2	2.55
Heated in Ar	1.6	-	2.2
Exposed to HF	1.7	-	-
Exposed to HCl	1.7	2.2	3.0
Fe Impurity	1.9	2.2	1.7

Figure Captions

Fig. 1: Representative spectra for the O 1s and Al 2p levels for a sample oxidized in a plasma discharge of O_2.

Fig. 2: Wide spectral scans for (a) a sample oxidized in an O_2 discharge and exposed to HF, and (b) a sample with significant amounts of Fe contamination due to residual ferrocene in the system.

Fig. 3: Peak positions for the Al 2p (oxide), Al 2s (oxide), O 1s, O 2s, O (Auger), C 1s and F 1s levels referenced to the Al 2p (bulk) line for the various samples.

Fig. 4: As in Fig. 3, except all peak positions are referenced to the Al 2p (oxide) line.

Fig. 5: Use of the Auger parameter to distinguish between various types of aluminas: positions of the Al 2p, O 1s and O 2s peaks relative to an oxygen Auger line for samples prepared in an O_2 discharge (■), thermally in O_2-enriched air (◇) and in liquid H_2O (▽).

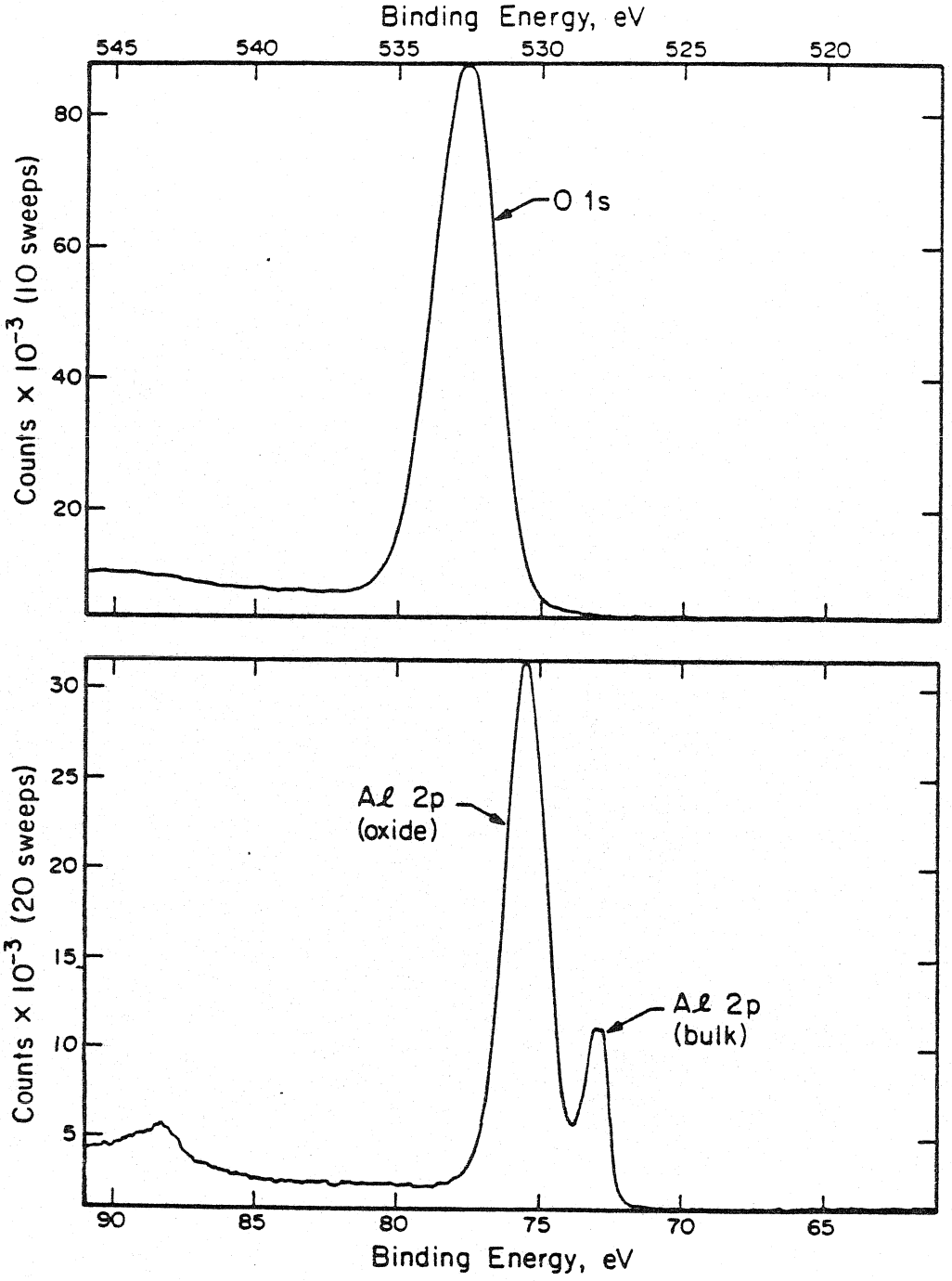
Binding Energy, eV
545
540
535
530
525
520
80
60
40
20
Counts x 10^{-3} (10 sweeps)
O 1s
30
25
20
15
10
5
Counts x 10^{-3} (20 sweeps)
Aℓ 2p
(oxide)
Aℓ 2p
(bulk)
90
85
80
75
70
65
Binding Energy, eV

Fig. 1

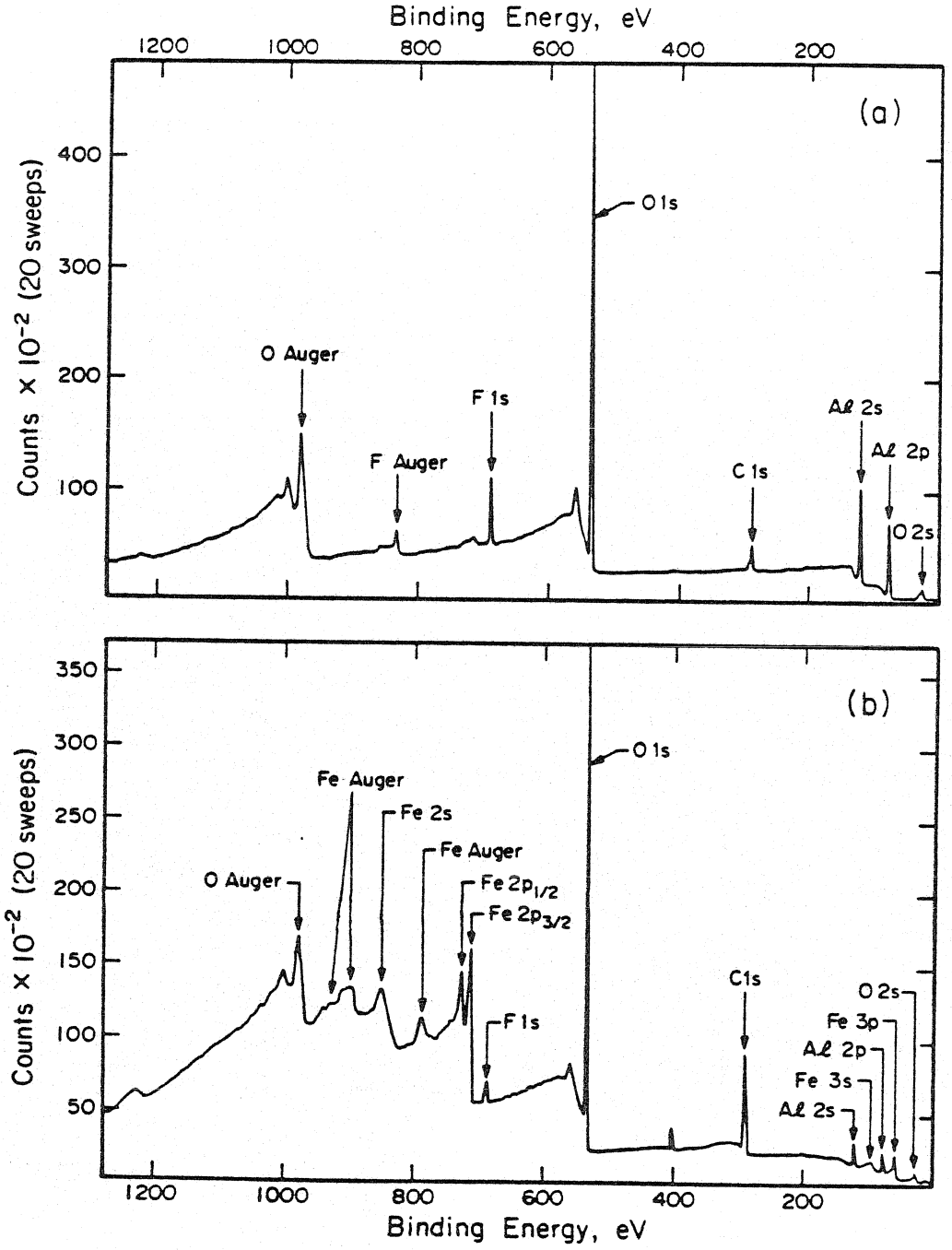
Binding Energy, eV
1200
1000
800
600
400
200
(a)
Counts x 10⁻² (20 sweeps)
400
300
200
100
O 1s
O Auger
F 1s
F Auger
C 1s
Al 2s
Al 2p
O 2s
(b)
350
300
250
200
150
100
50
O 1s
Fe Auger
Fe 2s
Fe Auger
O Auger
Fe 2p1/2
Fe 2p3/2
F 1s
C1s
O 2s
Fe 3p
Al 2p
Fe 3s
Al 2s
Binding Energy, eV

Fig. 2

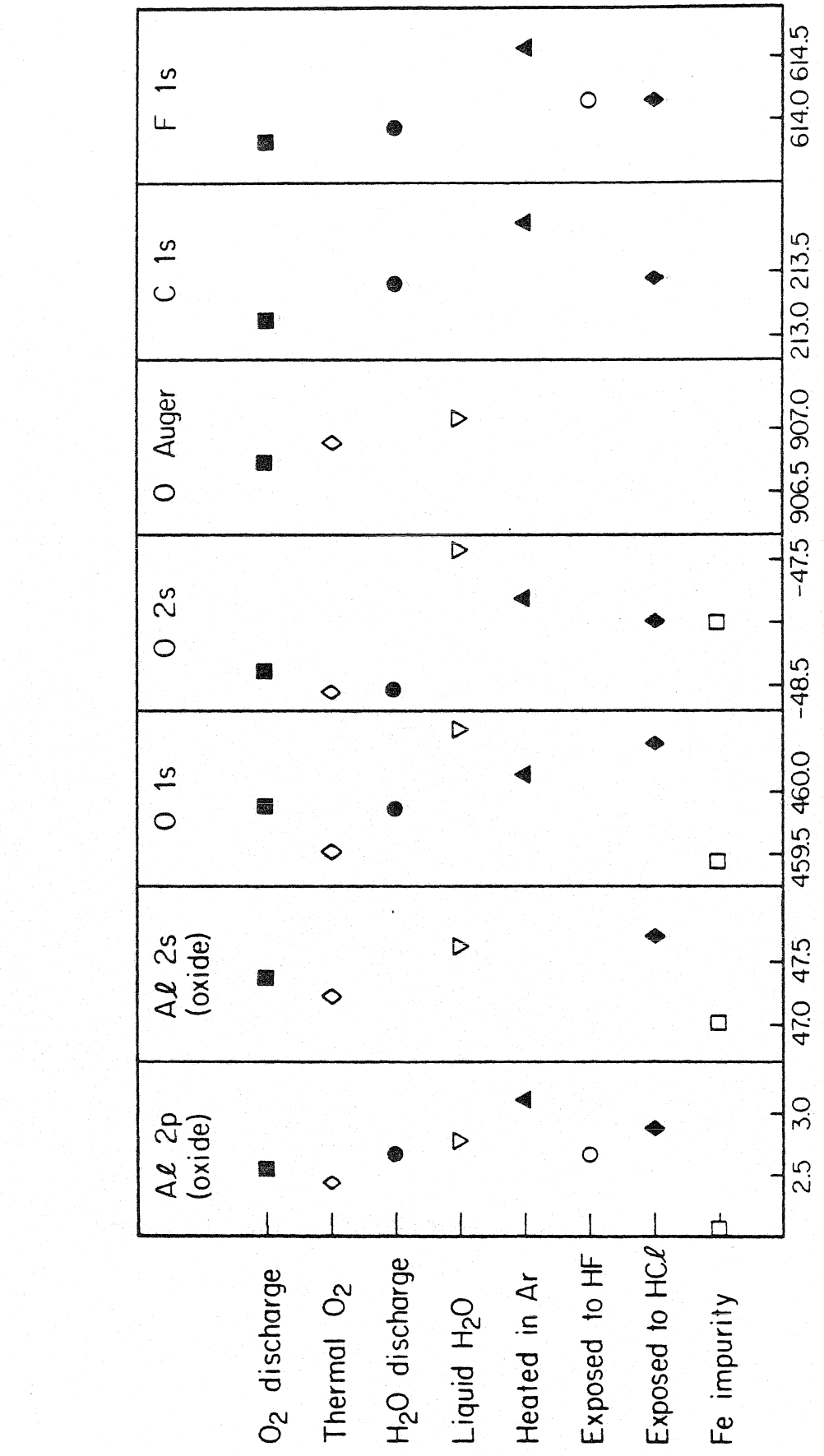
Aℓ 2p (oxide)
Aℓ 2s (oxide)
O 1s
O 2s
O Auger
C 1s
F 1s
O2 discharge
Thermal O2
H2O discharge
Liquid H2O
Heated in Ar
Exposed to HF
Exposed to HCℓ
Fe impurity
2.5 3.0 47.0 47.5 459.5 460.0 -48.5 -47.5 906.5 907.0 213.0 213.5 614.0 614.5
Differences From Aℓ 2p Bulk Peak, eV

Fig. 3

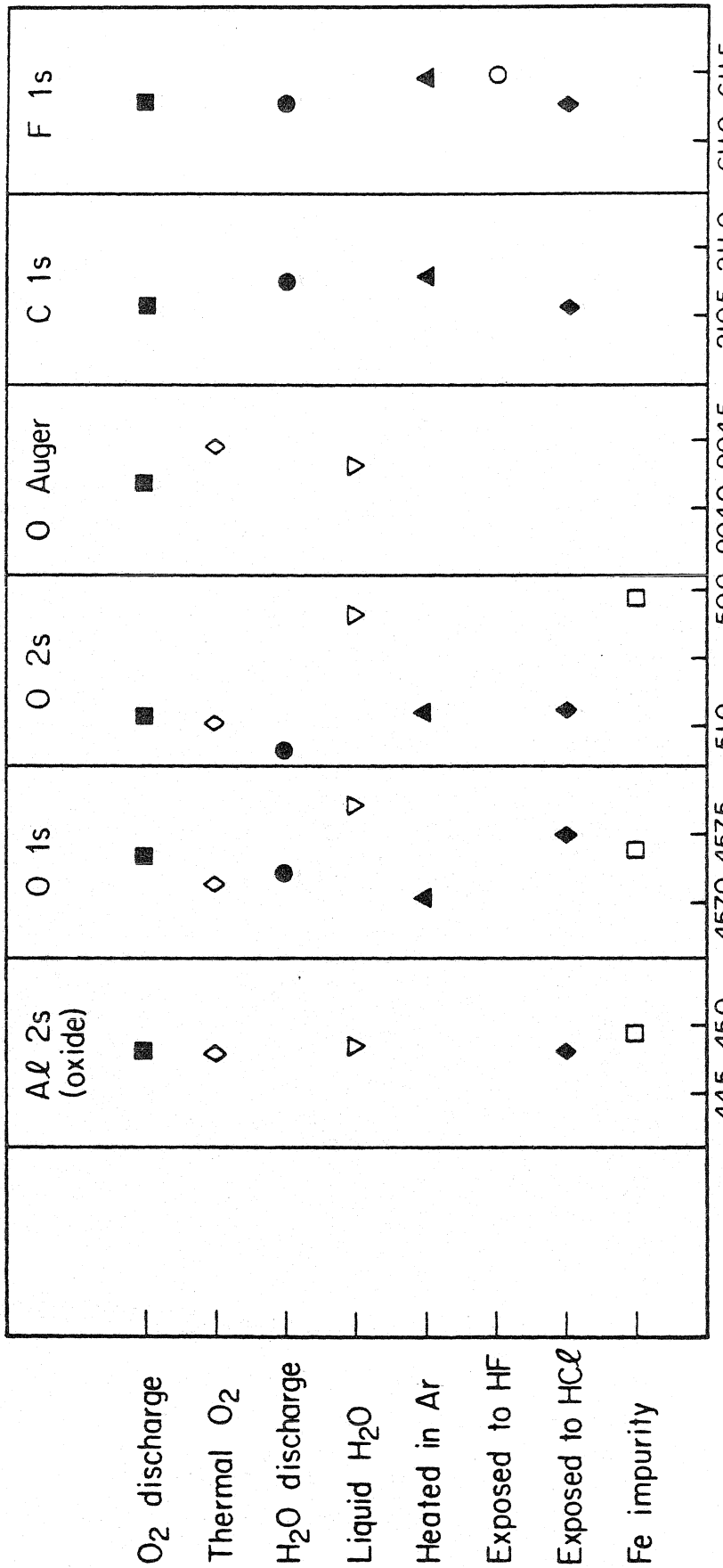
Aℓ 2s (oxide)
O 1s
O 2s
O Auger
C 1s
F 1s
O2 discharge
Thermal O2
H2O discharge
Liquid H2O
Heated in Ar
Exposed to HF
Exposed to HCℓ
Fe impurity
44.5 45.0 457.0 457.5 -51.0 -50.0 904.0 904.5 210.5 211.0 611.0 611.5
Differences From Aℓ 2p Oxide Peak, eV

Fig. 4

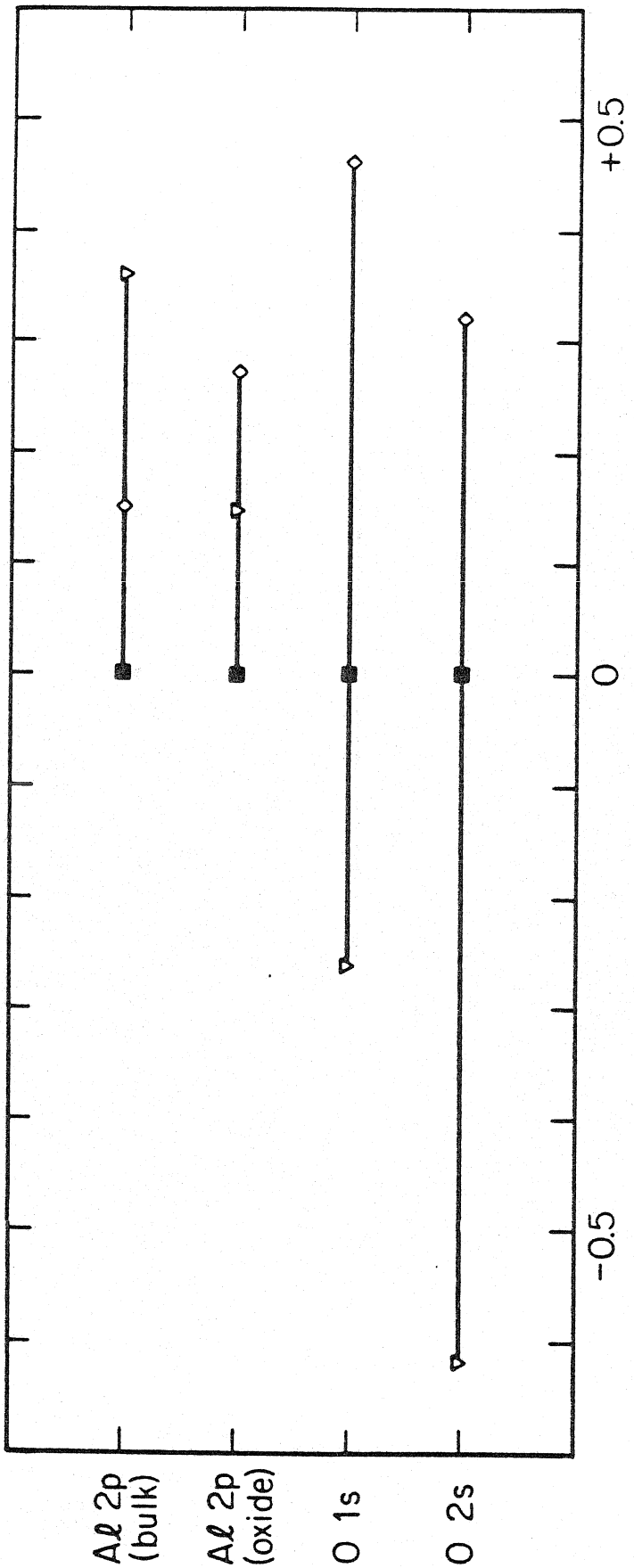
Aℓ 2p (bulk)
Aℓ 2p (oxide)
O 1s
O 2s
-0.5
0
+0.5
Differences From Oxygen Auger Line, eV
(relative to O_2 discharge sample)

Fig. 5

Appendix E

The Adsorption of Ethanol on Silver Clusters Supported on Alumina

Abstract

The adsorption of ethanol on islands of Ag supported on a surface of Al_2O_3 has been investigated utilizing both inelastic electron tunneling spectroscopy (IETS) to probe the vibrational structure of the adsorbed species, and transmission electron microscopy to characterize some of the physical properties of the solid surface. Results are reported for the number and average size of Ag clusters on the surface as the amount of Ag is varied up to a statistically-averaged coverage of approximately 10 Å. Vibrational spectra are shown for saturation coverage of ethanol as a function of Ag coverage. Peak shifts expected to arise due to the difference in electronegativities between Al and Ag are observed for the surface ethoxide species which form upon adsorption.

Inelastic electron tunneling spectroscopy (IETS) has been shown previously to be an effective tool for probing the vibrational structure of a number of reactants and reaction intermediates on metal oxide catalytic surfaces (1). Hansma and his co-workers (2) have reported recently the application of IETS to the study of CO chemisorbed onto alumina supported Rh particles. These results, together with unpublished work in our own laboratory for CO chemisorption on supported Ni, have enhanced the worth of IETS as an experimental tool significantly by increasing its potential applications to include at least some types of catalytic reactions which occur over supported metal catalysts. Due to the widespread industrial use and economic importance of supported metal catalysts, the present work was undertaken to expand further the range of supported metal catalytic systems which might be examined profitably utilizing IET spectroscopy. Specifically, we report here an IETS study of ethanol adsorbed on alumina supported Ag. This system represents one step in the oxidation reaction of alcohols to aldehydes over silver catalysts and is fundamentally different from the CO reactions on the Group VIII metals that have been examined previously.

Our experimental techniques, as well as the phenomenological and theoretical aspects of tunneling spectroscopy, have been reported in detail previously (3). Our model catalyst surfaces were prepared by oxidizing the top 20 to 30 Å of a freshly evaporated Al film in a plasma discharge of O_2, followed by the evaporation of small amounts of Ag onto the thin oxide film. The amount of Ag deposited was monitored with a quartz crystal oscillator located approximately one-third of the distance to the sample

from the evaporation source. This geometry permitted the oscillator, which is sensitive to changes on the order of approximately 0.5 Å in statistical coverage of Ag, to reflect accurately amounts of Ag at the sample surface with approximately ten times this sensitivity. Measurements were made on samples where the statistical coverage of Ag was varied up to approximately 10 Å.

The structure of Ag on the aluminum oxide was determined via transmission electron microscopy (TEM). The electron microscopy samples were prepared in our bell jar using carbon films supported on 400 mesh Cu grids as substrates. The Al and Ag evaporations and the plasma oxidation steps were identical to those for the tunneling samples, and TEM measurements were made over the same range of Ag coverage. The beam currents and voltages which were employed, 2 - 3 μA and 60 - 80 keV, respectively, were substantially below the levels that might be expected to stimulate Ag agglomeration or migration as judged from other studies (4). Typical results are illustrated in Fig. 1. The experimentally determined relationship between the number of Ag clusters and their average diameter and the statistical Ag coverage is shown in Fig. 2. The solid lines in Fig. 2 indicate only a "best fit" to the available data points; the line showing average particle diameter was drawn to include also a point approximately representing the atomic diameter of Ag near zero Ag coverage.

At room temperature, ethanol chemisorbs dissociatively on alumina to form aluminum ethoxide (5). Similar results have been noted on other surfaces (6), and the same type of structure can be expected to form on Ag also. Even though ethoxide formation occurs on both Ag and alumina, slight differences between the two species are expected to be manifest in their vibrational spectra. Takezawa and Kobayashi (7) have studied alcohol

adsorption on a number of surfaces and have established that hydrocarbon vibrational frequencies of surface ethoxides can be expected to increase with increasing electronegativity of the surface metal ion. The electronegativities of Ag and Al are 1.93 and 1.61, respectively, on the Pauling scale (8), and thus we expect slight shifts upward in frequency for the CH vibrations of silver ethoxide relative to the corresponding vibrational frequencies of the ethoxide formed on Al ions. Since even at the highest Ag coverages studied, much of the alumina surface is still available for ethanol adsorption, we anticipate spectra resulting from the superposition of vibrations from both Ag and Al ethoxide.

Spectra at room temperature for saturation coverage of ethanol over a range of Ag coverages are shown in Figs. 3 and 4. The low intensities of the hydrocarbon peaks even at saturation coverage result from the blockage of additional adsorption sites below 400 to 500 K by H_2O or OH formed during ethanol adsorption (5,6). Few noticeable changes occur in the spectra up to a statistical Ag coverage of 2.5 Å, probably due to the extremely large ratio of Al to Ag adsorption sites at these low coverages. As Ag coverage is increased beyond this point, however, features due to the Ag ethoxide species become more prominent. In Fig. 3, which shows the CH_2 and CH_3 deformation bands (at 1472, 1440, 1380 and 1360 cm^{-1} on alumina) (5,9), we can observe the decreasing intensity of the 1360 cm^{-1} band as well as the growth of new structure between 1380 and 1440 cm^{-1}, and at approximately 1470 cm^{-1} and above. Similar effects are evident in Fig. 4, which shows the CH stretching bands. These bands appear at approximately 2863, 2915 and 2952 cm^{-1} for the Al ethoxide structure. Again, as Ag coverage is increased, we can observe the growth

of new structure between 2865 and 2900 cm^{-1}, 2920 and 2950 cm^{-1}, and at approximately 2998 cm^{-1}.

Although not shown in Figs. 3 and 4, there are two other spectral features that should be mentioned. In previous work concerning ethanol adsorption on alumina, we have reported the observation of a C-C stretching peak near 911 cm^{-1}; the bulk Al-O stretching band at 935 cm^{-1}; and a broad, rounded peak at approximately 1055 cm^{-1} arising from the overlapping of an out-of-plane C-H bending mode (lower energy) and an Al-O-C stretching vibration (slightly higher energy). As the Ag coverage is increased, the C-C band shifts upward in energy until it is nearly coincident with the bulk Al-O mode. Also, the 1055 cm^{-1} feature becomes significantly sharper. We attribute this to a slight increase in the C-H bending frequency coupled with a decrease in frequency for the Al-O-C mode for molecules adsorbed on Ag relative to those on Al. These results are also consistent with our expectations based on the work of Takezawa and Kobayashi (7).

As expected due to the relative electronegativities of Ag and Al, ethanol adsorption on supported Ag produces an ethoxide the CH vibrational frequencies of which appear at slightly higher energies than the corresponding modes of ethoxide formed on the alumina support. The IET technique has been shown to be capable of distinguishing between these two very similar ethoxide species. More significantly, the observation of ethanol adsorption on alumina supported Ag opens up an entirely new class of important supported metal catalytic systems which can be studied utilizing IETS, thus demonstrating the increasing versatility and value of this spectroscopic technique.

ACKNOWLEDGMENTS

We wish to express our appreciation to Mr. Patrick F. Koen for his valuable technical assistance in obtaining the transmission electron micrographs.

References

1. J. Lambe and R. C. Jaklevic, Phys. Rev. 165, 821 (1968); B. F. Lewis, M. Mosesman and W. H. Weinberg, Surface Sci. 41, 142 (1974).

2. P. K. Hansma, in Inelastic Electron Tunneling Spectroscopy, p. 186 (T. Wolfram, Ed.), Springer-Verlag, N.Y., 1978;
P. K. Hansma, W. C. Kaska and R. M. Laine, J. Am. Chem. Soc. 98, 6064 (1976).

3. W. H. Weinberg, Ann. Rev. Phys. Chem. 29, 115 (1978).

4. J. W. Sprys and Z. Mencik, J. Catal. 40, 290 (1975).

5. H. E. Evans and W. H. Weinberg, submitted for publication;
R. G. Greenler, J. Chem. Phys. 37, 2094 (1962);
H. Arai, Y. Saito and Y. Yoneda, Bull. Chem. Soc. Jap. 40, 731 (1967).

6. S. L. Parrott, J. W. Rogers, Jr. and J. M. White, Appl. Surface Sci. 1, 443 (1978);
B. A. Morrow, L. W. Thompson and R. W. Witmore, J. Catal. 28, 332 (1973).

7. N. Takezawa and H. Kobayashi, J. Catal. 25, 179 (1972); 28, 335 (1973).

8. A. L. Allred, J. Inorg. Nucl. Chem. 17, 215 (1961).

9. R. C. Wilhoit, J. R. Burton, Fu-Tien Kuo, Sui-rong Huang and A. Viquesnel, J. Inorg. Nucl. Chem. 24, 851 (1962).

Figure Captions

Fig. 1: Transmission electron micrographs of Ag particles on alumina films for statistically averaged Ag coverages of (a) 2.5 Å, and (b) 10.0 Å.

Fig. 2: Number of Ag particles and their average diameters as a function of Ag coverage on the alumina surface.

Fig. 3: IET spectra in the range 1200 to 1600 cm^{-1} of ethanol adsorbed on Ag/Al_2O for statistical Ag coverages of (a) 0 Å, (b) 2.5 Å, (c) 5.0 Å, and (d) 10.0 Å.

Fig. 4: IET spectra in the range 2700 to 3100 cm^{-1} of ethanol adsorbed on Ag/Al_2O_3 for statistical Ag coverages of (a) 0 Å, (b) 2.5 Å, (c) 5.0 Å, and (d) 10.0 Å.

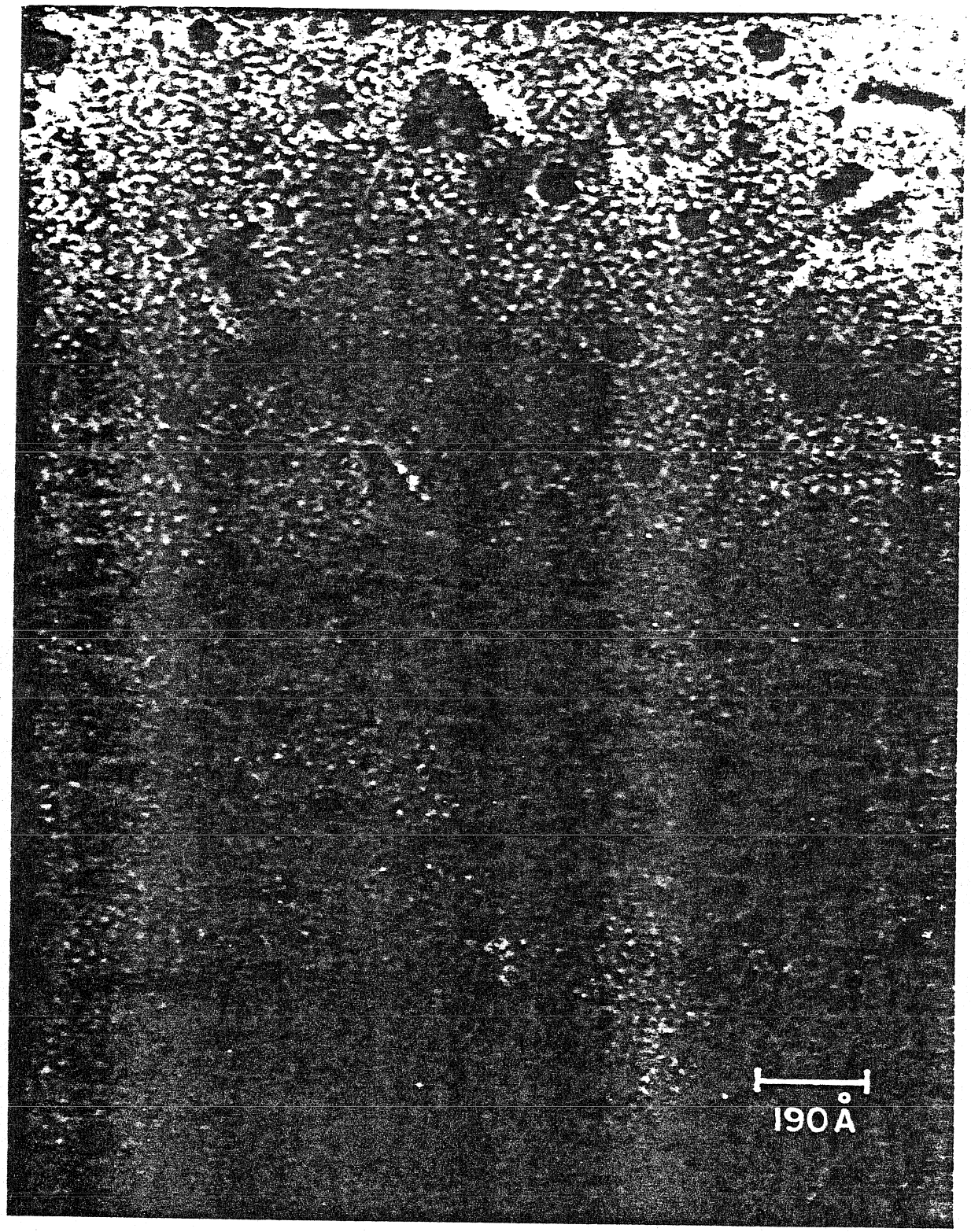

Fig. 1a

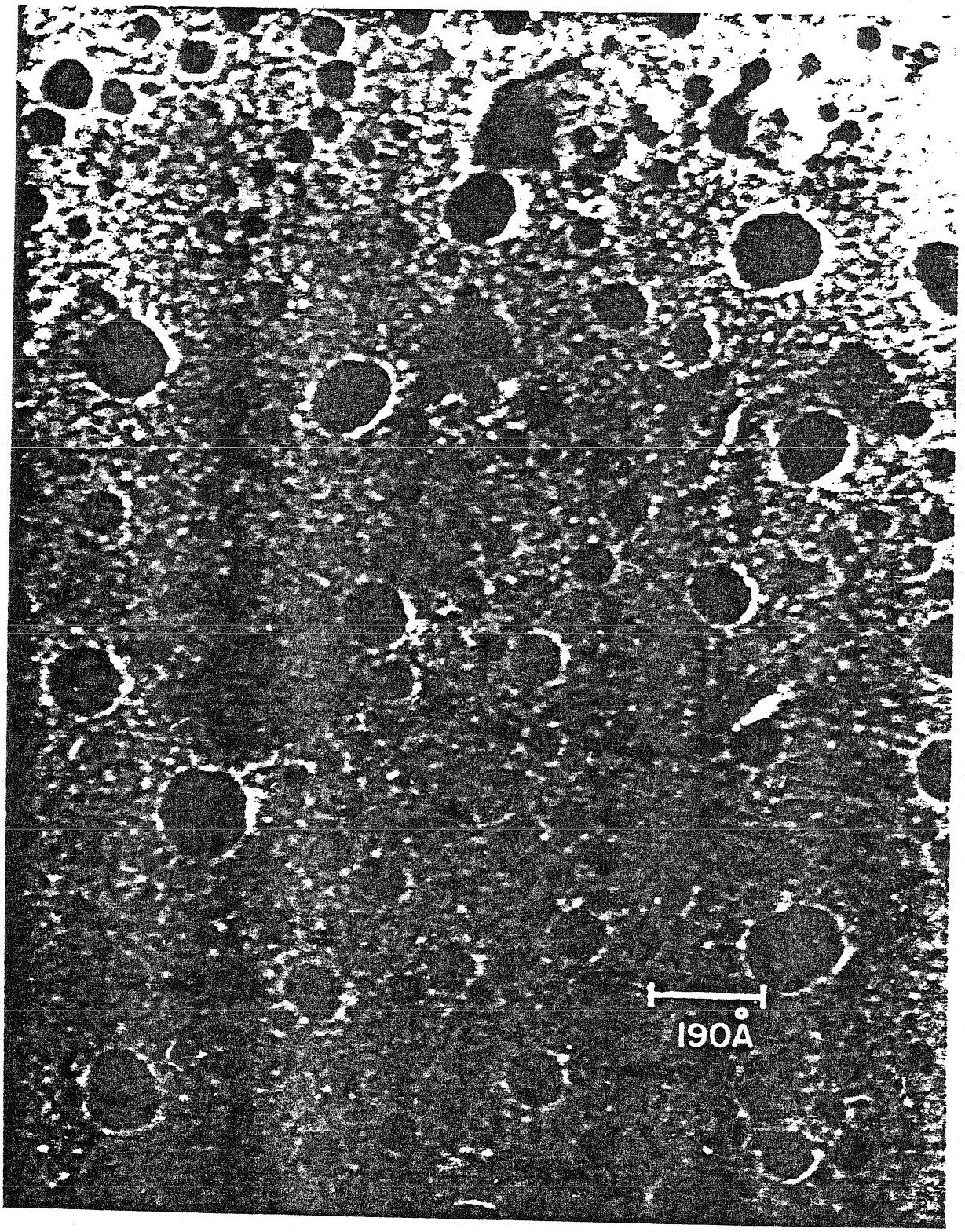

Fig. 1b

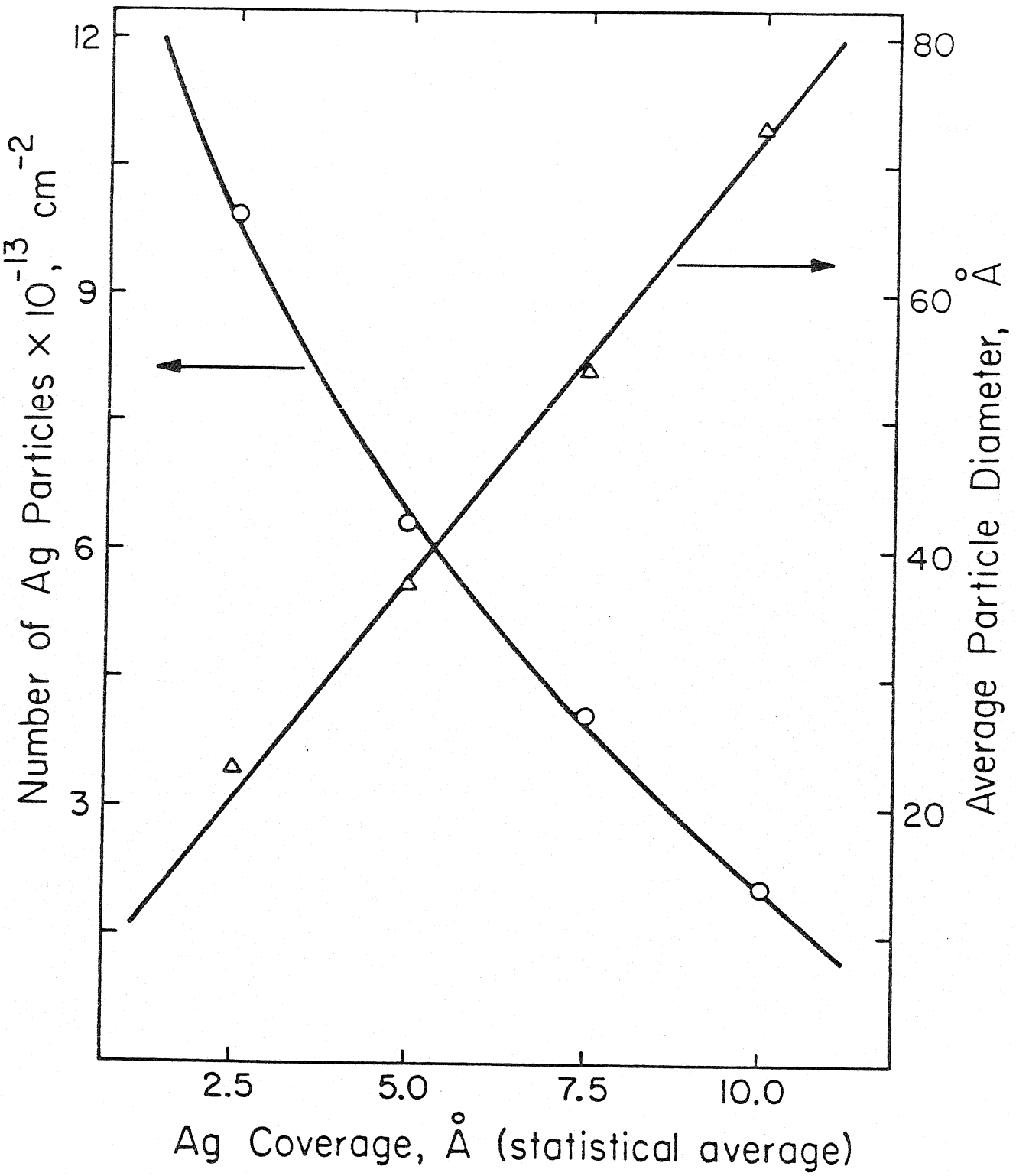
Number of Ag Particles x 10^{-13}, cm^{-2}
Average Particle Diameter, Å
Ag Coverage, Å (statistical average)
12
9
6
3
80
60
40
20
2.5
5.0
7.5
10.0

Fig. 2

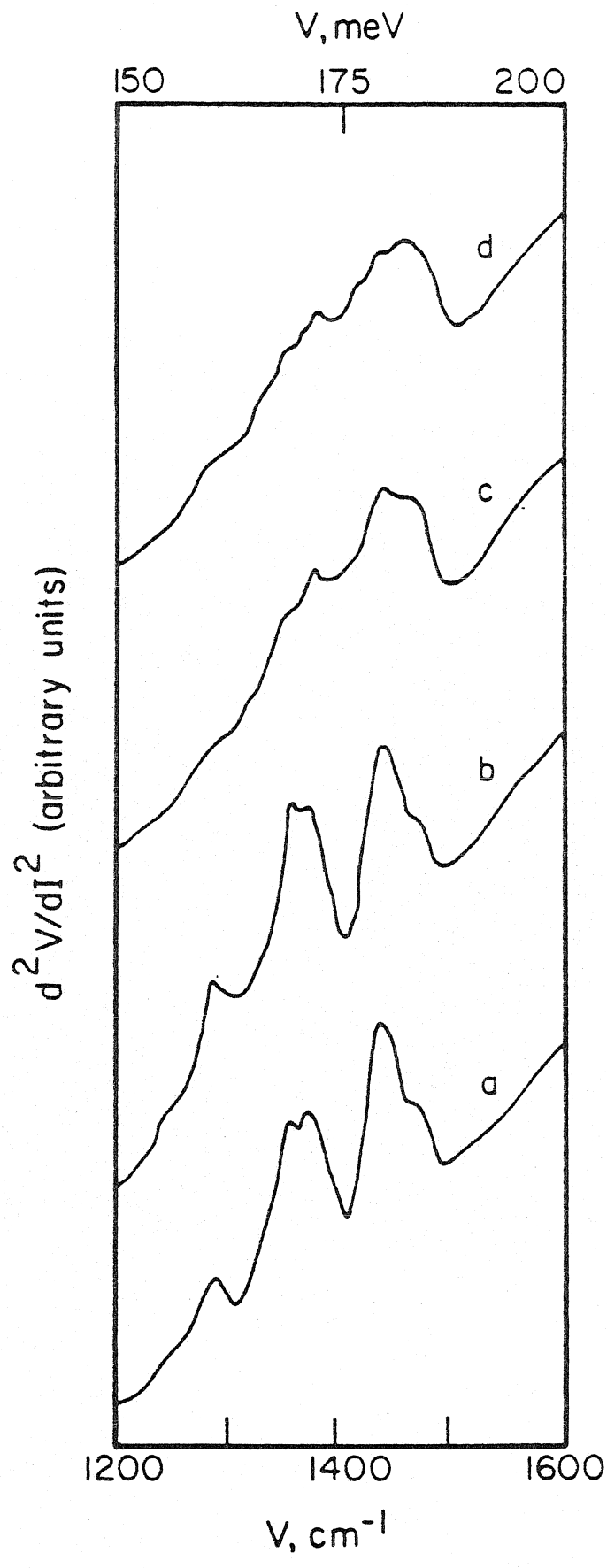
V, meV
150
175
200
d
c
b
a
d^2V/dI^2 (arbitrary units)
1200
1400
1600
V, cm^{-1}

Fig. 3

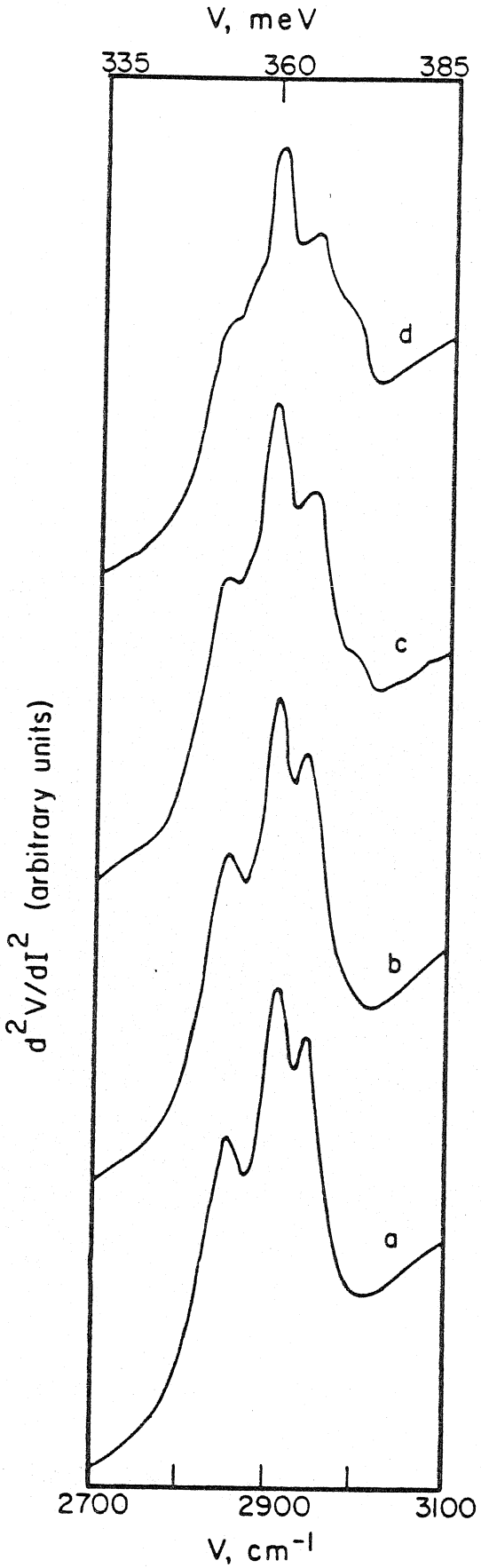
V, meV
335
360
385
d
c
b
a
d^2V/dI^2 (arbitrary units)
2700
2900
3100
V, cm^{-1}

Fig. 4